# Identification of low-valent iron-porphyrins: Electronic structure and reactivity towards $CO_2$ reduction

Dissertation

Zur

Erlangung des Doktorgrades (Dr. rer. nat.)

Der

Mathematische-Naturwissenschaftlichen Fakültat

Der

Rheinischen Friedrich-Wilhelms-Universität Bonn

Vorgelegt von

**Maxime Tarrago**

Aus

**Clamart, Frankreich**

Bonn, 2021

Angefertigt mit Genehmigung der Mathematisch-Naturwissenschäftlichen Fakultat der Rheinischen Friedrich-Wilhelms-Universität Bonn

Erstgutachter: Prof. Dr. Frank Neese
Zweitgutachter: Prof. Dr. Stefan Grimme
Tag der Promotion: 27. August 2021
Erscheinungsjahr: 2022

# Abstract

The need to close the carbon cycle becomes urgent as concentration of $CO_2$ in the earth atmosphere increases exponentially. Electrochemically-mediated conversion of $CO_2$ into biofuels is a possible solution to this problem, as it enables storage of energy while using the harmful $CO_2$ feedstock as starting material. Notably, low-valent iron-porphyrins have been established as the best and most selective family of homogeneous catalysts for $CO_2$ reduction into CO, a first step towards the synthesis of biofuel from $CO_2$. The purpose of this research project is to correlate the high activity of [Fe(TPP)] (TPP=tetraphenylporphyrin) towards $CO_2$ reduction with its peculiar electronic structure. With this knowledge in mind, a guideline for the synthesis of efficient and selective catalysts is proposed. To realize this purpose, we investigated the electronic structure of [Fe(TPP)], $[Fe(TPP)]^-$ and $[Fe(TPP)]^{2-}$ using a combination of theoretical chemistry coupled with experimental spectroscopic techniques, such as $^{57}$Fe Mössbauer, magnetometry measurements and X-ray absorption spectroscopy. After unambiguously determining the electronic structure of each of these species, a reactivity study was carried out to establish the correlation between electronic structure and reactivity.

Our results indicate that [Fe(TPP)] is a triplet iron(II) ground state with a quite unique almost three-fold orbital degeneracy of the $d_{xz}$, $d_{yz}$ and $d_{z2}$ orbitals. This peculiar electronic structure leads to a large, unquenched orbital angular momentum lying on the porphyrin plane, as observed experimentally. Comparing spectroscopic data of $[Fe(TPP)]^-$ and $[Fe(TPP)]^{2-}$ to that of [Fe(TPP)] led to the conclusion that the oxidation state of iron remains unchanged upon one- and two-electrons reduction of [Fe(TPP)]. In other terms, $[Fe(TPP)]^-$ and $[Fe(TPP)]^{2-}$ are best described as Fe(II) centers antiferromagnetically coupled with a porphyrin ligand radical and diradical, respectively. In fact, our reactivity study shows how the non-innocent porphyrin ligand in $[Fe(TPP)]^{2-}$ plays a major role in the high reactivity of the complex towards $CO_2$ reduction, by acting as an electron reservoir able to transfer electrons to the $CO_2$ molecule *via* the metal center. We stress that ligand non-innocence is a common feature in $CO_2$ reduction catalysts, but its role relative to catalytic activity has not yet received sufficient attention.

# Table of content

# Introduction

The increasing atmospheric concentration of greenhouse gases due to human activities has become an urgent environmental issue with multiple ramifications.[1,2,3] Among those greenhouse gases, one of the major concerns is $CO_2$, and its global atmospheric concentration has risen to an all-time record of 411 ppm in 2019.[4] To revert this trend while limiting the effect on human activity, industrialized societies need to adopt complementary measures.[5] The most mature technologies at our disposal consist of carbon capture and sequestration (CCS).[6] Those technologies in principle allow capture and storage of $CO_2$ in geological layers. However, the geological storage which follows a large-scale $CO_2$ capture may have unknown long-term ecological consequences. A seductive solution to circumvent this problem would be to use the $CO_2$ feedstock as a starting material for chemical manufacturing, in place of other hydrocarbons.[7] However, this solution may not be economically viable until the prices of other fossil fuels has risen significantly.

It is critical that the part of fossil fuels in the energy production decreases, in benefit of renewable sources of energy, among which photovoltaics[8] and wind turbines are the most plausible candidates due to their economic and technical maturity. However, due to the instability of the energy outputs of these sources, the need to indirectly store electrical energy arises. To date, the most scalable way to do so is to convert electric energy into chemical energy. In this regard, electrocatalytic reduction of $CO_2$ into biofuel may be a promising way to solve the problem originating from the instability of renewable energies while helping to close the carbon cycle.[9,10,11] It is therefore an intriguing topic in which research has invested a great deal of effort. $CO_2$ reduction can generate many products and the principal reactions are summarized in eq. 1-4[12,13]:

$$CO_2+2H^++2e^- \rightarrow CO+H_2O \quad (1)$$

$$CO_2+2H^++2e^{\#} \rightarrow HCOOH \quad (2)$$

$$CO_2+4H^++4e^- \rightarrow HCHO+H_2O \quad (3)$$

$$CO_2+6H^++6e^- \rightarrow CH_3OH+H_2O \quad (4)$$

Not all reduction products are directly usable as biofuels, and some need further processes. For instance, carbon monoxide reacts with $H_2$ via the well-known and industrially mature Fischer-Tropsch process to yield different hydrocarbons.[14]

From a thermodynamic point of view, $CO_2$ must be activated into $CO_2^{\bullet-}$ prior to any further reaction. This activation has a very negative potential (-1.9 V vs NHE),[15] consequently, the reaction often suffers from a prohibitively large overpotential. Thus, all the aforementioned reactions require appropriate catalysts. In general, a "good" catalyst is one that selectively catalyzes the desired reaction at a low overpotential while having a good turnover number (TON) and turnover frequency (TOF). Catalysis can be classified into two categories: heterogeneous and homogeneous. While less industrially relevant, homogeneous catalysis presents certain advantages such as the milder conditions usually required and the increased facility to carry out in-situ spectroscopic investigations. In fact, homogeneous catalysis can be viewed as a more fundamental approach to probe the mechanism and reactivity of a particular reaction. From an experimental perspective, mechanistic insights may be provided mostly by kinetic experiments[16] and spectroscopic measurements[17,18]. On the theoretical side, recent developments, in particular the progress of low-computational cost methods both in terms of calculation time and accuracy,[19,20] render quantum mechanics-based methods an invaluable tool to provide energetics, interpret spectroscopic data, and ultimately provide insights on the relationship between reactivity and electronic structure.

The research field of $CO_2$ reduction is more than thirty years old, and has been the subject of many studies. The subject of this thesis dissertation is the detailed elucidation of the electronic structure of the iron-tetraphenylporphyrinate complex ($[Fe(TPP)]^{2-}$, TPP=tetraphenylporphyrin) and of its excellent catalytic performances for $CO_2$ reduction. This goal is achieved by a systematic joint use of spectroscopic techniques and theoretical methods. However, before focusing on the iron-porphyrin family, we review here the state-of-the-art molecular catalysts available for $CO_2$ reduction, and aim to shed light to how a joint use of experimental and theoretical methods can lead to a better understanding of their reactivity and to a rational design of new generations of those catalysts. Of note, we focus solely on mononuclear catalysts which reactivity can be more easily compared with that of [Fe(TPP)].

## I. Formic acid generation

Formic acid is among the principal end products for $CO_2$ reduction in homogeneous catalysis. It can be a first step towards the reduction of $CO_2$ into methanol[21]. Alternatively,

reversible conversion of $CO_2$ and $H_2$ into formic acid may be a suitable way of storing hydrogen while utilizing $CO_2$ feedstock.[22] Interestingly, the reaction does not necessarily require the application of an external potential. In fact, formic acid can be generated by reaction with dihydrogen, where the latter works as a reductant (eq. 5).

$H_2 \rightarrow 2H^+ + 2e^-$ (5a)

$CO_2 + 2H^+ + 2\ e^- \rightarrow HCOOH$ (5b)

$CO_2 + H_2 \rightarrow HCOOH$ (5c)

On a thermodynamic point of view, the reaction (5c) is in fact reversible,[23,24] consequently, harsh conditions including high pressure of $H_2$ and $CO_2$ are often required to drive the reaction forward.

Most of the transition metal complexes showing a significant catalytic activity for $CO_2$ hydrogenation into formic acid are complexed with phosphine ligands. Among the most efficient homogeneous catalysts for this reaction, an iridium-based catalyst developed by Nozaki[25] (**1** in Figure 1) has shown the best performance up to date in terms of TON (3 500 000) and TOF (150 000 $h^{-1}$). Hazari has developed another Iridium-based catalyst[26] (**2** in Figure 1) which has shown excellent TON (348 000) and TOF (14 500 $h^{-1}$). For instance, a Rhodium catalyst (complex **3** in Figure 1) exhibits a TOF of 1335 $h^{-1}$.[27] A ruthenium phosphine catalyst (complex **4** in Figure 1) has a tremendous TOF of 95 000 $h^{-1}$.[28] Another ruthenium catalyst[29] (**5** in Figure 1) showed a TOF of 1400 $h^{-1}$. While the use of early-transition metal has an obvious economic interest, early transition metal-based catalysts tend to have lower performances than that of late-transition metals. For instance, iron catalysts (**8 and 9** in Figure 1) have shown a total TON of 727 over 20 hours,[30] and a TON of 1220 over 24 hours,[31] respectively. Nickel catalysts[32,33] (**7** and **6** in Figure 1) have TOF of 0.6 and 495, respectively. There are some exceptions: a cobalt catalyst[34] (**6** in Figure 1) shows a TOF of up to 74 000 $h^{-1}$.

**Table 1**: Representative examples of mononuclear transition metals exhibiting catalytic activity for $CO_2$ hydrogenation into formic acid and the highest associated turnover frequency.

| Catalyst name | Catalyst (labeled in Figure 1 | TOF($h^{-1}$) | Reference |
|---|---|---|---|
| [Ir(PNP)$(H)_3$] (PNP=2,6-bis((dipropylphosphanyl)methyl)pyridine) | **1** | 150 000 | 25 |
| [Ir(PNP')$(H)_2$] (PNP'=bis(2-(dipropylphosphanyl)ethyl)amine) | **2** | 14 500 | 26 |
| [Rh(hfacac)$(P(Cy)_2(CH_2)_4P(Cy)_2)$] (hfacac=hexafluoroacetylacetonate) | **3** | 1335 | 27 |
| [RuCl$(O_2CMe)(PMe_3)_4$] | **4** | 95 000 | 28 |
| [Ru$(PMe_3)_3(H)_2$] | **5** | 1400 | 29 |
| [Co$(P(Me)_2(CH_2)_2P(Me)_2)_2(H)$] | **6** | 74 000 | 34 |
| [Ni(BNOP)(H)] (BNOP=1,3-bis((dipropylphosphanyl)oxy)benzene) | **7** | 495 | 32 |
| [Ni$(P(Me)_2(CH_2)_2P(Me)_2)_2(H)$] | **6** | 0.6 | 33 |
| [Fe(PP3)(H)] (PP3=tris(2-(diphenylphosphanyl)ethyl)phosphane) | **8** | 36[a] | 30 |
| [Fe(PNP'')(CO)(H)$(BH_4)$] (PNP''=2-(dipropylphosphanyl)-N-(2-(dimethylphosphanyl)ethyl)-N-methylethan-1-amine) | **9** | 2458[b] | 31 |

a) Total TON of 727 over 20 hours

b) Total TON of 58990 over 24 hours.

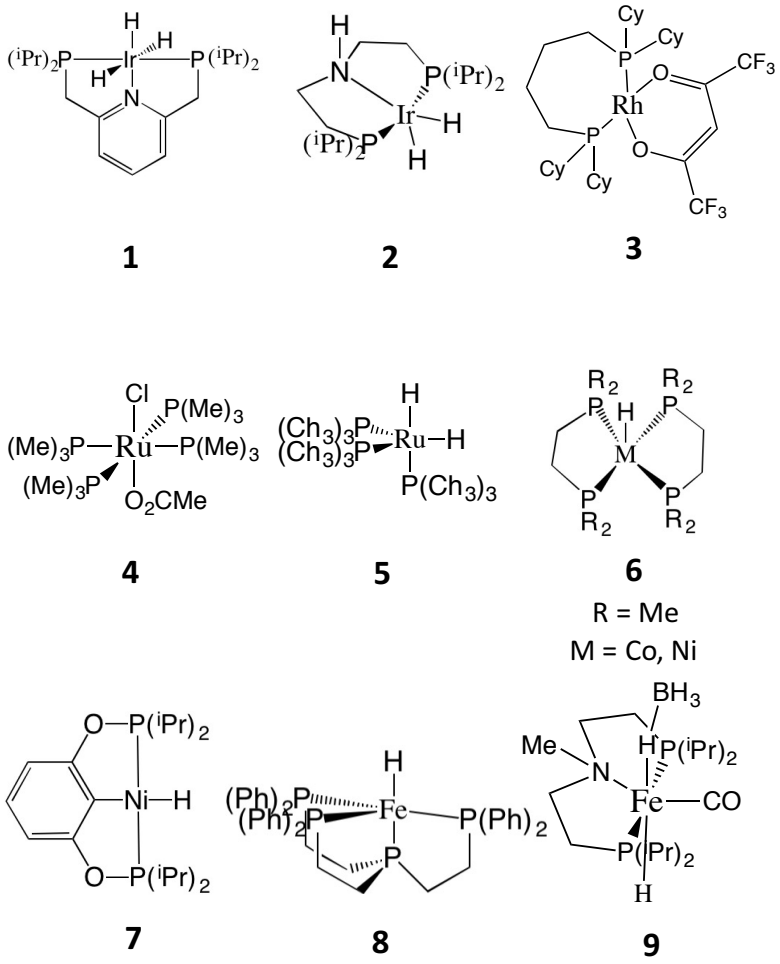


**Figure 1**: Lewis structure of the catalysts summarized in Table 1.

In general, the postulated mechanism for hydrogenation of $CO_2$ using $H_2$ consists of[23,35] (1) formation of a metal-hydride, (2) insertion of the $CO_2$ into the M-H bond forming a M-OCHO adduct, (3) departure and protonation of the $HCOO^-$ motif, yielding HCOOH and the metal complex with an empty coordination site, (4) formation of a M-$H_2$ adduct, (5) reductive elimination yielding a metal-dihydride, (6) deprotonation of the complex regenerating the metal-hydride (Figure 2). Note that the order of the steps, in particular that of deprotonation with respect to CO2 insertion, depends on the experimental conditions and studies.[36,37] Alternatively, another pathway has been proposed,[38] where the oxidation state of the metal does not change. This alternative pathway involves (1) formation of a metal-hydride, (2) insertion of the $CO_2$ into the M-H bond forming a M-OCHO adduct, (3) formation of a M($H_2$)(OCHO) adduct, (4) protonation of the $HCOO^-$ by one proton of the $H_2$ motif, leading to the departure of HCOOH and regeneration of the metal-hydride.

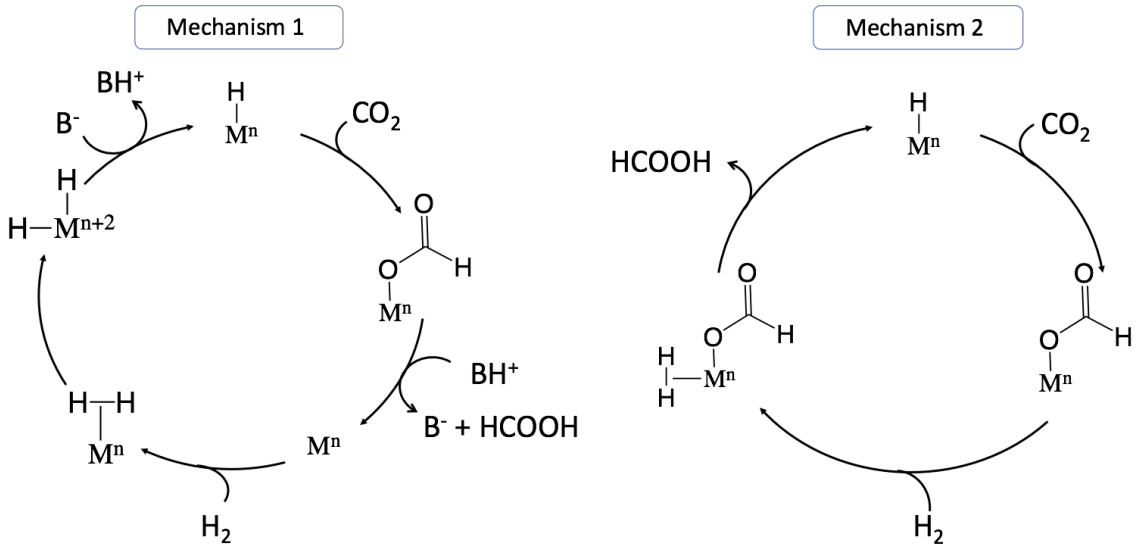


**Figure 2**: Schematic representation of the two possible catalytic cycles of the hydrogenation of $CO_2$ with $H_2$.

Rhodium-based catalysts have been studied via $^1H$ NMR spectroscopy[36] confirms that the $CO_2$ is inserted into the M-H bond. Kinetic experiments[38] performed on catalyst **4** are compatible with both the aforementioned catalytic cycle. While the reaction mechanism for this specific family of catalysts does not automatically extend to any other catalysts, it provides a mechanistic hypothesis which has since been confirmed via theoretical studies for many other catalysts.

Theory has provided a lot of insight on the reactivity of these catalysts over the years. DFT calculations seem to indicate that two steps are likely to have a substantial kinetic barrier, i.e. (1) the $H_2$ cleavage and (2) the hydride transfer steps.[23,35,39] Nozaki also suggested that the deprotonation of the complex in pathway 1 may be a potential RDS for the iridium complex **1**.[37] It is of great interest to lower those activation barriers by tuning either the metal or the ligand. For instance, calculations from Hazari[26] suggest that inclusion of a hydrogen bond donor in the second sphere of coordination allows to stabilize the transition state of the hydride transfer step. Computational studies also propose ideas to reduce the kinetic barrier of the $H_2$ splitting, specifically. Hence, calculations from Yang et. al.[23] suggest that intramolecular proton transfers may indeed favor the $H_2$ splitting step (see Figure 3).

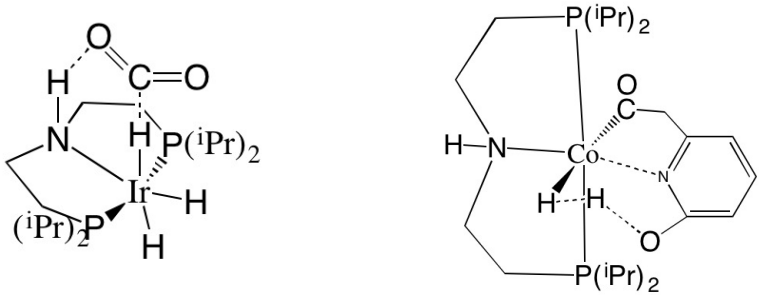


**Figure 3**: Transition state of the CO2 insertion step in the catalyst developed by Hazari stabilized by the presence of an hydrogen bond donor in the second sphere of coordination (left) and transition state of the H2 cleavage step in the computationally-designed catalyst by Yang, assisted by an intramolecular proton transfer (right).

It has been noted by several authors[40] that the kinetic barrier of these step is in general related to the *hydricity* of the complex, i.e. the affinity of the complex for the hydride, defined as[41]:

$$\Delta_r G_{\text{hyd}} = G(M^{n+}) + G(H^-) - G([M-H]^{(n-1)+}) \quad (6)$$

By definition, a complex with a more positive hydricity has a high hydride accepting ability. Catalysts with high hydricity tend to pass through a hydride transfer rate-determining step (RDS), while low hydricity complexes tend to have a dihydrogen cleavage RDS. Ye et al.[40] indeed found that increasing the electron-donating ability of the ligand *trans* to the transferred hydride significantly decreases the kinetic barrier, while simultaneously increasing the barrier for the $H_2$ splitting. Conversely, the addition of electron-withdrawing groups on the supporting ligands tends to simultaneously decrease the $H_2$ splitting barrier and increase the hydride transfer barrier. These studies indicate that tuning the hydricity of the catalysts is a suitable catalyst design strategy to accomplish the right "balance" between those two kinetic barriers.

Clearly, the examples above show that in silico design is a useful approach to achieve rational developments of more efficient catalysts. Computational chemistry is not only a predictive tool, but also one that enables to understand the electronic structure of the intermediates involved, in order to get insights on their reactivity, and use this knowledge to design the next generation of catalysts.

The production of formic acid from $CO_2$ may also be done electrocatalytically. Unlike in the former case, the electrons and protons necessary for the reaction 5b are no longer furnished simultaneously via the addition of dihydrogen, but separately through the addition of

protons from Brönsted acids and the addition of electron via electrolysis. The TOF depends on the electrolysis potential according to the following relationship[42]:

$$TOF = \frac{2k}{1+\exp\left(\frac{F}{RT}\left(E-E_{PQ}^{0}\right)\right)} \quad (7)$$

Where $k$ is the apparent kinetic constant of the chemical reaction, F is the faraday constant, R the perfect gas constant, T the temperature, E the potential of the electrolysis and $E_{PQ}^{0}$ is the standard redox potential of the catalysis.

The available catalysts for $CO_2$ reduction into HCOOH are rather scarce compared to the number of catalysts selectively catalyzing the CO2-to-CO conversion reaction. In fact, a review written by Francke[43] in 2018 and summarizing the homogeneous catalysts for $CO_2$ reduction in literature identified only 55 transition metal catalysts for HCOOH generation, against 125 transition metal catalysts for CO generation. Nevertheless, catalysts from late transitions metals such as iridium,[44] rhenium[45] and ruthenium,[46,47] and first-row transition metal complexes such as Fe,[48] Cobalt[49] and Nickel[50] have been reported. The catalytic performance of a few representative examples are summarized in Table 2.

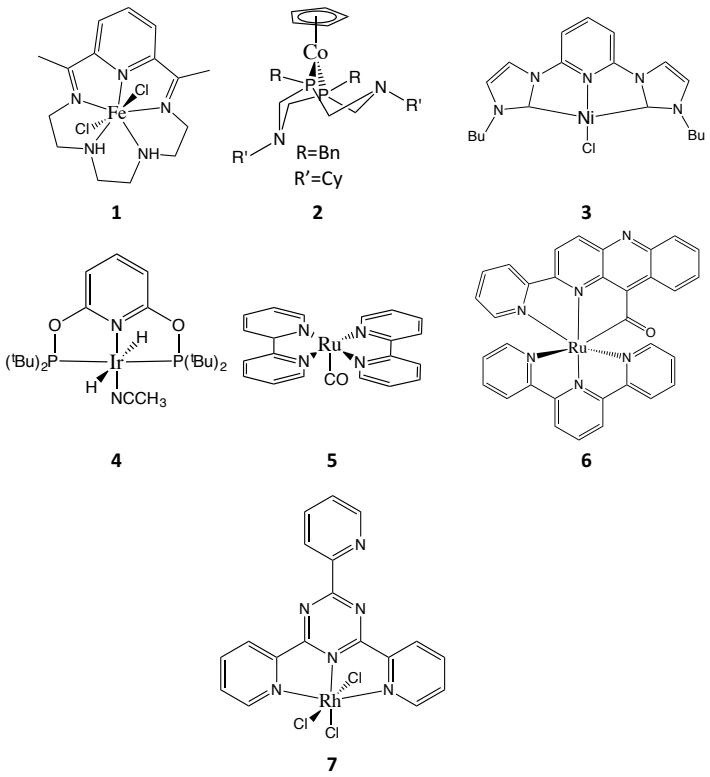


**Figure 4**: Lewis structure of the homogeneous electrocatalysts for $CO_2$-to-HCOOH conversion reaction summarized in Table 2.

**Table 2**: TOFs, Faradaic efficiency and electrolysis potential for 7 representative examples of mononuclear transition complexes exhibiting catalytic activity towards $CO_2$-to-HCOOH reduction reaction.

| Catalyst (number in Figure 4 shown within bracket) | E (V vs SCE)[a)] | TOF($h^{-1}$) | FE[c)] | Reference |
|---|---|---|---|---|
| [Fe(L)($CL_2$)] (L=2,13-dimethyl-3,6,9,12,18-pentaazabicyclo-[12.3.1]octadeca-1(18),2,12,14,16-pentaene) (**1**) | -1.3 | 420 | 75-80% | 373 |
| [Co($P^R_2N^{R'}_2$)(Cp)] ($P^R_2N^{R'}_2$=3,7-dibenzyl-1,5-dicyclohexyl-1,5,3,7-diazadiphosphocane, Cp=cyclopentadienyl) (**2**) | -1.8 | 650 (TON 23/1h) | 98% | 126 |
| [Ni(NHC1)(Cl)] (NHC1=3,3‘-(pyridine-2,6-diyl)bis(1-butyl-1H-imidazol-3-ium-2-ide)) (**3**) | -1.8 | 30 (TON 1/2h)[c] | 47%[b)] | 472 |
| [Ir(POCOP)(MeCN)($H)_2$(MeCN)] (POCOP=2,6=bis((di-tert-butylphosphanyl)oxy)pyridine) (**4**) | -1.45 vs NHE in MeCN | 20 (TON 40/25h) | 85% | 276 |
| [Ru($bpy)_2$CO] (**5**) | -1.5 | N. D. (TON 19.9/N.D.) | 38% | 350 |
| [Ru(tpy)(pbn-CO)] (pbn-CO=2-(pyridin-2-yl)benzo[b][1,5]naphthyridine-10-carbaldehyde) (**6**) | -1.1 | N. D. (TON 5.2/12h) | 42% | 490 |
| [Rh(tptz)($Cl)_3$] (tptz=2,4,6-tris(2-pyridyl)-1,3,5-triazine) (**7**) | -1.3 | N. D. (TON 10.8/1h) | 81% | 380 |

a) Potentials given vs a SCE reference electrode except mentioned otherwise.
b) TON and electrolysis time given within brackets when available.
c) FE given relative to the displayed potential.

The main difference with hydrogenation of $CO_2$ using $H_2$ as a simultaneous source of protons and electrons, is that in electrocatalysis the electrons are provided by the electrodes, while the protons are provided by Brønsted acids. Consequently, the mechanism is slightly different, and involves (1) the protonation of the metal to form a metal-hydride (2) the insertion of the $CO_2$ into the M-H bond, (3) the release of the $HCOO^-$ moiety and regeneration of the catalyst.[51,52] Most of the aforementioned catalysts have a faradaic efficiency lower than 85%. This low efficiency is largely explained by the competition of three reactions. First, the reaction always competes with hydrogen evolution reaction (HER). Because of the availability in Brønsted acid, the metal-hydride may react with a proton instead of a $CO_2$ molecule, releasing a dihydrogen molecule. This side-reaction is not a problem in $CO_2$ hydrogenation because the large experimental pressure of dihydrogen usually pushes the equilibrium towards formation of formic acid. The second side reaction is the generation of carbon monoxide. This happens when in place of a protonation, the metal center binds directly with the carbon of a $CO_2$ molecule. The reaction pathway that follows ends up after two proton transfers in the release of a carbon monoxide molecule and a water molecule (*vide infra*).

Some authors have pointed out the possibility of a second type of pathway for $CO_2$ electrocatalytic reduction into formic acid starting with a direct interaction between the $CO_2$ molecule and the unprotonated metal. Hence, first Sauvage et. Al.,[53] later confirmed by in-silico predictions of Ye et. al.,[54] have pointed out that the coordination mode of $CO_2$ to the Nickel-cyclam dictate the final reaction outcome; generation of either formic acid or carbon monoxide depends on whether the coordination mode is $\eta^1$-OCO or $\eta^1$-$CO_2$. From a mechanistic point of view, the electron donation of the metal center into the in-plane $\pi^*$ of $CO_2$ results in formation of the M-$CO_2$ adduct. The resulting $CO_2$ moiety is thus electron-rich, which enables protonation of either the carbon or the oxygen, depending on the site accessibility to proton donors. $\eta^1$-OCO adducts expose the carbon to protonation, thus generating a formate. On the other hand, $\eta^1$-$CO_2$ adducts expose the oxygen to protonation, eventually resulting in the formation of carbon monoxide (*vide infra*), as depicted in Figure 5. Generally, however, calculations suggest that the $\eta^1$-OCO binding mode is thermodynamically unfavorable due to the large interelectronic repulsion between the oxygen lone pair of $CO_2$ and the low- valent metal center. On the other hand, the $\eta^1$-$CO_2$ binding mode involves the donation of an electron from the $d_{z2}$ orbital of the

metal center to the rather electrophilic carbon of $CO_2$. Hence the direct formation of a M-$CO_2$ adducts is thermodynamically preferred over the second mode, and selectively yield carbon monoxide.

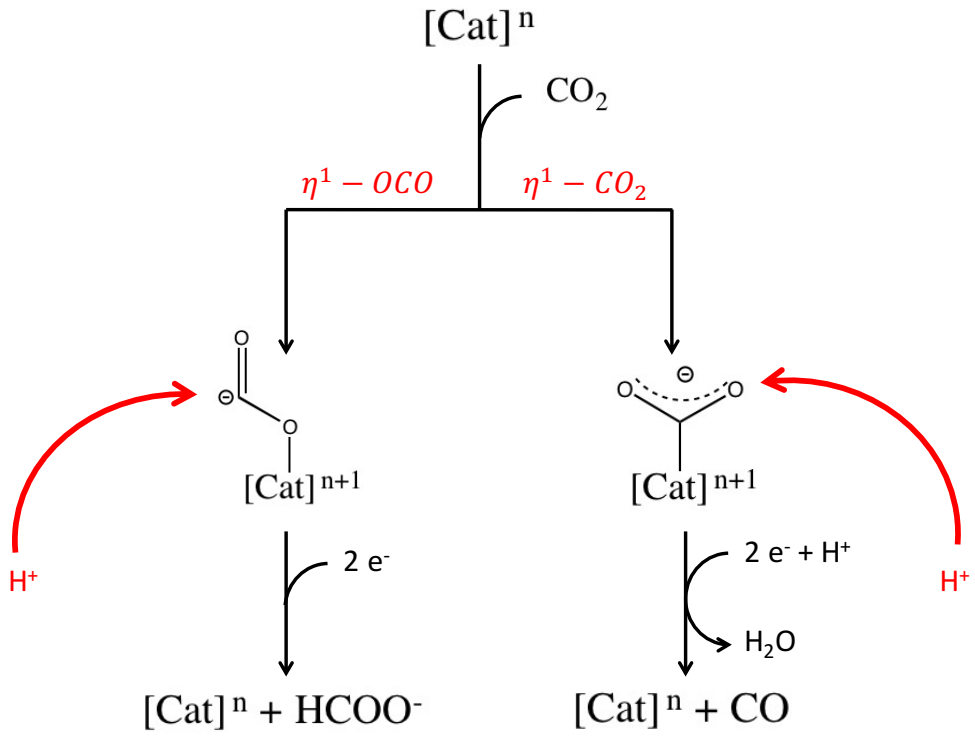


Figure 5: Schematic representation of the $\eta^1$-OCO and $\eta^1$-CO2 binding mode, leading to the formation of formic acid and carbon monoxide, respectively. $[Cat]^n$ refers to the catalyst of charge +n. Red arrows point at the available protonation site on the $CO_2$ motif, depending on the binding mode.

## II. CO generation

Although it cannot be used directly as a biofuel, carbon monoxide is a suitable C1 building block for the synthesis of hydrocarbons, in particular via the Fischer-Tropsch process.[14] Unlike the previous case, reduction of carbon dioxide into CO is usually done electrocatalytically.

Among the reported homogeneous catalysts, those which selectively reduce $CO_2$ into CO are the most commonly reported in literature, and some may reach faradaic efficiencies close to 100%. Although some late-transition metals-based catalysts, including rhenium,[55,56,57] ruthenium,[46, 58,59,60,61,62] molybdenum,[63, 64] tungsten,[63] palladium,[65,66,67,68] and iridium[69] have

been used as catalysts in $CO_2$-to-CO reduction, recent intense research efforts have been directed towards more earth-abundant first-row transition metals. Mononuclear early-transition metal complexes such as chromium,[63,64] manganese,[7071,72,] iron,[16,73,74,75,76,77], cobalt[48,76,78,79,80,81,82] and nickel[79,81,83,84,85,86] have been reported as having a catalytic activity towards $CO_2$-to-CO reduction.

Both in terms of TOF and selectivity, the iron-porphyrin family undeniably represents some of the most performant catalysts reported in the literature. [Fe(TPP)] exhibits a TOF of about $10^4$ $s^{-1}$ at a potential of -1.7 V vs SCE. The effect of tuning the substituents in the porphyrin ligand have been intensively studied.[87,88,89] In fact, a derivate of [Fe(TPP)] has been reported by Saveant et. Al.[90] to exhibit a tremendous TOF of $10^6$ $s^{-1}$! [Fe(TPP)] also exhibits a Faradaic efficiency of about 100%, making it *de facto* the most selective catalyst available in the literature. A more in-depth investigation of the iron-porphyrin family as catalysts for $CO_2$ reduction is the subject of this thesis dissertation. Although [Fe(TPP)] and its derivates stand out, other excellent catalysts have been reported. For instance, [Co(qpy)] exhibits an excellent TOF of 3.3 x $10^4$ $s^{-1}$ at a very mild potential of -1.3 V.[76] Its Faradaic efficiency with respect to CO formation, however, is only 87%. The [Re(R-bpy)$(CO)_3$] and [Mn(R-bpy)$(CO)_3$] also provide excellent catalytic performances. For instance, the catalysts [Re(Mes-bpy)$(CO)_3$] and [Mn($^t$Bu-bpy)$(CO)_3$] have TOFs of 6206 and 5000 $s^{-1}$ at potentials of -1.6 and -1.8 V, respectively.[55,70] They are also highly selective, with Faradaic efficiency of 98% and 96%, respectively. Of note, a large number of derivate exist for each of those catalysts,[56,57,91,92,93] the study of which is beyond the scope of this dissertation. More recently, an iron complex [Fe(bpy$^{NHEt}$PY2Me)] with a TOF of about 2000 $s^{-1}$ was reported.[74] A plethora of other catalysts for $CO_2$ reduction are available and will not be described in details here, but their catalytic performances, potential and faradaic efficiencies are summarized in 3.

Of note, the large majority of the aforementioned catalysts are transition metal complexes involving highly conjugated ligand platform. In fact, on the 35 catalysts reported in 3, 23 involve ligands possessing a π-system of 10 atoms or more. The specific nature of these ligands is multiple, and can be classified either as polypyridine, conjugated macrocycles, pyridine-diimine or NHC platforms. The conjugated nature of the ligand hints at the role of the ligand in accepting electrons necessary for $CO_2$ reduction, as is described in more details in Chapter 3.

**Table 3**: TOF, Faradaic efficiency and electrolysis potential for 35 representative examples of reported mononuclear transition metal complexes exhibiting catalytic activity for $CO_2$-to-CO reduction reaction.

| Catalyst (number in Figure 6 or Figure 7 shown within bracket) | E (V vs SCE)[a)] | TOF ($s^{-1}$)[b)] | FE[c)] | Reference |
|---|---|---|---|---|
| [Fe(TPP)] (**1**) | -1.7 | $>10^4$ (N.D.) | ~100% | 16,73 |
| [Co(qpy)] (qpy=quaterpyridine) (**2**) | -1.3 | 3.3 x $10^4$ (64/8h) | 87% | 76 |
| [Re(Mes-bpy)$(CO)_3$] (**3**) | -1.6 | 6206 (N.D.) | 96% | 55 |
| [Mn($^t$Bu-bpy)$(CO)_3$] (**3**) | -1.8 | 5000 (4/1.2h) | 98% | 70 |
| [Fe(bpy$^{NHEt}$PY2Me)] (bpy$^{NHEt}$PY2Me=6'-(1,1-di(pyridin-2-yl)ethyl)-N-ethyl-[2,2'-bipyridin]-6-amine) (**4**) | -1.5 | 2067 (N.D.) | 81% | 74 |
| [Fe(Cp1)$(CO)_3$] (Cp1=1,3-bis(tert-butyldimethylsilyl)-4,5,6,7-tetrahydro-2H-inden-2-one) (**5**) | -1.65 vs NHE (in CH3CN) | 324-728 (N.D.) | 96% | 75 |
| [Ru(mes-bpy)$(CO)_2(Cl)_2$] (**6**) | -1.8 | 320 (N.D.) | 95% | 60 |
| [$Mo(CO)_6$] (**7**) | -2.4 | 238 s-1 (8.1/2h) | 83-95% | 63 |
| [Co(Mc)] (Mc=2,4,6,8-tetraaza-1,3,5,7(2,6)-tetrapyridinacyclooctaphane) (**8**) | -2.3 | 170 (6.2/2h) | 98% | 78 |
| [$W(CO)_6$] (**7**) | N.D. | 159 s-1 (N.D.) | N.D. | 63 |
| [Ni(cyclam)] (cyclam=1,4,8,11-tetraazacyclotetradecane) | -1.9 | 90 (4/1h) | 90% | 83 |

| | | | | |
|---|---|---|---|---|
| (**9**) | | | | |
| [Ni(CNC)($NCCH_3$)] (CNC=2,6-bis(3-methyl-2,3-dihydro-1H-imidazol-1-yl)pyridine) | -1.8 | 90 s-1 | N.D. | 86 |
| (**10**) | | | | |
| [Co($tpy)_2$] (tpy=terpyridine) | -1.6 | 74 (N.D.) | 12% | 79 |
| (**11**) | | | | |
| [$Cr(CO)_6$] | N.D. | 24 s-1 | N.D. | 63 |
| (**7**) | | (N.D.) | | |
| [Co($N_4H$)] ($N_4H$=2,12-dimethyl-3,7,11,17-tetraazabicyclo[11.3.1]-heptadeca-1(7),2,11,13,15-pentane) | -1.7 | N.D. (4.1/0.6h) | 45% | 48 |
| (**12**) | | | | |
| [Ni($N_4H$)] | -1.3 | N.D. | 44% | 81 |
| (**12**) | | (2.1/1h) | | |
| [Cr(bpy)($CO)_3$] | -2.8 vs $Fc/Fc^+$ in | N. D. | N. D. | 64 |
| (**3**) | NMP | (N.D.) | | |
| [Co(L)] (L=2,13-dimethyl-3,6,9,12,18-pentaazabicyclo-[12.3.1]octadeca-1(18),2,12,14,16-pentaene) | -1.5 | N. D. (N.D.) | 82% | 48 |
| (**13**) | | | | |
| [Ru($bpy)_2$(CO)] | -1.5 | N.D. | 51% | 46 |
| (**14**) | | (TON 26.2/N.D.) | | |
| [Ru(bpy)(tpy)] | -1.5 vs NHE in | N.D. | 76% | 59 |
| (**15**) | MeCN | (5/5h) | | |
| [Fe(qpy)] | -1.2 | N.D. | 70% | 76 |
| (**2**) | | (12/4h) | | |
| [Fe(TPFc)] (TPFc=5,10,15-tris(pentafluorophenyl)corrole) | -1.6 | N.D. (N.D.) | N.D. | 77 |
| (**16**) | | | | |
| [Mn($\kappa^2$-($Ph_2$P)NMe($NC_5H_4$))($CO)_3$] | -1.9 | N.D. (N.D.) | 96% | 72 |

| | | | | |
|---|---|---|---|---|
| ($\kappa^2$-($Ph_2P$)NMe($NC_5H_4$)=N,N'-bis(diphenylphosphino)-2,6-di(methyl-amino)pyridine) (**17**) | | | | |
| [Co($N_4C$)] ($N_4C$=(4E, 11E)-2,5,7,7,9,14,14-heptamethyl-1,4,8,11-tetraazacyclotetradeca-4,11-diene) (**18**) | -1.5 | N. D. (9/1h) | 90% | 81 |
| [Co(TPP)] (**19**) | -1.8 | N.D. (19/1.4h) | 72% | 82 |
| [Pd(PPh,)2(Me-bpy)] (Me-bpy=4,4'-dimethyl-2,2'-Bipyridine) (**20**) | -1.3 vs Ag/Ag+ (MeCN) | N.D. | 81% | 66 |
| [Co(PPh,)2(Me-bpy)] (**20**) | -1.3 vs Ah/Ag+ (MeCN) | N. D. (8/0.8-3h) | 83% | 66 |
| [Ni($tpy)_2$] (**11**) | -1.3 | N.D. | 18% | 79 |
| [Mo(bpy)($CO)_3$] (**3**) | -2.3 vs Fc (in NMP) | N.D. | N.d. | 64 |
| [Ru(L')(napy)(DMSO)] (L'=N''-methyl-4'methylthio-2,2':6',4''-terpyridium, napy =naphtyridine) (**21**) | -1.1 | N.D. | 35% | 61 |
| [Ru(tptz)($CH_3CN)Cl_2$] (tptz = 2,4,6-tri(2-pyridyl)-1,3,5-triazine) (**22**) | -1.8 | N.D. (8/5h) | 92% | 61 |
| [Ru(PNNN)(CO)(Cl)(H)] (PNN=N-(di-tert-butylphosphanyl)-[2,2'-bipyridin]-6-amine) (**23**) | -1.3 vs SHE (MeCN) | N.D. (6.1/12h) | 61 | 62 |

| | | | | |
|---|---|---|---|---|
| [Pd(Me3-P$^{+}$etpE)(DMF)] (Me3-P$^{+}$etpE= (((2-(trimethyl-$\lambda^4$-phosphanyl)ethyl)phosphanediyl)bis(ethane-2,1-diyl)bis(diethylphosphane) (**24**) | -1.65 | N.D. (15/N.D.) | 45% | 67 |
| [Pd(CNC)Cl] (CNC=2,6-bis((3-butyl-2,3-dihydro-1H-imidazol-1-yl)methyl)pyridine) (**25**) | -2.3 vs $Ag/AgNO_3$ (MeCN) | N.D. (N.D.) | 52% | 68 |
| [Ir(L4)(ppy)($NCCH_3$)] (ppy=2-phenylpyridine) (**26**) | -1.2 | N.D. | ~100% | 69 |

d) Potentials given vs a SCE reference electrode except mentioned otherwise.
e) TON and electrolysis time given within brackets when available.
f) FE given relative to the displayed potential.

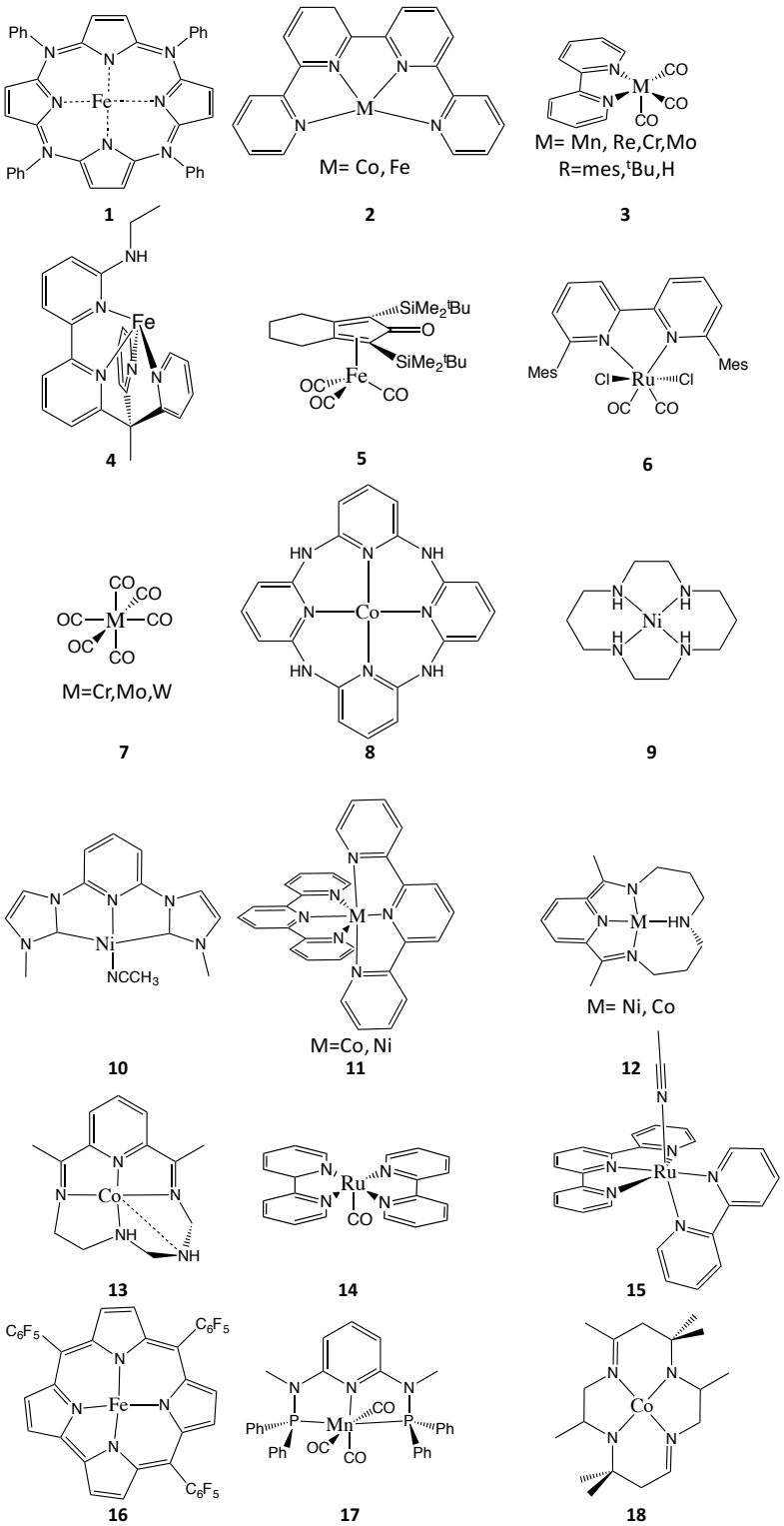


**Figure 6**: Lewis structure of the catalysts summarized in 3.

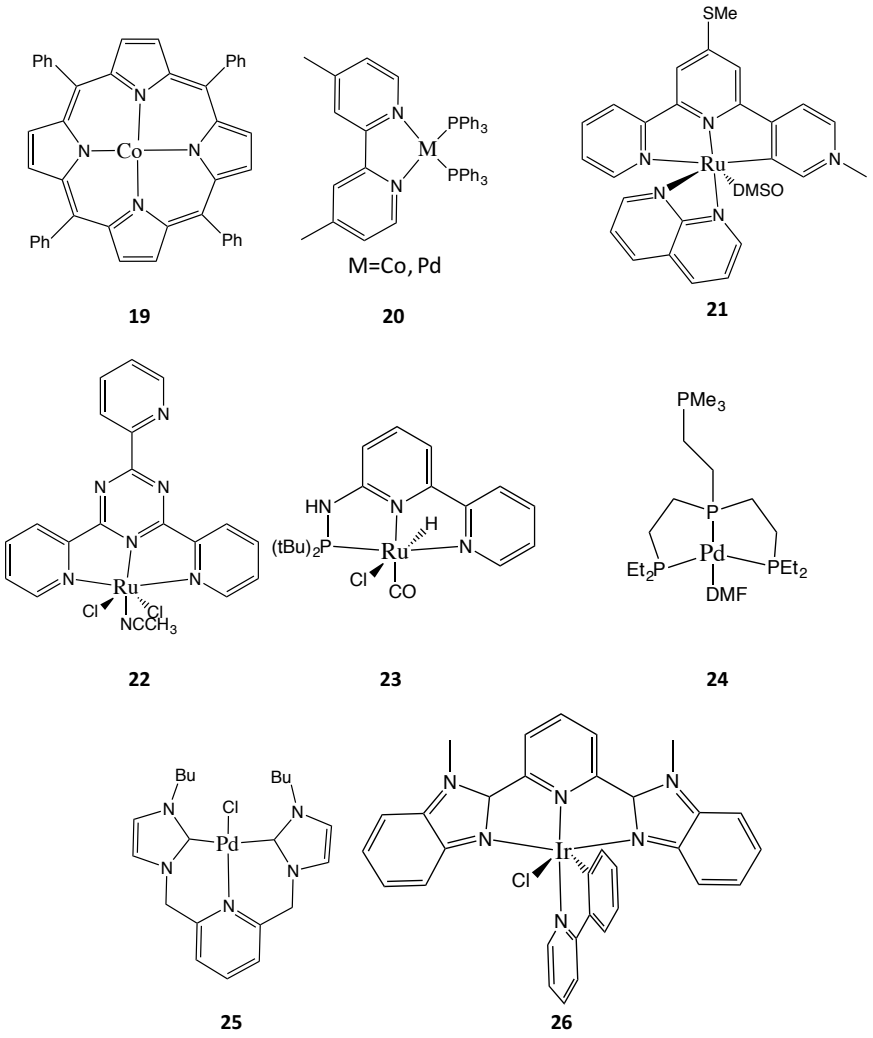


**Figure 7**: Lewis structure of the catalysts summarized in 3 (continuation).

Although a few catalysts are able to catalyze CO generation without a proton source, most catalysts require the presence of Brönsted acid to facilitate the reaction. The proposed mechanisms of proton-assisted CO generation are multiple depending on authors and catalytic systems. In general for mononuclear complexes, we have distinguished 5 different types of mechanism investigated in literature.[16,54,91] We labelled them type I, II.a, II.b, II.c and III (see Figure 8).

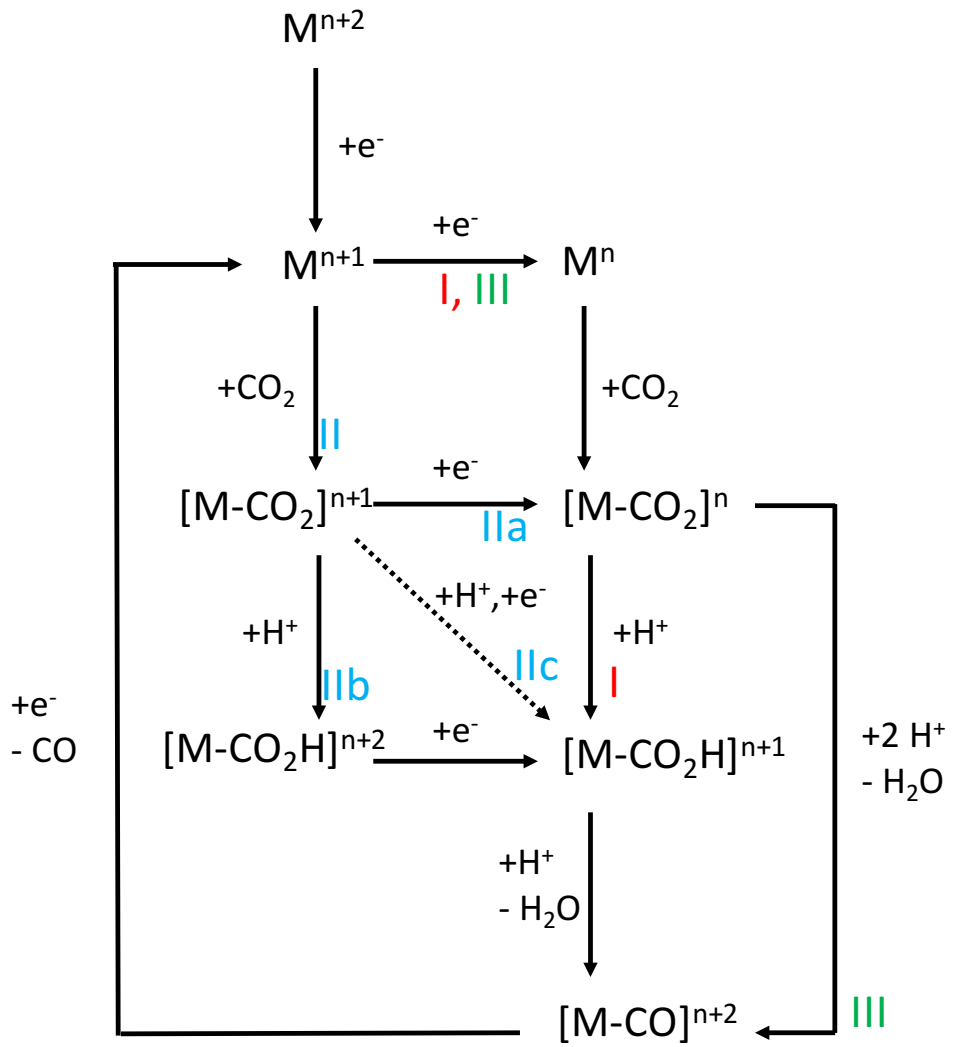


**Figure 8**: The possible pathways of CO2 reduction into carbon monoxide. The number n designs the charge of the catalyst. The roman numbers I (in red), IIa, IIb, IIc, (in blue) and III (in green) mark the mechanism types explicated in the text.

Type I corresponds to the following sequence: (1) first electron transfer the catalyst, (2) second electron transfer to the catalyst, (3) formation of a metal-$CO_2$ adduct, (4) protonation of the adduct, (5) proton-assisted cleavage of the C-O bond, and (6) one-electron reduction of the catalyst and dissociation of the CO moiety, bringing the state of the catalyst to the end of step (1). Many systems have been assigned a type I pathway, including [Mo(Mc)],[78] [Co($N_4$H)],[94] [Co(qpy)],[76] one of the possible mechanism of [Mn(bpy)($CO)_3$] (protonation-first pathway),[91] [Ru(bpy)$_2$(CO)][46] and [Fe(TPP)] according to some authors.[95]

Unlike in type I pathway where two electrons are transferred to the catalyst prior to the formation of the metal-$CO_2$ adduct, type II pathways generally correspond to a sequence of (1)

first electron transfer to the catalyst, (2) formation of a metal-$CO_2$ adduct, (3) protonation of the adduct and second electron transfer to the catalyst, (4) proton-assisted cleavage of the C-O bond, and (5) one-electron reduction of the catalyst and dissociation of the CO moiety, bringing the state of the catalyst to the end of step (1). In details, type II.a, II.b and II.c pathways are distinguishable via the order of the proton transfer relative to the electron transfer in step (3). In type II.a, the second electron transfer directly follows the formation of the metal-$CO_2$ adduct and precedes the protonation of the adduct. To the best of our knowledge, the type II.a mechanism has not been explicitely assigned to any of the aforementioned catalysts, although the order of the steps separating the formation of the adduct from the cleavage of the C-O bond is oftentimes left ambiguous. [48,76,96] In type II.b, the proton transfer follows the formation of the metal-$CO_2$ adduct and precedes the second electron transfer. Example of type II.b pathway include [Re(bpy)$(CO)_3$][58] or one of the pathways of [Mn(bpy)$(CO)_3$] (reduction-first pathway).[91] Finally, in type II.c pathway, it is possible that the proton and the electron are transferred simultaneously in one elementary step, i.e. a concerted proton-electron transfer (CPET).[97,98,99] According to Ye et. Al. on the basis of DFT calculations, [Ni(cyclam)] follows a type II.c mechanism.[54]

Finally, type III mechanism corresponds to a direct cleavage of the C-O bond following directly the formation of the adduct. The mechanism involves the following sequence: (1) first electron transfer to the catalyst, (2) second electron transfer to the catalyst, (3) elementary cleavage of the C-O bond assisted with a proton transfer, and (4) one-electron reduction of the catalyst and dissociation of the CO moiety, bringing the state of the catalyst to the end of step (1). Note that the type III is rarely investigated in the literature, and has been to our knowledge, only proposed by Costentin[16] for [Fe(TPP)].

In principle, type II mechanism are likely to occur at milder potentials than type I or III mechanisms. Indeed, the formation of the adduct triggers an electronic donation from the catalyst to the $CO_2$ motif, while the protonation increases the charge of the overall complex. Hence such chemical steps are expected to shift the second electron reduction potential of the resulting species towards more positive values compared to that of the molecular catalyst. However, in type II pathways the metal-$CO_2$ and metal-$CO_2H$ intermediates are expected to be energetically unfavorable compared to their counterpart in type I and III mechanisms. Indeed, in each case the higher charge state of the intermediate is likely to translate into a lesser ability to donate electrons to the $CO_2$ motif or accommodate a positive charge. Hence in general, the kinetics of the type II pathways are expected to be slower than that of type I and type III mechanisms.

Direct spectroscopic evidences of the intermediates involved in either of those mechanism are scarce. However, it is worthwhile to note that infrared evidences of $\eta^1$-$CO_2$ adducts of zero-valent iron and cobalt have been detected in the past. Those adducts decomposed above 60 K, suggesting their instability.[100] A cobalt(I) $\eta^1$-$CO_2$ adduct has been characterized by X-ray diffraction analyses,[101] although this complex was stabilized by the interaction with two $K^+$ ion. More recently, spectroscopic evidence of a cobalt-$CO_2$ adduct was found via IR spectroscopy in a study of the activity of [Co($N_4$H)] with respect to $CO_2$.[102]

DFT calculations usually suggest that formation of the $\eta^1$-$CO_2$ adduct and the C-O bond cleavage steps are the two potentially rate-determining steps of the reaction for many catalysts. For instance, calculations by Ye on nickel-cyclam suggested that the formation of the Ni-$CO_2$ adduct is only marginally stabilizing ($\Delta_r G = 1.7\ kcal/mol$). The rate-determining step is indeed the C-O bond cleavage and varies according to the pKa value of the Brønsted acid. For instance, the associated barrier is 21 kcal/mol in water. Kubiak found that the formation of the adduct [Re($CO)_3$(bpy)($CO_2$)]$^-$ underwent a prohibitive kinetic barrier unless in the presence of a stabilizing cation. [103] However, the C-O bond cleavage remained the rate-determining step (24.4 kcal/mol with methanol as proton donor). Joint evidences from experiments and theory provide once again a set of ideas to improve the performance of catalysts. For instance, following this line, the bipyridine ligand in [Re(bpy)($CO)_3$]$^-$ was modified in order to allow intramolecular proton transfers to $CO_2$ and stabilizing the $\eta^1$-$CO_2$ adduct via hydrogen bonds.[104]

As emphasized before, electrocatalytic generation of carbon monoxide always has to compete with formic acid generation or hydrogen evolution. Formic acid generation and $H_2$ evolution reaction are both initiated with the formation of a metal-hydride, whereas the first step of CO generation is the formation of a metal-$CO_2$ adduct. In fact, DFT calculations generally suggest that the kinetics of the metal-hydride formation step governs the selectivity for CO generation with respect to HCOOH or $H_2$ generation. For instance, in the case of [Re(bpy)($CO)_3$Cl] the formation of the metal-hydride ($\Delta_r G^0 = -39.8$ kcal/mol) is highly favored thermodynamically over the formation of the metal-$CO_2$ aduct ($\Delta_r G^0 = -10.5$ kcal/mol).[103] However, the former process requires a significant barrier ($\Delta_r G^{\neq}$ =21.8 kcal/mol) while the formation of the metal-$CO_2$ adduct has no barrier in the presence of a cation, indicating a kinetic origin to the selectivity of this complex towards CO generation. A more recent investigation on a derivate of [Fe(TPP)] also attributed the selectivity of CO generation over HER to a prohibitive barrier associated with the formation of the metal-hydride species.[105] As an additional illustration for this competition phenomenon, the addition of local proton sources in [Mn(bpy-R)($CO)_3$Br] (R=4-phenyl-6-(1,3-dihydroxybenzen-2-yl) increases drastically the

production of formic acid up to a faradaic efficiency of 22%,[106] likely because the formation of the metal-hydride is favored by the local proton source.

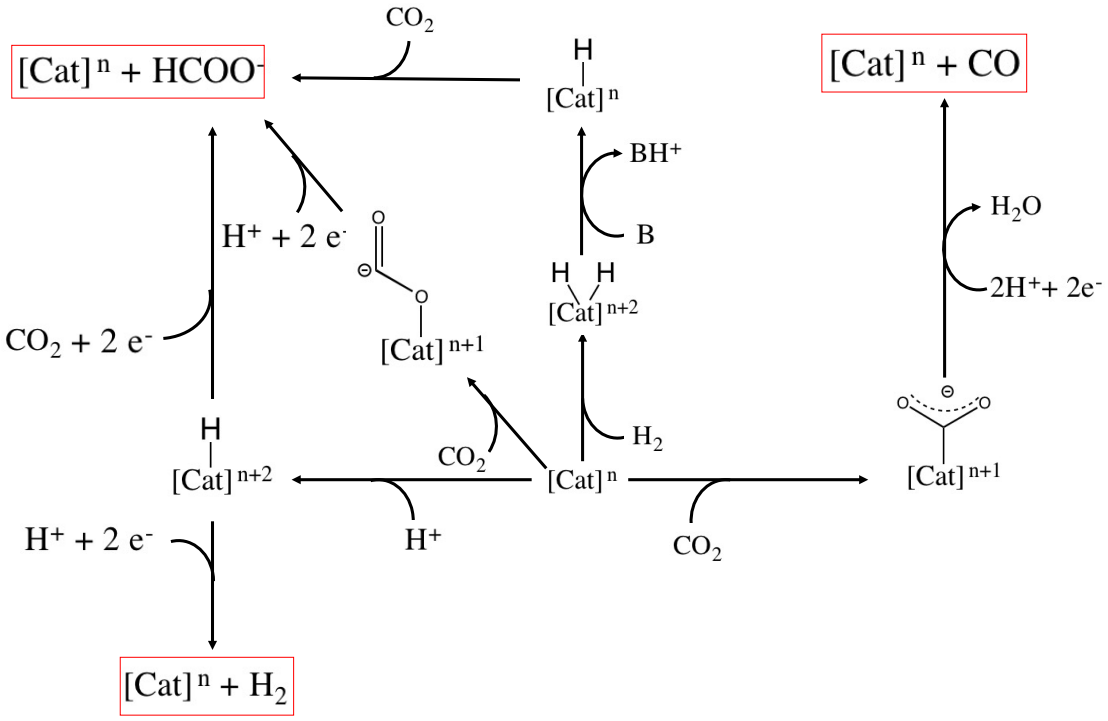


**Figure 9**: Schematic representation of all the reactions involving a two-electron reduction of CO2 and the competitive hydrogen evolution reaction.

The present introduction has detailed the state-of-the-art available homogeneous catalysts for the two 2-electrons reduction products of carbon dioxide, i.e. carbon monoxide and formic acid. All known mechanistic routes have been described, including the side reaction of hydrogen evolution. These routes are sometimes competing against each other and all are summarized in Figure 9. For carbon monoxide generation, it seems that the iron-porphyrin family constitute one of the most efficient and selective family of catalysts reported so far in the literature. We provided multiple examples where spectroscopy and theoretical chemistry were used in order to provide mechanistical insights on catalysts reactivity towards $CO_2$ reduction based on their electronic structure. Ultimately, such approaches aim at providing valuable insights into the rational design of new generations of catalysts. Following this strategy, the aim of this dissertation is to provide a complete understanding of the electronic structure of [Fe(TPP)], prototypical member of the iron-porphyrin family, and relate it to its reactivity towards $CO_2$ reduction. In order to get a complete picture of the electronic structure

of the catalyst, we first studied the molecular catalyst at all the oxidation states intervening in the reaction cycle, formally Fe(II), Fe(I) and Fe(0). Interestingly, these three forms are historically controversial. The electronic ground state of $[Fe^{II}(TPP)]$ has always been subject to debate and the likelihood of strong relativistic effects gives this system a remarkably peculiar magnetic behavior which still remains to be fully understood. The magnetic properties and electronic structure of this system has been first investigated in details in Chapter 1. The electronic structure of $[Fe(TPP)]^-$ and $[Fe(TPP)]^{2-}$ has also been controversial for decades, as the likelihood of the $\pi^*$-orbitals of the porphyrin ring to be the electron-accepting orbitals in the one- and two-electron reductions of $[Fe^{II}(TPP)]$ is still not clear. Elucidating the electronic structure of $[Fe(TPP)]^-$ and $[Fe(TPP)]^{2-}$, in particular regarding the physical oxidation state of the iron, is the purpose of Chapter 2. Once all these questions are answered and the electronic structure of the molecular catalyst is elucidated, DFT models of the reaction intermediates in the $CO_2$-to-CO conversion were built and tested against available experimental data. These models were used as a starting point to investigate the electronic structure-reactivity relationship of [Fe(TPP)] in $CO_2$ reduction. It is the subject of Chapter 3.

Probing the electronic structure of a system requires the joint use of theoretical and experimental methods. On one hand, experimental methods, and particularly spectroscopy, give insights on the investigated system's molecular properties, but the connection between those properties and the electronic structure of this system is often too complex to be inferred without using adapted theoretical models. On the other hand, theoretical methods provide a microscopic understanding of the electronic structure of a system, but may yield biased results for two reasons. First, these methods are all based on approximations which may introduce errors in the modelling of molecular properties. Second, regardless of the accuracy of a method, the relevance of the electronic structure of a modelled system obviously depends on how close it stands to the system of interest. Hence, without connection to the experiment, one has no guarantees that the investigated model is a correct depiction of the real molecule. In this project, extensive use has been made of experimental methods, such as SQUID, X-ray absorption and $^{57}$Fe Mössbauer. To model the electronic structure and reactivity of the investigated systems, computational methods including DFT and CASSCF/NEVPT2 have been used and completed with concepts of thermodynamics. All the theory underlying these methods, experimental and computational, and relevant to the present investigation will be described in the next chapter.

# Theory

## I. Magnetochemistry

### A. Physical origin of the magnetic moment

Some of the investigated compounds in this research have unpaired electrons. Measuring the molar magnetization of a paramagnetic molecular system can give information on the spin and electronic configuration of the ground state, as well as its excited states. Magnetochemistry measurement thus constitute an interesting probe of the electronic structure of a system.

Under an applied magnetic field, these molecular systems have magnetic moments oriented with respect to the applied field:[107]

$$\mu_\alpha = -\frac{dE}{dB_\alpha} \tag{8}$$

Where $\mu_\alpha$ is the $\alpha$-component (x, y or z) of the magnetic moment associated with an electronic state (microscopic magnetic moment), E the energy and $B_\alpha$ the α-component (x,y or z) of the applied magnetic field.

For paramagnetic molecules, the Zeeman effect dominates the field-dependent contribution to the energy:

$$\widehat{H_{Zee}} = \mu_B(g_e\vec{S} + \vec{L}) \cdot \overrightarrow{B_{ext}} \tag{9}$$

Where $\mu_B$ is the Bohr magneton, $g_e$ the g-factor of the electron spin ($g_e = 2.002319$),[108] $\vec{S}$ and $\vec{L}$ are the spin and orbital angular momentum vector operators of the molecular system, respectively, and $\overrightarrow{B_{ext}}$ is the applied magnetic field.

Hence, the microscopic magnetic moment $\vec{\mu}$ of a system provides information on the spin and electronic state, since the magnetic moment operator is related to the spin and orbital angular momentum operators:

$$\widehat{\mu_\alpha} = -\mu_B(g_e\widehat{S_\alpha} + \widehat{L_\alpha}) \tag{10}$$

Where $\widehat{S_\alpha}$ and $\widehat{L_\alpha}$ are the α-components (x,y or z) of the spin and orbital angular momentum vector operator, respectively. In the special case of atoms and other spherically-symmetric systems, each *non-relativistic state* (i.e. eigenstate of the Born-Oppenheimer Hamiltonian) may be described as a manifold of degenerate *magnetic sublevels* $|\lambda, S, M_S, L, M_L\rangle$ of same $\lambda$, $S$ and $L$ but different $M_S$ and $M_L$, where $S$ and $M_S$ are the spin quantum numbers, $L$ is the orbital angular momentum quantum number, and $M_L$ is the magnetic quantum number, with $-S \leq M_S \leq +S$ and $-L \leq M_L \leq +L$. $\lambda$ is a compound label that contains all necessary quantum numbers except $S$, $M_S$, $L$ and $M_L$. In this case, the magnetic moment is isotropic, i.e. it aligns on the magnetic field with the same projected value regardless of the direction of the field.

$$\langle \lambda, S, M_S, L, M_L | \widehat{\mu_\alpha} | \lambda, S, M_S, L, M_L \rangle = -\mu_B (g_e M_S + M_L) \quad (11a)$$

Where $\widehat{\mu_\alpha}$ is the component of the magnetic moment operator aligned to the direction of the applied field. Relationship (11a) holds because in a spherically symmetric environment, $\left[\widehat{H_{B.O.}}, \widehat{S^2}\right] = \left[\widehat{S_\alpha}, \widehat{S^2}\right] = \left[\widehat{H_{B.O.}}, \widehat{L_\alpha}\right] = [\widehat{H_{BO}}, \widehat{L^2}] = 0$ , which means that $S, M_S, L, M_L$ are good quantum numbers. However, in a non-spherical ligand-field, $[H_{B.O.}, L_\alpha] = [H_{BO}, L^2] = 0$ is no longer valid. Hence , $L, M_L$ are no longer good quantum numbers, and only the spin participates to the magnetic moment. The orbital angular momentum is *quenched*. In this case each non-relativistic state may be described as a degenerate manifold of magnetic sublevels $|\lambda, S, M_S\rangle$ of same $\lambda$ and $S$ but different $M_S$. The ensemble of degenerate magnetic sublevels constitutes a *multiplicity*. The number of magnetic sublevels in a multiplicity is (2S+1). For each of these magnetic sublevels,

$$\langle \lambda, S, M_S | \widehat{\mu_\alpha} | \lambda, S, M_S \rangle = g_e M_S \quad (11b)$$

The Born-Oppenheimer Hamiltonian, however, neglects a number of physical effects which tend to partially unquench the orbital angular momentum of the system. For transition metals, the most important of these terms is the spin-orbit coupling (SOC) interaction.[109]

$$\widehat{H} \approx \widehat{H_{B.O.}} + \widehat{H_{Zee}} + \widehat{H_{SOC}} \quad (12a)$$

$$\widehat{H_{SOC}} = 2\mu_B \sum_A \sum_i \frac{Z_A}{|R_A - r_i|^3} \vec{l_i^A} \cdot \vec{s_i} - 2\mu_B \sum_i \vec{s_i} \cdot \sum_{j \neq i} \frac{1}{|r_i - r_j|^3} \left( \vec{l_i^j} + 2\vec{l_j^i} \right) \quad (12b)$$

Where $Z_A$ is the atomic number of the atom A, $R_A$, $r_i$ are the position vectors of the atom A and electron $i$, $l_i^A$ is the orbital angular momentum operator of the electron choosing the atom A as

origin, $s_i$ is the spin angular momentum operator of electron *i*, and $l_i^j$ is the orbital angular momentum operator of the electron *i* choosing the electron *j* as origin.

The SOC effect gets stronger for elements with higher Z. For transition metals, the SOC is usually perturbative with respect to the Born-Oppenheimer Hamiltonian. However, unlike for atoms of the two first periods, it is not negligible and does have a significant effect on the magnetism of a molecular system.

Different approximations may be made to simplify the treatment of SOC. In one approximation widely used in this study, the SOC operator is approximated by its one-electron term, which in turn can be approximated to:

$$\widehat{H_{SOC}} = \zeta_A \sum_i \overrightarrow{l_i^A} \cdot \overrightarrow{s_i} \quad (12c)$$

Where $\zeta_A$ is the SOC constant of the atom A. The competition of SOC effect and ligand-field effect may give rise to an unusually large/small and anisotropic magnetic moment, due to the partial *unquenching* of the orbital angular momentum[110] and/or mixing between different spin states.[111] From a perturbative perspective, both effects can ultimately be traced to the SOC between low-lying non-relativistic states of same and different *S* quantum number, respectively. The nature and energy separation of these states, of course, stems from the ligand field around the metal. The magnetism of a system can therefore be a strong experimental evidence of the system's electronic and molecular structure.

The anisotropic alignment of the magnetic moment with respect to the applied magnetic field is therefore the consequence of SOC perturbations. It is usually described in terms of two phenomenological effects applied on the magnetic sublevels of a given multiplicity, namely the *zero-field splitting* (ZFS) and the *g-anisotropy* (in reference to the corresponding effect in spin Hamiltonian formalism, *vide infra*). The ZFS is an effect existing only for multiplicities higher than 2 (S>1/2). The degeneracy between magnetic sublevels of a same multiplicity is lifted because each $M_S$ eigenstate interacts differently with the excited states manifold via SOC. In the presence of a magnetic field, the ZFS competes with the Zeeman effect for certain field directions, a source of magnetic anisotropy. The *g-anisotropy* refers to the fact that the eigenvalues of $\widehat{\mu_\alpha}$ in a given multiplicity depend on the component $\alpha$=*x*,*y*,*z*. This effect stems from the mixing of excited non-relativistic states into the multiplicity via SOC interactions. It is conceptually different from the ZFS which stems from the energy splitting of the magnetic sublevels in the ground multiplicity (although both effects originate in large part from the SOC interactions). Of note, after the SOC perturbations, the magnetic sublevels within a given multiplicity are no longer eigenstates neither of the Born-Oppenheimer Hamiltonian, nor $\widehat{S_z}$ or

$\widehat{S^2}$ owing to the state mixing stemming from SOC interactions, and are not degenerate anymore due to the ZFS. However, the term of *multiplicity* is still used to describe these sublevels, because consideration of all these sublevels simultaneously is usually required in order to understand the magnetism of a system (*vide infra*).

Because modelling the magnetic behavior of a molecular system via its electronic structure requires a deep knowledge of the system that is not readily available to experimentalists, the Zeeman effect and ZFS are often expressed in term of a phenomenological, parametrized model Hamiltonian: the spin Hamiltonian.[109] This model allows the experimentalists to interpret a magnetochemistry measurement using a simple model without any previous knowledge of the wave-function besides the multiplicity of the non-relativistic ground state (2S+1).

In the spin Hamiltonian model, the magnetic moment operator is replaced by the operator:

$$\overrightarrow{\mu^{SH}} = -\mu_B \, g \cdot \tilde{S} \tag{13a}$$

And the Zeeman effect is described by the following Hamiltonian:

$$\widehat{H_{Zee}^{SH}} = \mu_B \, \overrightarrow{B_{ext}} \cdot g \cdot \tilde{S} \tag{13b}$$

Where $g$ is a 3x3 symmetric matrix, and $\tilde{S}$ is a pseudospin vector operator. The latter acts on the magnetic sublevels of a given multiplicity. Each of these sublevels are assigned the eigenvalue $\tilde{S}(\tilde{S}+1)$ to the operator $\widehat{\tilde{S}^2}$and an eigenvalue $M_{\tilde{S}}$ to the operator $\widehat{\tilde{S}_Z}$, such that $-\tilde{S} < M_{\tilde{S}} < +\tilde{S}$. The $\widehat{\tilde{S}_\alpha}$ operators acts in the basis of the magnetic sublevels in a manner parallel as the $\widehat{S_\alpha}$ operator act on the basis of their eigenvectors:

$$\langle \tilde{S}, M_{\tilde{S}} \mid \tilde{S}_\alpha \mid \tilde{S}, M'_{\tilde{S}} \rangle = \langle S, M_S \mid S_\alpha \mid S, M'_S \rangle \tag{14}$$

Where $\tilde{S} = S$, $M_{\tilde{S}} = M_S$ and $M'_{\tilde{S}} = M'_S$, $S$ and $M_S$ are the real spin quantum numbers. Note that the pseudo-spin is not identical to the real spin unless the SOC effect is negligible enough so the quantum numbers $S$ and $M_S$ are good quantum numbers. In this case however, the $g$-matrix is diagonal and its three diagonal values are equal to $g_e$.

The g matrix always possesses a set of proper axes, in which it is diagonal. In this frame, the g-matrix thus possesses three independent parameters ($g_{xx}$, $g_{yy}$ and $g_{zz}$). These three g-values contain the information relative to the *g-anisotropy*.

An important property of the spin Hamiltonian Zeeman operator is that there always exists a set of g-values such that for a multiplicity of 2 or 3, the spin Hamiltonian Zeeman operator (eq.

13b) reproduces all matrix elements of the Zeeman operator (eq. 9) in the basis of the magnetic sublevels *after perturbation by SOC*.[112] This property means that one can reproduce the Zeeman effect simply by parametrizing three g-values. We note here in passing that the sign of the g-values determines the relative orientation of the pseudospin vector with respect to the applied field, but has no influence on the description of the Zeeman effect.[112] However, the sign of the product $g_{xx}g_{yy}g_{zz}$ does have a physical significance.[113] To simplify the description and because this significance has no influence on the description of the magnetism in this study, we simply assumed that all three *g*-values are positive.

On the other hand, the spin Hamiltonian Zeeman operator does not describe any field-dependent coupling between the magnetic sublevels of a given multiplicity and those of higher-lying states. If the set of magnetic sublevels from a given multiplicity is significantly lower in energy than those higher-lying states, then those couplings can be neglected. However, in the case of orbitally-degenerate or near-degenerate non-relativistic states, this approximation is no longer valid and the spin Hamiltonian model is insufficient. A more detailed analysis of the shortcoming of this Hamiltonian is available in chapter 1.

Note that for multiplicities higher than 3, it is possible that the spin Hamiltonian does not reproduce the Zeeman matrix exactly, and require operators of higher orders in $\tilde{S}$ for an exact description of the Zeeman effect.[112] These higher-order operators are not needed in this study, since [Fe(TPP)], [Fe(TPP)]$^{-}$ and [Fe(TPP)]$^{2-}$ have multiplicities of 3, 2 and 1, respectively (see chapters 1, 2 and 3).

The ZFS effect is taken in account by the spin Hamiltonian ZFS operator (eq. 15a).

$$\widehat{H_{ZFS}^{SH}} = \tilde{S} \cdot \overline{\overline{D}} \cdot \tilde{S} \qquad (15a)$$

$\overline{\overline{D}}$ is a symmetric 3x3 tensor. It has a set of proper axes and its trace is zero, which leaves two independent parameters. By convention, $|D_{zz}| > |D_{yy}| \geq |D_{xx}|$

In the proper axis of D, the spin Hamiltonian ZFS is usually rewritten in a more convenient form (eq. 15b):

$$\widehat{H_{ZFS}^{SH}} = D\left(\tilde{S}_z^2 - \frac{\widetilde{S^2}}{3}\right) + E\,(\widetilde{S_x} - \widetilde{S_y}) \qquad (15b)$$

Where $D = \frac{3}{2}D_{ZZ}$ and $E = \frac{D_{xx}-D_{yy}}{2}$. $D$ is called the axial ZFS parameter, and $E$ is called the rhombicity parameter.

For a multiplicity equal to 3, there is always a value of D and E such that $H_{ZFS}^{SH}$ reproduces the ZFS of the magnetic sublevels. Like for the Zeeman effect, higher-order terms may be

necessary for multiplicities higher than 3,[112] but study of these operators is beyond the scope of this study.

Of note, the proper axes of the matrices $\overline{\overline{D}}$ and $g$ are not necessarily colinear. In principle, this may force the incorporation of additional parameters in the spin Hamiltonian to account for the rotation matrix between these axes. However, this difficulty does not arise for systems with symmetry axes of order superior or equal to 3, where the proper axes must be aligned to the axis of symmetry. In this investigation, the system possesses an effective $C_4$ symmetry, thus this additional layer of complexity will not be addressed.

Hence, the magnetic moments of the magnetic sublevels of a given multiplicity give information on its spin state. Furthermore, through resolving the anisotropy of the magnetic moments, one may get information on the *ZFS* and *g-anisotropy* effect due to the SOC perturbation, and ultimately, get information on the electronic structure of the ground and excited non-relativistic states manifold of the investigated system. A good example of in-depth analysis of the electronic structure of a system based on its magnetism will be provided in chapter 1.

## B. Macroscopic magnetization

### 1) High-temperature magnetization

Unfortunately, the microscopic magnetic moment of a molecular system is not directly observable, but experimentally one may measure the macroscopic magnetization of an ensemble of particles at a given temperature. Since the population of excited magnetic sublevels for such an ensemble follows a Boltzmann distribution,

$$\vec{M} = N_A \frac{\sum_i \vec{\mu_i} e^{-\frac{E_i}{k_B T}}}{\sum_i e^{-\frac{E_i}{k_B T}}} \tag{16}$$

Where $\vec{M}$ is the molar magnetization vector, $N_A$ the Avogadro number, $\vec{\mu_i}$ is the magnetic moment of the magnetic sublevel $i$, $E_i$ is the energy of the magnetic sublevel $i$, $k_B$ is the Boltzmann constant and $T$ is the temperature. A set of magnetic sublevels of a given multiplicity have a total energy:

$$E_i = E_{ZFS,i} - \vec{\mu_i} \cdot \overrightarrow{B_{ext}} \tag{17}$$

Where $E_{ZFS,i}$ is the ZFS energy.

Hence, eq. 16 becomes:

$$\vec{M} = N_A \frac{\sum_i \vec{\mu_i} e^{-\frac{E_{ZFS,i}}{k_B T}} e^{\frac{\vec{\mu_i} \cdot \vec{B_{ext}}}{k_B T}}}{\sum_i e^{-\frac{E_{ZFS,i}}{k_B T}} e^{\frac{\vec{\mu_i} \cdot \vec{B_{ext}}}{k_B T}}} \quad (18)$$

In general, at high temperatures, the Zeeman effect is much lower than $k_B T$, meaning that

$$\vec{M} \approx N_A \frac{\sum_i \vec{\mu_i} e^{-\frac{E_{ZFS,i}}{k_B T}} \left(1 + \frac{\vec{\mu_i} \cdot \vec{B_{ext}}}{k_B T}\right)}{\sum_i e^{-\frac{E_{ZFS,i}}{k_B T}} \left(1 + \frac{\vec{\mu_i} \cdot \vec{B_{ext}}}{k_B T}\right)} \quad (19a)$$

$$\vec{M} \approx \frac{N_A \sum_i \vec{\mu_i} e^{-\frac{E_{ZFS,i}}{k_B T}}}{\sum_i e^{-\frac{E_{ZFS,i}}{k_B T}} \left(1 + \frac{\vec{\mu_i} \cdot \vec{B_{ext}}}{k_B T}\right)} + \frac{N_A \sum_i \frac{(\vec{\mu_i} \cdot \vec{B_{ext}}) \vec{\mu_i}}{k_B T} e^{-\frac{E_{ZFS,i}}{k_B T}}}{\sum_i e^{-\frac{E_{ZFS,i}}{k_B T}} \left(1 + \frac{\vec{\mu_i} \cdot \vec{B_{ext}}}{k_B T}\right)} \quad (19b)$$

At high temperature limits, where $E_{ZFS,i} \ll k_B T$, all the exponential terms tend towards 1.
In the absence of a field, following time-reversal symmetry requirements,[114] any magnetic sublevel within a given multiplicity possessing a non-zero first-order magnetic moment has a degenerate counterpart with an exactly opposite magnetic moment. Therefore, the sum of magnetic moments within a given multiplicity is zero.

We now treat the case where *Zeeman couplings between the magnetic sublevels of the considered multiplicity and higher-lying sublevels are neglected*. As mentioned in subsection I.A, this is the case here the spin Hamiltonian is a valid approximation. In this case, the sum of the magnetic moments within the ground multiplicity remains zero regardless of the direction of the field, since the trace of a matrix (here the magnetic moments matrix in the basis of the magnetic sublevels of the multiplicity) remains unchanged upon unitary transformation. The consequence is that the first term of eq. 19b vanishes. The expression of the $\alpha$ component of the magnetization thus becomes:

$$\vec{M} \approx \frac{N_A \sum_i \frac{(\vec{\mu_i} \cdot \vec{B_{ext}}) \vec{\mu_i}}{k_B T}}{2S+1} \quad (19c)$$

Although the angular-dependence of the magnetization can be resolved on single crystals, in the general case, the measured samples are powder-distributed. In this case, the observable magnetization corresponds to the averaged magnetization over all directions of the sphere, i. e., if $\vec{e_B}$ is the unitary vector carrying the direction of the field,

$$\langle M \rangle \approx \frac{1}{4\pi} \int_{\phi=0}^{\phi=2\pi} \int_{\theta=0}^{\theta=\pi} \left(\vec{M} \cdot \vec{e_B}\right) sin\theta \, d\theta d\phi \quad (19d)$$

$$\langle M \rangle \approx \frac{N_A B_{ext}}{(2S+1)3k_B T} \sum_i \langle \mu_i^2 \rangle \quad (19e)$$

$$\chi T = \frac{\langle M \rangle T}{B_{ext}} = \frac{N_A}{(2S+1)3k_B} \sum_i \langle \mu_i^2 \rangle \quad (19f)$$

The magnetic susceptibility $\chi$ of a system is defined as the ratio of the magnetization by the magnetic field norm. It becomes apparent from (19f) that at high temperature, $\chi T$ reaches a regime independent of temperature (Curie law). Note that some authors use the effective magnetic moment $\mu_{eff} = \left(\frac{3k_B}{N{\mu_B}^2}\chi T\right)^{\frac{1}{2}}$ rather than $\chi T$, because the former has units of Bohr magneton.

Using the spin Hamiltonian expression for the magnetic moment (eq. 13a), eq. 19f becomes the eq. 20.[107]

$$\chi T = \frac{\langle M \rangle T}{B} \approx \frac{N_A {\mu_B}^2}{3k_B} g_{av}^2 \tilde{S}(\tilde{S}+1) \quad (20)$$

With $g_{av}^2 = \frac{g_{xx}^2 + g_{yy}^2 + g_{zz}^2}{3}$.

Importantly, in this regime the magnetization is independent of the ZFS and of the g-anisotropy. However, it depends to a large extend of the unperturbed non-relativistic ground state multiplicity. However, it also depends on the average g-value, which may deviate from $g_e$ if the orbital angular momentum is significantly unquenched and/or if the ground multiplicity is a spin mixture. Oftentimes, the average g-value is deduced from high-temperature magnetic susceptibility measurements; while ZFS parameters are deduced from low-temperature measurements (*vide infra*).

Note that when the Zeeman coupling with higher-lying states are no longer negligible, the magnetic moment of each magnetic sublevel is affected accordingly. In fact, the magnetic sublevels of the ground multiplicity cannot be diagonalized independently from the higher-lying multiplicities. As a result, the sum of the magnetic moments within the multiplicity is not necessarily zero. It will now be shown that under this condition, the first term in eq. 19b does not cancel out. Suppose the total Hamiltonian is diagonalized in the basis of the magnetic sublevels of the ground multiplicity. We take the resulting eigenvectors *i* as basis. Then, following perturbation theory, we have:

$$\langle \mu_{\alpha,i} \rangle = \langle \mu_\alpha \rangle_i^{(1)} + \langle \mu_\alpha \rangle_i^{(2)} \quad (21a)$$

Where the first term of eq. 21a corresponds to the magnetic moment in the absence of Zeeman couplings with higher-lying terms. The second term can be estimated via second-order perturbation theory.

$$\langle \mu_\alpha \rangle_i{}^{(2)} = -\frac{d}{dB_{ext,\alpha}}\left[\sum_j \frac{\langle j|\vec{\mu}\cdot\overrightarrow{B_{ext}}|i\rangle\langle i|\vec{\mu}\cdot\overrightarrow{B_{ext}}|j\rangle}{E_i - E_j}\right] \quad (21b)$$

Where $j$ runs over all sublevels except for the sublevels of the same multiplicity as $i$, since the Hamiltonian matrix is already diagonal in this basis. Of note, the term within bracket is negative by construction since $E_i - E_j < 0$ (the sublevel $i$ belongs to the ground multiplicity). Consequently, $\langle \mu_\alpha \rangle_i{}^{(2)}$ is positive by construction. Hence the sum of $\langle \mu_\alpha \rangle_i{}^{(2)}$ does not cancel out. Inserting eq. 21a and 21b into eq. 19b, remembering that the first term in eq. 21a is the magnetic moment in the absence of Zeeman couplings with higher-lying terms, the sum of $\langle \mu_\alpha \rangle_i{}^{(1)}$cancel out, and after a bit of mathematic treatment,

$$M_\alpha \approx -\frac{N_A}{2S+1}\sum_{\beta,j,i} \frac{B_\beta\left\{\langle j|\widehat{\mu_\alpha}|i\rangle\langle i|\widehat{\mu_\beta}|j\rangle + \langle j|\widehat{\mu_\beta}|i\rangle\langle i|\widehat{\mu_\alpha}|j\rangle\right\}}{E_i - E_j} + \frac{N_A \sum_i \frac{(\overrightarrow{\mu_i}\cdot\overrightarrow{B_{ext}})\mu_{i,\alpha}}{k_B T}}{2S+1} \quad (21c)$$

Here $\alpha$ and $\beta$ correspond to the x,y,z components. The first term becomes dominant at high temperature since by opposition to the second, it is not temperature-dependent. The corresponding susceptibility therefore gives rise to a Temperature Independent Paramagnetism (TIP), which manifests itself in that the $\chi T$ measurement does not reach a plateau at high-temperature, but instead exhibit a linear increase with temperature.[115]

2) Low-temperature magnetization

While the measurement of the magnetic susceptibility at high temperature gives information on the spin state and on the presence of significantly unquenched orbital angular momentum or spin mixture, the measurement of the magnetization at low temperature, on the other hand, gives extensive information about the ZFS. Within the magnetic sublevels of a given multiplicity, the macroscopic magnetization generally decreases as the temperature increases. The temperature profile of the magnetization (eq. 18) depends on the ZFS parameters. In systems with low ZFS in general, the Curie temperature is reached at lower temperature, since lower temperatures are required to reach the regime $E_{ZFS,i} \ll kT$. Furthermore, the evolution of the temperature profile of the magnetization in the low-temperature region strongly depends of the ZFS. Systems with non-degenerate ground magnetic sublevel isolated from the other

sublevels of its multiplicity (odd multiplicity systems with positive D and/or large rhombicity) tend to exhibit a constant magnetization at low-temperature. In such systems, the ground sublevel remains the only populated sublevel for a long range of temperature over which the macroscopic magnetization is essentially due to the ground sublevel, which is temperature-independent. On the contrary, systems where the ground magnetic sublevel is close to degenerate, (systems with large negative D and low rhombicity and/or even multiplicity systems), the magnetization exhibits a rapid decay with temperature. In those configurations, several magnetic sublevels with different magnetic moments are being rapidly populated via Boltzmann distribution as temperature increases, making the overall magnetization highly dependent on temperature.

The field-dependence dependence of the magnetization at a given temperature is also related to the ZFS. Indeed, in high-field limit, i. e. $D \ll \beta g B$, the effect of the ZFS is negligible and the magnetization arises from first-order magnetic moments. Hence, along the direction of the field:

$$\overrightarrow{\mu_i} = \mu_B \langle i | g_e \vec{S} + \vec{L} | i \rangle \tag{22}$$

The magnetic sublevel *i* is an eigenvector of the Zeeman Hamiltonian. Hence, in the high-field limit, the magnetization is independent of the applied field.

On the other hand, in low-field limit, $E_{ZFS} \gg \beta g_e B$, the ZFS dominates over the Zeeman effect. The Zeeman effect thus becomes perturbative and the magnetic moment of each sublevel is described by first and second-order contributions (Van Vleck approximation).[107] The latter is linear with the applied field and inverse proportional to the ZFS energies (eq. 23).

$$\langle \hat{\mu}_{\alpha,i} \rangle = \langle \hat{\mu}_\alpha \rangle_i{}'^{(1)} + \langle \hat{\mu}_\alpha \rangle_i{}'^{(2)} \tag{23a}$$

$$\langle \hat{\mu}_\alpha \rangle_i{}'^{(1)} = \mu_B \langle i | \widehat{\mu_\alpha} | i \rangle \tag{23b}$$

$$\langle \hat{\mu}_\alpha \rangle_i{}'^{(2)} = -\sum_{\beta, j \neq i} \frac{B_\beta \{ \langle j | \widehat{\mu_\alpha} | i \rangle \langle i | \widehat{\mu_\beta} | j \rangle + \langle j | \widehat{\mu_\beta} | i \rangle \langle i | \widehat{\mu_\alpha} | j \rangle \}}{E_i - E_j} \tag{23c}$$

The unperturbed sublevels *i* and *j* are SOC (or ZFS in a SH formalism) eigenstates instead of total Hamiltonian eigenstates. Hence, in low-field limit, the magnetization is linear with the field.

The overall field profile of low-temperature magnetization, i. e., the transition from low-field to high-field limit, as well as the slope of the low-field limit profile, is also highly dependent on the ZFS parameters, as seen in Figure 10. Hence, the simultaneous fit of the temperature and

field profile of the low-temperature magnetization (VTVH) is a strong assignment of the zero-field splitting.

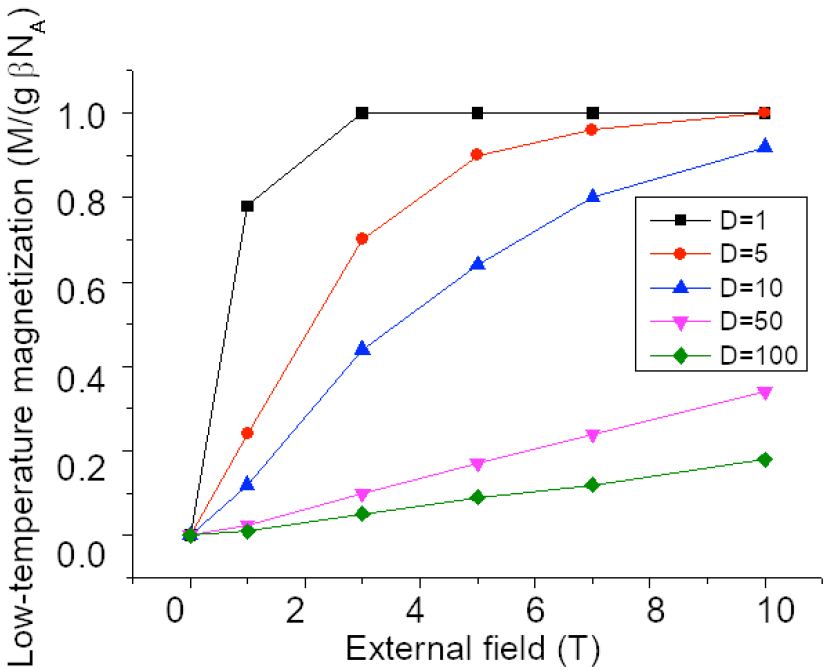


**Figure 10**:Evolution of the field profile of low temperature average magnetization for a S=1 system with isotropic g-value g=$g_e$, $E$=0 and different axial ZFS parameters $D$=1, 5, 10, 50 and 100 $cm^{-1}$. For D=1 and D=5, the system operates its transition to high-field limit within the investigated field range. For D=50 and D=100, the system remains in low-field limit over the investigated range.

## II. $^{57}$Fe Mössbauer

The $^{57}$Fe Mössbauer spectroscopy is a $\gamma$-ray absorption spectroscopy used to probe with an extreme precision the local electronic structure of an iron center. In details, this spectroscopy is based on the resonant absorption of a gamma photon of 14.4 keV by an iron nucleus in its ground state. Due to the large half-time of the iron nucleus,[116] the absorption line is very narrow and the technique is dependent on the use of a source able to produce photons of the exact energy. Those photons are obtained by electron capture of $^{57}$Co into $^{57}$Fe in its excited nuclear state followed by the deexcitation of the $^{57}$Fe. The recoilless deexcitation of $^{57}$Fe produces a photon of precisely 14.4 keV.

Paradoxically, while the absorption is a nuclear process, the Mössbauer spectroscopy makes use of the very narrow absorption line of the absorber to detect extremely subtle shifts resulting from the electrons-nucleus interactions (hyperfine effects). To account for these subtle shifts, the energy of the source is slightly modulated by Doppler effect, by moving it forward or backwards from the absorber. For this reason, the energy of Mössbauer spectra is expressed in terms of the velocity of the source (in mm/s). The velocity is related to the energy by the expression of the Doppler effect[117] :

$$E_n = E_\gamma \left(1 + \frac{v_n}{c}\right) \quad (24)$$

Where $E_\gamma$ is the energy of the incident gamma photon ($E_\gamma = 14.4$ keV), $v_n$ the velocity of the source, and $c$ the speed of light.

The hyperfine effects can be classified into two kinds. The *electric* hyperfine interactions, correspond to the electrostatic interactions between the iron nucleus and the electrons surrounding it. The *magnetic* hyperfine interactions correspond to the interaction between the iron nuclear spin and the magnetic field created by the electrons surrounding it.

## A. Electric hyperfine interactions

The electric hyperfine interactions regroup all electric interactions between the iron nucleus and the electrons surrounding it. Since the charge distribution of the nucleus changes upon nuclear excitation, the electric hyperfine interactions do not cancel out exactly, and the absorption energy of the photon is modulated accordingly.

The Taylor expansion (up to second-order) of the electrostatic interaction between the nucleus and the electronic potential is:

$$E_{el} = \int \rho_N V(\vec{r}) d\tau \approx \int \rho_N V(0) d\tau + \sum_\alpha \int \rho_N V_\alpha x_\alpha d\tau + \frac{1}{2} \sum_\alpha \sum_\beta \int \rho_N V_{\alpha\beta} x_\alpha x_\beta \, d\tau \quad (25)$$

Where $\rho_N$ is the charge distribution within the nucleus, $V(\vec{r})$ is the electrostatic potential described by the electrons, $V_\alpha = \frac{dV}{dx_\alpha}$, and $V_{\alpha\beta} = \frac{d^2V}{dx_\alpha dx_\beta}$ are the $\alpha$ and $\beta$ (x,y,z) components of the electric field vector and electric field gradient (EFG) tensor at the center of charge of the nucleus, respectively. The terms $x_\alpha$ and $x_\beta$ represent the $\alpha$ and $\beta$ components of the position vector. The term $d\tau$ is the infinitesimal volume element $d\tau = dxdydz$.

The first term corresponds to the electrostatic potential of the nucleus treated as a point charge and enters in the composition of the usual Born-Oppenheimer Hamiltonian. The second term is zero, because the center of charge of the nucleus is always in a stable position with respect to the electrons (Hence the potential gradient in any direction is zero). The third term on the other hand, is non-zero. Since $\rho_N$ is different for the ground and excited nuclear state, it becomes apparent that the third term in eq. 25 slightly modulates the absorption energy of the photon. It is also apparent that this effect is correlated to the electrostatic potential of the electrons surrounding the iron nucleus, hence hinting that knowledge of these electric hyperfine interactions may bring information on the electronic structure surrounding iron.

The third term in eq. 25 ($E_{el}^{(2)}$) may be reorganized into a sum of monopole and quadrupole contributions (first and second term, respectively, in eq. 26)[118]:

$$E_{el}^{(2)} = E_{monopolar}^{I} + E_{Q}^{I} \tag{26a}$$

$$E_{el}^{(2)} = \frac{1}{6}\sum_{\alpha} \int \rho_N \, V_{\alpha\alpha} r^2 \, d\tau + \frac{1}{6}\sum_{\alpha}\sum_{\beta} \int \rho_N \, V_{\alpha\beta}(3x_\alpha x_\beta - r^2\delta_{\alpha\beta}) \, d\tau \tag{26b}$$

Here, *r* is the norm of the position vector. The monopolar contribution cannot be evaluated precisely because the nuclear charge distribution is not known. However, under the approximation that the nucleus is a uniformly-charged sphere, this term can be treated classically to yield the following energy term[116]:

$$E_{monopolar}^{I} = -\frac{2\pi}{5} e^2 Z_{Fe} {R_I}^2 \rho_{el}(0) \tag{27a}$$

Where e is the elementary charge of the electron, $Z_{\mathrm{Fe}}$ the charge of the iron nucleus, $R_I$ the radius of the nucleus in a given nuclear state of nuclear spin I, and $\rho_{el}(0)$ is the electronic density at the charge center of the nucleus. Because $R_I$ changes from one nuclear state to another, the interaction energy does not cancel out during the excitation process, leading to an energy modulation as described by the following equation:

$$\Delta E_{monopolar} = -\frac{2\pi}{5} e^2 Z \rho_{el}(0)\{{R_I}'^2 - {R_I}^2\} \tag{27b}$$

Note that this term is not zero for the source, and modulates the energy of the incident photons, as well as the resonant energy of the absorber. In fact, this term is the physical origin of the isomer shift $\delta$, which corresponds to the difference of monopolar interaction energy of the absorber with respect to that of the source.

$$\delta = \Delta\Delta E_{monopolar} = -\frac{2\pi}{5} e^2 Z\left\{{R_I}'^2 - {R_I}^2\right\}\{\rho_{el}^{absorber}(0) - \rho_{el}^{source}(0)\} \tag{27c}$$

Where $\rho_{el}^{absorber}(0)$ and $\rho_{el}^{source}(0)$ correspond to the electron density at the center of charge of the source and of the absorber, respectively. Interestingly, the isomer shift is proportional to the s-electrons density, since those are the only ones with non-zero density at the charge center of the nucleus. The s-density at the nucleus is sensitive to any effect susceptible to expand or contract the electronic density around the nucleus, making the isomer shift very sensitive to oxidation state and chemical environment of the iron. Specifically, isomer shifts are sensitive to the number of coordination and soft character of the ligands, [116] as well as the spin state of iron since it influences iron-ligand bond lengths. Although trends have been established to correlate isomer shifts with oxidation and spin states of iron,[116] the many competing physical effects determining the isomer shift make the use of computational chemistry-based methods almost unavoidable for a precise assignment (*vide infra*).

The second term in eq. 26 corresponds to the quadrupolar interactions. In principle, the direct use of that term implies the knowledge of the charge distribution of the nucleus. However, recognizing that the expression $(3x_\alpha x_\beta - r^2\delta_{\alpha\beta})$ may be expressed as a rank 2 spherical tensor operator, the quadrupolar interactions Hamiltonian may be expressed, after a mathematical derivation described elsewhere,[118] using the nuclear spin operators according to eq. 28a:

$$\widehat{H_Q^I} = \frac{eQ}{6I(2I-1)} \sum_\alpha \sum_\beta V_{\alpha\beta} \left\{\frac{3}{2}\left(I_\alpha I_\beta + I_\beta I_\alpha\right) - \delta_{\alpha\beta} I^2\right\} \quad (28a)$$

Where the quadrupolar moment of the nucleus Q is a constant of the nuclear quantum number I. Note that the nuclear spin of the nuclear ground state of $^{57}$Fe is I=1/2, while its excited state is characterized by a nuclear spin I=3/2. $I_\alpha$ and $I_\beta$ are the $\alpha$ and $\beta$ components of the Nuclear spin vector operator $\vec{I}$. Noting that $V_{\alpha\beta}$ is a tensor, one deduces that a set of proper axes may always be used. Since the tensor is traceless, $V_{\alpha\beta}$ may be described in this frame by two parameters, $V_{zz}$ and $\eta = \frac{V_{xx}-V_{yy}}{V_{zz}}$. By convention, $|V_{zz}| \geq |V_{yy}| \geq |V_{xx}|$, hereby insuring that $0 \leq \eta \leq 1$. At this point it is worthwhile to introduce the notion of *nuclear magnetic sublevels*, which correspond to the multiplicity of simultaneous $I^2$ and $I_z$ eigenstates $|I, M_I\rangle$, with $-I < M_I < +I$. In the absence of electric quadrupolar interactions (or magnetic interactions, *vide infra*), these sublevels are degenerate. Following the Hamiltonian of eq. 28a, the quadrupolar interactions split the magnetic sublevels of the excited nuclear state (I=3/2) into two doublets, separated by a value determined by $V_{zz}$ and $\eta$:

$$\Delta E_Q = \frac{eQV_{zz}}{2}\left(1 + \frac{\eta^2}{3}\right)^{\frac{1}{2}} \quad (28b)$$

On the other hand, the ground nuclear state (I=1/2) is not affected by quadrupolar interactions because the quadrupolar moment Q associated with this nuclear state is zero.

Like for the monopolar interaction, the quadrupole splitting energy should in principle be substracted to that of the source, but the symmetry of the source is cubic, meaning that there is no EFG at the nucleus. Hence the energy of the emitted photons is not affected by any quadrupole splitting.

The contribution of the electronic wavefunction to the quadrupole splitting arises from the EFG tensor $V_{\alpha\beta}$. This EFG tensor is highly sensitive to the local electronic structure of the iron, and is influenced by the iron's electronic configuration, ligand field and iron-ligand covalency.

In a ligand-field approximation, the iron center consists of filled 1s, 2s, 2p and 3s subshells, as well as a partially-filled 3d subshell. Electronic density from electrons populating entirely filled subshells has a cubic symmetry, hence participation of these electrons to the EFG is zero. Hence, in this approximation only the population of the d-electrons may induce a non-zero EFG at the nucleus.

However, the ligand-field picture is often qualitatively correct at most. To analyze further the origin of the EFG, one must often consider the mixing between iron-based and ligand-based orbitals. Furthermore, the polarization of the core shells under the action of the ligand field may lead to small departure from perfect cubic symmetry. The analysis of ligand orbital participation and core polarization effects on the EFG tensor is not straightforward and requires the use of computational chemistry-based methods (*vide infra*).

Inferring the electric hyperfine effects parameters from a Mössbauer spectrum in the absence of a magnetic field is rather easy. The $^{57}$Fe Mossbauer spectrum exhibits a doublet. The splitting between doublets corresponds to the quadrupole splitting. The energy difference between the center of the doublet and the reference energy (velocity of the source $v_n = 0\ mm/s$) corresponds to the isomer shift (Figure 11)

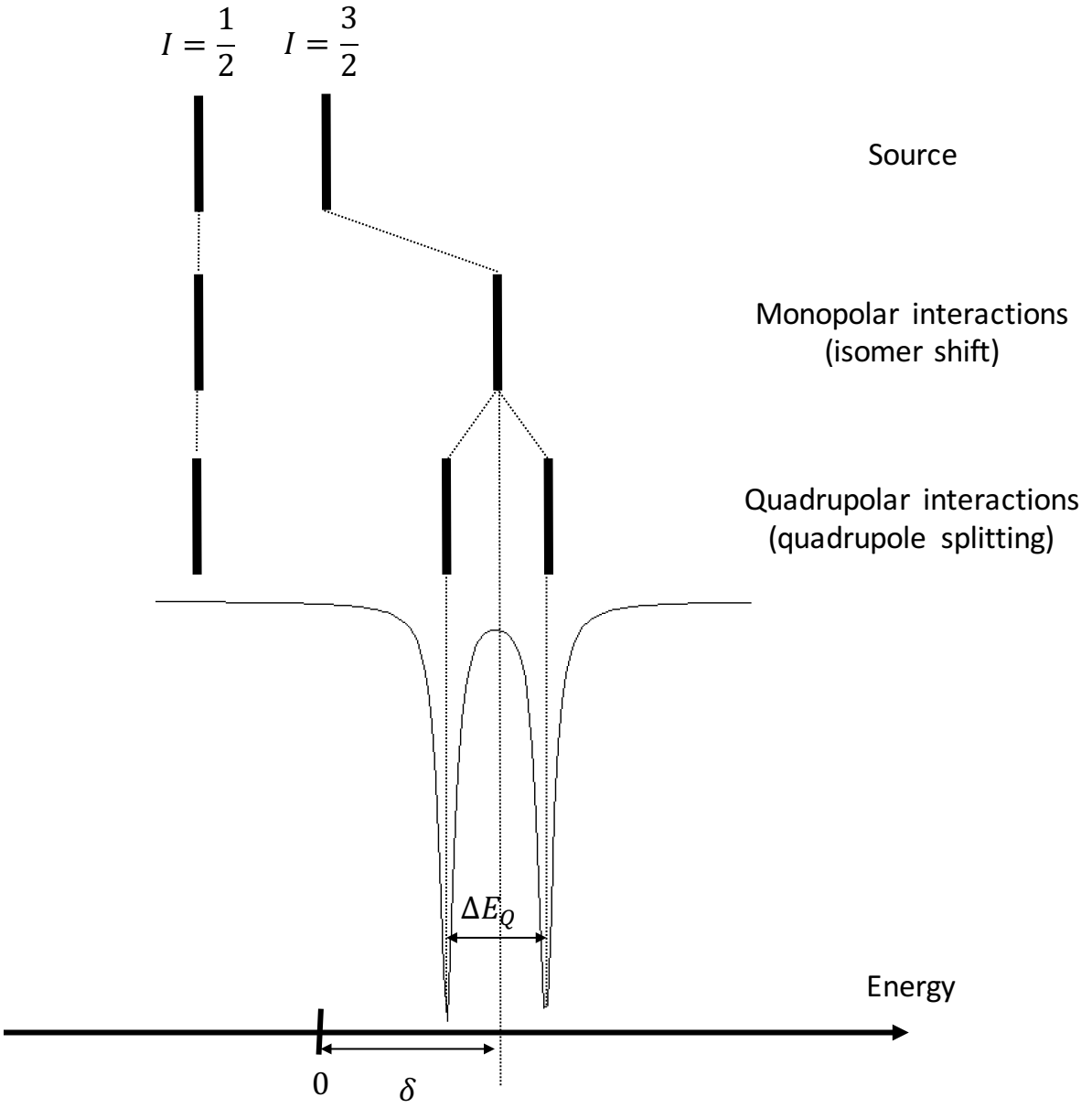


**Figure 11**: (Top) schematic representation of the $\gamma$-photon absorption energies relative to the ground nuclear state, as modulated by the monopolar and quadrupolar interactions. (Bottom) Corresponding $^{57}$Fe Mössbauer spectrum lines. Isomer shifts and quadrupole splitting are identified on the spectrum as $\delta$ and $\Delta E_Q$. The energy reference is taken as the excitation energy of the source.

## B. Magnetic hyperfine interactions

### 1) Magnetic hyperfine interactions alone

As already stated in this section, the ground nuclear state of iron may be described with its nuclear spin angular momentum, which is characterized by a spin number I=1/2. The excited nuclear state on the other hand, has a nuclear spin of I=3/2. In the absence of electric quadrupolar effects and magnetic effects, each of these states are composed of (2I+1) degenerate nuclear magnetic sublevels $|I, M_I\rangle$ with $-I < M_I < +I$. This degeneracy is lifted in the presence of a magnetic field because the nuclear spin tends to align with a magnetic field due to the Nuclear Zeeman effect:

$$\widehat{H_{Zee}^{Nuc}} = -g_N \beta_N \vec{I} \cdot \overrightarrow{B_{ext}} \tag{29}$$

The term $g_N$ corresponds to the g-factor of iron. It is different for the nuclear state I=1/2 ($g_N = 0.181$) than for the nuclear state I=3/2 ($g_N = -0.103$).[116] $\beta_N$ corresponds to the nuclear magneton. Notably, the sign of the g-factor is different between these nuclear states. Consequently, under a positive magnetic field, the sign of the $M_I$ values for the lowest-lying nuclear magnetic sublevel is positive for the I=1/2 states and negative for the I=3/2 states (Figure 12). Although the splitting of the nuclear magnetic sublevels gives rise to eight possible transitions, magnetic spectra (in the absence of a quadrupole splitting) give rise to a six-lines pattern. The reason is inferred from the consideration that the Mössbauer transition are mostly magnetic dipole transitions. Those have selection rules of $\Delta M_I = 0, \pm 1$, which make two of those eight transitions forbidden.

The magnetic splitting of the nuclear magnetic levels may be due to an externally applied magnetic field and/or a field created at the nucleus by the electrons surrounding it, through hyperfine effects.

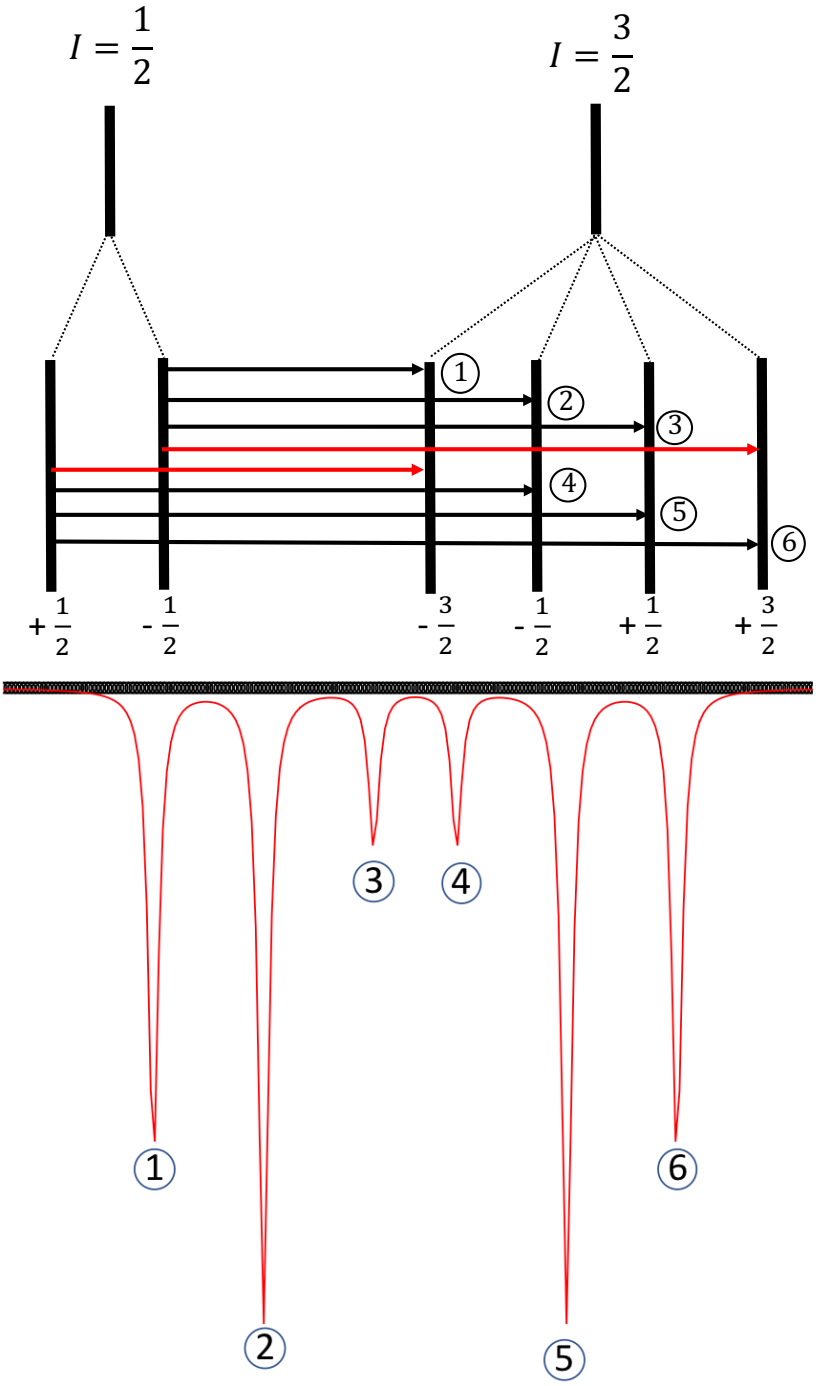


**Figure 12**: (Top) Magnetic splitting of the ground (I=1/2) and excited (I=3/2) nuclear states of $^{57}$Fe under a magnetic field. Each nuclear magnetic sublevel is labelled by its $M_I$ value. In this case no electric quadrupolar interactions are considered. Allowed transitions are displayed as black arrows and labelled by numbers from 1 to 6. Forbidden transitions are displayed as red arrows. (Bottom) Schematic representation of the corresponding $^{57}$Fe Mössbauer spectrum. Each line of the spectrum is labelled with the number corresponding with the associated transition.

and associated transition in Mossbauer spectroscopy. The intensity ratios of the transition lines will be discussed later. The red transition are magnetic-dipole forbidden transitions.

The magnetic hyperfine interactions regroup all interactions between the nuclear spin of iron and the magnetic field created by the electrons surrounding it. The latter originates either from the orbital or spin momenta of the electrons surrounding the iron.

Usually, the magnetic hyperfine interactions are a sum of three components, i. e. the Fermi-contact interactions (eq. 30b), the spin-dipole interactions (eq. 30c) and the orbital interactions (eq. 30d). Those three interaction Hamiltonian take the form[119]:

$$\widehat{H_{HFC}} = \widehat{H_{FC}} + \widehat{H_{SD}} + \widehat{H_{LI}} \tag{30a}$$

$$\widehat{H_{FC}} = \mu_B \beta_N g_e g_N \vec{I} \cdot \left[\sum_i \frac{8\pi}{3} \delta(r_i) \vec{s_i}\right] \tag{30b}$$

$$\widehat{H_{SD}} = \mu_B \beta_N g_e g_N \vec{I} \cdot \left[\sum_i \frac{3(\vec{r_i} \cdot \vec{s_i})\vec{r_i}}{r_i^5} - \frac{\vec{s_i}}{r_i^3}\right] \tag{30c}$$

$$\widehat{H_{LI}} = 2\mu_B \beta_N g_N \vec{I} \cdot \sum_i \frac{\vec{l_i}}{r_i^3} \tag{30d}$$

Here the sum i runs over all electrons, $r_i$ is the radius of the electron position with respect to the iron center and $\delta(r_i)$ is the dirac function. Each of these interactions may be viewed as a Nuclear Zeeman interaction between the nuclear spin and a magnetic field generated by the electrons, defining the Fermi-contact, spin-dipole interaction and orbital internal field operators:

$$\widehat{H_{HFC}} = -g_N \beta_N \vec{I} \cdot \overrightarrow{B_{int}} \tag{31a}$$

$$\overrightarrow{B_{int}} = \vec{B}_{FC} + \vec{B}_{SD} + \vec{B}_{LI} \tag{31b}$$

$$\vec{B}_{FC} = -\frac{8}{3}\pi g_e \mu_B \sum_i \delta(r_i) \vec{s_i} \tag{31c}$$

$$\vec{B}_{SD} = -g_e \mu_B \sum_i 3 \frac{\vec{r_i}(\vec{s_i} \cdot \vec{r_i})}{r_i^5} - \frac{\vec{s_i}}{r_i^3} \tag{31d}$$

$$\vec{B}_{LI} = -2\mu_B \sum_i \frac{\vec{l_i}}{r^3} \tag{31e}$$

Note that because the nuclear Magneton is lower than the Bohr Magneton by a factor of about 1800, the electronic Zeeman effect is much stronger than the nuclear Zeeman effect. This means that under magnetic fields fields of a few hundreds of Gauss, the coupling between nuclear spin and electronic spin is negligible. In this approximation, the effect of the hyperfine coupling on the electronic wave-function may be neglected and the electronic Hamiltonian may be solved separately from the nuclear Hamiltonian. Thus, the electronic operators of eq. 31c, 31d and 31e may be replaced by their expectation values over a given magnetic sublevel. Obviously, the internal field operators are sublevel-specific, which leads to an additional layer of complexity when several magnetic sublevels are simultaneously populated (*vide infra*).

The Fermi contact field is a pure contact effect arising from the spin polarization of the s-orbitals. It is always colinear and proportional to the spin angular momentum. It is lying in the same direction as the spin vector. The proportionality between the spin angular momentum and Fermi-Contact field is rather independent of the system, and generally (but not always) follows the 220kG/spin unit,[120,121,122] thus giving a rather direct information on the spin state of a system.

The spin-dipole field also depends on the spin angular momentum. Its orientation with respect to the overall spin angular momentum depends on the orientation of the latter. In fact, eq. 31d may be reorganized the following way:

$$\vec{B}_{SD} = -g_e \mu_B \sum_i r^{-3} \bar{\bar{f}}(i) \cdot \vec{s_i} \quad (32)$$

Where $f_{\alpha\beta}(i) = \left\{\frac{3x_\alpha x_\beta}{r^2} - \delta_{\alpha\beta}\right\}$ are the components of the one-center reduced EFG tensor. $\delta_{\alpha\beta}$ is the Kronecker delta. Because of this term, the orientation of the spin-dipole field with respect to the spin angular momentum is strongly dependent on the electronic configuration of the iron. Paradoxically, while arising from the spin angular momentum, the spin-dipole field anisotropy depends on the electronic structure of the iron center.

The last component, the orbital contribution, is isotropic with respect to the orbital angular momentum. Unlike the Fermi contact field, for systems without spontaneous magnetization this component is always lying in the opposite direction to that of the orbital angular momentum vector.

Similar to the magnetic moment, the internal field operator may be reproduced exactly in the basis of electronic magnetic sublevels for a multiplicity of 2 or 3 using the pseudospin operator:

$$\overrightarrow{B_{int,SH}} = -\frac{A}{g_N \beta_N} \cdot \tilde{S} \quad (33a)$$

$$\widehat{H_{HFC}^{SH}} = \vec{I} \cdot A \cdot \tilde{S} \quad (33b)$$

Where $\overrightarrow{B_{int,SH}}$ is the internal field operator and $H_{HFC}^{SH}$ the hyperfine coupling Hamiltonian described by the spin Hamiltonian formalism. $A$ is the symmetric hyperfine matrix. Since it is symmetric, there is a set of axes in which it is diagonal. Like the hyperfine field, the hyperfine matrix can be divided into three components, i.e. the Fermi-contact, spin-dipole and orbital matrix. Each of these components have signs which describe the direction of the hyperfine field with respect to the applied field. Those are determined with respect to the sign of the electronic g-values since they determine the direction of the pseudospin vector with respect to the applied

field. As specified in section I, we use here an assumption in which all g-values are considered positive.

The Fermi contact contribution is isotropic, i.e. all components are equivalent. Because the Fermi-contact field is opposite in direction to that of the applied field, the Fermi-contact matrix contribution is always negative. In an ionic system without any significantly unquenched orbital angular momentum, $A^{FC} \approx -22\ T$. It can deviate significantly in case of spin mixture or unquenched orbital angular momentum and/or if the spin density is significantly delocalized to the ligand.[123]

The spin-dipole contribution is anisotropic. In fact, the trace of the matrix is zero (it can deviate slightly from zero in case of strongly mixed magnetic sublevels, see Chapter 1), which means that the sign of all three components cannot be identical unless the contributions are zero. The signs of the x,y,z components of this term depends on the electronic structure of the ground multiplicity. It is usually much weaker than the Fermi-contact term,[116] but not always negligible.

The orbital contribution may be anisotropic depending on the symmetry of the ligand field, since it depends on the orbital angular momentum. Unlike the spin-dipole contribution, it is not traceless. Most importantly, the orbital contribution can be either positive or negative because the orbital field always lies on the opposite direction as that of the orbital angular momentum. The later may be lying in opposite direction as that of the applied field (if it is unquenched due to the near-degeneracy of a more than half-filled subshell), in which case the orbital contribution is positive. There are cases where it may also be lying in the same direction as that of the field (if it is unquenched due to the near-degeneracy of a less than half-filled subshell). In this case, the orbital contribution is negative Regardless, a positive A value is usually the experimental proof that a significant orbital angular momentum is unquenched, assuming that the spin-dipole contribution is weaker than the fermi-contact contribution (see chapter 1).

Finally, note that while the hyperfine effects may be described in spin Hamiltonian, the description of the hyperfine fields suffers from the same shortcomings as the description of magnetic moments in case of near-degenerate non-relativistic states (see Chapter 1).

Taken together, all three components of the field may bring information on the spin state and electronic structure of iron. Additionally, absorption lines depend on the relative orientation of the gamma-ray propagation vector and the total magnetic field. This impacts the line absorption pattern differently depending on the ZFS parameters. In this study, we consider

the case where the gamma photon propagation vector is perpendicular to the applied magnetic field (perpendicular mode).

For an easy-plane of magnetization (integer spin, D>0, low rhombicity), the internal field created by the electron is usually lying close to the projection of the applied field on the plane of the proper magnetic axis. In this situation, the powder-distributed spectrum is dominated by configurations in which the total magnetic field is close to perpendicular to the propagation vector. In this configuration, the line intensities follow a pattern close to 3:4:1:1:4:3. On the other hand, for an easy-axis of magnetization, (non-integer spin or integer spin with D<<0 and low rhombicity), the internal field is mostly lying along one axis regardless of the orientation of the field. In this case, in the powder-distributed spectrum the orientation of the propagation vector with respect to the total field is rather ubiquitous. In this situation, the line intensities follow a pattern close to 3:2:1:1:2:3.

At high temperature, when several electronic magnetic sublevels are thermally populated, the Mössbauer line pattern depends on the electronic relaxation time compared to the nuclear Larmor precession time. In the fast electronic relaxation limit, when the electronic relaxation time is much lower than the nuclear Larmor precession time, the nucleus experiences the averaged field created by all populated electronic magnetic sublevels, weighted by their Boltzmann population. In the slow electron relaxation limit, when the electronic relaxation time is faster than the nuclear Larmor precession time, each populated magnetic state induces a different field on the nucleus, and the resulting spectrum is a sum of individual six-line patterns each corresponding to one populated electronic magnetic state, weighted by the corresponding Boltzmann population. Intermediate situations between those two limits exist, although rather difficult to model. The issue will not be addressed in this study.

2) Competition of magnetic hyperfine and electric hyperfine interactions

It must be noted that in systems with a non-zero electric-field gradient at the nucleus, the splitting of the nuclear magnetic sublevels has to competes with the quadrupole splitting effect. In cases where the magnetic effects are dominant, the quadrupolar interaction may be treated at the second-order perturbation theory and any sublevel mixing due to this effect may be neglected. In this case one merely observes a shift of the absorption lines, without a significant change in the intensity ratios. The shift of the absorption lines depends on the relative orientation of the total field and the electron field gradient tensor[116]:

$$E_{M,Q}\left(I=\frac{3}{2},M_I\right)=-g_N\beta_N B_{ext}M_I+\mu_N\frac{(-1)^{|M_I|+\frac{1}{2}}eQV_{ZZ}}{8}\left(3Cos^2\theta-1+\eta\sin^2\theta\cos 2\phi\right) \quad (34)$$

Note that the nuclear magnetic levels of same $|M_I|$ are affected identically by the quadrupole splitting, such as only the distance between lines 1 and 2 and that between 5 and 6 changes under the action of the quadrupolar effect.

On the other hand, for cases where the quadrupole splitting is dominating, the nuclear Zeeman effect may be treated as a second-order perturbation. In case of low asymmetry parameters, the line pattern looks like a low-energy triplet and high energy doublet for a positive $V_{ZZ}$ or a low-energy doublet and high-energy triplet for a negative $V_{ZZ}$. The reason may be inferred from the fact that the unperturbed doublets may be considered as pure $|\frac{3}{2}, \pm\frac{1}{2}\rangle$ and $|\frac{3}{2}, \pm\frac{3}{2}\rangle$ nuclear magnetic sublevels, and due to the forbidden transitions involving the $|\frac{3}{2}, \pm\frac{3}{2}\rangle$ nuclear magnetic sublevels, the observer may only see two distinct transitions involving the $|\frac{3}{2}, \pm\frac{3}{2}\rangle$ doublet as the final state, whereas three distinct transitions involving $|\frac{3}{2}, \pm\frac{1}{2}\rangle$ are visible . For systems with a large asymmetry parameter, the $|I, M_I\rangle$ levels are mixed together. Hence the line pattern of the spectrum appears as two symmetric triplets.

For case where no effect is clearly dominant over the other, diagonalization of the total Hamiltonian is necessary for the resolution of the transition energies. The nuclear magnetic sublevels may be mixed depending on the relative orientation of the electric-field gradient tensor and that of the total magnetic field. Interpretation of the intensity ratios is not straightforward and must be calculated exactly for each relative orientation of (1) the EFG tensor principal axis, (2) the total magnetic field and (3) the incident gamma-rays. For a transition involving two nuclear magnetic sublevels consisting of a mixture of $|I, M_I\rangle$, the transition intensity is proportional to the modulo square of the transition intensity:

$$\left|\langle I_1, A|\widehat{H_{int}}|I_2, B\rangle\right|^2 =$$

$$\sum_M \sum_{M'} \sum_{M''} \sum_{M'''} C_M^* \, C_{M'}^* C_{M''} C_{M'''} \, \langle I_1, M|H_{int}|I_2, M''\rangle\langle I_2, M'|H_{int}|I_1, M'''\rangle \qquad (35a)$$

Where the nuclear magnetic sublevels $|I_1, A\rangle$ and $|I_2, B\rangle$ are linear combination of the nuclear magnetic sublevels $|I_1, M\rangle$, $|I_1, M'\rangle$ and $|I_2, M''\rangle$, $|I_2, M'''\rangle$, respectively. The interaction Hamiltonian $\widehat{H_{int}}$ is the magnetic-dipole transition Hamiltonian described elsewhere[124].

The angular-dependence of the source with respect to the quantization axis is hidden in the term $\langle I_1, M|H_{int}|I_2, M''\rangle\langle I_2, M'|H_{int}|I_1, M'''\rangle$. For a non-polarized source, this expression breaks down into:

$$\langle I_1, M|H_{int}|I_2, M''\rangle\langle I_2, M'|H_{int}|I_1, M'''\rangle. =$$
$$\left\langle I_1, M, \Delta M_{M,M''}\middle|I_2 M''\right\rangle\left\langle I_1, M''', \Delta M_{M,M'}\middle|I_2, M'\right\rangle F^{\Delta M_{M,M'}}_{\Delta M_{M,M''}}(\theta,\phi) \quad (35b)$$

Where the terms $\left\langle I_1, M, \Delta M_{M,M''}\middle|I_2 M''\right\rangle$ and $\left\langle I_1, M, \Delta M_{M,M''}\middle|I_2 M''\right\rangle$ are Clebsch-Gordon coefficients and $F^{\Delta M_{M,M'}}_{\Delta M_{M,M''}}(\theta,\phi)$ are functions of the relative orientation between the quantization axis and the incident gamma-ray. Both have been tabulated elsewhere. [116]

## III. X-ray absorption spectroscopy

In this study, K-edge XAS spectroscopy and in particular the analysis of pre-edge structure has been used to determine the physical oxidation state of the reduced forms of [Fe(TPP)]. K-edge XAS spectroscopy corresponds to the absorption spectrum corresponding to excitation from the 1s orbital of iron to orbitals near the continuum. Usually, a typical K-edge spectrum is separated in three regions, from higher to lower energy: (1) the high energy region (EXAF region), (2) the edge region and (3) the pre-edge region. The high energy region corresponds to excitations from the 1s orbital to the continuum. The analysis of this region gives structural information such as the nature of the ligating atoms and iron-ligand bond lengths. EXAFS investigation is beyond the scope of this investigation. Instead, we focus on the edge and pre-edge regions which correspond to excitations from the 1s to 4p orbitals and 1s to 3d orbital, respectively. In general, the edge region is characterized by intense lines because the associated transition correspond to $\Delta l = +1$ (where $l$ is the azimuthal quantum number of the orbital). Therefore, they are electric-dipole allowed. On the contrary, the pre-edge region is characterized by much weaker line intensities, because the associated transition corresponds to $\Delta l = +2$. Therefore, they are electric dipole forbidden, and only allowed through electric quadrupolar interactions, the latter being much weaker than the former.[125] Of note, however, in non-centrosymmetric systems, the mixture of 3d orbitals with small amounts of 4p orbitals is symmetry-allowed, and may subsequently increase the intensity of the pre-edge region. The excitation energies in the pre-edge and edge region are strongly dependent on a number of factors.[125] The factor of interest in this study is the oxidation state of the iron center. Indeed, upon reduction of the metal center, the higher screening predominantly increases the energy of the 1s orbital. This phenomenon dominates over the destabilization of the valence orbitals, and overall the excitation energy decreases. For instance, in the octahedral iron in $K_2NaFe^{III}F_6$, the

energy of the edge in region and that of the transition in the pre-edge region are shifted by +4 and +1.3 eV compared to the corresponding structure of the octahedral complex $KFe^{II}F_3$ complex.[126] On the other hand, the complex $K_3[Fe^{III}(CN)_6]$ has an edge structure only 1 eV superior to the $K_4[Fe^{II}(CN)_6]$ complex, respectively, because despite their formally different oxidation state, strong backdonation phenomena reduce the changes in electronic density on the iron center. Of note, the coordination number, nature of the ligand and geometry of the complex also affects the edge and pre-edge transition energies. The competition of these different effects may give rise to difficulties in comparing non-structurally equivalent systems. In that regard, the use of time-dependent density functional theory (TD-DFT) to predict the K-edge spectrum and analyze the underlying electronic structure of a given compound is a considerable asset (*vide infra*).[127] Unfortunately, prediction of edge structures via TD-DFT is nearly impossible due to the low accuracy of TD-DFT for the prediction of excitations near the continuum (*vide infra*) and the exceedingly high number of individual transitions populating this region. Thus, in this study we focus on the analysis of the pre-edge region via TD-DFT (see Chapter 2).

## IV. Thermochemistry

In this study, Gibbs free energy was calculated in order to (1) get an estimation of the kinetics of the CO2-to-CO reduction reaction catalyzed by [Fe(TPP)], and (2) get an estimation of the redox potentials of the reduced states of [Fe(TPP)] (see chapter 3).

The Gibbs free energy is particularly important in reactivity since in transition state theory, it provides the theoretical kinetic constants of a given elementary reaction step through the Eyring equation[128]:

$$k = \frac{k_B T}{h}\, e^{-\frac{\Delta G^{\neq}}{k_B T}} \tag{36a}$$

Where k is the kinetic constant of an elementary step, $h$ the Planck constant and $\Delta G^{\neq}$ is the activation free energy of the step, i.e. the free energy difference between the transition state and the reactant state. Knowledge of the kinetic constants may enable to compute the TOF of a catalytic systems, providing that all intermediates and transition states are known, and the catalytic system has reached a steady-state regime.[129,130,131] Hence, for a sequence of reactions (cycle or otherwise) in a steady-state regime, the rate of reaction can be written:

$$\frac{r}{[I_i]} = \frac{\Delta}{\sum_j M_{ij}} \tag{36b}$$

Where Δ is defined in Eq. 36c, and $M_{ij}$ are the elements of the matrix defined in Eq. 36d.

$$\Delta = k_1 k_2 .. k_N - k_{-1} k_{-2} .. k_{-N} \quad (36c)$$

$$\widehat{M} = \begin{pmatrix} k_2 k_3 .. k_N & k_{-1} k_3 .. k_N & \dots & k_{-1} k_{-2} .. k_{-(N-1)} \\ k_3 k_4 .. k_1 & k_{-2} k_4 .. k_1 & \dots & k_{-2} k_{-3} .. k_{-N} \\ \dots & \dots & \dots & \dots \\ k_1 k_2 .. k_{N-1} & k_{-N} k_2 .. k_{N-1} & \dots & k_{-N} k_{-1} .. k_{-(N-2)} \end{pmatrix} \quad (36d)$$

For a completely homogeneous catalytic reaction, the TOF can be computed as:

$$TOF = \frac{\Delta}{\sum_{i,j} M_{ij}} \quad (36e)$$

Of note, in the electrocatalytic reduction of $CO_2$, certain elementary steps of the catalytic cycle may only occur at the electrode. In such cases, the concentration of the intermediates is not homogeneous and Eq. 36e cannot be used to estimate the TOF; instead a more complex mathematical treatment is required.[42] An example of such treatment is given in the annex of Chapter 3 to estimate the turnover frequency of [Fe(TPP)] from its calculated free energy surface.

The Gibbs free energy is also related to most thermodynamic properties, such as the absolute Nernst potential:

$$E^0 = \frac{G^0_{ox} - G^0_{red}}{n_e F} \quad (37)$$

Where $G^0_{ox}$ is the Gibbs free energy of the oxidized system, $G^0_{red}$ is the Gibbs free energy of the reduced system, both in standard conditions and $F$ is the Faraday constant.

The Gibbs free energy can be decomposed in an entropy and enthalpy contribution:

$$G = H - TS \quad (38)$$

$H$ is the enthalpy term and $S$ the entropy term. Each of these two terms have numerous components (Figure 13), which need to be calculated by different methods. Furthermore, several corrections must be added in the case of a solvated system compared to the gas phase. First, we describe all these components in gas phase. Then we extend the discussion to cases involving a solvated system.

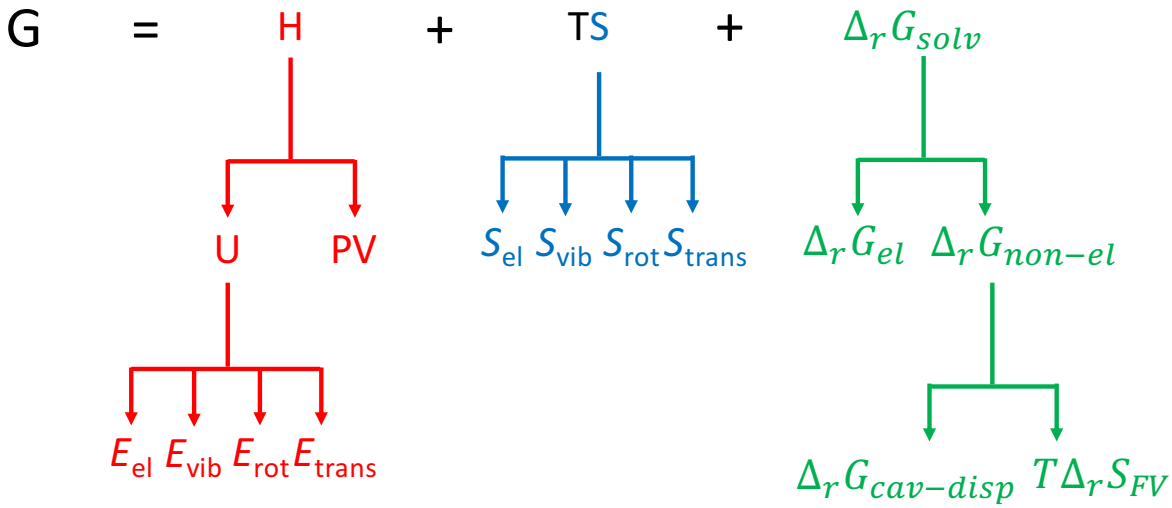


**Figure 13**: Decomposition of the components entering the composition of the free energy explicitely calculated in this study. In red are all the components relative to calculation of the enthalpy (H) in gas phase. In blue are all the components relative to the entropy (S) in gas phase. In green are represented all the components relative to the free energy of solvation ($\Delta_r G_{solv}$). All components are discussed in the text.

A. Enthalpy term

The enthalpy term is defined as:

$$H = U + PV \tag{39a}$$

Where U is the internal energy of the system (*vide infra*) and PV is the product of pressure and volume. The second term is usually calculated in the perfect gas approximation, i.e.

$$H = U + k_B T \tag{39b}$$

In the usual Born-Oppenheimer approximation, which assumes that nuclear motion is decoupled from electronic motion, the internal energy term U can be decomposed into an electronic term and a nuclear term, i.e.

$$U = E_{el} + E_{Nuc} \tag{39c}$$

The first term encompasses the kinetic energy of the electrons, the inter-electronic electrostatic repulsion, the electron-nuclei electrostatic attraction, and the nuclei-nuclei electrostatic repulsion for a given set of nuclear coordinates, while the second corresponds to

the energy of vibration, rotation and translation of the nuclear system.[132] In practice, the electronic energy is calculated by DFT, as will be further developed in the next section.

The second term, under the usual rigid rotor approximation which assumes that the vibration motions are decoupled from the rotation motions, can be decomposed in three independent terms, i. e. vibrational, rotational and translational energy ($E_{vib}$, $E_{rot}$ and $E_{trans}$).

$$E_{Nuc} = E_{vib} + E_{rot} + E_{trans} \quad (39d)$$

In this study, the nuclear system is treated as a quantum object only for the calculation of the vibrational energy. The rotational and translational energies are both treated classically.

In the rigid rotor approximation, the rotational energy is derived from the classical partition function of a rigid rotor and yields for a non-linear polyatomic molecule:[132]

$$E_{rot} = \frac{3}{2} k_B T \quad (39e)$$

The translational energy is derived according to the same method and also yields:

$$E_{trans} = \frac{3}{2} k_B T \quad (39f)$$

Finally, the vibrational energy is calculated in this study using the harmonic oscillator approximation, in which the electronic potential is estimated by a Taylor expansion of the electronic energy up to the second order with respect to the nuclear coordinates. Under this approximation, and substituting the electronic Hessian eigenvectors (normal modes of vibration) to the nuclear coordinates, the energy associated with each mode of vibration can be calculated as[132]:

$$E_{i,k} = \left(\nu_i + \frac{1}{2}\right) \hbar \lambda_k{}^{\frac{1}{2}} \quad (39g)$$

$\nu_i = 0,1, \ldots + \infty$ are the vibrational quantum numbers, $\lambda_k$ is the eigenvalue of the mass-weighted Hessian matrix associated with the mode k, and $\hbar = \frac{h}{2\pi}$.

Note that in the harmonic oscillator approximation, the vibration of the normal modes of vibration are decoupled, which enables to treat the partition function of the system as a product of the individual partition function of each mode of vibration. The total vibrational energy depends on the thermally populated levels. It may be derived easily from the partition function as:[132]

$$E_{vib} = \sum_k \hbar\lambda_k^{\frac{1}{2}} \left( \frac{1}{2} + \frac{1}{e^{\frac{\hbar\lambda_k^{\frac{1}{2}}}{kT}} - 1} \right) \quad (39h)$$

Since for each mode, the ground vibrational mode has a non-zero vibrational energy, the total vibration energy is non-zero even at the 0 K limit. This energy is referred to as *zero-point energy*, and correspond to the sum of the individual mode energies in their ground vibrational state ($v_i = 0$). It is straightforwardly calculated from eq. 39g and it can be verified that this energy indeed corresponds to the limit of eq. 39h when T → 0 K. Thus, one can decompose the vibrational energy into a zero-point energy and a thermal energy, such as:

$$E_{ZPE} = \frac{\sum_k \hbar\lambda_k^{\frac{1}{2}}}{2} \quad (39i)$$

$$E_{Th} = \sum_k \frac{\hbar\lambda_k^{\frac{1}{2}}}{e^{\frac{\hbar\lambda_k^{\frac{1}{2}}}{kT}} - 1} \quad (39j)$$

Note that the calculation of the vibrational energies requires the knowledge of the nuclear mass-weighted Hessian eigenvalues $\lambda_k$. Diagonalization of the electronic Hessian is a somewhat computationally expensive task, usually performed with density functional theory (*vide infra*) and is usually bottle neck of thermochemistry calculations.

## B. Entropy term

The second component of eq. 38 is the entropy. The entropy of a system accounts for the number of configurations accessible to this system.[133]

$$S = \frac{k_B \, d(TlnQ)}{dT} \quad (40a)$$

Where $Q$ is the system's partition function. The entropy can be decomposed into 4 components, i.e electronic, vibrational, rotational and translational entropy.[132,134]

$$S = S_{el} + S_{vib} + S_{rot} + S_{trans} \quad (40b)$$

In the Born-Oppenheimer and rigid rotor approximations, those three components are not coupled and can be calculated independently using one partition function for each component.

For the purpose of calculating the electronic entropy, the ground non-relativistic state is considered to be the only accessible at room temperature. If one neglects any zero-field

splitting, the electronic entropy therefore only accounts for the degenerate $M_S$ levels and solely depends on the multiplicity of the system,[132]

$$S_{el} = k_B \ln (2S + 1) \tag{40c}$$

The rotational entropy can be derived from the corresponding partition function and yields:[132,134]

$$S_{rot} = k_B (\frac{3}{2} + \ln \left( \frac{\pi^{\frac{1}{2}}}{\sigma_r} \left[ \frac{2Ik_BT}{\hbar^2} \right]^{\frac{3}{2}} \right) \tag{40d}$$

Where $\sigma_r$ is the rotational symmetry number of the molecule, and $I$ is the average inertia moment of the molecule, i. e. $I = \left(I_x I_y I_z\right)^{\frac{1}{3}}$.

The translational entropy may also be determined from the translational partition function, and yield:[132,134]

$$S_{trans} = k_B \left( \frac{3}{2} \ln \left[ \frac{2\pi m_M k_B T}{h^2} \right] + \frac{5}{2} + \ln(V_S) \right) \tag{40e}$$

Where $m_M$ corresponds to the mass of the molecule. The only ill-defined term in this expression is $V_S$, which corresponds to the volume occupied by the molecule. In the gas phase, the calculation is made at a constant pressure of about P=1 atm and using the ideal gas expression, $V_S = \frac{k_B T}{P}$.

The vibrational entropy may be derived from the vibrational partition function in the harmonic oscillator approximation,[132] and yields:

$$S_{vib} = k_B \sum_k \frac{\hbar \lambda_k^{\frac{1}{2}}}{k_B T \left( e^{\frac{\hbar \lambda_k^{\frac{1}{2}}}{k_B T}} - 1 \right)} - \ln \left( 1 - e^{-\frac{\hbar \lambda_k^{\frac{1}{2}}}{k_B T}} \right) \tag{40f}$$

Like for the vibrational energy, the vibrational entropy requires the eigenvalues of the nuclear Hessian, which is computationally expensive.

## C. Solvation free energy

So far, the free energy terms were computed for a molecular system in an ideal gas state. Some corrections need to be applied in order to calculate the free energy of a solvated molecule. Specifically, the electrostatic and non-electrostatic (dispersion) interactions between the solvent and the solute need to be calculated. Furthermore, the creation of a cavity able to contain the solute (cavitation) has a significant entropic and enthalpic cost.[135] Finally, the loss of volume available to the solute in solution compared to the gas phase significantly decreases the translational entropy.

Calculation of solute-solvent interactions by including explicitly the first spheres of solvation is possible,[136] although the high computational cost is prohibitive for the purpose of this study. Consequently, the electrostatic solute-solvent interactions were calculated using the implicit solvent model CPCM,[137] which calculates such interaction by incorporating an additional solute-solvent interaction term in the Hamiltonian to be solved by the self-consistent field.

$$H_{cpcm} = H_{vacuum} + V_{solute-solvent} \quad (41)$$

The form and derivation of the term $V_{solute-solvent}$ is beyond the scope of this study and will not be described here. Note that it has been intensively described elsewhere.[137] Its inclusion in the Hamiltonian enables the calculation of $\Delta_r G_{el}$ (Figure 13) by computational methods such as density functional theory (*vide infra*).

The cavitation and dispersion correction terms can be computed as a linear function of the cavity surface (defined through Van der Vaals radii of the atoms of the solute). This assumption is based on the experimental findings that for alkane chains, the hydration energy is proportional to the alkane chain's surface area.[138]

$$\Delta_r G_{cav-disp} = 1.321 + 0.0067639\, A_M \quad (42)$$

Where $A_M$ is the surface of the cavity determined from van-der-Waals radii of the solute's atoms (in Angströms squared). The parameters of this equation were determined by linear regression of the free energy of hydration versus surface area (defined through Van der Vaals radii of the atoms of the solute) for a set of 24 hydrocarbons.[139] This method assumes that the cavitation and dispersion energy is not dependent on anything else than the surface area, and in particular, dependent neither on the nature of the solvent nor the nature of the solute. Hence this approximation should be regarded with caution.

The entropy of a system is significantly different in solution compared to the gas phase. This is principally due to the loss of translational entropy due to the lower volume accessible to the system. The electronic and vibrational components of the entropy of the system are usually not strongly affected by the solute-solvent interaction. The rotational entropy is also very weakly affected, and subtle changes may only arise from a loss of available volume due to the gyration of the solute.[134] Those changes are usually weak[140,141] and will not be discussed here.

Estimation of the loss of entropy due to the lower accessible volume is tackled with a certain success by free volume theory.[134] According to this method, the solute and the solvent are both approximated as hard spheres, and the volume accessible to the system is calculated as the radius of a solvent cavity multiplied by the average number of cavity accessible to the system. The calculation of the volume accessible only requires the density and molar mass of the solvent and the volume of both the solute and the solvent (typically define through the Van-der-Waals radii of the atoms).

$$V_{access} = \left[1 + 4\left(\frac{1}{1-\frac{\max\left\{\left(\frac{M_W}{N_A\rho}\right)^{\frac{2}{3}} - V_S^{\frac{2}{3}}; 0\right\}}{\left(\frac{M_W}{N_A\rho} - V_S\right)^{\frac{2}{3}} + V_M^{\frac{2}{3}}}} - 1\right)\frac{\left(V_M^{\frac{1}{3}} + \left[\frac{M_W}{N_A\rho} - V_S\right]^{\frac{1}{3}}\right)^2}{\left[\frac{M_W}{N_A\rho} - V_S\right]^{\frac{2}{3}} + V_S^{\frac{2}{3}}}\right]\left(V_M^{\frac{1}{3}} + \left[\frac{M_W}{N_A\rho} - V_S\right]^{\frac{1}{3}}\right)^3 \quad (43)$$

Here, $M_W$ and $\rho$ are the molar and volumic mass of the solvent, respectively, $V_S$ is the volume of the solvent molecule and $V_M$ is the volume of the solute.The value of $V_{access}$ is then to be substituted to $V$ in eq. 40e to get the translation entropy in solution, and ultimately $T\Delta S_{FV}$. Although the corresponding expression is complicated, free volume theory gives reasonable agreement with the experiment[134] and is conceptually satisfying.

# V. Density Functional theory

## A. Calculation of a single-determinant wave-function and electronic energy

The first computational method used throughout this study is Density Functional Theory. It has been used to calculate the electronic and vibrational energy of various systems, as well as the Mössbauer parameters (isomer shift and quadrupole splitting).

The theory underlying density functional theory (DFT) has been extensively described for decades in the literature[142,143] and will not be reviewed here. For the purpose of this study, it is enough to know that DFT enables the estimation[142] of the energy and electronic density of a molecular system. It relies on the self-consistent solvation of the Kohn-Sham equations, themselves depending on the choice of an exchange and correlation functional. In this study, DFT was used consistently to calculate the electronic energy, the Hessian matrix which is necessary for the calculation of vibrational energies and free energy, which in turn enables an estimation of the kinetics of the reaction (*vide supra*). The method was also used for calculation of $^{57}$Fe Mössbauer isomer shifts and quadrupole splittings.

DFT enables the description of the electronic correlation energy (unlike Hartree-Fock theory) at relatively small computational costs. In general, the quality of the description of the exchange and correlation energies via a specific functional follows Jacob's ladder. The more accurate is the energy description of the functional, the more computationally expensive is the resolution of the Kohn-Sham equations. Hence, the Generalized Gradient Approximation (GGA) functionals, in which the description of the exchange and correlation energy depends of the density as well as the density gradient, are generally both less computationally expensive and less accurate than the hybrid functionals, in which a part of the exchange energy is described by Hartree-Fock theory. In this study, we limit ourselves to these two families of functionals.

Computational chemistry in general (including but not limited to DFT) requires the use of a set of basis functions used to describe the wavefunction of the system. In particular, the use of those functions allows to shift the Kohn-Sham differential equation problem into an algebraic equation problem (where coefficients of the basis functions are the variables). In the present study, the Ahlrichs[144] basis sets were the most commonly used, together with the CP(PPP) basis set[145] whenever a precise description of the s-type orbitals were needed (*vide infra*).

Linear combinations of basis set functions form molecular orbitals (MO), which are optimized by solving the Kohn-Sham equations. In DFT, the wave-function is described by an antisymmetrized product of occupied MOs (determinant). The form of the wavefunction implies that DFT is an intrinsic single-reference method, and will not be able to provide a good energy description of intrinsically multi-determinantal systems, i.e. systems which must be described by linear combination of determinants. Example of such systems include for instance antiferromagnetically-coupled systems or open-shell singlets. The best DFT approach to circumvent these problems is "broken-symmetry" DFT, which provides a single-determinant solution. This solution turns out to be a mixture of different spin states.[146] Various methods exist to estimate the energy of a pure multiplet from a broken-symmetry energy.[147]

One of the most widely calculated molecular properties available with DFT is the electronic energy and molecular Hessian. In reactivity, these components are an essential part of the Gibbs free energy (*vide supra*). As mentioned above, free energy enables to get a qualitative estimation of the kinetic and thermodynamic properties of a system. Note that to this date, the accuracy range of DFT is not enough to predict the kinetic constants quantitatively. Indeed, the typical error of reaction energy calculations by hybrid functional (with the TZVPP basis set) is about 6 to 8 kcal/mol. This number was found in a benchmark study by Grimme[148] (benchmarked with respect to the CCSD(T) method at the complete basis set limit). Because of the exponential term of eq. 36a, the kinetic constant may thus be underestimated or overestimated by a factor of about $10^4$-$10^6$ . This makes DFT inapt to quantitatively predict the kinetics of a reaction, but may provide qualitative insights on the nature of the mechanism (see Chapter 3).

## B. Calculation of $^{57}$Fe Mössbauer parameters

In this study, DFT was also used as a tool to calculate the $^{57}$Fe Mössbauer electric hyperfine parameters, i. e., isomer shift (eq. 27c) and quadrupole splitting (eq. 28b).

In principle, calculation of the $^{57}$Fe isomer shift requires the accurate calculation of the density at the nucleus $\rho(0)$. While this value can be calculated at virtually no computing cost from the electronic wave-function, it has been shown to be strongly dependent on the functional and the basis set, which suggests that DFT is not accurate enough to predict absolute density at the nucleus. On the other hand, variations of the calculated density compared to a reference show a linear correlation to the experimental isomer shift,[145] or

$$\delta \approx \alpha \left( \rho_{DFT}(0) - \rho_{DFT}^{ref}(0) \right) + \beta \qquad (44)$$

The chemical trend of $^{57}$Fe isomer shifts is thus reasonably well reproduced by DFT, although systematic errors are presents. Those errors show in that the parameters of the linear regression ($\alpha$and $\beta$) are dependent on the used basis set and functional. Linear regressions of the calculated density of a set of 21 mononuclear iron complexes against their experimental $^{57}$Fe iron isomer shift by Römelt[149] suggested that the quality of the isomer shift description is slightly superior for hybrid functionals than for pure GGA functionals. The study also suggested that the use of CP(PPP),[145] a strongly uncontracted basis set providing good description of the s-type function at the nucleus, improves significantly the quality of the fit. Finally, this study, in agreement with earlier studies,[150] suggests that the use of zero-order relativistic corrections to the Hamiltonian did not improve the quality of the fit, which may be rationalized by the fact that the core s-orbitals density, which is most strongly affected by relativistic effects, is not significantly affected by the chemical environment. Consequently, in the present study, a systematic procedure was used to calculate the $^{57}$Fe Mössbauer isomer shifts. The density is calculated using the B3LYP functional, the basis set CP(PPP) for iron atoms and the basis set Def2-TZVP for all other atoms. No relativistic correction was used. We note here in passing that the linear regression is, to some extent, dependent on the type of bonds engaged by the iron, and several authors report the need to build their own calibration curves for iron oligomers or iron heterobimetallic complexes.[151,152,153]

The calculation of the $^{57}$Fe quadrupole splitting follows eq. 28b. It requires the knowledge of the nuclear moment Q, $V_{ZZ}$ and $\eta$. The former is taken at 0.16 barn in this study,[150] while the components of the electronic EFG tensor can be accessed rather easily from the electronic wavefunction. Indeed, $\widehat{V_{\alpha\beta}}$ is a sum of one-electron operators:

$$V_{\alpha\beta} = \langle\Psi|\widehat{V_{\alpha\beta}}|\Psi\rangle = \langle\Psi|\sum_i r_i^{-3} f_{\alpha\beta}(r_i)|\Psi\rangle \quad (45a)$$

In DFT, because the wavefunction is a single determinant, the EFG tensor components can be decomposed into MO-wise contribution using Slater-Condon rules.

$$V_{\alpha\beta} = \sum_i \langle i|r_i^{-3} f_{\alpha\beta}(r_i)|i\rangle \quad (45b)$$

Where *i* corresponds to the occupied MOs. In this study, each MO contribution was further decomposed atomic-orbital contributions:

$$\langle i|V_{\alpha\beta}|i\rangle = \sum_{\mu}^{Fe}\sum_{\nu}^{Fe} C_{\mu i}^{*}C_{\nu i}\langle\mu|r_i^{-3}f_{\alpha\beta}(r_i)|\nu\rangle + \left(\sum_{\mu}^{Fe}\sum_{\nu}^{L} + \sum_{\mu}^{L}\sum_{\nu}^{Fe}\right)C_{\mu i}^{*}C_{\nu i}\langle\mu|r_i^{-3}f_{\alpha\beta}(r_i)|\nu\rangle + \sum_{\mu}^{L}\sum_{\nu}^{L} C_{\mu i}^{*}C_{\nu i}\langle\mu|r_i^{-3}f_{\alpha\beta}(r_i)|\nu\rangle + \left(\sum_{\mu}^{L}\sum_{\nu}^{L'} + \sum_{\mu}^{L'}\sum_{\nu}^{L}\right)C_{\mu i}^{*}C_{\nu i}\langle\mu|r_i^{-3}f_{\alpha\beta}(r_i)|\nu\rangle \quad (45c)$$

In eq. 45c, the MO $i$ is decomposed into a linear combination of atomic orbitals $\mu$ and $\nu$ belonging to the iron center (Fe), or to the ligands (L and L'). The $C_{\mu i}$ correspond to the coefficient of the atomic orbital $\mu$ in the MO $i$.

The first term of eq. 45c corresponds to the so-called one-center contribution because it regroups atomic orbitals belonging to the iron center only. It can be further decomposed into a valence orbitals and core orbitals contribution. It mainly arises from the d-population of iron, but may also be modulated by (1) the mixing of Fe-based d-orbitals with ligand orbitals, and (2) the polarization of the core orbitals of iron. The one-center contribution is generally the most important contribution, but not always (see Chapter 1).

The second term is the two-center "bond contribution", which arises due to the covalency of the bonds engaged by the iron center. The third term is the two-center "point-charge contribution", which corresponds to the participation of the ligand-based electronic density. This contribution is usually rather weak. Finally, the fourth term is called three-center contribution and is generally very weak.

The quadrupole splitting may be calculated rather accurately by DFT. A study involving 10 mononuclear iron complexes found the root mean square deviation between calculated and experimental quadrupole splitting to be 0.57 mm/s.[150] The quadrupole splittings were calculated at the B3LYP level of theory, using the CP(PPP) basis set on iron and the TZVP basis set on all other atoms. No significant improvement was found when adding relativistic correction, since the EFG mainly arises from the valence electrons. Consequently, in the present study, the same procedure applied to systematically calculate the isomer shift was also applied for the calculation of quadrupole splitting.

## VI. Time-dependent DFT (TD-DFT)

TD-DFT is a variant of Kohn-Sham DFT, in which the time-dependent Kohn-Sham equation[154] is solved for a non-relativistic ground state responding linearly (i.e. to the first-order) to a time-dependent perturbation. In practice, it leads to the resolution of an eigenvalue equation in the orbital space in which the eigenvalues themselves are the transition energies and the eigenvectors the transition amplitudes. TD-DFT as a method to calculate excited non-relativistic states stands out for its low computational cost and relative accuracy. However, it suffers from the same shortcomings as ground state DFT. Both rely on an approximate exchange-correlation functional, and the accuracy of TD-DFT results are only as good an approximation as the functional itself. Furthermore, the method itself tends to fail in accurately predicting the energies of Rydberg states and excitations involving extended $\pi^*$ orbitals, due to the inaccurate long-range behavior of most functionals.[154] Also of note, the charge-transfer excitation energies are usually considerably underestimated by TD-DFT.[155]

In this investigation, TD-DFT has been used exclusively in order to calculate the pre-edge region of the Fe K-edge spectrum in $[Fe(TPP)]^-$ and $[Fe(TPP)]^{2-}$. Because of the inaccurate description of near-continuum transitions by TD-DFT, the edge region has not been modelled and this study focuses instead on local 1s-to-3d transition, which are not long-range and do not involve any $\pi^*$ orbital, nor any charge-transfer excitation. In that region, this method is expected to yield good results. In fact, a previous investigation on 10 iron complexes showed that the DFT functional BP86 (GGA functional) and B3LYP (hybrid functional) reproduced the experimental pre-edge intensity features with a predicted vs experimental value correlation coefficient of 0.96-0.98.[127] Furthermore, although the absolute excitation energies are off by several eV (2.2 to 171 eV, depending on the functional choice and the use of scalar relativistic correction), errors are to a large part systematic, and the peak energy *shift* from system to system, which contains the relevant information, is rather well described. Indeed, after correcting the excitation energy in the set of 10 complexes for a systematic value, the absolute standard deviation drops to much smaller values (0.4 to 2.2 eV, depending mostly on the choice of the functional and scalar relativistic correction). This hints at the necessity to rely on calibration curves to get rid of the systematic errors in 1s-to-3d excitation energies. One such curve has been built in Chapter 2.

## VII. Complete Active Space Self Consitent Field (CASSCF)

### A. Calculation of a multireference wave function and associated energy

The second computational method technique used in this study was the Complete Active Space Self-Consistent Field (CASSCF) method. Throughout this study, the CASSCF method was used to calculate the excited non-relativistic states of a system and provide insights on the magnetic properties of the investigated molecular systems.

The principle underlying this method consists in (1) a Hartree-Fock calculation, (2) a full configuration interaction calculation on a small subset of the orbital space created in step 1 (active space), and (3) optimization of the orbital coefficients to minimize the energy of the system for the given CI expansion. Step 2 and 3 are repeated iteratively until convergence of the energy and/or orbital gradient.[156]

This method has several advantages. Most importantly, unlike (ground state) DFT, it gives access to the excited non-relativistic states. This knowledge is crucial to understand the physical origin of molecular magnetism in transition metal complexes, which is closely related to the interaction of close-lying non-relativistic states through SOC (*vide supra*). Second, since it is a multireference method, it can be used to describe inherently multireference and/or multi-determinantal systems such as for instance antiferromagnetically-coupled systems and open-shell singlets. Most importantly for this study and unlike DFT, it is able to provide $\widehat{S^2}$ eigenfunctions which is fundamental for the description of the SOC interactions, and therefore, the magnetism of a system.

On the other hand, because the method provides a full configuration interaction only on a small subset of orbitals, it neglects a large part of the dynamical correlation which arise from small interactions between the Slater determinants manifold. For a good description of dynamical correlations, coupled-cluster methods are preferred. Another problem inherent to the method is the choice of the active space. The choice of restraining the configuration interaction to a limited subset of orbital is motivated by the prohibitive computational cost of the full configuration interaction. The downside, obviously, is that the solution will be strongly dependent on the choice of the active space. Thus, a reasonable CASSCF result requires chemical intuition, unlike more “black box” methods like DFT or coupled-cluster.

How to choose the active space? In transition metal complexes and especially in order to calculate the magnetic properties of a system, the five valence d-orbitals must be added,

because (1) the d-d excited states are often closely-lying to the ground state, and (2) the d-d excitations are the most likely to contribute significantly to the SOC effect. Notably, the method tends to underestimate bond covalency. Thus, if the d-orbitals are significantly antibonding, inclusion of the corresponding bonding orbitals may improve the description of covalency. Finally, the first empty d-shell (the 4d shell in case of 3d transition metals like iron) is sometimes added to account for the double shell effect.[157] This improves the description of the energy by enabling the d-orbital to expand. Of course, the choice of the active space needs to be adapted to the problem at hand. If one is interested in charge transfer excitation, inclusion of ligand-based orbitals in the active space is obviously primordial.

The energy of CASSCF states must be regarded with caution since errors of several thousand wavenumbers may occur.[158] To recover a substantial amount of dynamic correlation, perturbation theory to the second order is often used to correct the energy of the CASSCF states (but not the state compositions). Several methods of multireference perturbation theory exist and are characterized by their non-perturbed Hamiltonian. In this study, we use the N-Electron-Valence state Perturbation Theory at the second-order (NEVPT2).[159]

## B. Calculation of magnetic properties using CASSCF wave functions, NEVPT2 energies and effective Hamiltonian theory

One of the application of CASSCF/NEVPT2 is the calculation of magnetic properties. The ground state and closely-lying excited states accessible by this method can be perturbed by spin-orbit and Zeeman couplings. Diagonalization of the SOC and Zeeman Hamiltonian in the space of the calculated non-relativistic states may enable calculation of the magnetic properties beyond the Born-Oppenheimer approximation, such as magnetic susceptibility, EPR transitions, hyperfine effects… In order to compare a given calculation to experimentally-resolved parameters, it is often useful to calculate the spin Hamiltonian matrices, g, D and A (*vide supra*). This is usually done via effective Hamiltonian theory, although more direct methods can be used. In effective Hamiltonian theory, the Hamiltonian expressed in a large space (here the space of the resolved non-relativistic states) is projected onto a more restricted subspace (here the magnetic sublevels of the ground non-relativistic state) using an effective Hamiltonian.[109]

$$H_{eff} = H_{aa} + H_{ab}(E - H_{bb})^{-1}H_{ba} \quad (46a)$$

Where the subscript a and b describe the restricted space and the large space, respectively. The energy E appearing in this equation corresponds to the eigenvalue of the total Hamiltonian. To simplify equation, the Hamiltonian is decomposed into an unperturbed (Born-Oppenheimer Hamiltonian) and a perturbed Hamiltonian (SOC, Zeeman effect and hyperfine couplings). The following approximations are used: (1) the energy E is approximated to the eigenvalue of the unperturbed Hamiltonian and (2) the Hamiltonian $H_{bb}$ is approximated to the non-perturbed Hamiltonian. Under those two approximations, we get the following expression for the effective Hamiltonian matrix elements.

$$\langle 0SM_S|H_{eff}|OSM_S'\rangle = E_0\delta_{MM'} + \langle 0SM_S|H_1|0SM_S'\rangle + \sum_{b,S',M''} \frac{\langle 0SM_S|H_1|bS'M_S''\rangle\langle \mu S'M_S''|H_1|bSM_S'\rangle}{E_0 - E_\mu} \quad (46b)$$

Where the $|b\ S'M''\rangle$ states correspond to the non-relativistic states of the subspace b, $E_\mu$ is its unperturbed energy, $E_0$ is unperturbed energy of the state $|OSM_S\rangle$, $H_1$ is the perturbation Hamiltonian

The spin Hamiltonian parameters may be extracted by imposing that the effective Hamiltonian matrix elements match the spin Hamiltonian matrix elements one by one. The derivation and expression of the spin Hamiltonian parameters expression is rather tedious and will not be repeated here, but it is described elsewhere in details.[109]

Hence the effective Hamiltonian theory, used in addition to the CASSCF/NEVPT2 method enables to get an estimation of the magnetic properties of a system. However, as stated earlier, errors of several thousands of wavenumbers are not uncommon with the CASSCF/NEVPT2 method,[158] and errors in relative energies may lead to dramatic shifts in the calculated magnetic properties. Therefore, CASSCF/NEVPT2 results should always be regarded with caution. In this study, this method is always coupled with experimental measurements, and is merely employed as a way to provide a qualitative insight on the electronic structure and/or magnetism of a system.

# Chapter 1: elucidation of the electronic structure of [Fe(TPP)]

*The author of this thesis single-handedly built all the effective Hamiltonian, developed the program to simulate magnetometric and $^{57}$Fe Mössbauer spectroscopy measurements, and performed the ab-initio and DFT calculations. He participated to the acquisition of the experimental magnetometric and Mössbauer spectroscopy measurements. He did not participate in the acquisition and simulation of the THz-EPR data, neither in the synthesis of [Fe(TPP)].*

## I. Introduction

Despite intensive experimental and theoretical investigations in the past, the exact nature of the ground state of [Fe(TPP)] (**1**) has never been fully established. Specifically, the room-temperature effective magnetic moments ($\mu_{eff}$) measured for various crystalline forms obtained by different preparation procedures range from 4.0 to 4.4 $\mu_B$ ($\mu_B$ = Bohr magneton).[160] The values are considerably lower than the spin only value (4.9 $\mu_B$) for a quintet state ($S$ = 2), but substantially larger than that (2.8 $\mu_B$) for a triplet state ($S$ = 1). Although early studies[161] have assigned a high spin quintet state to **1**, consensus has been finally reached that the ground state is a triplet. A high-spin $d^6$ configuration would inevitably populate the Fe $d_{x2-y2}$ orbital, which is strongly σ-antibonding with respect to the interaction between the iron center and the four nitrogen atoms of the porphyrin ligand. In fact, the Fe-$N_{TPP}$ bond distances (1.97 Å) determined by X-ray crystallography for **1**[160] are significantly shorter than those found for the related high-spin ($S$ = 5/2) ferric porphyrin complex, [$Fe^{III}$(TPP)Cl] (2.06 Å)[162] and for [$Zn^{II}$(TPP)] (2.04 Å).[163] Note that for the latter two complexes, the Fe $d_{x2-y2}$ orbital is known to be singly and doubly occupied, respectively. These experiment findings thus provide a strong support for the notion that complex **1** features an $S$ = 1 spin ground state, instead of an $S$ = 2 state.[164]

Complex **1** features a square-planar coordination geometry; therefore, the Fe-$d_{xy}$, -$d_{xz}$, -$d_{yz}$ and -$d_{z2}$ orbitals are all essentially non-bonding in nature and nearly degenerate. As a

consequence, the triplet ground state of complex **1** can be assigned to four distinct electron configurations (Figure 14), all having a vacant $d_{x2-y2}$ orbital, namely, (a) $^3A_{2g}$ with a $(d_{xy})^2(d_{z2})^2(d_{xz,yz})^2$ configuration, (b) $^3E_g$(A) $(d_{xy})^2(d_{z2})^1(d_{xz,yz})^3$, (c) $^3E_g$(B) $(d_{xy})^1(d_{z2})^2(d_{xz,yz})^3$ and (d) $^3B_{2g}$ $(d_{xy})^1(d_{z2})^1(d_{xz,yz})^4$. Here, the symmetry of each state was labelled by the irreducible representations of the $D_{4h}$ point group. As verified below, all experimental results are consistent with the assumption that **1** belongs to the $D_{4h}$ point group despite the core distortion effects.

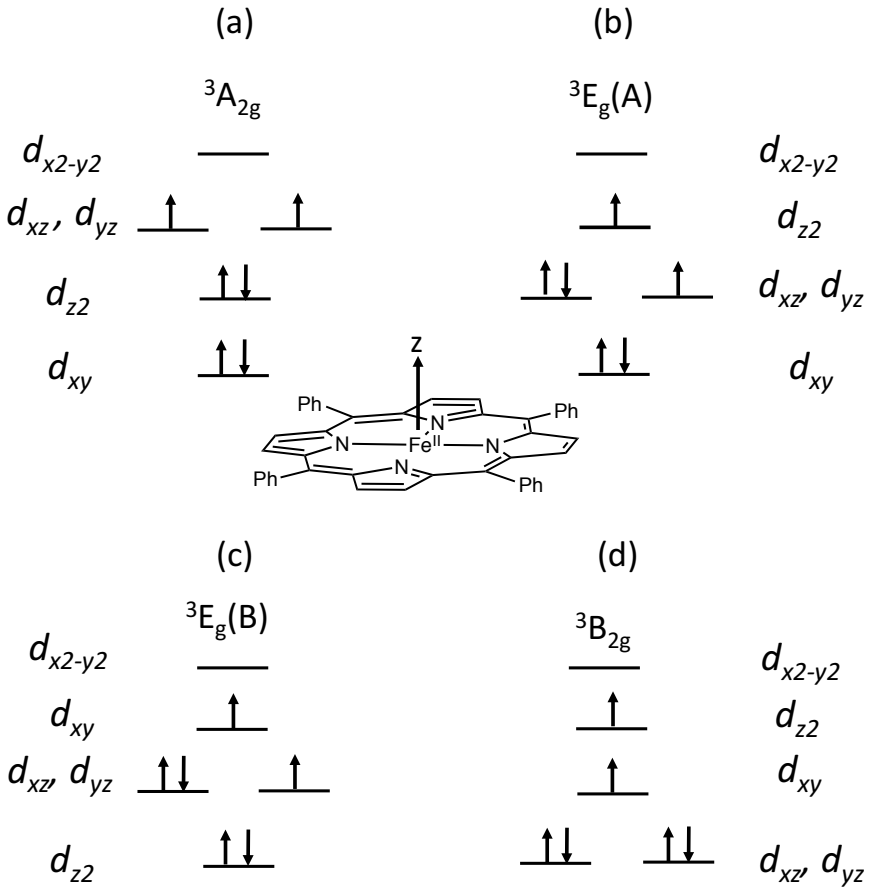


**Figure 14**: The four low-lying triplet electronic configurations of **1** with an unpopulated $d_{x2-y2}$ orbital.

Experimentally, Mössbauer studies on **1**[165] and resonance Raman measurements on related complex [Fe(OEP)] ($OEP^{2-}$ = octaethylporphyrinate dianion)[166] suggested the $^3E_g$ ground state. On the contrary, a range of experimental investigations using X-ray diffraction,[167] $^1$H NMR,[168] applied field Mössbauer spectroscopy,[169] and in particular magnetometry,[160] all attributed the $^3A_{2g}$ ground state to **1**.

Theoretical studies have also led to a number of contradictory assignments. Early CASSCF computations reported by Choe et. al. on [Fe$^{II}$(Por)] (Por = porphyrinate dianion), a truncated

model of **1**, predicted a quintet ground state with a $(d_{xy})^1(d_{z2})^2(d_{xz,yz})^2(d_{x2-y2})^1$ electron configuration.[170] It is known that the CASSCF method often tends to overstabilize high spin states.[171] Thus, to obtain more reliable spin-state energetics, second-order perturbative treatments such as CASPT2 or NEVPT2 are required to capture dynamic correlation effects. Indeed, CASPT2 calculations substantially reduce the quintet-triplet gap by more than 4200 $cm^{-1}$. However, the triplet-quintet estimated energy separation computed by Choe remains ~6700 $cm^{-1}$.[170] On the other hand, accurate CCSD(T) calculations estimated the quintet state to be 804 $cm^{-1}$ above the lowest-energy triplet state.[172] For the relative energy of the $^3A_{2g}$ and $^3E_g$ states, stochastic CASSCF calculations including all porphyrin π-orbitals in the active space recently reported by Alavi and coworkers[173] revealed that $^3E_g$ is about 175 $cm^{-1}$ lower in energy than $^3A_{2g}$. Qualitatively the same conclusion was reached by earlier configuration interaction (CI) and multi-reference Möller-Plesset[174] perturbation computations.[175] In contrast, CASSCF/CASPT2 and CCSD(T) calculations published by Choe,[170] Pierloot[176], Radón[172] and Bistoni[177] and coworkers all favored the $^3A_{2g}$ ground state, and CCSD(T) calculations delivered an energy gap of ~600 $cm^{-1}$ between the $^3E_g$ and $^3A_{2g}$ states.

The contradictory assignments of the electronic structure of **1** point to a situation where neither experiments nor quantum chemical calculations alone can unambiguously answer the question. The present chapter therefore presents dedicated efforts to elucidate the intriguing electronic structure of **1** through a combined spectroscopy-based theoretical and experimental study. Specifically, guided by the computational results we design an effective Hamiltonian that is able to simultaneously simulate all spectroscopic data derived from our variable temperature and variable field (VTVF) magnetization and Mössbauer measurements with only one common set of parameters. Note that Boyd et al[160] and Lang et al,[169] have employed magnetometry and applied field Mössbauer spectroscopy, respectively, to probe the electronic structure of **1**. To fit the magnetometry and Mössbauer spectroscopy data, two different models based on the ligand-field theory have been proposed. Different from the aforementioned work, the present contribution provides a universal model to simultaneously simulate these two sets of experimental data, and, more importantly, aims to build up a detailed magneto-structure correlation of **1**, which, to the best of our knowledge, has not been reported to date.

## II. Technical Details

### A. Experimental protocols

#### 1) Synthesis

All reactions were carried out in an inert glovebox argon atmosphere. Stabilizer free THF was purchased at *Acros Organics*. Before use, it was degassed by freeze-pump-thaw technique (3 cycles), stirred over sodium for two days and stored over molecular sieve (4 Å). Heptane was purchased at *Acros Organics*, degassed by bubbling argon through for one hour and stored over molecular sieve (4 Å). [Fe(TPP)Cl] was purchased at *Sigma Aldrich* with 95% purity (porphin residue). Sodium anthracenide was prepared by a previously described procedure.[178] After reduction, all samples were stored at -40 °C inside the glovebox. [FeTPP$(THF)_2$] was prepared according to the procedure published by Scheidt et al.[179]

*Sodium anthracenide:* Anthracene (1.26 g, 7.07 mmol, 1.1 equivalents) is dissolved in THF (32 mL). Metallic sodium (148 mg, 6.44 mmol, 1 equivalent) is added to the solution. The reaction mixture is stirred for 24 hours. No further workup is needed; the dark blue solution can be directly used as reducing agent.

*[Fe(II)TPP$(THF)_2$]:* FeClTPP (100 mg, 0.142 mmol, 1 equivalent) is dissolved in THF (12 mL). Sodium anthracenide (0.2 M solution, 0.71 mL, 1 equivalent) is added slowly via a syringe to prevent local excess of reducing agent. The solution is stirred at room temperature for 30 minutes and then filtered over a PTFE syringe filter, layered with heptane (48 mL) and set aside for crystallization at -40 °C for 2-3 days. The mother liquor is removed and the remaining solid is washed with little heptane (3 x 1 mL). Mössbauer (80 K, solid, relative to α-Fe): $\delta$ = 0.95 mm/s, $\Delta E_Q$ = 2.64 mm/s. UV-Vis (2-MeTHF, RT): $\lambda_{max}$ 425 nm, 545 nm, 605 nm.

*[Fe(II)TPP]:* [Fe(II)TPP$(THF)_2$] is dried at 100 °C in high vacuum ($10^{-2}$ mbar) for 60 minutes. Thermogravimetric measurements confirm the loss of two THF molecules from the THF adduct: $m_{\text{before thermogravimetry}}$ = 9.3 mg; $m_{\text{after thermogravimetry}}$ = 7.56 mg. $\Delta m_{calcd}$ for [M - 2 THF] = 1.73 mg; $\Delta m_{exp}$ = 1.74 mg. Mössbauer parameters (80 K, solid, relative to Fe): $\delta$ = 0.56 mm/s, $\Delta E_Q$ = 1.32 mm/s. UV-Vis (2-MeTHF, RT): $\lambda_{max}$ 425 nm, 545 nm, 605 nm.

2) Magnetic susceptibility measurements

Magnetic susceptibility data were measured from powder samples of solid material immobilized in eicosane in the temperature range 2 - 300 K by using a SQUID susceptometer with a field of 1 T (MPMS-7, Quantum Design, calibrated with standard palladium reference sample, error <2%). Multiple-field variable-temperature magnetization measurements were done at 1, 4, and 7 T also in the range 2- 300K with the magnetization equidistantly sampled on a 1/T temperature scale.

3) Mössbauer spectroscopy measurements

Mössbauer spectra were recorded on conventional spectrometers with alternating constant acceleration of the γ-source. The minimum experimental line width was 0.24 mm/s (full width at half-height). The sample temperature was maintained constant either in an Oxford Instruments Variox cryostat or a cryogen-free, closed-cycle Mössbauer magnet cryostat from Cryogenic Ltd. The latter is a split-pair super-conducting magnet system for applied fields up to 7 T. The temperature of the sample can be varied in the range 1.7 K to 300 K. The field at the sample is perpendicular to the γ-beam. The $^{57}$Co/Rh source (1.8 GBq) was positioned at room temperature inside the gap of the magnet system at zero-field position, by using a re-entrant bore tube. The detector was an Ar/10%$CH_4$-filled end-window type proportional counter for the zero-field measurements, and a Si-Drift diode (150 mm$^2$ SDD CUBE) of a AXAS-M1 system from Ketek GmbH with vacuum-tight 200 mm stainless steel finger, which was inserted into the cryostat to position the diode also in the gap of the magnet. Isomer shifts are quoted relative to iron metal at 300 K.

4) THz-EPR

THz-EPR experiments were performed at the THz beam line of the synchrotron BESSY II, Helmholtz-Zentrum Berlin. The experiment is described elsewhere in great detail.[180] 12 mg of polycrystalline powder of **1** was mixed with PE powder, grinded and pressed into a TPX sample holder. An Hg arc lamp was used for irradiation. Inside the FT-IR spectrometer (IFS 125, Bruker) the radiation was divided by a 6 µm Mylar multilayer beam splitter. Mirro movements corresponded to a scanner velocity of 40 kHz and an experimental resolution of 1 cm$^{-1}$. The

sample was placed in the VTI of an Oxford Optistat magnet with outer TPX and inner diamond windows and kept at a temperature of 5 K. Radiation passed through the magnet (and the sample) in Voigt configuration and was detected with a Infrared 4.2K Si bolometer. At each field, 256 scans were acquired.Spectra are shown as Magnetic field division spectra (MDS), where the spectrum for the field $B_0$ is obtained by dividing a spectrum measured at $B_0$ + 1 T by a spectrum measured at $B_0$ (further details on how to analyze MDS can be found in ref. 180. Simulations were perfomed with EasySpin[181] and its extensions for frequency-domain EPR.[182]

## B. Details relative to the modelization

### 1) Computational details

All calculations were performed using the ORCA v.4.0 package.[183]
All calculations were carried out on experimental structures determined by X-ray diffraction analysis, after the hydrogen positions were optimized at the BP86/def2-TZVP level of theory.[144,184] Normal SCF ($1\times10^{-6}$ Eh), normal geometry convergence criteria and a grid level 5 were used for these calculations. Because of the high flexibility of porphyrins, three core conformations, namely, ruffled, saddled and planar,[160] have been found for the crystal structure of various forms of complex **1** and its derivatives. In particular, the distinct core conformations have slightly different Fe-N bond lengths and disparate packing modes, which likely leads to their different electronic structures, a behavior observed for high spin Fe(III)-porphyrins.[185] Therefore, all calculations were performed on three crystal structures, each corresponding to a four-coordinated iron(II) complex crystallised in one of the three aforementioned porphyrin conformation.[160]

The DFT single point calculations were carried out using the functional B3LYP, the basis set CP(PPP) for the iron and the basis set Def2-TZVP for all other atoms. Normal SCF ($1\times10^{-6}$ Eh) convergence criterium in combination with a grid level of 7 for iron and 5 for all other atoms were used for these calculations. $^{57}$Fe isomer shifts were calculated using the calibration curve developed by Römelt.[149] The physical origin of the EFG tensor was analysed by breaking it down into one-center, two-center "bond", two-center "point-charge" and three center contributions, according a prior methodology.[145] The one-center contribution of the MOs was further broken down into three contributions, i.e. core orbitals, d-orbitals and ligand orbitals contribution according to the following method. All quasi-restricted orbitals[186] identified as predominantly iron 1s, 2s, 2p, 3s and 3p were identified as "core". The sum of their contribution

was labeled as core contribution. All orbitals but the core orbitals were localized using Pipek-Mezey algorithm.[187] The contribution from the localized orbitals mainly composed of Fe-3d atomic orbital were labelled as d-orbital contribution. The remaining of the one-center contribution was labeled as ligand contribution.

For the CASSCF calculations of 8 electrons in 11 orbitals, the active space composition is described in subsection IV.B.1. The calculations were performed in gas phase in conjunction with the Def2-TZVP basis set for all atoms.[144] The normal convergence criteria were selected (energy convergence threshold $1\times10^{-7}$ Eh and orbital gradient convergence threshold $1\times10^{-3}$), in combination with a grid level of 6. The quasi-restricted orbitals[186] from a single-point DFT calculation were used for the initial guess of each CASSCF calculation. The orbitals were optimized in order to minimize the CASSCF energy state-averaged over the four lowest triplet states and the lowest quintet state. Dynamical correlation was added to the CASSCF energy using the strongly-contracted second-order N-electron Valence Perturbation Theory (NEVPT2).[159]

2) Numerical simulations of the magnetic susceptibility

In the present study, the simulated magnetic susceptibility was calculated after the diagonalization of an electronic Hamiltonian which form will be discussed later. For this purpose, a program was coded in Fortran90 and will be briefly described here.

The program works in two steps, i.e. (1) calculation of a molar magnetization which is dependent on the temperature and the direction of the applied magnetic field vector with respect to the molecular frame (represented by the angles $\theta_1$ and $\phi$, see Figure 15), and (2) numerical powder-averaging of the direction-dependent magnetization.

The temperature-dependent macroscopic magnetization along the applied magnetic field is defined according to eq. 19c and can be rewritten as eq. 47a using the partition function of the thermally-populated magnetic sublevels:

$$M(B_{\text{ext}},\theta_1,\phi,T) = N_A k_B T \frac{dln\left(Q_1(B,\theta_1,\phi,T)\right)}{dB} = N_A k_B T \frac{\ln\left(Q_1\left[B_{\text{ext}}+\frac{dB}{2},\theta_1,\phi,T\right]\right)-\ln\left(Q_1\left[B_{\text{ext}}-\frac{dB}{2},\theta_1,\phi,T\right]\right)}{dB} \quad (47a)$$

Where $Q_1$, the partition function, is defined as:

$$Q_1(B_{\text{ext}},\theta_1,\phi,T) = \sum_i e^{-\frac{E_i(B_{ext},\theta_1,\phi)}{k_B T}} \quad (47b)$$

The energies $E_i$ corresponds to the eigenvalues of the diagonalized Hamiltonian, and $dB$ corresponds to the infinitesimal increment of the field norm. They are dependent on the applied field intensity ($B_{\text{ext}}$) and direction because of the Zeeman interaction term. To calculate magnetization according to eq. 47a, the infinitesimal incrementation of $B_{\text{ext}}$ ($dB$) was approximated to 0.1 T, and the Hamiltonian matrix was diagonalized twice, i.e. once to calculate $Q_1\left(B_{\text{ext}} + \frac{\mathrm{d}B}{2}, \theta_1, \phi\right)$ and once to calculate $Q_1\left(B_{\text{ext}} - \frac{\mathrm{d}B}{2}, \theta_1, \phi\right)$.

In a second step, the averaged magnetization is calculated from the direction-dependent magnetization. For a powder sample, the applied magnetic field is assumed to be randomly oriented with respect to the molecular framework. Hence, the averaged magnetization is the average of the direction-dependent magnetization over all possible directions of the magnetic field's directional vector, or:

$$\bar{M} = \frac{1}{4\pi}\int_0^{2\pi}\int_0^{\pi} M(B_{\text{ext}}, \theta_1, \phi, T) sin\theta_1 d\theta d\phi \qquad (47c)$$

The infinitesimal increments $d\theta_1$ and $d\phi$ were both approximated as $0.01\pi$ radians, and the integration was performed numerically.

3) Simulation of the Mössbauer spectra

Likewise, a code was written to simulate the $^{57}$Fe Mössbauer absorption spectra after diagonalization of a nuclear Hamiltonian which form will be described in details later. The calculation was made in three steps. (1) An absorption function, corresponding to the number of photons absorbed over the number of photons emitted, is calculated. This absorption function depends on the doppler shift $v$, the direction of the applied magnetic field described by the angles $\theta_1$ and $\phi$, and the direction of the propagation vector of the incident $\gamma$-wave $\vec{k}$ with respect to the molecular frame, described by only one angle $\theta_2$ (*vide infra*). Note that one angle is enough to describe the propagation vector $\vec{k}$ because the Mössbauer spectrometer is in perpendicular mode (the field at the sample is perpendicular to the $\gamma$-beam). (2) The absorption function is averaged over all directions of the propagation vector on the plane normal to the applied magnetic field. (3) The absorption function is averaged over all possible directions of the applied magnetic field. Step (2) and (3) account for the powder distribution of the sample and result in the calculation of the average spectrum.

The direction-dependent absorption function is calculated as a sum of Lorentzian functions:

$$Y(E_{\mathrm{n}}, B_{\mathrm{ext}}, \theta_1, \phi, \theta_2, T) = I_{\max} \sum_{i,j} \frac{A_{\mathrm{ij}}(B_{\mathrm{ext}}, \theta_1, \phi, \theta_2, T)}{\left(\frac{\omega}{2}\right)^2 + \left(E_{\mathrm{n}} - E_{\mathrm{ij}}(B_{\mathrm{ext}}, \theta_1, \phi, T)\right)^2} \quad (48a)$$

All the terms involved in eq. 48a are now described in details. $I_{\max}$ is a scaling factor adjusting the total absorption function. This factor was set arbitrarily to match the experimental spectra. Note that because the number of recoilless emissions depends on the temperature, so does the total absorption. Hence, the factor $I_{\max}$ was rescaled for each temperature at which the experimental Mössbauer spectrum was measured. $\omega$ determines the spectral line width. It is chosen arbitrarily to match the experimental spectra, although one unique factor $\omega$ was chosen for all absorption lines and spectra regardless of the temperature. The sum runs for every possible transition from an initial nuclear magnetic sublevel $i$ (I=1/2) to a final sublevel $j$ (I=3/2). The factor $E_{\mathrm{n}}$ corresponds to the energy of the incident photon. $E_{\mathrm{ij}}$ is the resonant energy corresponding to the transition from the nuclear state $i$ (I=1/2) and the nuclear state $j$ (I=3/2) (substracted to the emission energy of the $\gamma$-photon, 14.4 keV). It is inferred from the nuclear states energy and hence requires the diagonalization of the nuclear Hamiltonian. $A_{\mathrm{ij}}(B_{\mathrm{ext}}, \theta_1, \phi, \theta_2, T)$ is the squared transition intensity corresponding to the transition from the nuclear state $i$ to the nuclear state $j$.

Calculation of the $A_{\mathrm{ij}}$ requires the state composition of the nuclear Hamiltonian eigenvectors which is obtained by diagonalization of the nuclear Hamiltonian. Because the quadrupole splitting and magnetic hyperfine coupling/nuclear Zeeman effects are competing, those eigenvectors are linear combinations of $|I, M_I\rangle$. Consequently, the terms $A_{\mathrm{ij}}$ must be calculated using eq. 35a-35b. Note that to calculate the expression of $A_{\mathrm{ij}}$, the angles describing the direction of the propagation vector in the molecular frame are required. These can be obtained along the following procedure. The axes $x$, $y$ and $z$ of the molecular framework are described by the directional vectors $\overrightarrow{e_\iota}$, $\overrightarrow{e_J}$, $\overrightarrow{e_k}$, respectively. The two successive rotations transforming the vector $\overrightarrow{e_k}$ into the directional vector of the applied magnetic field $\overrightarrow{e_B}$ is noted $\hat{R}$. $\hat{R}$ consists in a rotation around the axis $y$ by an angle $\theta_1$ followed by a rotation around the axis $z$ by an angle $\phi$. Finally, we note $\overrightarrow{e_\iota'}$ and $\overrightarrow{e_J'}$ the products of the transformation $\hat{R}$ applied to $\overrightarrow{e_\iota}$ and $\overrightarrow{e_J}$, respectively (Figure 15). $\overrightarrow{e_\iota'}$, $\overrightarrow{e_J'}$ and $\overrightarrow{e_B}$ are orthonormal, and hence the propagation vector $\vec{k}$ can be described with respect to $\overrightarrow{e_\iota'}$ and $\overrightarrow{e_J'}$:

$$\vec{k} = Cos(\theta_2)\overrightarrow{e_\iota'} + Sin(\theta_2)\overrightarrow{e_J'} = Cos(\theta_2)\hat{R}(\theta_1, \phi)\overrightarrow{e_\iota} + Sin(\theta_2)\hat{R}(\theta_1, \phi)\overrightarrow{e_J} \quad (48b)$$

It appears from eq. 48b that the angles describing the direction of the propagation vector $\vec{k}$ in the molecular frame can be described as functions of $\theta_1$, $\theta_2$ and $\phi$. Thus, as mentioned above, only one additional angle $\theta_2$ is necessary to describe the direction of the propagation vector.

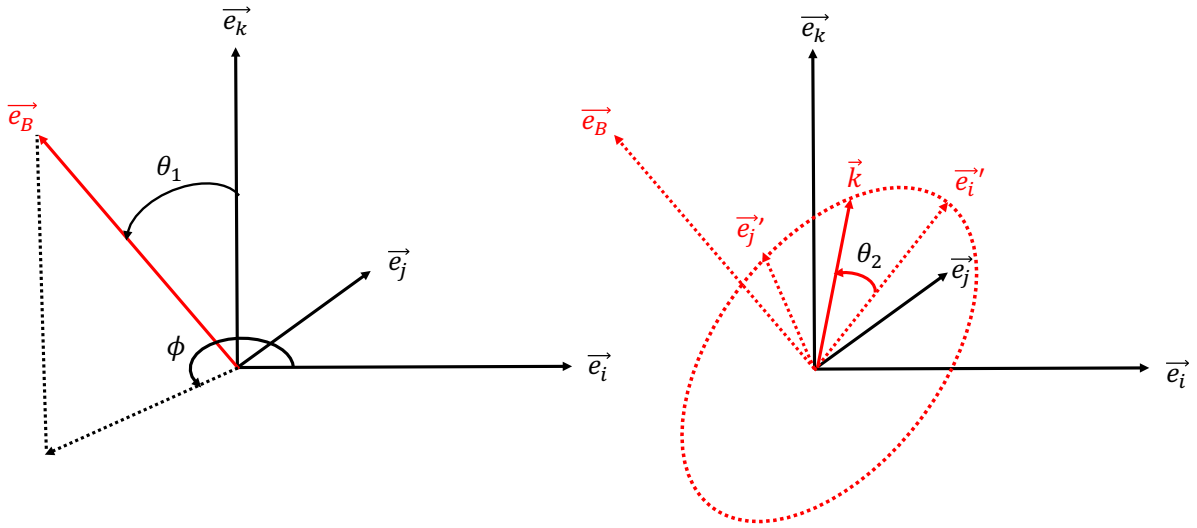


**Figure 15**: (left) Orientation of the applied field directional vector $\vec{e_B}$ (red) in the molecular framework represented by the directional vectors $\vec{e_i}$, $\vec{e_j}$ and $\vec{e_k}$ (black) and (right) orientation of the propagation vector $\vec{e_B}$ (red) and the directional vectors $\vec{e_i}'$, $\vec{e_j}'$ and $\vec{e_B}$ (dashed red) in the molecular framework (black). The dashed red circle represents the plane normal to the vector $\vec{e_B}$.

Because the sample is a powder and because the set-up is in perpendicular mode, a random distribution of the propagation vector direction is assumed on the plane normal to the applied magnetic field vector. As apparent in eq. 48b, this direction is described by the angle $\theta_2$. Hence, the direction-dependent absorption function is averaged over an angle $\theta_2$ in the range 0 to $2\pi$:

$$\bar{Y}(E_{\mathrm{n}}, B_{ext}, \theta_1, \phi, T) = \frac{1}{2\pi} \int_0^{2\pi} Y(E_{\mathrm{n}}, B_{ext}, \theta_1, \phi, \theta_2, T) d\theta_2 \qquad (48c)$$

The infinitesimal increment $d\theta_2$ was approximated to $0.02\pi$ radians, and the integration was performed numerically.

Finally, because the sample is a powder, a random orientation of the applied magnetic field vector with respect to the molecular framework is assumed. Hence, the function $\bar{Y}(E_{\mathrm{n}}, B_{\mathrm{ext}}, \theta_1, \phi)$ is averaged over all possible directions of the magnetic field. This leads to the final expression for the powder-averaged absorption function:

$$\bar{\bar{Y}}(E_{\mathrm{n}}, B_{\mathrm{ext}}, T) = \frac{1}{4\pi} \int_0^{2\pi} \int_0^{\pi} \bar{Y}(E_{\mathrm{n}}, B_{\mathrm{ext}}, \theta_1, \phi, T) \sin(\theta_1)\, d\theta_1 d\phi \quad (48d)$$

The infinitesimal increments $d\theta_1$ and $d\phi$ were both approximated as $0.02\pi$ radians, and the integration was performed numerically.

Because conventionally, the spectrum displays a transmission rather than an absorption function, the final spectral shape is described by the function:

$$T(E_{\mathrm{n}}, B_{\mathrm{ext}}, T) = 1 - \bar{\bar{Y}}(E_{\mathrm{n}}, B_{\mathrm{ext}}, T) \quad (48e)$$

## III. Experimental results

### A. THz-EPR

In the zero-field THz-EPR spectra of **1** (see Figure 16), a maximum, surrounded by minima, was observed at approximately 94.5 $cm^{-1}$. With increasing magnetic field the maximum split into two, with one blue- and the other red-shifted. The corresponding minima at slightly higher energies blue shifts and become more intense with increasing field. The zero-field position of the maximum directly provides the axial ZFS term ($D$). In terms of the $S = 1$ spin Hamiltonian (eq. 13b and 15b), this correspond to $D \sim 94.5$ $cm^{-1}$. For a triplet in zero field two EPR transitions are allowed. The fact that we observe only one transition indicates that two of the three states are (almost) degenerate. In the language of the spin Hamiltonian, this corresponds to negligible $E/D$, consistently with the postulated four-fold symmetry of the molecule. Nevertheless, simultaneous spin Hamiltonian simulations of zero field and field dependent spectra allowed an estimate of $E$~1.1 cm. $g_{\perp}$ (=$g_{xx}$, $g_{yy}$) had only minor influence on the simulations (for $g_{\perp} < 4$) and could not be determined. In contrast, $g_{\parallel}$ (=$g_{zz}$) had a clear impact. We found the best agreement for $D = 94.4$ $cm^{-1}$, $E = 1.1$ cm and $g_{\parallel} = 1.7$ (Figure 16).

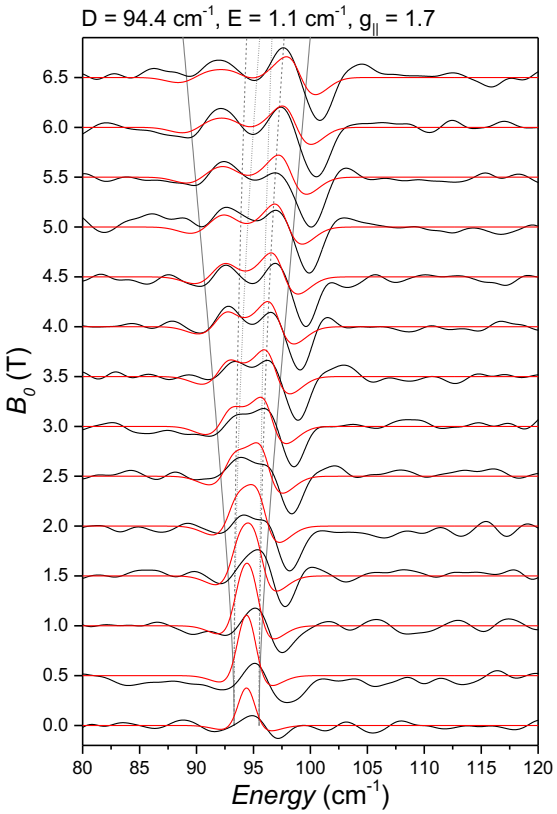


**Figure 16**: THz-EPR spectra of **1**. Data (black line) is rescaled and offset according to the applied magnetic field $B_0$. Simulation with the parameters shown on top of the plot are shown in red. Gray lines in the back indicate calculated transition energies for a magnetic field applied along the *x*- (dashed), *y*- (dotted), and *z*-axis (solid).

## A. Variable temperature and variable field (VTVF) magnetic susceptibility measurements

### 1) Low-temperature susceptibility and magnetization

As visible in Figure 17, below ca. 120 K, the effective magnetic moment $\mu_{eff}$(T) of **1** shows a strong drop, typical of systems having strong ZFS.[107] In accordance with the large ZFS, isofield magnetization curves, M($\mu_B B_{ext}/kT$), measured at $B_{ext}$ = 1, 4 and 7 T, show a strong nesting behavior. In fact, the magnetization at 2.0 K is almost linear with the applied field, hinting that the system is still close to the low-field limit, even under a field of up to 7 T, an observation compatible with a very large and positive ZFS. The plateau-shaped magnetization curve at low-temperature for the 4 and 7 Tesla curves also suggest a well-isolated ground state, as described in the Theory chapter (subsection I.B.2). Only the low-temperature magnetization under 1 T seems to exhibit a sharp decrease with temperature, seemingly incompatible with a

large, positive ZFS. This discrepancy, however, is likely to be explained by the presence of [Fe(TPP)(THF)$_2$] impurities (S=2) with a much lower lower ZFS[188] (see subsection III.B.3).

2) High-temperature measurements

The effective magnetic moment $\mu_{eff}$ determined at 298 K (4.24 $\mu_B$) is consistent with earlier studies.[160] It is markedly higher than the spin-only value for a triplet state (2.8 $\mu_B$), but much lower than expected for a quintet state (4.9 $\mu_B$). This may indicate, as specified in the Theory chapter, either a spin mixture between the triplet and the quintet, or a large participation of the orbital angular momentum to the magnetic moment. Furthermore, the effective magnetic moment does not reach a plateau at high temperature but keeps steadily increasing, a behavior quite typical of a TIP, as specified in the Theory chapter (subsection I.B.1). Similar non-Curie behavior of four-coordinated iron(II)-porphyrins has been previously investigated by $^1$H NMR studies.[189]

3) Spin Hamiltonian simulations

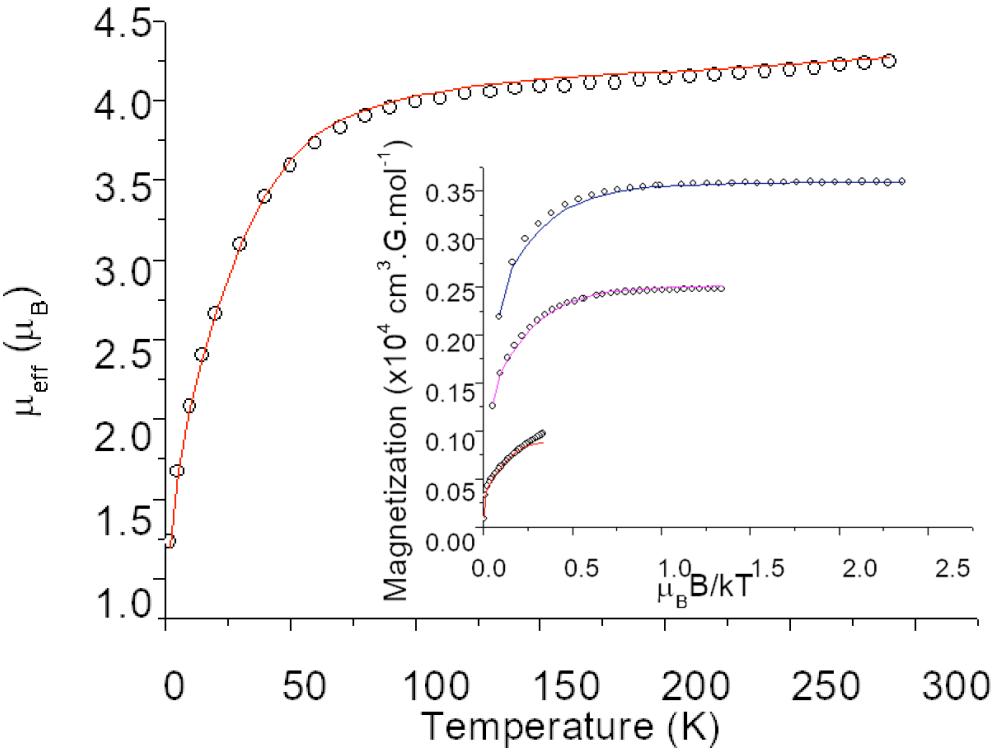


**Figure 17***:* Effective magnetic moment under an applied field of 1 T and isofield magnetization curves with applied fields of 1, 4 and 7 T (inset) of **1**. Dots represent experimental measurements and the solid lines represent the best fits obtained from the simulation using the spin Hamiltonian under 1 (red), 4 (pink) and 7 T(blue). Spin Hamiltonian parameters include

$D$ = 94 cm$^{-1}$, $E/D$ = 0, $g_{//}$ = 1.7, $g_{\perp}$=3.05, TIP= 1000× 10$^{-6}$ emu, and 7.7% of $S$ = 2 [Fe(TPP)(THF)$_2$] impurities were taken into account in the simulation.

A global simulation with the usual spin Hamiltonian of $S$ = 1 of all magnetic data yielded a satisfactory fit with parameters $D$ = 94 cm$^{-1}$, $E/D$ = 0, $g_{//}$ = 1.7, $g_{\perp}$=3.05 ($g_{av}$ = 2.7) and a TIP value of 1000× 10$^{-6}$ emu (Figure 17). Due to the high molecular symmetry, the principal axes of the $g$-matrix and $\overline{\overline{D}}$ tensor are collinear. The rhombicity $E/D$ and $g_{//}$, were fixed according to the THz-EPR results above (see subsection III.A). The rapidly decreasing behavior of the low-field (1T) magnetization could not be reproduced with such a large ZFS but this discrepancy was solved by the inclusion of 7.7% S=2 impurities. The effect of those impurities is maximal at low-field, because the S=2 impurities are close to the high-field limit for which low-temperature magnetization is field-independent, while **1** remains close to weak-field limit throughout the field series, for which magnetization is proportional to the field (see Theory chapter, subsection I.B.2). Hence the ratio of the signal from the impurities over the signal from **1** is maximal at low field. Consequently, the low-field magnetization exhibits the sharp decrease due to the lower $D$ S=2 impurities while magnetization at higher field is dominated by the plateau-shaped magnetization of **1**. Alternatively, the impurities might also be high-spin Fe(III) products generated by air oxidation as documented in earlier publications.[160,161] Simulations with 5.2% $S$ = 5/2 impurity also yielded a global fit of similar quality (Figure A1 in the annex).

Despite the good fit, the large magnitude of the deduced ZFS, the average $g$ value, and, in particular, the phenomenological TIP correction cast doubt on the validity of the spin Hamiltonian treatment, which requires an energetically well isolated, non-degenerate non-relativistic ground state without first order orbital angular momentum. In contrast, our results suggest that **1** possesses closely spaced low-lying states (see Theory chapter, subsection I.B.1). More important is that the spin Hamiltonian analysis does not allow us to determine directly whether $^3A_{2g}$ or $^3E_g$ is the non-relativistic ground state, therefore the present situation calls for the use of a more physically transparent model.

## B. VTVF Mössbauer spectroscopy

### 1) Electric hyperfine effects

A zero-field Mössbauer measurement at 10 K (Figure 18) showed that complex **1** possesses an isomer shift ($\delta$) of 0.56 mm/s and an absolute quadrupole splitting ($|\Delta E_Q|$) of 1.31 mm/s (eq.

27c and 28a, respectively). The isomer shift is consistent with the values (0.52 – 0.57 mm/s) reported earlier for **1**, as well as those for the related porphyrin complexes ([Fe(OEP)], $\delta$ = 0.62 mm/s, and [Fe(OEC], OEC = trans-7,8-dihydro-octaethylporphyrin), $\delta$ = 0.63 mm/s).[190] The quadrupole splitting measured for our sample is comparable to that found for complex **1** having a slightly ruffled core (1.51 mm/s),[160,169] as well as those for [Fe(OEP)] with (1.71,[190] +1.60[191]). On the other hand, it is significantly lower than **1** with a saddle core conformation[160] (2.21) or [Fe(OEC)] (2.55).[190] Previous authors have attributed this disparity in the iron(II)-porphyrin family to distinct electronic configurations of the iron in otherwise chemically similar compounds. This brings further credence to the hypothesis of closely lying non-relativistic states in iron(II)-porphyrin systems (see subsection IV.A).[160] The sign of the quadrupole splitting of **1** was resolved later by application of a magnetic field, and is shown to be positive (see subsection III.C.2). This result is surprising for an iron configuration where the $d_{x2-y2}$ orbital (large positive contribution to the z-component of the EFG) is expected to be unoccupied, thus shifting the overall d-orbital contribution, usually dominant, towards negative values (see Theory chapter, subsection II.A).

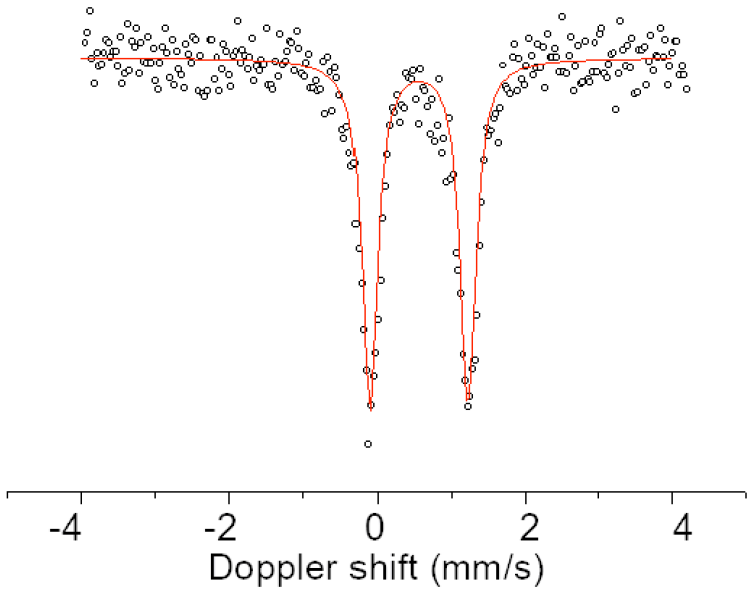


**Figure 18:** Zero-field Mössbauer spectrum of **1** at 80 K.The solid line corresponds to the best fit obtained for a quadrupole splitting of $\Delta E_Q = \pm 1.31$ mm/s and $\delta = 0.56$ mm/s.

2) Magnetic hyperfine effects

To gain further insight into the electronic structure of complex **1**, VTVF $^{57}$Fe Mössbauer studies were conducted. As shown in Figure 19, the magnetic splitting of the spectra recorded at 1.7 K is moderately large, but strongly field-dependent. Each spectrum shows a unique pattern determined by differentially competing nuclear Zeeman and electric quadrupole interaction. The pattern and, in particular, no more than six resolved lines are characteristic of fast paramagnetic relaxation. In this limit, the temperature- and field- dependent hyperfine fields of the powder spectra are Boltzmann-weighted averages of the contributions from all magnetic sublevels (cf. Theory chapter, subsection II.B.1).

The Mössbauer spectrum obtained at 1T/1.7 K (Figure 19) is a typical case of weak field limit. The low-energy triplet and high-energy doublet line pattern is typical of a positive quadrupole splitting with a very low asymmetry parameter (see Theory chapter, subsection II.A). Moreover, the weak magnetic splitting reveals a low internal field incompatible with a first-order spin or orbital angular momentum. In the spin Hamiltonian picture this behavior would be typical for an integer spin system ($S = 1$) with a low-lying $M_S = 0$ level arising from a large positive ZFS. The drastic increase of the magnetic splitting with applied fields suggests a positive internal field, as verified below by simulations. As elaborated in the Theory chapter (subsection II.B.1), this is a characteristic feature of a large orbital contribution to the $^{57}$Fe hyperfine interaction. Here, the positive orbital contribution dominates over the otherwise overwhelming negative Fermi contact contribution from the electronic spin. Such situations are frequently encountered for systems having sizeable orbital angular momenta. [116,192]

The 1.7K/7T spectrum (Figure 19) approaches the typical six-line pattern for the high-field limit of mixed magnetic and electric hyperfine interactions[116] (see Theory chapter, subsection II.B.2), where the nuclear Zeeman splitting is significantly stronger than the quadrupole interaction (due to the presence of a strong induced internal field). In this situation, the high intensity of the $\Delta M_I = 0$ lines (lines 2 and 5 from left to right) indicates an easy *x/y*-plane of magnetization, as expected for a large axial ZFS with a "$M_S = 0$" ground level. Moreover, the shift of the inner four lines of the spectrum with respect to the outer two reveals a negative quadrupole shift. However, in the actual high-field limit of hyperfine interactions, the quadrupole shift in the first-order approximation arises only from the components of the EFG tensor along the dominating internal field. However, since the internal field from "$M_S = 0$" is predominantly oriented in the *x/y* plane due to the large ZFS ($D > 80$ cm$^{-1}$), only the negative $V_{xx}$ and $V_{yy}$ components of the EFG are sensed in the measurement (see eq. 34).

Because the EFG is a traceless tensor, the sign of the main component $V_{zz}$ is positive and so is $\Delta E_Q$, which is consistent with our interpretation of the weak-field spectrum (1.7 K, 1 T). Here we can safely assume that the EFG tensor is collinear with the principal axes of the ZFS because of the effective four-fold rotation symmetry.

3) The spin Hamiltonian simulation

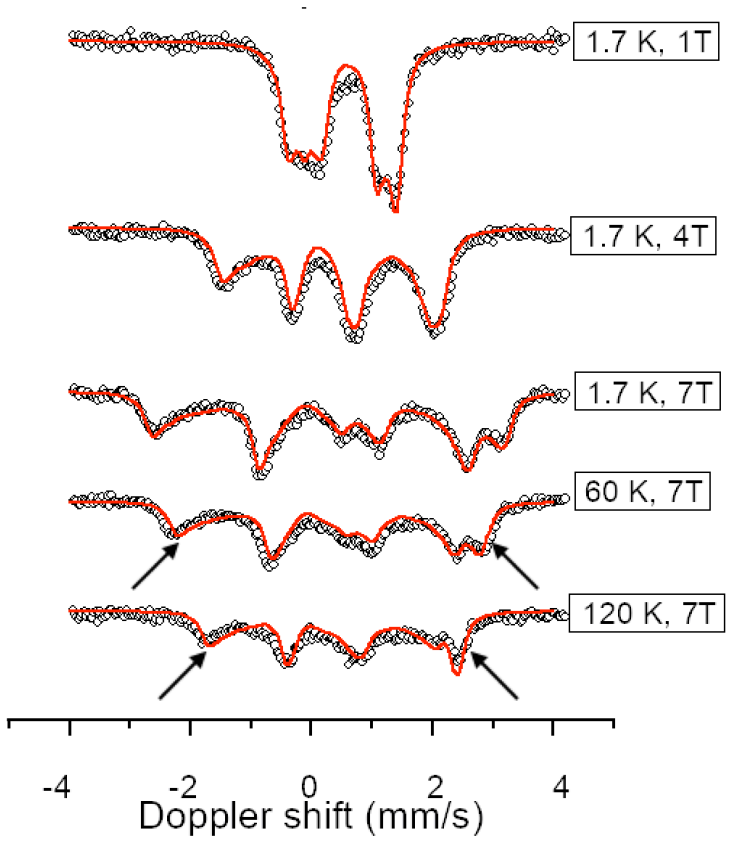


**Figure 19:** spin Hamiltonian fit of **1** at 1.7 K under 1 T, at 1.7K under 4 T, at 1.7 K under 7T, at 60 K under 7 T and at 120K under 7T. The dots correspond to the experimental measurements and the red line corresponds to the spin Hamiltonian fit, using the following phenomenological parameters: $g_\perp = 3.05$, $g_\parallel = 1.7$, $D = 94$ cm$^{-1}$, $\frac{E}{D} = 0$, $\frac{A_\perp}{g_N \beta_N} = 50.0$T, $\Delta E_Q = +1.31$ mm/s and $\delta = +0.56$ mm/s. In all case, $A_\parallel$ was unresolved and arbitrarily set to zero. The black arrows indicate the small misfits at high temperature.

We attempted to simulate the entire VTVF Mössbauer spectra using the usual spin Hamiltonian (see eq. 13b, 15b, 28a and 33b). Note that the principal axes of the $\overline{\overline{D}}$, EFG tensors, $g$ and $A$ matrices are collinear due to the high symmetry of the molecule. The $D$, $E/D$ and $g$-values were fixed to those determined by the magnetometry and THz-EPR measurements, $V_{zz}$

was fixed to that determined by the zero-field measurement, $\eta$=0 on the ground of the high molecular symmetry, and only the hyperfine matrix was allowed to vary. The whole VTVH series can be fitted satisfactorily with a unique $\frac{A_\perp}{g_N\beta_N}$ value of 50.0 T (Figure 19). Such a large, positive $A_\perp$ strongly suggests the presence of a sizeable orbital angular momentum along the *xy* plane (see Theory chapter, subsection II.A.1). The $A_\parallel$ parameter could not be resolved as expected for systems with very large positive *D* values. Finally, we note in passing that the magnetic splitting of **1** is slightly underestimated at higher temperature even with our best spin Hamiltonian fit (Figure 19). This misbehavior is very faint, but is still physically relevant as discussed in subsection VII.A.

Previously Lang and coworkers[169] proposed a phenomenological Hamiltonian to simulate the variable temperature Mössbauer spectra of **1** recorded at a fixed magnetic field of 3.2 T. In their approach, each Mössbauer spectrum at a given temperature was fitted with a temperature-dependent ω matrix for parametrizing the nuclear Zeeman effect, $H = -g_N\beta_N\vec{I}\cdot(1+\omega)\vec{B}$. Apparently, this model does not allow to easily extract the electronic-structure information of **1** and therefore does not provide insight into the nature of its ground state.

The analysis of these experimental results leads to a double conclusion. First, a deep understanding of the physical origin of the quadrupole splitting is necessary for a complete understanding of the electronic structure of the ground state of **1**. As mentioned above, the sign of the quadrupole splitting of **1** is counter-intuitive, and the origin of the large disparity in quadrupole splitting values throughout the iron-porphyrin family is ill-understood. Hence, in-depth study of the electric quadrupole effects is required but calls for the use of more advanced computational models.

Furthermore, and much more importantly, the magnetometry and applied field Mössbauer measurements altogether suggest that the magnetic properties of compound **1** cannot be properly described by the usual $S = 1$ spin Hamiltonian, although reasonable simulations can be obtained. Instead, all experimental data indicate that the ground non-relativistic state of **1** features a small energy separation from the low-lying excited non-relativistic states, which leads to considerable field-induced mixing between these states and the ground state. Such interactions are not accounted for by the spin Hamiltonian model.

Following those observation, we have separated the next section into two parts. First, we investigate the origin of the zero-field Mössbauer parameters by means of DFT calculations to shed more light on the electronic structure of the non-relativistic ground state. Second, we investigate the low-lying excited non-relativistic states of **1** by means of an ab-initio investigation.

## IV. DFT and ab-initio calculations

### A. DFT calculations

#### 1) Energetic considerations

To investigate the physical origin of the zero-field Mössbauer parameters of **1**, and to study the possible effect of the porphyrin core-conformation, DFT calculations were carried out in gas-phase on the ruffled, saddle and planar porphyrin conformations (see computational details). For each core-conformations, it was possible to converge a solution corresponding to the $^3A_{2g}$ iron electronic configuration $(d_{xy})^2(d_{xz})^1(d_{yz})^1(d_{z2})^1$, and a solution corresponding to the $^3E_g$ iron electronic configuration $(d_{xy})^2(d_{xz})^2(d_{yz})^1(d_{z2})^1$. The results are summarized in Table 4. Irrespective of the core-conformation, the $^3A_{2g}$ solution was always found slightly lower in energy, but the energy gap between the two solutions is too small to be conclusive with regard to the nature of the non-relativistic ground state. However, this result hints at a very small energy separation between the $^3A_{2g}$ and $^3E_g$ states, as already suggested by the available experimental data.

**Table 4**: Relative energy of the $^3A_{2g}$ and $^3E_g$ states ($\Delta E = E(^3E_g) - E(^3A_{2g})$), and electric hyperfine parameters ($^{57}$Fe isomer shift $\delta$ and quadrupole splitting $\Delta E_Q$ for each core conformation and electronic configuration, calculated by DFT.

| **Core conformation** | $\Delta E(cm^{-1})$ | $\delta(^3A_{2g})$ (mm/s) | $\delta(^3E_g)$ (mm/s) | $\Delta E_Q(^3A_{2g})$ (mm/s) | $\Delta E_Q(^3E_g)$ (mm/s) |
|---|---|---|---|---|---|
| Planar | 482 | 0.40 | 0.49 | +0.433 | +1.115 |
| Ruffled | 454 | 0.38 | 0.48 | +0.596 | +1.256 |
| Saddle | 389 | 0.38 | 0.46 | +0.532 | +1.322 |

#### 2) Calculated Mössbauer parameters

The Mössbauer isomer shifts and quadrupole splittings for each of the core-conformation and non-relativistic ground state are summarized in Table 4. Neither the isomer

shift nor the quadrupole splitting seems to have a significant dependence on the core conformation. However, the nature of the electronic configuration ($^3A_{2g}$ or $^3E_g$) has a tremendous impact on the Mössbauer parameters. The $^3A_{2g}$ configuration exhibits a lower quadrupole splitting and a larger isomer shift by about 0.6-0.7 mm/s and 0.1 mm/s, respectively, compared to the configuration $^3E_g$. The calculated quadrupole splitting value obtained for the $^3E_g$ configuration is consistent with an earlier DFT study on iron-porphyrins.[193] Although the best agreement with the experimental Mössbauer parameters ($\Delta E_Q = +1.31\ mm/s$ and $\delta$=0.56 mm/s) is for the $^3E_g$ electronic configuration, we show in the next section that the magnetism of **1** is strictly incompatible with a $^3E_g$ ground state (see subsection VII.B).

Absolute parameters calculated with DFT may suffer from large deviations from the experiment. By contrast, the comparison of these parameters between chemically similar systems is an approach likely to be more insightful, because of the large error compensation afforded by their chemical similarity. Following this approach, we observe that the quadrupole splitting dependence on the non-relativistic ground state found above is consistent with an earlier hypothesis by Scheidt and coworkers.[160] In their study, the authors claim that the quadrupole splitting variability in the iron(II)-porphyrin family is a marker of the non-relativistic ground state variability. In details, $^3A_{2g}$ ground states exhibit quadrupole splitting values of around +1.5, while $^3E_g$ ground states exhibit quadrupole splitting parameters superior to 2. For instance, ruffled core-conformation has a quadrupole splitting of $\Delta E_Q = +1.51\ mm/s$, while **1** in a saddle core-conformation has a quadrupole splitting of $\Delta E_Q = +2.21\ mm/s$. The authors attribute this large difference to a difference in the electronic ground state, i.e. $^3A_{2g}$ for the former and $^3E_g$ for the latter. The experimental quadrupole splitting shift ($\Delta\Delta E_Q = +0.70\ mm/s$) is compatible with the presently calculated differences for $^3A_{2g}$ and $^3E_g$ configurations (Table 4). Furthermore, the present investigation suggests that core conformation does not influence significantly the quadrupole splitting values beyond a possible change in the electronic configuration. Taken together, both observations bring credence to Scheidt's hypothesis. As such, this would rather suggest that in the present work, **1** ($\Delta E_Q = +1.31\ mm/s$) possesses a $^3A_{2g}$ ground state.

3) Physical origin of the quadrupole splitting

To investigate the physical origin of the quadrupole splitting and the difference between the $^3A_{2g}$ and $^3E_g$ configuration, the $z$-component of the electric-field gradient tensor is decomposed into three components, as elaborated in the Theory chapter (subsection V.B). The

1-center, two-center "bond", two-center "point-charge" and three-center contributions for the $^3A_{2g}$ and $^3E_g$ electronic configuration are summarized in Table 5 for the ruffled porphyrin conformation. For a deeper understanding, the one-center contribution is further decomposed into core orbitals, valence orbitals and primarily ligand-based orbitals. Note that only one core conformation is considered here because it was already shown that the core conformation is irrelevant to the calculated zero-field Mössbauer parameters for a given non-relativistic ground state (Table 4).

**Table 5**: Breakdown of the contribution to the total $V_{zz}$ (a.u.$^{-3}$) into 1-center, 2-center "bond", 2-center "point-charge" and 3-center, for the $^3A_{2g}$ and $^3E_g$ state of the ruffled core conformation.

| **Electronic ground state** | 1-center (core/ d-orbitals/ ligands) | 2-center "bond" | 2-center "point-charge" | 3-center | Total |
|---|---|---|---|---|---|
| $^3A_{2g}$ | -1.03 (-0.06/ -3.55/ +2.58) | 1.40 | 0.00 | -0.01 | +0.36 |
| $^3E_g$ | -0.07 (-0.03/ -2.62/+2.58 | 0.82 | +0.01 | -0.01 | +0.75 |

In both configurations, the $V_{zz}$ is dominated by the ligand contributions, i.e. (1) the one-center ligand orbitals contributions and (2) the two-center bond contribution, both of which are positive. In fact, the underlying explanation is that the primarily nitrogen-based $\sigma$-orbitals mix significantly with the empty $d_{x2-y2}$ and the $4p_{x,y}$ of iron (Figure 20), both of which have large and positive contributions to the $V_{zz}$. These observations support the hypothesis of a large participation of the porphyrin ligand to the quadrupole splitting, and explain the experimentally-observed positive quadrupole splitting.

As evident from Table 5, the difference between the $^3A_{2g}$ and the $^3E_g$ configuration is mainly explained by the d-orbitals contribution to the one-center component. The d-orbital contribution is much lower for the $^3A_{2g}$ configuration than for the $^3E_g$ configuration, consistently with the promotion of one electron from the $d_{z2}$ orbital (very large, negative contribution to the $V_{ZZ}$) to the $d_{xz}$ (small, negative contribution).[116]

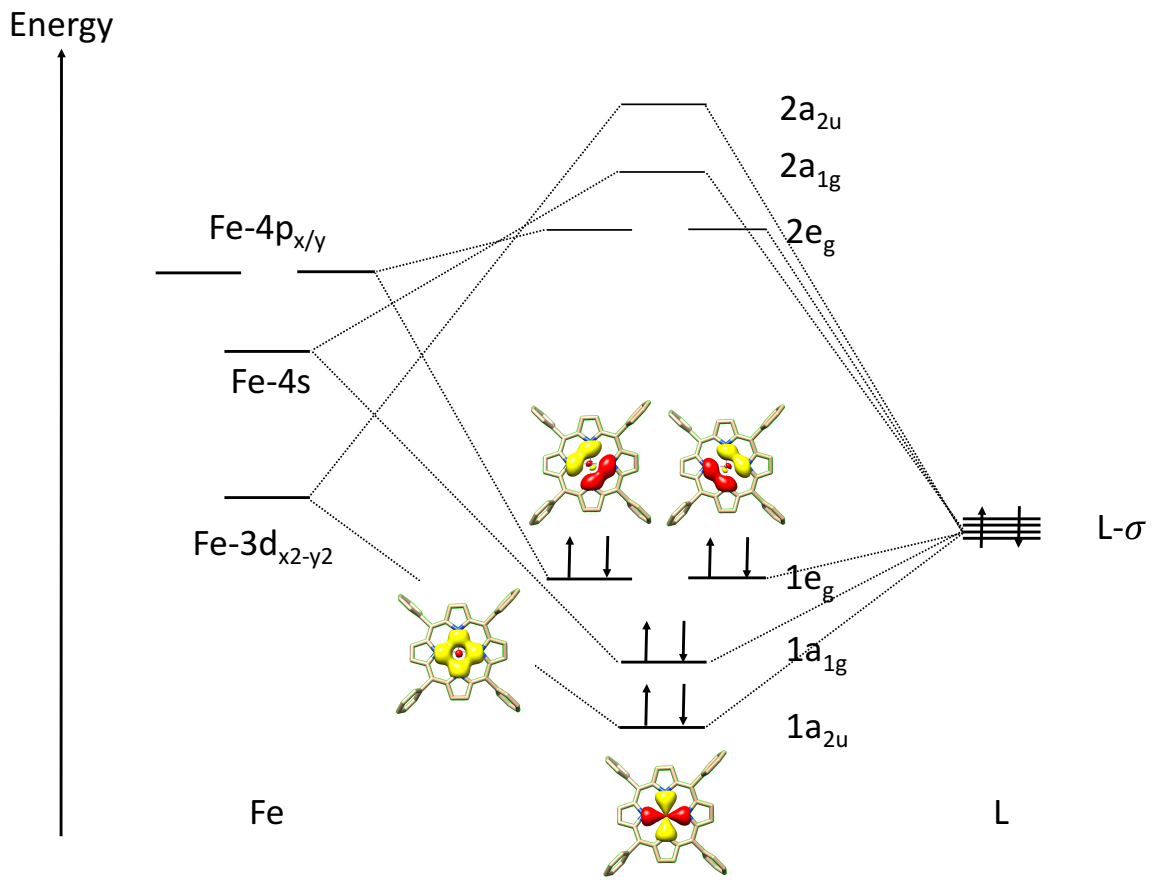


**Figure 20**: orbital diagram of **1** in a ruffled core conformation showing the mixing of the symmetry-adapted, doubly-occupied nitrogen-based orbitals (right-hand side) and unoccupied Fe-based AO (left-hand side) responsible for the large contribution of the ligand orbitals to the quadrupole splitting value. Hydrogens are omitted for clarity. Carbons are represented in beige, nitrogens in blue and iron in orange. Orbitals are represented in red (positive part) and yellow (negative part).

The present DFT investigation is non-conclusive with respect to the nature of the ground state, but provided insights about a number of points. First, these results predict that the quadrupole splitting of **1** is positive, consistently with the experiment, because the *z*-component of the EFG tensor is dominated by the contribution of the porphyrin ligand. The Mössbauer parameters of **1** were found independent of the core-conformation *for a given electronic configuration*. By contrast, we found that the quadrupole splitting is very sensitive to the electronic configuration of the ground state. These results suggest that the quadrupole splitting value may be used a marker of the non-relativistic ground state in the iron(II)-porphyrin family, a notion already investigated by previous authors.[160] If that is the case, the experimental variability of quadrupole splitting values within the four-coordinated iron(II)-porphyrins family

implies that very subtle changes in the ligand field or crystal packing effect are enough to swap the non-relativistic ground state, because the ligand environment is almost identical in all these compounds. Thus, this observation brings yet another argument in favor of the existence of near-degenerate electronic configurations in four-coordinated iron(II)-porphyrins.

The DFT-calculated energies suggest the presence of at least three closely-lying non-relativistic states. However, the energy separation of these states falls within the error range of DFT,[148] which makes the assignment of the ground state non-conclusive. Furthermore, Kohn-Sham DFT is an intrinsic ground state method relying on the variational principle. The description of excited states is neither practical nor well founded theoretically. In the next subsection, we investigate the low-lying non-relativistic states by means of CASSCF/NEVPT2 calculations, a method well-suited for the description of excited states.

## B. CASSCF/NEVPT2 calculations

### 1) Choice of the active space

To investigate the electronic structure of **1** and the effect of different core-conformations, CASSCF(8,11)/NEVPT2 calculations on the ruffled, saddle and planar porphyrin conformations have been carried out in gas-phase. The five valence d-orbitals are included to the active space to account for the d-d excitations. As expected for a square-planar ligand-field, preliminary DFT results show that the $d_{x2-y2}$ orbital is strongly antibonding. Therefore, to account for the covalency effect, the symmetry-adapted bonding counterpart of this orbital was added to the active space. On top of that, a second d-shell was added in order to account for the well-known double shell effect (see Figure 21).[157]

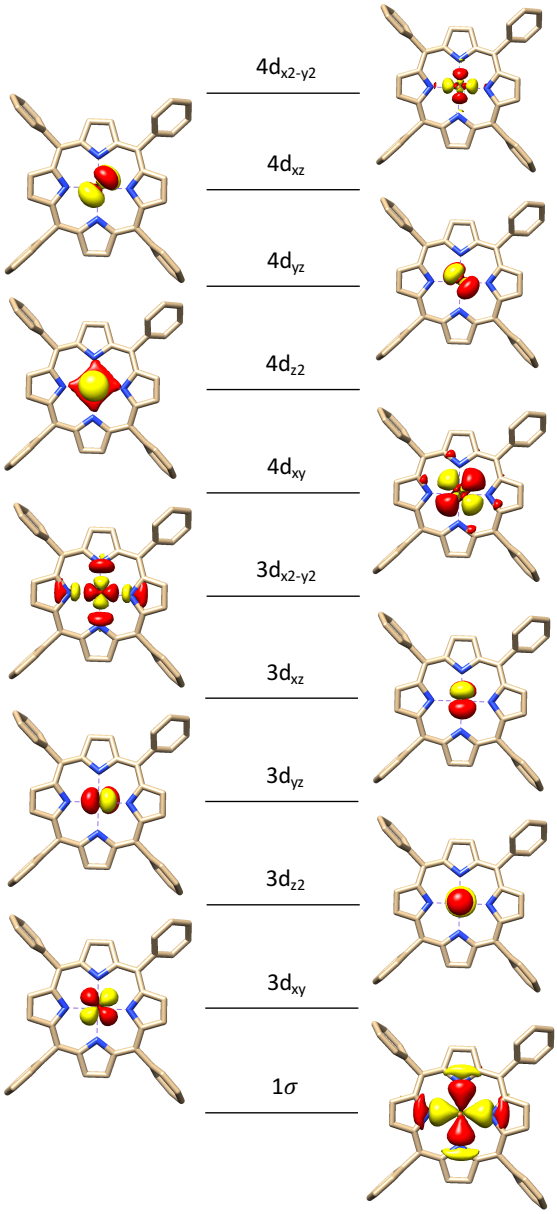


**Figure 21**: Active space CAS(8,11) for **1** (ruffled conformation). The active space is composed of the valence d-shell (3d), the double d-shell (4d), plus the $\sigma$-bonding counterpart of the $3d_{x2-y2}$ orbitals (1σ). The same active space was used for **1** in saddle conformation and [Fe(TTP)] in planar conformation.

2) Energetic considerations

Gratifyingly, irrespective of the core conformations, the calculations delivered the same energetic ordering of the four lowest-lying triplet states (Table 6), consistent with earlier work.[160,168,169,172] Specifically, the lowest-energy state was predicted to be $^3A_{2g}$ having a leading configuration (90%) of $(d_{xy})^2(d_{z2})^2(d_{xz,yz})^2$, and none of the remaining electron configurations

has a weight exceeding 1%. The $^3E_g$ state with two nearly degenerate components was found to lie approximately 1000 $cm^{-1}$ above $^3A_{2g}$. The dominant electron configuration of $^3E_g$ is $(d_{xy})^2(d_{z2})^1(d_{xz,yz})^3$, and both components contain non-negligible contributions (10 – 15%) from the $(d_{xy})^1(d_{z2})^2(d_{xz,yz})^3$ electron configuration. It is worthwhile to note that the core distortion does not discernibly lift the two-fold degeneracy of the $^3E_g$ state (the highest splitting being only 20.0 $cm^{-1}$, Table 6) all in agreement with the axial symmetry postulated above. Finally, a $^3B_{2g}$ state with a leading electron configuration of $(d_{xy})^1(d_{z2})^1(d_{xz,yz})^4$ (90%) was computed to be situated at considerably higher energy (> 4000 $cm^{-1}$). While the quintet state $^5A_{1g}$ having a leading configuration $(d_{z2})^2\,(d_{xy})^1\,(d_{x2-y2})^1\,(d_{xz})^1\,(d_{yz})^1$ (>90%) was predicted to be the ground state by the CASSCF approach, further computations including NEVPT2 corrections swap the lowest-energy state from $^5A_{1g}$ to $^3A_{2g}$.

**Table 6***:* Vertical excitation energy with respect to the $^3A_{2g}$ ground state ($cm^{-1}$), D ($cm^{-1}$) and g (no units) spin Hamiltonian parameters for different core conformations of complex **1** estimated by CASSCF(8,11)/NEVPT2 calculations and effective Hamiltonian theory.

| **Core conformation** | $^3E_g$(xz) | $^3E_g$(yz) | $^3B_{2g}$ | $^5A_{1g}$ | D | $g_{zz}/g_{yy}/g_{xx}$ ($g_{av}$) |
|---|---|---|---|---|---|---|
| Planar | 979 | 997 | 4937 | 172 | 99 | 1.94/3.09/3.10 (2.76) |
| Ruffled | 919 | 919 | 4753 | 783 | 102 | 1.89/3.04/3.04 (2.71) |
| Saddle | 835 | 855 | 4753 | 895 | 102 | 1.88/3.05/3.07 (2.72) |

The small energy difference between $^3A_{2g}$ and $^3E_g$ is unfortunately not decisive and within the uncertainty range of the quantum chemical methods employed. CASSCF calculations typically tend to overestimate excitation energies, and even with the second order perturbative corrections, such as NEVPT2, errors of several thousands of wavenumbers are not uncommon.[158,194] Thus, the non-relativistic ground state of **1** being either $^3A_{2g}$ or $^3E_g$ cannot be unambiguously assigned on the basis of the calculations.

3) Calculation of the magnetic susceptibility and spin Hamiltonian parameters

The magnetic susceptibility is calculated numerically after diagonalization of the total Hamiltonian (including Born-Oppenheimer, SOC and Zeeman effect) in the basis of the states calculated via CASSCF. Those states include three magnetic sublevels for each triplet non-relativistic state, plus five sublevels for the $^5A_{1g}$. The total size of the Hamiltonian thus amounts to a 14x14 matrix. The corresponding calculated effective magnetic moment is shown in Figure

22. Irrespective of core conformation, the agreement with the experimental data is remarkable for ab-initio calculations. In particular, the present calculation accounts for the large room-temperature $\mu_{\text{eff}}$ and the TIP, as well as the large ZFS. The calculation of Mössbauer parameters (via effective Hamiltonian theory, see Theory chapter, subsection VII.B) confirms the large ZFS and average g-value, consistently with the experiment ($D$>80 cm$^{-1}$ and $g_{\text{av}} = 2.7$).

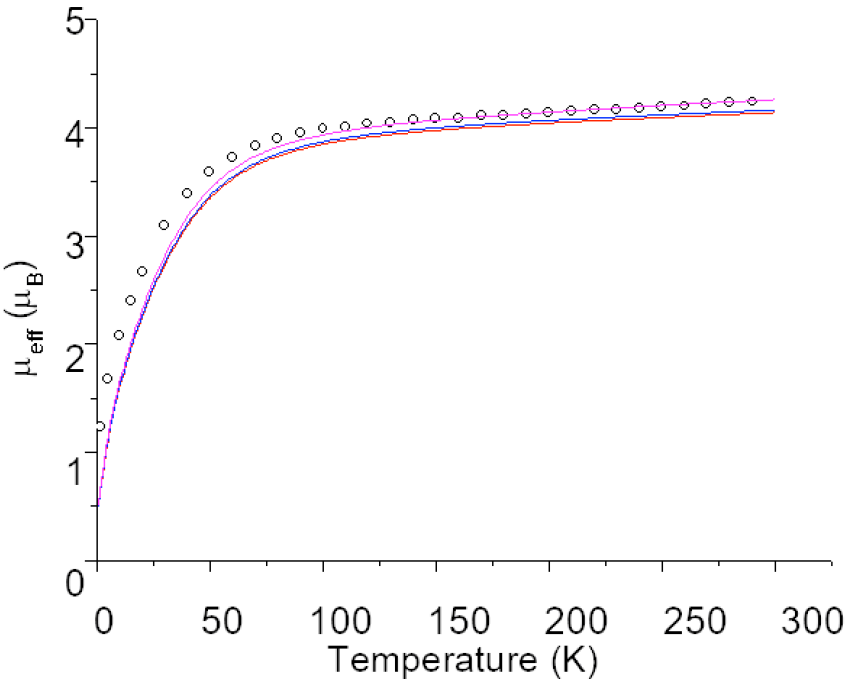


**Figure 22**: Temperature-dependence of the $\mu_{\text{eff}}$ of **1** under 1 Tesla calculated from the CASSCF wavefunctions and NEVPT2 energies for the ruffled (red solid line), saddle (blue solid line) and planar (pink solid line) core conformation, and experimentally measured effective magnetic moment measurements of **1** (dots).

The theoretical results revealed that the $^3A_{2g}$, $^3E_g$ and $^5A_{1g}$ states are energetically well-isolated from other excited states. The energetic proximity of $^3A_g$ and $^3E_g$ further corroborates the notion that the Fe-$d_{xy}$, -$d_{xz}$, -$d_{yz}$ and -$d_{z2}$ orbitals are close in energy for **1**, which features a square planar coordination geometry. More importantly, the magnetic susceptibility calculated by ab-initio calculations shows a remarkable agreement with the experiment and suggests that the SOC-induced coupling of the $^3A_{2g}$, $^3E_g$ and $^5A_{1g}$ states is responsible for the unusual magnetism of **1**. In fact, in the present case SOC is expected to considerably mix these non-relativistic states, because their energy separation is comparable to the effective SOC constant for Fe(II) (~400 cm$^{-1}$)[195].

In order to (1) correlate those results with all the available experimental data and (2) provide a qualitative understanding of the magnetism of **1**, we decided to construct a simplified effective Hamiltonian based on the first-principle study above. This Hamiltonian first treats SOC and Zeeman interactions between the nine magnetic sublevels arising from simplified $^3A_{2g}$ and $^3E_g$ non-relativistic states (see section V). Later, the model is enlarged to include the $^5A_{1g}$ state, but it is shown that the enlargement of the effective Hamiltonian has a marginal effect on the magnetism of **1**. Finally, the electronic Hamiltonian is completed with a nuclear Hamiltonian to treat electric and magnetic hyperfine interactions. Such a treatment therefore allowed us to perform physically justified simulations of all the experimental data beyond the usual spin Hamiltonian formalism.

## V. Simulation of the magnetometric data with an enlarged effective Hamiltonian

### A. Developpement of an effective Hamiltonian beyond the spin Hamiltonian formalism

#### 1) Setting up the effective Hamiltonian

To set up a parametrized effective Hamiltonian for the simulation of the magnetic data of complex **1**, we carried out a ligand-field type analysis, and the dominant electron configurations of the $^3A_{2g}$ and $^3E_g$ states were chosen as the non-relativistic basis. The basis functions were constructed using pure iron d-orbitals. In the present case, the covalency effects can be safely neglected, because the orbitals used to construct the $^3A_{2g}$ and $^3E_g$ states are all essentially non-bonding. By convention, the porphyrin plane was referred to as the *xy* plane, and its normal vector was chosen as the *z* axis. For $M_S = +1$, the basis functions are given by

$$\left|^3A_{2g}, +1\right\rangle = |d_{xy}\overline{d_{xy}}d_{xz}d_{yz}d_{z2}\overline{d_{z2}}| \tag{49}$$

$$|^3E_g(xz), +1\rangle = cos(\theta)\left|^3E_gA(x), +1\right\rangle + sin(\theta)|^3E_gB(x), +1\rangle \tag{49a}$$

$$|^3E_g(yz), +1\rangle = cos(\theta)|^3E_gA(y), +1\rangle + sin(\theta)|^3E_gB(y), +1\rangle \tag{49b}$$

Here, |…| denotes a normalized Slater determinant, orbitals without a vinculum (ex: $d_{xy}$) represent alpha spinorbitals and those with a vinculum (ex: $\overline{d_{xy}}$) correspond to beta spinorbitals.

$\theta$ was introduced to describe the mixing of the two $E_g$ states as suggested by the CASSCF calculations. For these degenerate $E_g$ states, the label *xz* or *yz* indicates whether the function transforms as the quadratic functions *xz* or *yz* in the $D_{4h}$ point group. The label "+1" refers to the $M_s$ of the wave-function.

$$\left|{}^3E_gA(xz),+1\right\rangle = |d_{xy}\overline{d_{xy}}d_{xz}d_{yz}\overline{d_{yz}}d_{z2}| \quad (49c)$$

$$\left|{}^3E_gB(xz),+1\right\rangle = |d_{xy}d_{xz}\overline{d_{xz}}d_{yz}d_{z2}\overline{d_{z2}}| \quad (49d)$$

$$\left|{}^3E_gA(yz),+1\right\rangle = |d_{xy}\overline{d_{xy}}d_{xz}\overline{d_{xz}}d_{yz}d_{z2}| \quad (49e)$$

$$\left|{}^3E_gB(yz),+1\right\rangle = |d_{xy}d_{xz}d_{yz}\overline{d_{yz}}d_{z2}\overline{d_{z2}}| \quad (49f)$$

Similarly, one can write down the basis functions for $M_S = 0$, and –1.

The energy splitting of the ${}^3A_{2g}$ and ${}^3E_g$ states was set as a fitting parameter, $\Delta E$ = E(${}^3E_g$) – E(${}^3A_{2g}$). To avoid the over-parametrization, the splitting of the two ${}^3E_g$ components was neglected, as suggested by the marginal splittings (< 20 $cm^{-1}$) obtained by the CASSCF/NEVPT2 calculations. SOC and Zeeman interactions were considered by using the single-electron Hamiltonians:

$$\widehat{H_{el}} = \widehat{H_{\Delta E}} + \widehat{H_{SOC}} + \widehat{H_{Zee}} \quad (50a)$$

$$\widehat{H_{el}} = \mathrm{E(X)}\delta_{X,X'}\delta_{M_s,M_s'} + \zeta\sum_i \vec{l_i}\cdot\vec{s_i} + \mu_B(g_e\vec{S}+\vec{L})\cdot\overrightarrow{B_{ext}} \quad (50b)$$

Here, *i* runs over the electrons, E(X) corresponds to the energy of the unperturbed states of symmetry representation X ($A_{2g}$, $E_g$(xz) or $E_g$(yz)), the Kronecker deltas $\delta_{X,X'}$ and $\delta_{Ms,Ms'}$ are equal to 1 if the symmetry representation and the $M_S$ of the unperturbed states in the bra and ket are identical. The first term in $\widehat{H_{el}}$ introduces the adjustable energy gap $\Delta$E = $E({}^3E_g)$ – $E({}^3A_{2g})$ between ${}^3A_{2g}$ and ${}^3E_g$ states. The form chosen for the SOC Hamiltonian is described by eq. 12c and the Zeeman effect is described by eq. 9.

$\zeta$, the effective SOC constant of iron, is fixed to be $\zeta = 400$ $cm^{-1}$, a value typically suggested for iron(II) (400-430 $cm^{-1}$),[109] and from earlier work on **1**.[160] The matrix elements for each of these operators were reduced into $\widehat{s_{\iota,\alpha}}$ ($\alpha$=*x*,*y*,*z*) matrix elements in the $|\frac{1}{2},\pm\frac{1}{2}\rangle$ basis and matrix elements of $\widehat{l_{\iota,\alpha}}$in the pure real d-orbital basis using the Slater-Condon rules:

$$\langle\Psi_0|\zeta\ \textstyle\sum_i \vec{l_i}\cdot\vec{s_i}|\Psi_0\rangle = \zeta\sum_i\langle\phi_i|\vec{l}|\phi_i\rangle\cdot\langle\chi_i|\vec{s}|\chi_i\rangle \quad (51a)$$

$$\langle\Psi_0|\textstyle\sum_i \mu_B\left(2\vec{s_i}+\vec{l_i}\right)\cdot\overrightarrow{B_{\mathrm{ext}}}|\Psi_0\rangle = \mu_B\sum_i\left(2\langle\chi_i|\vec{s}|\chi_i\rangle + \langle\phi_i|\vec{l}|\phi_i\rangle\right)\cdot\overrightarrow{B_{\mathrm{ext}}} \quad (51b)$$

$$\left\langle\Psi^{\phi_2\chi_2}_{\phi_1\chi_1}|\zeta\ \textstyle\sum_i \vec{l_i}\cdot\vec{s_i}|\Psi_0\right\rangle = \zeta\langle\phi_2|\vec{l}|\phi_1\rangle\cdot\langle\chi_2|\vec{s}|\chi_1\rangle \quad (51c)$$

$$\left\langle \Psi_{\phi_1\chi_1}^{\phi_2\chi_2} \middle| \sum_i \mu_B \left(2\vec{s_i} + \vec{l_i}\right) \cdot \overrightarrow{B_{\text{ext}}} \middle| \Psi_0 \right\rangle = 2\mu_B \langle\phi_2|\phi_1\rangle\langle\chi_2|\vec{s}|\chi_1\rangle \cdot \overrightarrow{B_{\text{ext}}} + \mu_B \langle\chi_2|\chi_1\rangle\langle\phi_2|\vec{l}|\phi_1\rangle \cdot \overrightarrow{B_{\text{ext}}} \quad (51d)$$

The matrix elements on the right-hand side of eq. 51a-51d are tabulated in the literature.[109] $\Psi_0$ is a given normalized Slater determinant constituted of an antisymmetrized product of spin orbitals $\phi_i\chi_i$ (the $\phi_i$ are the space functions and $\chi_i$ are the spin functions). $\Psi_{\phi_1\chi_1}^{\phi_2\chi_2}$ corresponds to a Slater determinant obtained from $\Psi_0$ by promotion of 1 electron from the spinorbital $\phi_1\chi_1$ to the spinorbital $\phi_2\chi_2$ Note that matrix elements involving Slater determinants which spinorbital population differ by more than one excitation are zero. Finally, the problem amounts to the diagonalization of a 9x9 matrix (Figure 23).

$\widehat{H_{\text{el}}} =$

| $\lvert^3A_{2g},0\rangle$ | $\lvert^3A_{2g},-1\rangle$ | $\lvert^3A_{2g},+1\rangle$ | $\lvert^3E_g,B_1\rangle$ | $\lvert^3E_g,B_2\rangle$ | $\lvert^3E_g,E_-\rangle$ | $\lvert^3E_g,E_+\rangle$ | $\lvert^3E_g,A_1\rangle$ | $\lvert^3E_g,A_2\rangle$ |
|---|---|---|---|---|---|---|---|---|
| 0 | $2\mu_B B_-$ | $2\mu_B B_+$ | | | $\mu_B C B_-$ | $\mu_B C B_+$ | $-\frac{\zeta}{\sqrt{2}}C$ | |
| $2\mu_B B_+$ | $-2\mu_B B_z$ | | $-\frac{\mu_B C B_-}{\sqrt{2}}$ | $\frac{\mu_B C B_-}{\sqrt{2}}$ | $-\frac{\zeta}{2}C$ | | $\frac{\mu_B C B_+}{\sqrt{2}}$ | $-\frac{\mu_B C B_+}{\sqrt{2}}$ |
| $2\mu_B B_-$ | | $+2\mu_B B_z$ | $\frac{\mu_B C B_+}{\sqrt{2}}$ | $\frac{\mu_B C B_+}{\sqrt{2}}$ | | $-\frac{\zeta}{2}C$ | $\frac{\mu_B C B_-}{\sqrt{2}}$ | $\frac{\mu_B C B_+}{\sqrt{2}}$ |
| | $-\frac{\mu_B C B_+}{\sqrt{2}}$ | $\frac{\mu_B C B_-}{\sqrt{2}}$ | $\Delta_{A-E}-\frac{\zeta}{2}A$ | $2\mu_B B_z + A\mu_B B_z$ | $-\sqrt{2}\mu_B B_+$ | $-\sqrt{2}\mu_B B_-$ | | |
| | $\frac{\mu_B C B_+}{\sqrt{2}}$ | $\frac{\mu_B C B_-}{\sqrt{2}}$ | $2\mu_B B_z + A\mu_B B_z$ | $\Delta_{A-E}-\frac{\zeta}{2}A$ | $\sqrt{2}\mu_B B_+$ | $-\sqrt{2}\mu_B B_-$ | | |
| $\mu_B C B_+$ | $-\frac{\zeta}{2}C$ | | $-\sqrt{2}\mu_B B_-$ | $\sqrt{2}\mu_B B_-$ | $\Delta_{A-E} - A\mu_B B_z$ | | $\sqrt{2}\mu_B B_+$ | $\sqrt{2}\mu_B B_+$ |
| $\mu_B C B_-$ | | $-\frac{\zeta}{2}C$ | $-\sqrt{2}\mu_B B_+$ | $-\sqrt{2}\mu_B B_+$ | | $\Delta_{A-E} + A\mu_B B_z$ | $\sqrt{2}\mu_B B_-$ | $-\sqrt{2}\mu_B B_-$ |
| $-\frac{\zeta}{\sqrt{2}}C$ | $\frac{\mu_B C B_-}{\sqrt{2}}$ | $\frac{\mu_B C B_+}{\sqrt{2}}$ | | | $\sqrt{2}\mu_B B_-$ | $\sqrt{2}\mu_B B_+$ | $\Delta_{A-E}+\frac{\zeta}{2}A$ | $2\mu_B B_z - A\mu_B B_z$ |
| | $-\frac{\mu_B C B_-}{\sqrt{2}}$ | $\frac{\mu_B C B_-}{\sqrt{2}}$ | | | $\sqrt{2}\mu_B B_-$ | $-\sqrt{2}\mu_B B_+$ | $2\mu_B B_z - A\mu_B B_z$ | $\Delta_{A-E}+\frac{\zeta}{2}A$ |

**Figure 23**: The $\widehat{H_{el}}$ matrix (Eq. 50a) in the basis of the symmetry-adapted $|^3E_g, \text{Y}\rangle$ states, where $E_g$ is the representation of the parent non-relativistic state and Y is the $D_4$ double-group irreducible representation of the magnetic sublevel (detailed state compositions in terms of the $|^3E_g(\text{x}), \text{M}_S\rangle$ and $|^3E_g(\text{y}), \text{M}_S\rangle$ magnetic sublevels described in eq. 53a-53b and eq. 55a-55e), and $|^3A_{2g}, \text{M}_S\rangle$ magnetic sublevels. $H_\Delta$ terms are displayed in red. $\widehat{H_{SOC}}$ terms are displayed in green. $\widehat{H_{Zee}}$ terms are displayed in brown (spin Zeeman) and blue (orbital Zeeman). For clarity, zero matrix elements are omitted, and the following substitution have been used: $\text{A} = \cos 2\theta$;

$B_{\pm} = \frac{1}{\sqrt{2}}\left(B_x \pm iB_y\right)$; $C = \sqrt{3}\cos\theta - \sin\theta$. $B_x$, $B_y$ and $B_z$ are the three components of the applied magnetic field $B_{ext}$.

2) Simulation of the experimental data

The resulting 9 × 9 matrix of the electronic Hamiltonian ($\widehat{H_{el}}$) was diagonalized, and the magnetic susceptibility was directly computed from the resulting energies, according to the method described in subsection II.B.2. The magnetic susceptibility was fitted by hand to the experimental susceptibility. For simulations of the actual experimental magnetic data, in addition to $\Delta E$, the mixing angle $\theta$ that controls the relative weight of $^3E_g$(A) and $^3E_g$(B) in the $^3E_g$ state was taken as another fitting parameter. A satisfactory global fit to all data yields $\Delta E$ = 950 cm$^{-1}$, and $\theta$ = -0.13$\pi$ (Figure 24).

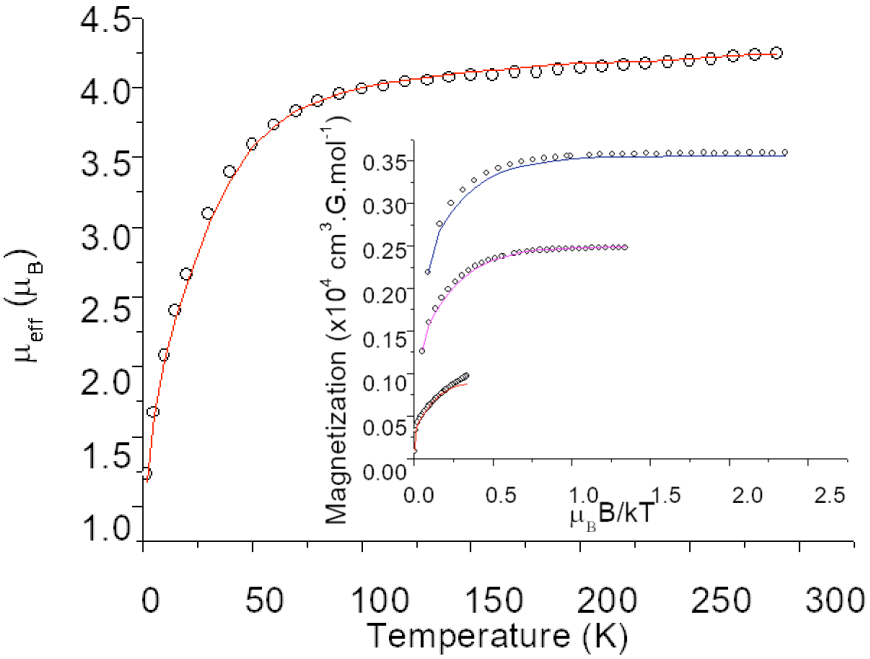


**Figure 24**: Effective magnetic moment under an applied field of 1 T and isofield magnetization curves of **1** under applied fields of 1 (red), 4 (pink) and 7 T (blue) (inset) of **1**. The solid lines represent the best fits obtained by the simulation using the effective Hamiltonian, eq. 50a-50b. The parameters of the Hamiltonian are $\Delta E$ = 950 cm$^{-1}$, and $\theta$ = -0.13$\pi$. The simulation takes into account 7.7% $S$ = 2 [Fe(TPP)(THF)$_2$] impurity.

Our results revealed that the $^3A_{2g}$ state is situated below $^3E_g$ by 950 cm$^{-1}$, and the $^3E_g$(A) configuration makes the leading contribution (90%) to the $^3E_g$ state. This configuration is in

remarkable agreement with the CASSCF/NEVPT2 calculations described in subsection IV.B. Although our assignment of the non-relativistic ground state is the same as that proposed by Mitra and coworkers,[160] our conclusion was grounded on the simultaneous fit of all data derived from magnetic susceptibility and VTVF magnetization measurements, whereas only the former set of data was used in the earlier work.

The simulations with the effective Hamiltonian also nicley reproduce the single-crystal susceptibility data reported by Mitra et. al,[160] which shows large magnetic anisotropy of **1**, defined as the difference in the susceptibility for fields perpendicular ($\chi_{\perp}$) and parallel ($\chi_{\parallel}$) to the defined z-axis (Figure 25). The striking difference between the large $\chi_{\perp}$ and vansihing $\chi_{\parallel}$ values below 50 K nicely demonstrates the easy-plane of magnetization for the low-lying magnetic sublevel of **1** (i.e $M_s = 0$ in the spin Hamiltonian description).

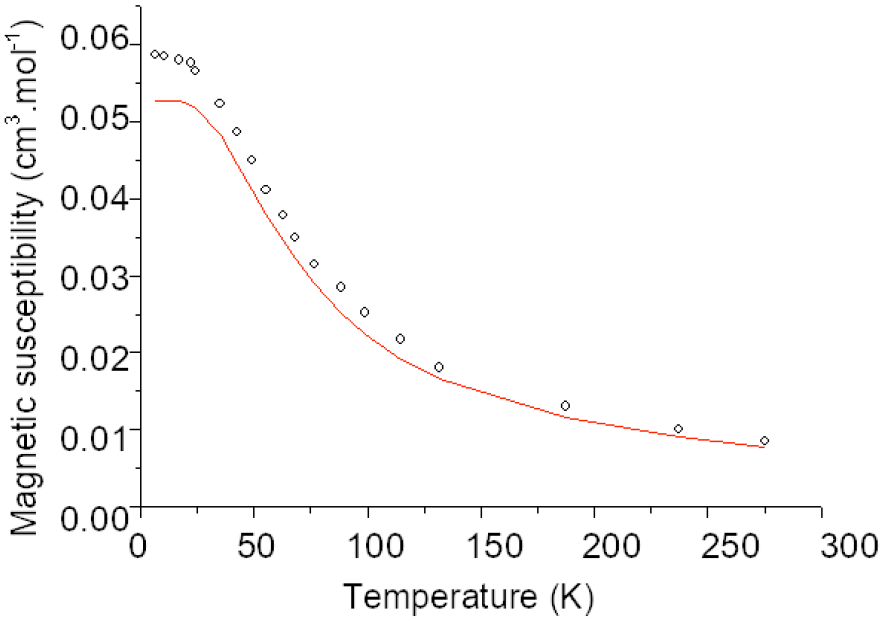


**Figure 25**: magnetic anisotropy of **1**, taken as $\chi_{\perp} - \chi_{\parallel}$, calculated using the effective Hamiltonian with the following parameters: $\Delta E = 950$ cm$^{-1}$, $\theta = -0.13\pi$ (red line), and experimental measurements as taken from ref. 160 (dots). No impurities are considered in the calculation.

To understand the unusual magnetic behavior exhibited by **1**, it is of interest to disentangle the effects of SOC within the low-lying $^3A_{2g}$ and $^3E_g$ non-relativistic states. After SOC, three low-lying magnetic sublevels are separated from other excited states by ca. 1000 cm$^{-1}$. Moreover, the three magnetic sublevels are split into a singlet ($|\phi_0\rangle$) lying below a degenerate

doublet ($|\phi_{\pm}\rangle$) by about 94 $cm^{-1}$ (Figure 26). This situation resembles the $S$ = 1 spin Hamiltonian description given in subsections III.B.3 and III.C.3, with an axial ZFS $D > 90$ $cm^{-1}$, and the rhombicity $E/D$ = 0. However, these three magnetic sublevels are multiconfigurational in nature, because they contain 12-15% of the $^3E_g$ state (see subsection V.B). In the next subsection, it is shown how the peculiar electronic structure of **1** , and in particular the effect of SOC on the non-relativistic ground state, induces its remarkable magnetism.

## B. Connection between the magnetism of the system and its electronic structure

### 1) Effect of the SOC

In contrast to the non-degenerate $^3A_{2g}$ non-relativistic ground state, the two essentially degenerate $^3E_g$ excited non-relativistic states yield magnetic sublevels with an unquenched orbital angular momentum along the $z$ direction due to in-state SOC of $^3E_g$ (first-order SOC). In the following, we first consider in-state SOC of $^3E_g$ and then deal with the out-of-state SOC between $^3A_{2g}$ and $^3E_g$ states (second order SOC and higher).

Diagonalization of the SOC matrix of the six magnetic sublevels of $^3E_g$ yield three non-Kramers doublets, labeled as $|^3E_g, M_S, \pm\rangle$ ($M_S = \pm 1, 0$) which are also eigenfunctions of $L_z$ with eigenvalues:

$$\langle {}^3E_g, M_S, \pm | L_z | {}^3E_g, M_S, \pm \rangle = \pm Cos(2\theta) \tag{52}$$

The state composition of the $|\ E_g, M_S, \pm\rangle$ magnetic sublevels is given by eq. 53a and 53b:

$$|{}^3E_g, M_S, +\rangle = \frac{1}{\sqrt{2}} \left( |{}^3E_g(yz), M_S\rangle - i\, |{}^3E_g(xz), M_S\rangle \right) \tag{53a}$$

$$|{}^3E_g, M_S, -\rangle = \frac{1}{\sqrt{2}} \left( |{}^3E_g(yz), M_S\rangle + i\, |{}^3E_g(xz), M_S\rangle \right) \tag{53b}$$

Although the SOC operator (eq. 12c) does not follow the Russel-Sanders scheme, in the present case, the energies of the three doublets of $^3E_g$ are given by their $S_z$ and $L_z$ eigenvalues:

$$E = \Delta E \mp \frac{\zeta}{2} M_S Cos(2\theta) \ = \Delta E - \frac{\zeta}{2}\, M_S \langle L_z \rangle \tag{54}$$

Note that two of the three doublets are accidentally degenerate according to the irreducible representations of the $D_4$ point group. Specifically, the magnetic sublevels of $^3E_g$ transform as $E + A_1 + A_2 + B_1 + B_2$ in the $D_4$ double group. The higher-lying and lower-lying doublets are

accidentally degenerate and transform as $A_1$ + $A_2$, and $B_1$ + $B_2$, respectively. Only the intermediate doublet actually belong to the double representation E. The symmetry-adapted magnetic sublevels are labeled as $|^3E_g, \mathrm{Y}\rangle$, where Y corresponds to the $D_4$ double-group irreducible representation of the sublevel, and are linear combination of $|\ ^3E_g, M_S, \pm\rangle$:

$$|^3E_g, \mathrm{A}_2\rangle = \frac{1}{\sqrt{2}}\left(|^3E_g, +1, -\rangle + |^3E_g, -1, +\rangle\right) \quad (55a)$$

$$|^3E_g, \mathrm{A}_1\rangle = \frac{1}{\sqrt{2}}\left(|^3E_g, +1, -\rangle - |^3E_g, -1, +\rangle\right) \quad (55b)$$

$$|^3E_g, \mathrm{E}_\pm\rangle = \mp|^3E_g, 0, \pm\rangle \quad (55c)$$

$$|^3E_g, \mathrm{B}_2\rangle = \frac{1}{\sqrt{2}}\left(|^3E_g, +1, +\rangle + |^3E_g, -1, -\rangle\right) \quad (55d)$$

$$|^3E_g, \mathrm{B}_1\rangle = \frac{1}{\sqrt{2}}\left(|^3E_g, +1, +\rangle - |^3E_g, -1, -\rangle\right) \quad (55e)$$

The three magnetic sublevels of $^3A_{2g}$, which transform as E + $A_1$ in the $D_4$ double group, remain degenerate in the in-state (first order) SOC treatment. The degeneracy will be lifted by higher order SOC, for which the sublevels of the $^3E_g$ and $^3A_{2g}$ states that transform as the same irreducible representation can interact with each other. Such interactions, in fact, gives rise to the ZFS of the $^3A_{2g}$ non-relativistic ground state.

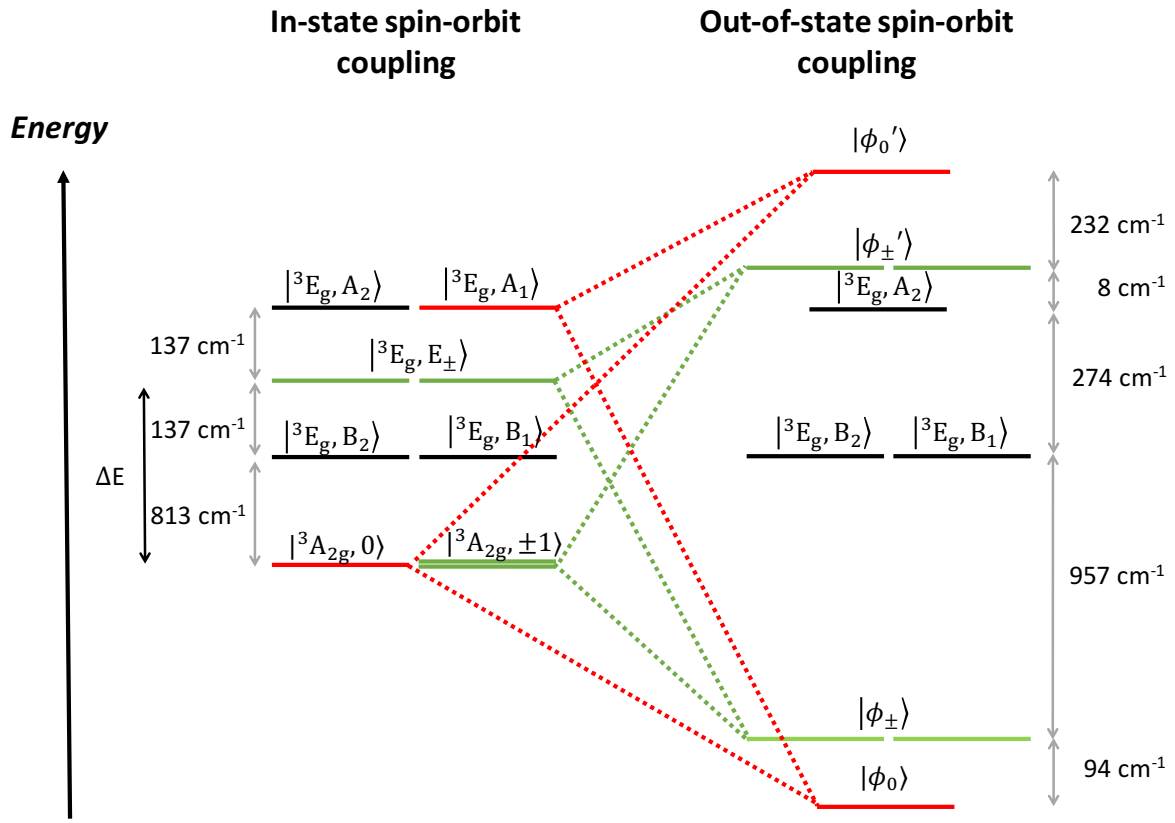


**Figure 26***:* Final energy splitting deduced by the simulation with the effective Hamiltonian in the absence of any applied field that describes the in-state and out-of-state SOC of the nine magnetic sublevels . On the left side, the symmetry-adapted magnetic sublevels arising from first-order SOC are named $|X, \mathrm{Y}\rangle$, where $X$ is the $D_{4h}$ point-group irreducible representation of the non-relativistic state and Y is the $D_4$ double-group irreducible representation of the magnetic sublevel. The dotted lines represent state coupling through the out-of-state SOC (green lines couple E sublevels, and red lines couple $A_1$ sublevels). On the right side, the sublevels $|\phi_0\rangle$, $|\phi_+\rangle$, $|\phi_-\rangle$, $|\phi_+'\rangle$, $|\phi_-'\rangle$, $|\phi_0'\rangle$ represent the magnetic sublevels resulting from out-of-state SOC.

2) Understanding the large ZFS

Hereafter, we employed the second-order perturbation theory to estimate the ZFS of the three low lying magnetic sublevels. Clearly, due to the energetic close proximity of the $A_{2g}$ and $E_g$ non-relativistic states, the second-order perturbation approximation is not sufficient to give a quantitative treatment of the SOC; however, it can provide insights into the origin of the ZFS. The energy lowering of each magnetic sublevel of $^3A_{2g}$ due to the out-of-state SOC is:

$$E^{(2)}(|^3A_{2g}, 0\rangle) = \frac{|\langle {}^3A_{2g},0|\widehat{H_{soc}}|{}^3E_g,A_1\rangle|^2}{\Delta E + \frac{\zeta}{2} Cos(2\theta)} \quad (56a)$$

$$E^{(2)}(|^3A_{2g},\pm1\rangle) = \frac{|\langle^3A_{2g},\pm1|\widehat{H_{soc}}|^3E_g,E_\pm\rangle|^2}{\Delta E} \quad (56b)$$

Therefore,

$$\Delta = E^{(2)}(|^3A_{2g},\pm1\rangle) - E^{(2)}(|^3A_{2g},0\rangle). \quad (56c)$$

Note that $\Delta$ is the equivalent of $D$ in the spin Hamiltonian language, i.e. the splitting between the ground singlet and upper doublet. In the present case, the coupling element $|\langle^3A_{2g},0|H_{soc}|^3E_g,A_1\rangle|^2 = 1.97\,\zeta^2$ was found to be twice as large as $|\langle^3A_{2g},\pm1|H_{soc}|^3E_g,E_\pm\rangle|^2 = 0.99\,\zeta^2$ and $|\Delta E| >> \zeta/2$. In detail, $E^{(2)}(|^3A_{2g},0\rangle)$ = –291 cm$^{-1}$, $E^{(2)}(|^3A_{2g},\pm1\rangle)$ = –167 cm$^{-1}$, and $\Delta$= 124 cm$^{-1}$. Thus, this analysis showed that the strong out-of-state SOC between $A_{2g}$ and $E_g$ is the origin of the large ZFS observed for complex **1**.

3) Relationship betweeen the magnetism of **1** and the multi-configurational nature of its ground state

Our analysis above showed that complex **1** features strong easy-plane of magnetization at low temperatures. While this result is not surprising for a system with a large axial ZFS parameter and a low rhombicity, the large room-temperature $\mu_{eff}$ hints at the possibility that other factors are at play. Effectively, calculation of the spin and orbital angular momentum expectation values in the magnetic sublevels $|\phi_0\rangle$ and $|\phi_\pm\rangle$ shows that along the quantization axis z, the $|\phi_\pm\rangle$ sublevels have large first-order spin angular momenta and residual first-order orbital angular momenta (Table 7). The ground magnetic sublevel $|\phi_0\rangle$ has no first-order angular momentum along the quantization axis as is always the case for non-degenerate magnetic sublevels. However, upon application of an applied field on the *xy* plane, the magnetic sublevels $|\widetilde{\phi_0}\rangle$,$|\widetilde{\phi_\pm}\rangle$ (the eigenstates of the total Hamiltonian for an applied field along the *xy* plane) acquire field-induced orbital and spin angular momenta. Those angular momenta have similar amplitudes (Table 7). They are both lying antiparallel to the direction of the field on the *xy* plane, and their norms are independent on the azimuthal direction of the applied field, giving rise to an easy-plane of magnetization as observed experimentally.

**Table 7**: Expectation values for spin and orbital angular momenta and total magnetic moments $\langle\mu_\alpha\rangle = -\langle L_\alpha\rangle + 2\langle S_\alpha\rangle$ ($\mu_B$) for the three lowest-lying magnetic sublevels of **1** obtained from diagonalization of the Hamiltonian $\widehat{H_{el}}$ (eq. 50a-50b), under an applied field of 7 T along the

z-direction ($|\phi_0\rangle$,$|\phi_\pm\rangle$) and the x-direction ($|\widetilde{\phi_0}\rangle$,$|\widetilde{\phi_\pm}\rangle$). The parameters of $\widehat{H_{el}}$ are $\Delta E$ = 950 cm$^{-1}$, $\theta = -0.13\pi$.

| State | $\langle S_x \rangle$ | $\langle L_x \rangle$ | $\langle \mu_x \rangle$ | State | $\langle S_z \rangle$ | $\langle L_z \rangle$ | $\langle \mu_z \rangle$ |
|---|---|---|---|---|---|---|---|
| $\|\widetilde{\phi_0}\rangle$ | -0.20 | -0.25 | 0.65 | $\|\phi_0\rangle$ | 0 | 0 | 0 |
| $\|\widetilde{\phi_-}\rangle$ | 0 | -0.03 | 0.03 | $\|\phi_-\rangle$ | -0.885 | -0.08 | 1.85 |
| $\|\widetilde{\phi_+}\rangle$ | 0.20 | 0.22 | -0.62 | $\|\phi_+\rangle$ | 0.885 | 0.08 | -1.85 |

The existence of a first-order orbital angular momentum in $|\phi_\pm\rangle$ and of a field-induced orbital angular momentum in $|\widetilde{\phi_0}\rangle$, $|\widetilde{\phi_\pm}\rangle$ (Table 7) is a direct consequence of the multireference character of these magnetic sublevels. Obviously, the multireference character of the sublevels is the direct consequence of SOC induced mixing of the $^3A_{2g}$ and $^3E_g$ non-relativistic states. The magnetic sublevels can in fact be written as:

$$|\phi_0\rangle = 0.92|^3A_{2g}, 0\rangle + 0.39\ |^3E_g, A_1\rangle \quad (57a)$$

$$|\phi_\pm\rangle = 0.94|^3A_{2g}, \pm\rangle + 0.34\ |^3E_g, E_\pm\rangle \quad (57b)$$

Since the symmetry adapted $^3E_g$ states are linear combination of the states $|^3E_g, M_S, \pm\rangle$, eq. 57a and 57b become:

$$|\phi_0\rangle = 0.92\ |^3A_{2g}, 0\rangle + 0.27\ [\ |^3E_g, +1, -\rangle|-|^3E_g, -1, +\rangle\ ] \quad (57c)$$

$$|\phi_\pm\rangle = 0.94|^3A_{2g}, \pm1\rangle \mp 0.34\ |^3E_g, 0, \pm\rangle \quad (57d)$$

Three distinct electronic configurations enter in the composition of this magnetic triplet, i.e. $|^3A_{2g}, M_S\rangle$ and $|^3E_g, M_S, \pm\rangle$. The first-order orbital angular momentum in $|\phi_\pm\rangle$ is directly related to the first-order orbital angular momentum of $|^3E_g, 0, \pm\rangle$ that enters in its composition (see eq. 52). The field-induced orbital angular momentum along the *xy* plane appears due to the *x*- and *y*- components of the orbital Zeeman coupling between $|\phi_0\rangle$ and $|\phi_\pm\rangle$. These couplings are non-zero because of the elements $\langle ^3A_{2g}, 0|\hat{L}_{x,y}|^3E_g, 0, \mp\rangle$ and $\langle ^3E_g, \pm1, \mp1\ |\hat{L}_{x,y}|^3A_{2g}, \pm\rangle$ (see Figure 23). They are both sizeable due to the large configuration mixing within the magnetic sublevels $|\phi_0\rangle$ and $|\phi_\pm\rangle$.

The large easy-plane of magnetization observed in **1** is characteristic of the peculiar almost *three-fold* degeneracy of the $^3A_{2g}$ and $^3E_g$ non-relativistic states. As emphasized above, the low-lying triplet consists of a low-lying singlet $|\phi_0\rangle$ below a degenerate doublet $|\phi_\pm\rangle$ (*E/D=0* in the spin Hamiltonian language). Furthermore, the relative weight of $^3E_g$(xz), $^3E_g$(yz)

and $^3A_{2g}$ configuration within the $|\phi_0\rangle$ and $|\phi_\pm\rangle$ triplet is such that the coupling elements $\langle\phi_0|\hat{L}_x|\phi_\pm\rangle$ and $\langle\phi_0|\widehat{S_x}|\phi_\pm\rangle$ are identical to the coupling elements $\langle\phi_0|\hat{L}_y|\phi_\pm\rangle$ and $\langle\phi_0|\hat{S}_y|\phi_\pm\rangle$ (to a phase factor). Taken together, all these features ensure that the eigenvalues of $H_{el}$ are independent of the azimuthal direction of the applied field. In other words, both spin and orbital angular momenta align equivalently to any field direction on the *xy* plane. Importantly, all these features (the positive axial ZFS with $E/D$=0 and the peculiar relative weight of $^3E_g$(xz), $^3E_g$(yz) and $^3A_{2g}$ in the magnetic triplet) originate from the almost *three-fold* near-degenerate non-relativistic states of **1** consisting of a $^3A_{2g}$ ground state below a symmetry-enforced degenerate $^3E_g$ state. Were the ground state simply described as $^3A_{2g}$, one would not observe the large ZFS or any significant orbital angular momentum. Were the ground state the *two-fold* degenerate $^3E_g$, then after SOC the lowest-lying magnetic states would be the $|^3E_g, \pm1, \pm\rangle$ non-Kramer doublet as defined in eq. 53a and 53b, which has a significant first-order spin and orbital momenta along the z-direction. In this case, the system would therefore admit an easy-axis of magnetization rather than an easy-plane.[196] If the ground state was $^3A_{2g}$ closely-lying to two *non-degenerate* $^3E_g$(xz) and $^3E_g$(yz) components, the SOC interactions would be such as the $|\phi_\pm\rangle$ doublet would split and the relative weight of the$^3E_g$(xz), $^3E_g$(yz) and $^3A_{2g}$ configurations within the triplet would change. Ultimately, this would lead to a preferential alignment of the spin and orbital angular momenta along either the *x* or *y* axis (Figure 27). Instead, the presently observed easy-plane of magnetization with an important participation of the orbital angular momentum indicates a *three-fold* near-degenerate non-relativistic states consisting of a $^3A_{2g}$ non-degenerate state below a degenerate $^3E_g$ excited state.

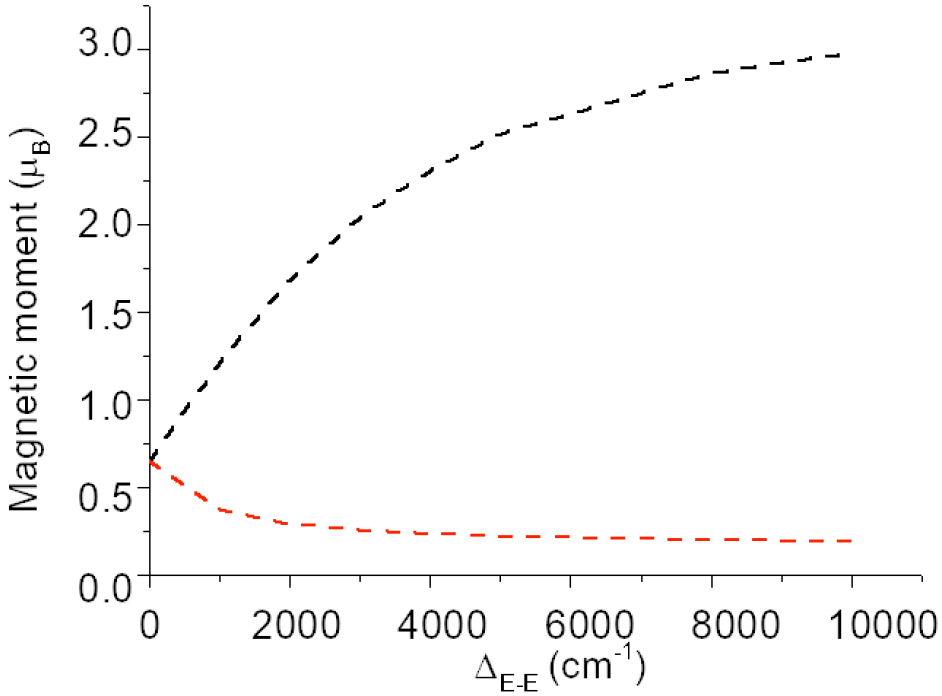


**Figure 27**: Magnetic moment of the ground sublevel along the x (black) or y direction (red) under a field of 7 T aligned along the corresponding direction, for different values of $\Delta_{E-E} = E\left({}^3E_g(yz)\right) - E\left({}^3E_g(xz)\right)$. The value $\Delta E$ is chosen so that the state $^3$E$_g$(yz) is always separated from the $^3$A$_{2g}$ by a constant value, i.e. 950 cm$^{-1}$. $\Delta_{E-E} = 0$ case corresponds to the present situation with a *three-fold* degeneracy limit, where the magnetic moment aligns along any direction of the plane; while large values of $\Delta_{E-E}$ correspond to situation closer to a *two-fold* degeneracy limit, where the magnetic moment aligns preferentially along one direction.

4) Spin Hamiltonian parameters

The field-induced orbital angular momentum along the *xy* plane is the main responsible for the large room-temperature $\mu_{\text{eff}}$ (4.3 $\mu_B$) compared to a pure spin triplet (2.8 $\mu_B$). The origin of the room-temperature $\mu_{\text{eff}}$ is most easily rationalized in a spin Hamiltonian formalism, where the expression of $\mu_{\text{eff}}$ is a simple function of the principal *g*-values (eq. 20). Furthermore, unlike the present model, the spin Hamiltonian formalism is a "common language" spoken by most spectroscopists. In that regard, we believe that the establishment of this system's spectroscopic signature will be easier if said magnetism can be reduced to a set of spin Hamiltonian parameters. Gratifyingly, it is possible to calculate the spin Hamiltonian parameters best reproducing the magnetism of the present model. The method, based on a previous work from Chibotaru and coworkers,[112] is detailed in the annex of this chapter. However, as convenient as

this approach may be, one must not forget that the spin Hamiltonian model does not capture *all* physical effects related to the near-degeneracy of the three non-relativistic states $^3A_{2g}$ and $^3E_g$. The subsection VII.A of this chapter is dedicated to the shortcomings of the spin Hamiltonian in the present case.

The principal *g*-values extracted from the present model are $g_{xx} = g_{yy} = g_\perp = 3.05$ and $g_{zz} = g_\parallel = 1.85$, consistently with our previous spin Hamiltonian simulations. Further decomposition of these g-values into a spin ($g_{\parallel,S}$ and $g_{\perp,S}$) and orbital ($g_{\parallel,L}$ and $g_{\perp,L}$) contribution reveals that the orbital angular momentum has a non-negligible contribution in the $g_\parallel$ value ($g_{\parallel,S} = 1.77$, $g_{\parallel,L} = 0.08$), and a gigantic contribution in the $g_\perp$ values ($g_{\perp,S} = 1.91$, $g_{\perp,L} = 1.14$).

The z-component of the g-matrix is slightly inferior to 2, because the $|^3E_g, 0, \pm\rangle$ configuration in the $|\phi_\pm\rangle$ doublet only participates to the first-order orbital angular momentum, but not to the spin angular momentum. Since the former has a smaller g-value (1.0) than the latter (2.0), the mixing of the $|^3E_g, 0, \pm\rangle$ and $|^3A_{2g}, \pm1\rangle$ within $|\phi_0\rangle$ reduces the overall $g_{zz}$ value compared to a pure $|^3A_{2g}, \pm1\rangle$ contribution. On the other hand, the *x*- and *y*- components of the *g*-matrix are considerably higher than the isotropic *g*-values, consequence of the considerable orbital Zeeman couplings between the $|\phi_0\rangle$ and $|\phi_\pm\rangle$ (*vide supra*). Of note, the $g_{xx}$ and $g_{yy}$ principal values are identical, a notion in line with the easy-plane of magnetization of **1** investigated in the previous subsection. The average *g*-value calculated from these three principal values reaches 2.7, which is similar to the phenomenological fit of subsection III.B.3 and explains the large room temperature $\mu_{eff}$ (except the non-Curie behavior, see subsection VII.A).

Hence, the *g*-anisotropy and the unusually large $\mu_{eff}$ value for **1** are the direct consequence of the considerable mixing between the $^3E_g$ and $^3A_{2g}$ states via SOC. They constitute the experimental proof of the multiconfigurational nature for the ground state of **1**. The two gigantic and identical *g*-values $g_{xx}$ and $g_{yy}$ constitute the spectroscopic signature of this system. It is characteristic of a *three-fold near-degeneracy*, where a non-degenerate non-relativistic ground state mixes considerably with two degenerate excited states via SOC.

5) Inclusion of the quintet state $^5A_{1g}$

*Ab*-initio calculations predict the $^5A_{1g}$ state very close to the ground state. Experimental observations rule out the possibility that it might be the ground non-relativistic state,[160,164,167]

but the possibility that it has a sizeable effect on the magnetism of **1** cannot be neglected. Furthermore, mixed intermediate- and high-spin states have been observed before for Fe(III) porphyrin systems.[111] To examine the effect of the $^5A_{1g}$ state, we have enlarged the model space to include it into the effective Hamiltonian.

The effect of including the $^5A_{1g}$ state as low as 800 cm$^{-1}$ above the non-relativistic ground state in the model is marginal (Figure 28). In detail, it slightly reduces the magnetic susceptibility at low temperature, while having little to no effect on the room-temperature $\mu_{\mathrm{eff}}$.

The low-temperature changes may all be explained by the increase of ZFS axial parameter (114 cm$^{-1}$) compared to the value found without including the $^5A_{1g}$ state (94 cm$^{-1}$). The increase of the ZFS axial parameter reduces the Zeeman interaction between ground and excited magnetic sublevels, hereby reducing the magnetic moment of the ground state along the *xy* plane. Since the ground magnetic sublevel is the only significantly populated sublevel at low temperature, this effect entirely explains the decrease of low-temperature magnetic susceptibility upon inclusion of the $^5A_{1g}$ state into the model.

On the other hand, the high-temperature susceptibility is only marginally affected by the inclusion of the $^5A_{1g}$ state because the average g-value remains almost identical. We indeed found that the corresponding average *g*-value is 2.72, only 0.01 higher than the average value calculated without including the quintet state. The transverese *g*-value is 3.06, which is almost identical to the value found without inclusion of the $^5A_{1g}$ state (3.05). In details, however, the $g_{L,\perp}$ decreases significantly compared to the value calculated without including the $^5A_{1g}$, but this downshift is compensated by a similar upshift of $g_{S,\perp}$. Similarly, the parallel g-value is almost unaffected by the inclusion of the quintet state (1.87 and 1.85 with and without inclusion of $^5A_{1g}$, respectively). However, this overall similarity hides a slight upshift of $g_{S,\parallel}$ compensated by a slight downshift of $g_{L,\parallel}$ (see Table 8) upon inclusion of the quintet state.

**Table 8**: Effect of the inclusion of the quintet state $^5A_{1g}$ on the g-values of **1**. $g_L$ and $g_S$ correspond to the orbital and spin components of the g-values. $g_{av}$ refers to the average g-value.

| $^5A_{1g}$ state? | $g_\perp$ ($g_{L,\perp}$/ $g_{S,\perp}$) | $g_\parallel$ ($g_{L,\parallel}$/ $g_{S,\parallel}$) | $g_{av}$ |
|---|---|---|---|
| Not included | 3.05 (1.14/1.91) | 1.85 (0.08/1.77) | 2.71 |
| Included | 3.06 (0.95/2.11) | 1.87 (0.06/1.81) | 2.72 |

In general, including the quintet state increases the $g_S$ values and decreases the $g_L$ values. The former phenomenon is readily explained by the mixing of S=2 character into the S=1

magnetic triplet. The latter phenomenon is more indirect. The mixing of the quintet state into the magnetic triplet decreases the $^3A_{2g}$ and $^3E_g$ components, both of which are responsible for the large orbital angular momentum in this system. By opposition, there is no first-order orbital angular momentum in $^5A_{1g}$. Likewise, there is no orbital Zeeman coupling element between the $^5A_{1g}$ and $^3E_g$ or $^3A_{2g}$ states susceptible to induce additional orbital angular momentum under an applied field. Hence the mixing of the $^5A_{1g}$ state into the ground triplet may only decrease its total orbital angular momentum.

These findings show that the inclusion of the quintet state $^5A_{1g}$ have little to no effect on the overall magnetism of the system. They also show that the inclusion of the $^5A_{1g}$ state cannot be responsible for the large orbital angular momentum of **1**, which is an experimentally observed key feature of this system (see section VI). Hence, we do not consider it further.

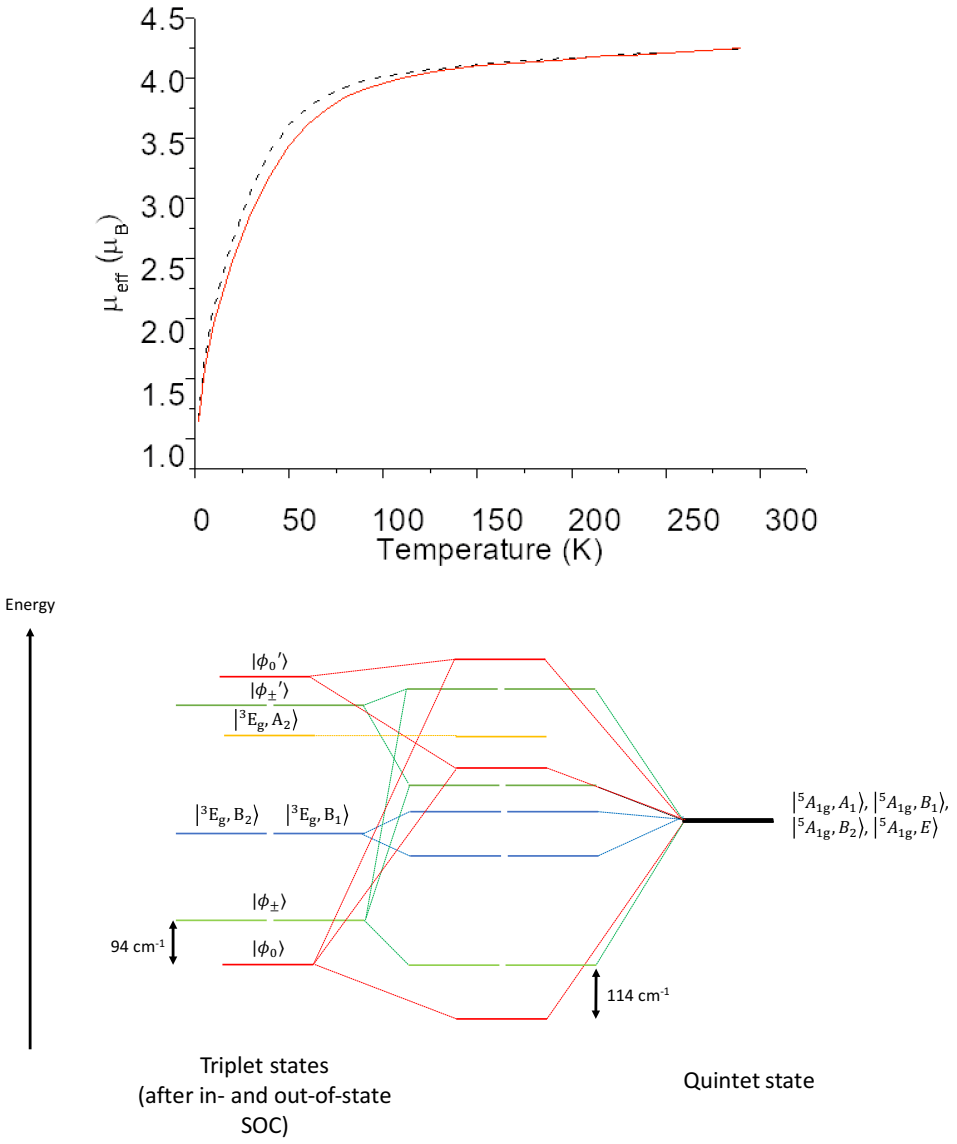

**Figure 28***:* (Top) effect of the inclusion in the effective Hamiltonian of the $^5A_{1g}$ state 800 cm$^{-1}$ above the $^3A_{2g}$ state on the temperature-dependent $\mu_{eff}$ of **1**. The red line and the black dashed line correspond to the effective magnetic moment of **1** with and without the $^5A_{1g}$ state included in the model, respectively. (Bottom) energy diagram showing the magnetic sublevels resulting from the SOC between the magnetic sublevels arising from the non-relativistic states $^3A_{2g}$ and $^3E_g$ states after in- and out-of-state SOC (left-hand side) and the symmetry-adapted magnetic states arising from the $^5A_{1g}$ non-relativistic state (right-hand side). The color code represents the representation of the coupling sublevels in the $D_4$ point group. E sublevels are shown in green, $B_1$ and $B_2$ sublevels are shown in blue, and the $A_1$ sublevels are shown in red. The $A_2$ sublevel is shown in orange.

## VI. Consistent simulation of the Mössbauer spectra using the same effective Hamiltonian

### A. Completing the effective Hamiltonian with a nuclear Hamiltonian and simulating the experimental data

1) Setting up the nuclear Hamiltonian

To simulate the applied-field $^{57}$Fe Mössbauer data of **1** shown in Figure 30, the electronic Hamiltonian ($\widehat{H_{el}}$) of eq. 50a-50b was complemented by the following nuclear-spin and hyperfine Hamiltonian ($\widehat{H_{nu}}$),[119]

$$\widehat{H_{nu}} = \widehat{H_{\mathrm{Q}}} + \widehat{H_{Zee}^{Nuc}} + \widehat{H_{\mathrm{HFC}}} \quad (58)$$

The first term represents the usual quadrupole interaction (eq. 28a), the second the nuclear Zeeman interaction (eq. 29), and the third the magnetic hyperfine interaction. The last one is a sum of three contributions, i.e. the Fermi contact contribution ($\widehat{H_{\mathrm{FC}}}$, eq. 30b), the spin-dipole contribution ($\widehat{H_{\mathrm{SD}}}$, eq. 30c) and the orbital contribution ($\widehat{H_{\mathrm{LI}}}$, eq. 30d).

The following approximations were invoked to compute the magnetic hyperfine interaction, $\widehat{H_{\mathrm{HFC}}}$. First, because in the presence of applied fields larger than a few hundred Gauss, the electronic Zeeman interaction is much stronger than all other interactions involving the nuclear spin, the nuclear and electronic states are largely decoupled. As such, one can replace the

electron spin and orbital angular momenta operators in $\widehat{H_{\mathrm{HFC}}}$ by their expectation values, and diagonalize the electronic and nuclear Hamiltonians separately.

Second, we neglected anisotropic covalency for different d orbitals by replacing the individual $r_i^{-3}$ operators by a unique expectation value $\langle r_d^{-3}\rangle$ for the Fe-$d_{xy}$, -$d_{xz}$, -$d_{yz}$ and -$d_{z2}$ orbitals.[197] Therefore, the nuclear Hamiltonian can be simplified to:

$$\widehat{H_{\mathrm{nu}}} = \widehat{H_{\mathrm{Q}}} - g_{\mathrm{N}}\beta_{\mathrm{N}}\vec{I}\cdot\overrightarrow{B_{\mathrm{eff}}} = \widehat{H_{Q}} - g_N\beta_N\vec{I}\cdot\left(\overrightarrow{B_{\mathrm{int}}} + \overrightarrow{B_{\mathrm{ext}}}\right) \quad (58a)$$

Where the effective field $\overrightarrow{B_{\mathrm{eff}}}$ is the vector sum of the applied ($\overrightarrow{B_{\mathrm{ext}}}$) and internal field ($\overrightarrow{B_{\mathrm{int}}}$). The internal field $\overrightarrow{B_{\mathrm{int}}}$ is given by:

$$\overrightarrow{B_{\mathrm{int}}} = -2\mu_B\langle r_d^{-3}\rangle\langle\vec{L}\rangle - 2\mu_B\langle r_d^{-3}\rangle\left\langle\left[\sum_i \frac{3(\vec{r}_i\cdot\vec{s}_i)\vec{r}_i}{{r_i}^2} - \vec{s}_i\right]\right\rangle - A_{FC}\langle\vec{S}\rangle\,. \quad (58b)$$

The three terms in eq. 58b correspond to the orbital, spin-dipole and Fermi contact contributions to the internal field, $\overrightarrow{B_{int}^{LI}}$, $\overrightarrow{B_{int}^{SD}}$ and $\overrightarrow{B_{int}^{FC}}$, respectively (see Theory chapter, subsection II.B.1). Two parameters, namely $A_{FC}$ and $\langle r_d^{-3}\rangle$, cannot be calculated within the scope of this model because our initial assumptions neglect any spin polarization or expansion/contraction of the d-orbitals. Therefore, they must be either assigned a value or fitted against the experimental data (see subsection VI.A.2).

The first and the third terms of eq. 58b are straightforward to calculate using Slater-Condon rules.

$$\langle\Psi_0|\vec{L}|\Psi_0\rangle = \sum_i\langle\phi_i|\vec{l}|\phi_i\rangle \quad (59a)$$

$$\left\langle\Psi_{\phi_1\chi_1}^{\phi_2\chi_2}|\vec{L}|\Psi_0\right\rangle = \langle\phi_2|\vec{l}|\phi_1\rangle\cdot\langle\chi_2|\chi_1\rangle \quad (59b)$$

$$\langle\Psi_0|\vec{S}|\Psi_0\rangle = \sum_i\langle\chi_i|\vec{s}|\chi_i\rangle \quad (59c)$$

$$\left\langle\Psi_{\phi_1\chi_1}^{\phi_2\chi_2}|\vec{S}|\Psi_0\right\rangle = \langle\phi_2|\phi_1\rangle\cdot\langle\chi_2|\vec{s}|\chi_1\rangle \quad (59d)$$

The matrices elements on the right-hand side are tabulated in the literature. The second term (spin-dipole contribution) may be reorganized into the one-center reduced electric-field gradient tensor operator projected onto the spin:

$$\left\langle\left[\sum_i \frac{3(\vec{r}_i\cdot\vec{s}_i)\vec{r}_i}{{r_i}^2} - \vec{s}_i\right]\right\rangle = \left\langle\sum\bar{\bar{f}}_i\cdot\vec{s}_i\right\rangle \quad (60a)$$

$$\left\langle\Psi_0\left|\sum_i \frac{3(\vec{r}_i\cdot\vec{s}_i)\vec{r}_i}{{r_i}^2} - \vec{s}_i\right|\Psi_0\right\rangle = \sum_i\langle\phi_i|\bar{\bar{f}}|\phi_i\rangle\cdot\langle\chi_i|\vec{s}|\chi_i\rangle \quad (60b)$$

$$\left\langle\Psi_{\phi_1\chi_1}^{\phi_2\chi_2}\left|\sum_i \frac{3(\vec{r}_i\cdot\vec{s}_i)\vec{r}_i}{{r_i}^2} - \vec{s}_i\right|\Psi_0\right\rangle = \langle\phi_2|\bar{\bar{f}}|\phi_1\rangle\cdot\langle\chi_2|\vec{s}|\chi_1\rangle \quad (60c)$$

Where $f_{\alpha\beta} = \frac{3x_\alpha x_\beta}{r^2} - \delta_{\alpha\beta}$. The one-center reduced EFG tensor $\bar{\bar{f}}$ (see Theory chapter, subsection II.B.1) is a pure angular tensor and its matrix elements in the basis of the pure d-orbitals are tabulated in the literature.[109]

Finally, since the experimental spectra showed that the system is in the regime of fast paramagnetic relaxation, the $^{57}$Fe nuclei in the sample do not experience an individual internal field for each populated magnetic sublevel, but a thermally averaged internal field given by,

$$\langle \overrightarrow{B_{\text{int}}} \rangle = \frac{\sum \overrightarrow{B_{\text{int}_i}} e^{-\frac{E_i}{k_B T}}}{\sum e^{-\frac{E_i}{k_B T}}} \tag{61}$$

where the $E_i$ are the energies of the three lowest-energy magnetic sublevels of **1**.
Eventually, the problem amounts to the calculation of the internal field expectation values from the eigenvectors of $\widehat{H_{\text{el}}}$ and diagonalization of a 6x6 nuclear Hamiltonian (Figure 29).

$\widehat{H_{\text{Nu}}} =$

| $\left\|\frac{1}{2},+\frac{1}{2}\right\rangle$ | $\left\|\frac{1}{2},-\frac{1}{2}\right\rangle$ | $\left\|\frac{3}{2},-\frac{3}{2}\right\rangle$ | $\left\|\frac{3}{2},-\frac{1}{2}\right\rangle$ | $\left\|\frac{3}{2},+\frac{1}{2}\right\rangle$ | $\left\|\frac{3}{2},+\frac{3}{2}\right\rangle$ |
|---|---|---|---|---|---|
| $\frac{g_N\beta_N}{2}B_{eff,z}$ | $-\frac{g_N\beta_N B_{eff,-}}{\sqrt{2}}$ | | | | |
| $-\frac{g_N\beta_N B_{eff,+}}{\sqrt{2}}$ | $-\frac{g_N\beta_N}{2}B_{eff,z}$ | | | | |
| | | $-\frac{3g_N^*\beta_N B_{eff,z}}{2} + \frac{eQV_{zz}}{4}$ | $-\sqrt{\frac{3}{2}}g_N^*\beta_N B_{eff,+}$ | | |
| | | $-\sqrt{\frac{3}{2}}g_N^*\beta_N B_{eff,-}$ | $-\frac{g_N^*\beta_N}{2}B_{eff,z} - \frac{eQV_{zz}}{4}$ | $-\sqrt{2}g_N^*\beta_N B_{eff,+}$ | |
| | | | $-\sqrt{2}g_N^*\beta_N B_{eff,-}$ | $\frac{g_N^*\beta_N}{2}B_{eff,z} - \frac{eQV_{zz}}{4}$ | $-\sqrt{\frac{3}{2}}g_N^*\beta_N B_{eff,+}$ |
| | | | | $-\sqrt{\frac{3}{2}}g_N^*\beta_N B_{eff,-}$ | $\frac{3g_N^*\beta_N}{2}B_{eff,z} + \frac{eQV_{zz}}{4}$ |

**Figure 29**: Nuclear Hamiltonian matrix (eq. 58a) in the basis of the nuclear magnetic sublevels of iron $|I, M_I\rangle$. $\widehat{H_{HFC}} + \widehat{H_{Zee}^{Nuc}}$ terms are shown in brown and $\widehat{H_Q}$ terms are shown in green. Of note, $g_N$ and $g_N^*$ represent the $g$-factor of the ground and excited nuclear state, respectively. For clarity, zero matrix elements have been omitted. $B_{eff,\pm} = \frac{1}{\sqrt{2}}\left(B_{eff,x} \pm iB_{eff,y}\right)$.

2) Consistent simulation of all the experimental data

To simulate the Mössbauer data, the expectation values of the electronic operators involved in eq. 58b were directly calculated from diagonalization of $H_{el}$ with the parameters determined in subsection V.A.2 (Figure 24). However, under the approximations of the above effective Hamiltonian, neither $\langle r_d^{-3} \rangle$ nor $A_{FC}$ can be calculated. Instead, the value of $A_{FC}$ was fixed to 21.5 T, according to the empirical rule that the Fermi contact contributions is 22 T/spin or 21 T/spin for most ferric and ferrous complexes.[120,121,122,123,198] The remaining parameter $\langle r_d^{-3} \rangle$ was allowed to vary freely during the fit. As shown in Figure 30, a satisfactory global simulation of all VTVF Mössbauer spectra yielded $\langle r_d^{-3} \rangle = 5.4\ a.u.^{-3}$. This value is similar to that found for the metallic iron (5.5 a.u.$^{-3}$),[109] thereby indicating that the expansion effect of the ligand field counteracts the contraction due to the high oxidation state of iron.

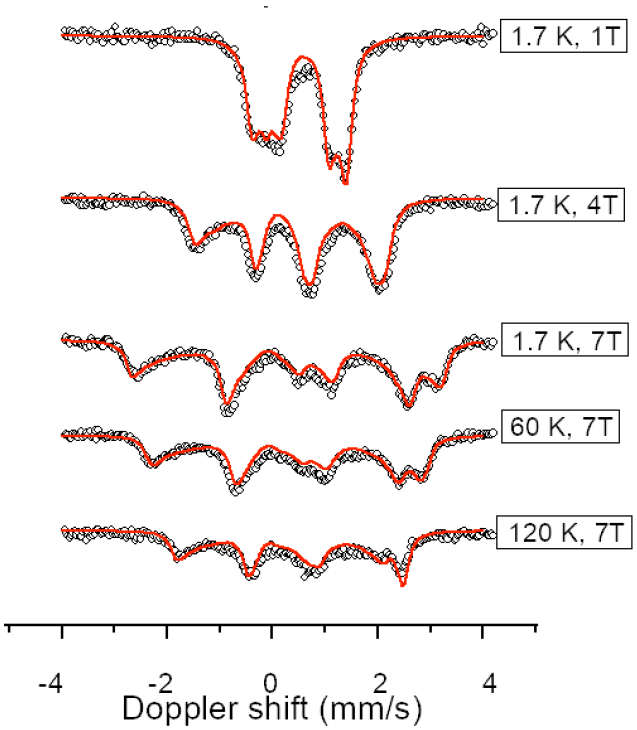


**Figure 30**: Applied field Mössbauer spectra of **1** recoded at different temperatures, from top to bottom: 7 T, 1.7 K; 4 T, 1.7 K; 1 T, 1.7 K; 7 T, 60 K; 7 T, 120 K. The solid lines represent the best fits obtained from the simulation using the effective Hamiltonian, eq. 50a-50b and 58a. The fits were obtained with the following parameters, $\Delta E = 950$ cm$^{-1}$, $\theta = -0.13\pi$ and $\langle r_d^{-3} \rangle$ = 5.4 a.u.$^{-3}$ The dots represent the experimental measurements.

In summary, all experimental data (shown in Figure 24 and Figure 30, respectively) could be fitted very satisfyingly with the same electronic and nuclear Hamiltonian. In comparison with the spin Hamiltonian which is phenomenological and requires the parametrization of six components ($g_\perp$, $g_\parallel$ $D$, $A_\perp$, $A_\parallel$, TIP), our model is physically more transparent and only requires the parametrization of three components, i.e. the unrelativistic energy difference between the $^3E_g$ and $^3A_{2g}$ states $\Delta E$, the relative weight of the $^3E_g$(A) and $^3E_g$(B) configurations described by $\theta$, and $\langle r_d^{-3} \rangle$, which considerably adds to the credence of the conclusion. Furthermore, unlike for the spin Hamiltonian simulations of subsection III.C.3, no misfit of the Mössbauer spectra is observed at high temperature. Note that fitting the applied field Mössbauer spectra also requires two more parameters, namely, the quadrupole splitting and isomer shift, but they can be determined unambiguously from the zero-field Mössbauer spectra. Therefore, they do not undermine the quality of the simulation of the applied field Mössbauer spectra.

## B. Connection between the hyperfine field and the electronic structure of **1**

### 1) Low-temperature hyperfine field

At low temperatures, no internal field is induced under an applied field along the z-direction. On the other hand, under an applied field along the xy plane, a strong, positive internal field (i.e. same direction as that of the applied field) appears on the *xy* plane. The internal field is positive because the orbital field (positive) dominates over the Fermi-contact field (negative). The third contribution, the spin-dipole field, is by far the smallest of the three contribution (Table 9). Finally, the norm of this internal field does not depend on the azimuthal direction of the applied field.

The overall internal field is dominated by the microscopic internal field of the ground magnetic sublevel $|\phi_0\rangle$, which is the only significantly populated level due to the large axial ZFS parameter. The ground sublevel is non-magnetic and has no first-order orbital and/or spin angular momentum along the z-direction, hence it induces no internal field along that axis. However, under an applied field along the *xy* plane, strong field-induced spin and orbital angular momenta appear (see subsection V.B.3). The internal field on the *xy* plane is the direct consequence of these large field-induced angular momenta acquired by the ground sublevel (eq. 58b). Obviously, the overall positive internal field is the direct consequence of the large field-induced orbital angular momentum of **1**, and is therefore a direct experimental proof of the

multiconfigurational character of the ground sublevel. The fact that the internal field norm does not depend on the azimuthal direction of the applied field reflects the easy-plane magnetization of **1**. As developped in the subsection V.B.3, this behavior is due to the remarkable *three-fold* near-degeneracy of the non-relativistic states $^3A_{2g}$ and $^3E_g$.

2) High-temperature hyperfine field

At higher temperature, under an applied field along the *xy* plane the internal field norn decreases. On the other hand, under an applied field along the *z*-direction a small, positive internal field appears along the same direction. Within this small field, the spin-dipole field (positive) is as large as the Fermi-contact field (negative), which is rather uncommon, and the orbital field (positive) is the smallest contribution (Table 9).[116]

The change in the internal field profile can be entirely attributed to the population of the $|\phi_{\pm}\rangle$ doublet. Under an applied field along the *xy* plane, the field-induced spin and orbital angular momenta of the excited doublets are either smaller or opposite in direction to that of the ground sublevel (Table 7), hence the overall internal field is averaged out due to the fast electron relaxation limit (see eq. 61). The z-component of the internal field stems from the first-order spin and orbital angular momenta of the $|\phi_{\pm}\rangle$ doublet. For that component, the Fermi contact field is particularly small due to the mixing of $M_S = \pm 1$ and $M_S = 0$ configurations in the $|\phi_{\pm}\rangle$ doublet. On the other hand, the spin-dipole field is strong and positive, steming from the contributions of the singly-occupied orbitals in the $M_S = \pm 1$ configuration $^3A_{2g}$ ($d_{xz}$, $d_{yz}$). Both those orbitals have positive contributions to the spin-dipole field.[109] Along this direction, the orbital contribution is very small because the sublevels $|\phi_{\pm}\rangle$ only have a very small first-order orbital angular momentum due to the presence of $|^3E_g 0, \pm\rangle$ character. However, taken together, the orbital field and spin-dipole field (positive) are larger than the Fermi-contact field (negative).

**Table 9**: Decomposition of the Fermi contact, spin-dipole and orbital contributions of the internal field of **1**, at a temperature of 1.7 K and 60 K under an applied field of 7 Tesla along x and z, respectively.

| Temperature (K) | Direction of the applied Field | Component of the internal field | Total internal field (T) | Fermi-contact contribution (T) | Spin-dipole contribution (T) | Orbital contribution (T) |
|---|---|---|---|---|---|---|
| 1.7 | x | x | 10.6 | -4.3 | -1.8 | 16.7 |
| | z | z | 0 | 0 | 0 | 0 |
| 60 | x | x | 8.3 | -3.2 | -1.3 | 12.8 |
| | z | z | 0.1 | -0.5 | 0.5 | 0.1 |

3) Spin Hamiltonian parameters

For qualitative interpretation, the spin Hamiltonian *A* matrix values associated with the present model were calculated. The procedure is exactly similar to the one we used to calculate the *g*-values in section V. More details on the calculation procedure are available in the annex. The following spin Hamiltonian parameters were calculated: $\frac{A_{\perp}}{g_N \beta_N} = 47.5\ T$; $\frac{A_{/\!/}}{g_N \beta_N} = 4.6\ T$. Note that the $A_{\perp}$ parameter is somewhat lower than that deduced from the phenomenological fit of subsection III.C.3. The origin of this difference is related to the relative failure of the spin Hamiltonian formalism, and explicated in subsection VII.A. Furthermore, the z-component of the *A* matrix could not be resolved in subsection III.C.3 due to the large positive ZFS, while the present methodology allows us to calculate it from the effective Hamiltonian. The three components of the *A* matrix are positive, although the z-component is extremely weak (Table 10). This situation is very rare for transition metal complexes and is connected to the strong multiconfigurational character of the ground state of **1**. The $A_{\perp}$ is positive because it is dominated by the orbital component; that is a direct observation of the orbital angular momentum of **1** and a strong experimental proof of the multireference character of its ground state. The fact that the x- and y- components of the *A* matrix are identical is in-line with the easy-plane of magnetization in **1** detailed in subsection V.B.3. Taken together, the positive and identical $A_{xx}$ and $A_{yy}$ are characteristic of the *three-fold near-degeneracy* of the non-relativistic states of **1**. In the $A_{\parallel}$ component, the Fermi-contact and spin-dipole cancel each other out, leaving only the positive contribution from the small first-order orbital angular momentum due to the presence of $|^3E_g 0, \pm\rangle$ character in the magnetic sublevels (see subsection V.B.3). Finally,

two out of the ordinary features need to be acknowledged: (1) the Fermi contact matrix is slightly anisotropic, and (2) the trace of the spin-dipole matrix departs slightly from zero (0.6 T). The first feature has been noted before in other systems featuring strong SOC.[199] Both these features originate from the large multiconfigurational character of the magnetic sublevels.

In summary, the two positive and identical $A_{xx}$ and $A_{yy}$, as well as the two gigantic and identical $g_{xx}$ and $g_{yy}$, are characteristic of the *three-fold* near-degeneracy developed above, and therefore constitute the spectroscopic signature of this system.

As stated before in this subsection, the spin Hamiltonian model does not capture all the physics of the system. First, the calculated value of $A_{\perp}$ is significantly lower than that of the phenomenological fit. Second, even the phenomenological fit, although providing a good description of the low-temperature measurement, slightly misfits the high-temperature measurements. In the next subsection, we discuss the nature of the spin Hamiltonian model and its limits.

**Table 10** Calculated spin Hamiltonian A($\cong A/g_N\beta_N$) values (in Tesla) for each contribution of the hyperfine field: Fermi Contact (FC), spin-dipole (SD) and orbital contribution (L)

| Contribution | Total | FC | SD | L |
|---|---|---|---|---|
| $A_{\perp}$ | 47.5 | -20.6 | -8.8 | 76.9 |
| $A_{\parallel}$ | 4.6 | -19.0 | 18.2 | 5.4 |

## VII. Comments and outreach

### A. Comments on the limits of the spin Hamiltonian formalism

It was shown in subsections III.B.3 and III.C.3 that the failure of the spin Hamiltonian manifests itself both in magnetometry measurements and Mössbauer spectra. For the former, the failure manifests itself by an unusually large TIP. For the latter, the $A_{\perp}$ value calculated from the effective Hamiltonian leads to a considerably underestimated magnetic splitting of the magnetic Mössbauer spectra (Figure 32). Yet, the effective Hamiltonian from which those parameters are extracted yields a very satisfactory fit. Even when increasing the $A_{\perp}$ value to fit the experimental magnetic splitting at low temperature, a slight misfit remains at higher temperature (Figure 19). So, what is the physical origin of these misbehaviors?

All the aforementioned failures of the spin Hamiltonian formalism share the same origin: they are due to the fact that the spin Hamiltonian formalism completely neglect the field induced second-order Zeeman interactions between the low-lying triplet and excited states (Figure 31). Such interactions stabilize the low-lying magnetic sublevels by increasing their field-induced spin and orbital angular momenta. Obviously, this means that each and every magnetic moment and internal field is underestimated by the spin Hamiltonian formalism owing to the neglection of these couplings.

By construction, such couplings cannot be satisfyingly reproduced by the spin Hamiltonian formalism. As developed above, this phenomenon always stabilizes all magnetic sublevels, which deviates the trace of the Zeeman matrix from zero (see Theory chapter, subsection I.B.1). By contrast, the trace of the Zeeman matrix is always zero in the spin Hamiltonian formalism. Hence the spin Hamiltonian formalism is unable to reproduce appropriately these Zeeman couplings for all sublevels simultaneously, and as such, is unable to reproduce the associated field-induced magnetic moments and internal fields.

As shown in Figure 31, the second-order Zeeman interactions are state-specific; specifically, the ground singlet ($|\phi_0\rangle$) and the upper doublet ($|\phi_\pm\rangle$) interacts with distinct excited states, mostly through the transverse orbital Zeeman interaction. Therefore, the introduced spin and orbital angular momenta to the low-lying triplet is not identical for the ground singlet and the upper doublet. The correction for the upper doublet is larger than that for the ground singlet due to the differential energetic proximity.

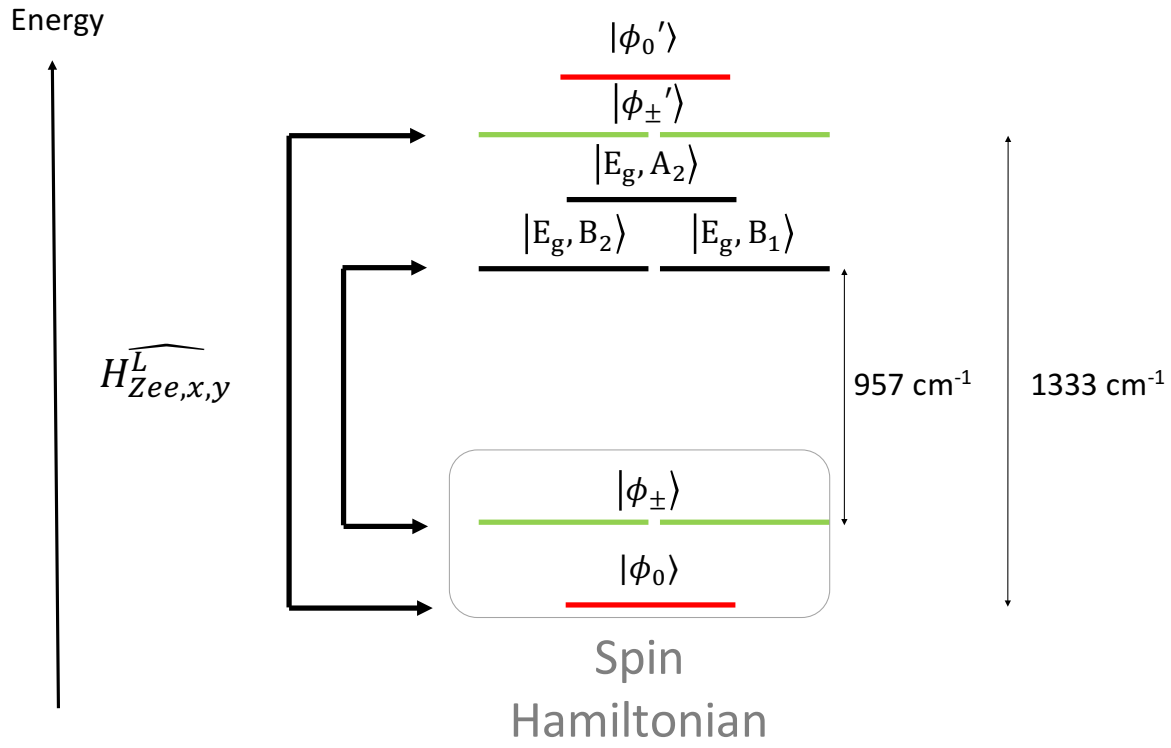


**Figure 31**: Representation of the second-order Zeeman coupling of the ground triplet with the excited magnetic sublevels after in-state and out-of-state SOC. The color code is the same as that used for Figure 4. The black arrows on the left side represent the *x*,*y*-component of the orbital Zeeman coupling ($\widehat{H^L_{Zee,x,y}}$) between the magnetic sublevels. The sublevelx $|\phi_\pm\rangle$ (green) interact with the sublevels $|E_g, B_1\rangle$ and $|E_g, B_2\rangle$; the sublevel $|\phi_0\rangle$ (red) interacts with the sublevels $|\phi_\pm'\rangle$.

In the case of magnetometry measurements, the second-order Zeeman effects are typically accounted for by invoking an *ad-hoc* TIP correction to the magnetic susceptibility (see Theory chapter, subsection I.B.1). Here, since the correction is state-specific, the overall magnetization correction should in principle be dependent on temperature. However, we found that the introduced magnetic moment is negligible for $\mu_\parallel$ and only accounts for a rather constant increase of $\mu_\perp$ for each magnetic sublevels in the triplet (0.01, 0.03 and 0.02 Bohr magnetons for $|\widetilde{\phi_0}\rangle$ , $|\widetilde{\phi_-}\rangle$ and $|\widetilde{\phi_+}\rangle$, as shown in Table 11). Consequently, the thermally averaged susceptibility correction is only marginally dependent on temperature, and can be reasonably approximated to an ad-hoc TIP correction, as done in the phenomenological fit.

**Table 11***:* Comparison of the magnetic moments ($\mu_B$) and the internal fields (T) of the low-lying triplet ($|\widetilde{\phi_0}\rangle$, $|\widetilde{\phi_\pm}\rangle$) computed under an applied field of 7 T under the *x* direction, calculated by the spin Hamiltonian with $D$ = 94 cm$^{-1}$ , $g_\perp$ = 3.05, $A_\perp = 47.5$ T,and by the effective Hamiltonian with with $\Delta E$ = 950 cm$^{-1}$, θ = –0.13π and $\langle r_d^{-3}\rangle$ = 5.4 a.u.$^{-3}$

| Average observable | Magnetic sublevel | Spin Hamiltonian | Effective Hamiltonian |
|---|---|---|---|
| $\mu_\perp$ | $\|\widetilde{\phi_0}\rangle$ | 0.64 | 0.65 |
| | $\|\widetilde{\phi_-}\rangle$ | 0.0 | 0.03 |
| | $\|\widetilde{\phi_+}\rangle$ | -0.64 | -0.62 |
| $B_{\mathrm{int},\perp}$ | $\|\widetilde{\phi_0}\rangle$ | 9.8 | 10.6 |
| | $\|\widetilde{\phi_-}\rangle$ | 0 | 1.4 |
| | $\|\widetilde{\phi_+}\rangle$ | -9.8 | -8.6 |

The description of the internal fields in the spin Hamiltonian formalism suffers from the same bias as the magnetic moment description, as they also depend on the spin and orbital angular momenta (eq. 58b). Furthermore, the orbital angular momentum contribution to the internal field is about 160% of the total field. By comparison, the orbital angular momentum contribution to the magnetic moment is only 37%. Hence the negligible change in the magnetic moment, mostly due to orbital Zeeman coupling terms, translates into an increase of 0.8 T in the internal field of the ground singlet and 1.4 and 1.2 T in the internal fields of the upper doublets. As a result, the internal field delivered by the spin Hamiltonian is always lower than that computed by the effective Hamiltonian (Figure 32), and the fit quality slightly worsens with temperature.

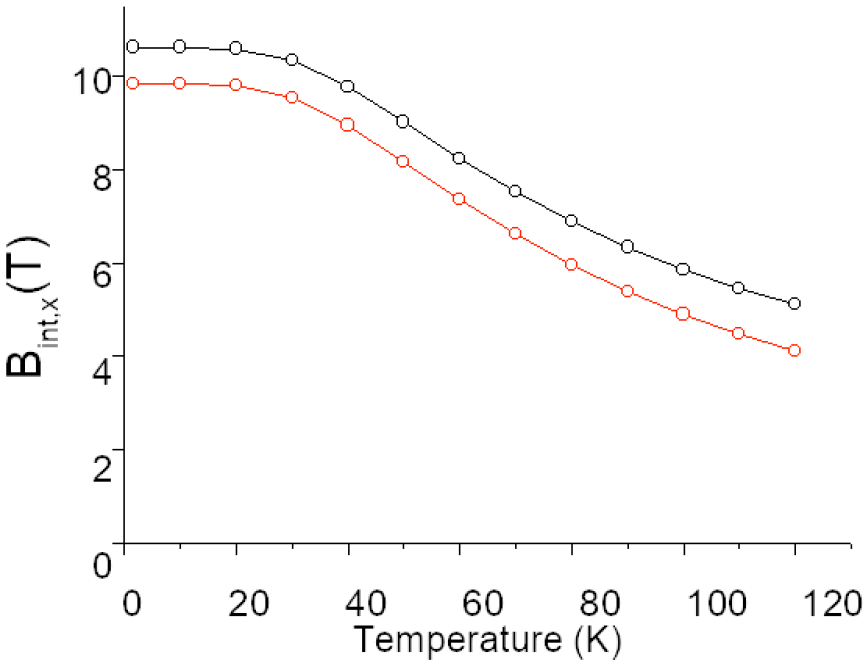


**Figure 32***:* Temperature-dependence of the Boltzmann averaged internal field (eq. 61) under an applied field of 7 T along the *x* direction, calculated by the spin Hamiltonian (red) with D = 94 cm$^{-1}$ , $g_{\perp} = 3.05$ , $g_{\perp} = 1.85$ and $A_{\perp}$= 47.4 and by the effective Hamiltonian (black) with $\Delta E$ = 950 cm$^{-1}$, θ = –0.13π and $\langle r_d^{-3} \rangle$ = 5.4 a.u.$^{-3}$

Note that in a phenomenological approach it is possible to improve the apparent quality of the spin Hamiltonian at a given temperature fit by adjusting the overall A matrix. This is why the low-temperature fit in the subsection III.C.3 seems satisfying. However, despite the higher quality fit, such approach is not conceptually satisfying because it *does not* improve the individual description of each magnetic sublevel. In fact, due to the invariant trace of the spin Hamiltonian Zeeman matrix, it is not possible to describe the correct behavior of all three magnetic sublevels simultaneously (*vide supra*). Instead, adjusting the A matrix to improve the description of one magnetic sublevel's internal field is always done at the cost of worsening the description for the remaining magnetic sublevels. Hence, even the phenomenological set of parameters of subsection III.C.3 introduces a misfit at high temperature, when the remaining magnetic sublevels are populated.

## B. Comments on the electronic structure of **1**

Taken together, all peculiar magnetic properties observed for complex **1** are in fact the manifestations of its electronic-structure feature that its low-lying triplet possesses the

substantial unquenched orbital angular momentum in the *xy* plane, which eventually stems from admixture of $^3E_g$ into the closed spaced $^3A_{2g}$ electronic sublevels induced by SOC. As a consequence, the electronic structure of complex **1** is best formulated as having an almost triple degeneracy. If the ground state was best described as $^3A_{2g}$, the system would have no sizeable unquenched orbital angular momentum. If it were as the doubly degenerate $^3E_g$ state, the system would exhibit uniaxial magnetic properties featuring an unquenched orbital angular momentum along one direction rather than in a plane.

Due to SOC-induced mixing of the $^3A_{2g}$ and $^3E_g$ states, the ground state of **1** is of a bona fide multiconfigurational character. In the present context, a configuration is interpreted as an occupation-number vector with individual orbital occupations being either 0, 1 or 2. The situation is distinctly different from multi-determinantal states, where a linear combination of several Slater determinants is required to satisfy spin-symmetry constraints. Note that in the latter cases all required Slater determinants still belong to the same electron configuration, but differ in the spin label, viz. spin-up or spin-down, that is assigned to each electron in a given Slater determinant. In this regard, most antiferromagnetically coupled transition metal oligomers are multideterminantal, instead of multiconfigurational. While the multiconfigurational character is often deduced by computations, the extent of configuration mixing is to some extent dependent on the choice of orbitals, and, more importantly, such computational findings need to be validated by experimental evidence in order to unambiguously establish the multiconfigurational nature of the electronic structure of interest. In fact, there are very few, if any, cases where an authenticated multiconfigurational nature (with contributions of more than one configurations exceeding, say, 10%) is strongly implied by the analysis of experimental data in conjunction with high-level calculations, like the present case.

### C. *Three-fold* degeneracy against *two-fold* degeneracy

Hence all experimental data consistently point out to a non-degenerate $^3A_{2g}$ non-relativistic ground state for **1**, highly mixed via SOC with a degenerate $^3E_g$ pair of excited non-relativistic states. Consequently, the ground state is highly multiconfigurational, which induces a considerable orbital angular momentum along the porphyrin plane. The orbital angular momentum aligns to an external field on the porphyrin plane due to the considerable orbital Zeeman mixings of the $^3A_{2g}$ and $^3E_g$ configuration. This situation is intrinsically connected to the peculiar ligand-field of iron(II)-porphyrin which we call *three-fold degeneracy*, because (1)

the ground state is non-degenerate, and (2) the high symmetry of the porphyrin plane ensures the degeneracy of the excited state. This situation is similar to that of cobalt(II) porphyrins, which has been intensely analyzed with EPR spectroscopy.[200] The g-values of [Co(II)(OEP)], for instance, were found at about $g_\perp = 3.4$; $g_\parallel = 1.6$. The magnetic anisotropy is due the distribution of five electrons in very closely-lying $d_{z2}$, $d_{xz}$ and $d_{yz}$ orbitals. The large $g_\perp$ are markers of the low-lying d-d excitations from the non-degenerate ground state $^2A_{2g}$ to the degenerate $^2E_g$ non-relativistic states of cobalt(II)-porphyrin systems.[201] Note that some five-coordinated Fe(III) heme systems also have a similar three-fold near-degeneracy leading to a $g_\parallel$ inferior to 2 and two identical $g_\perp$ close to 3.[202] Those systems also have two positive $A_\perp$ values resolved by Mössbauer spectroscopy. Those observations are consistent with a $(d_{xz,yz})^4(d_{xy})^1$ non-degenerate ground state and closely lying degenerate $(d_{xz,yz})^3(d_{xy})^2$ excited states. By contrast, other Fe(III) heme systems have a predominantly large magnetic moment and a large, positive internal field along the *z*-direction, indicative of a two-fold degenerate $^2E_g$ ground state $(d_{xz,yz})^3(d_{xy})^2$. consistently with the wide majority of reported systems with an unquenched orbital angular momentum.[196] For instance, a low coordinate $S$ = 3/2 Fe(I) complex, $[LFe^I(HCCPh)]^0$ (L = HC(C[$^t$Bu]N-[2,6-diisopropylphenyl])$_2$]$^-$ ), was found to have a large effective *g* factor of 8.9 with the other two *g* components less than 0.3 in the X-band EPR spectra and a large and positive internal field in the applied field Mössbauer spectra.[196] Note that the maximum effective spin-only *g* value of quartet systems is only 6. The proposed ground state with the electron configuration of $(d_{z2},d_{yz})^3(d_{xy})^2(d_{xz})^1(d_{x2-y2})^1$ has nearly two-fold degeneracy. Representative examples of non-Kramers systems are a range of two coordinate linear high spin ferrous complexes.[203] Unlike complex **1**, such systems were always found to feature easy axis magnetization as a consequence of their gigantic negative *D* values and vanishing rhombicity ($E/D \sim 0$). Hence, usually their low-lying non-Kramers doublets can be probed by using X-band EPR, in particular in parallel detection mode. Typically, they feature an effective *g* factor (>10) that by far exceeds the spin-only value of 8, and a large and positive internal field along the same direction, both findings indicative of their doubly degenerate ground state with the electron configuration of $(d_{xy},d_{x2-y2})^3(d_{xz})^1(d_{yz})^1(d_{z2})^1$. A series of planar three coordinate $S$ = 2 Fe(II) complexes, $[LFe^{II}X]^0$ (L = β-diketiminate; X = Cl$^-$, $CH_3^-$, NHTol$^-$ , NH$^t$Bu$^-$), also belong to this category.[196]

Those experimental observations together with our understanding of the system **1**, lead us to propose the following general description of systems with a *three-fold degeneracy*, similar to the system **1**, as opposed to systems with only *two-fold degeneracy*. For the former case, (1) the system exhibits a large magnetic moment (two high g-values) along the plane of

magnetization due to the orbital angular momentum aligned on the plane and parallel to the spin angular momentum. On the other hand, in *two-fold degenerate* systems, the situation is similar to the *in-state SOC* described above (Figure 26), and the system exhibits a very large magnetic moment (one high *g*-value) along the easy-axis due to a first-order orbital angular momentum parallel to the spin angular momentum. Note these observations are similar to those made by previous authors for S=1/2 systems.[201] To the best of our knowledge however, **1** constitutes the first S=1 system to be unambiguously identified as a *three-fold* near degenerate system.

All the aforementioned system share one common feature in that the subshell formed by the near-degenerate orbitals is more than half-filled. The situation is likely to be different in systems presenting a less than half-filled subshell. Second-order perturbation theory predicts that an excitation from a doubly to a singly occupied MO introduces a positive *g* shift, whereas a transition from a singly to an unoccupied MO gives a negative *g* shift. Therefore, It is likely than less than half-filled subshells behave in exactly opposite ways to the more than half-filled systems, i.e. the orbital angular momentum is antiparallel to the spin, rather than parallel. In other words, *three-fold degenerate* would have two g-values significantly lower than 2, while *two-fold* degenerate systems would have one g-value significantly lower than 2. For instance, in $[Fe^{V}(N)(TPP)]$,[204] a near-axial EPR spectrum with $g$ = 1.0, 1.70, and 1.83 is correlated with a two-fold degenerate electronic configuration of $(d_{xy})^2(\pi^*)^1$ ($\pi^*$ denotes the two $\pi$ antibonding conbinations formed by the Fe $d_{xz/yz}$ and N/O $p_{x/y}$ atomic orbitals). Earlier work showed that octahedral $[Ti^{III}(OH_2)_6]^{3+}$ complexes in titanium caesium alum ($TiCs(SO_4)_2.12H_2O$) undergoes weak trigonal distortions, which lifts the triple degeneracy of the $T_{2g}$ ground state and yields an orbital singlet slightly below a doublet, a bonding situation similar to complex **1**. Its EPR spectrum show a reversed pattern with $g_{\parallel}$ = 1.25, and $g_{\perp}$ = 1.14,[205] compared to $[Fe^{V}(N)(TPP)]$. Although we note that in both these examples, all three g-values are significantly down-shifted, we observe the pattern $g_{\parallel} < g_{\perp}$ in *two-fold degenerate* systems and $g_{\parallel} > g_{\perp}$ in *three-fold degenerate* systems.

## VIII. Conclusion

The present work reports a detailed study of the electronic structure of the triplet ground state of **1** using a combined spectroscopic and computational approach. The theoretical results suggest a near-degeneracy of the $^3A_{2g}$ and $^3E_g$ non-relativistic states. An effective Hamiltonian,

which explicitly takes the SOC and Zeeman interaction of $^3A_{2g}$ and $^3E_g$ into account, was proposed. Our results point out that at the Born-Oppenheimer level, the ground state for complex **1** is $^3A_{2g}$. However, because of their near-degeneracy, both states are highly mixed by SOC effect (the ground state is actually weighted at 85% $^3A_{2g}$ and 15% $^3E_g$). This effect manifests itself experimentally in a large ZFS, a large g-tensor anisotropy, a large deviation of $\mu_{eff}$ from the spin-only value, and most importantly, a large orbital field (positive) along the *xy* plane. Indeed, the large SOC coupling splits the magnetic sublevels of the electronic ground state by 94 $cm^{-1}$, and the consequent non-relativistic state mixing restores a large, magnetically-induced orbital angular momentum along the porphyrin plane. The near-degeneracy of the $^3A_{2g}$ and $^3E_g$ non-relativistic states also manifests itself in the failure of the spin Hamiltonian formalism to fit consistently both the magnetometric data and Mössbauer spectra. Specifically, the energetic proximity of the non-relativistic states gives rise to sizeable Zeeman couplings that are neglected by the spin Hamiltonian model.

The consistency of the fit for all VT and VTVF magnetometric and Mössbauer data lends considerable credence to the results of the effective Hamiltonian model, despite the small number of fitting parameters (3). Remarkably, the results of the effective Hamiltonian are in very close agreement with the ab-initio calculation. Furthermore, this model enables a detailed analysis of the relationship between electronic structure and experimental magnetic behavior. It shows beyond reasonable doubt that **1** is one of the rare truly multiconfigurational systems available throughout literature. While the multiconfigurational nature of a system is usually claimed by the means of ab-initio calculations, it is often dictated by the choice of orbitals and often lacks any experimental proof. Most importantly, the rationalization of the magnetic behavior of **1** provides a direct, experimental and quantitative proof of its multiconfigurational ground state.

Through comparison with the related systems, in particular those with nearly doubly degenerate ground states, we propose the following spectroscopic signature for systems with degenerate non-relativistic ground states. For complexes having *three-fold near-degenerate* ground states, if their nearly degenerate orbitals are more than half filled, they exhibit two *g* values that are substantially larger than 2 and for S>1/2 systems, whereas if their nearly degenerate orbitals are less than half filled, they likely exhibit a pattern of $g_\perp < g_\parallel$. In the case of complexes having doubly degenerate non-relativistic ground states, if their nearly degenerate orbitals are more than half filled, their EPR spectra likely show only one considerably large *g* component, whereas if their nearly degenerate orbitals are less than half filled, their EPR spectra

likely characterized by $g_{\perp} < g_{\parallel} \leq 2$. Further theoretical and experimental investigations are necessary to verify the applicability of the proposed spectroscopic signature.

# Chapter 2: Elucidation of the electronic structure of $[Fe(TPP)]^{-}$ and $[Fe(TPP)]^{2-}$

*The author of this thesis took care of the DFT modelling of the reduced complexes, including the molecular and electronic structure analysis, as well as calculation of the Mössbauer parameters. Although he initially did not take part in the TD-DFT calculations at the time of the associated article publication, he reproduced them later for the purpose of a more in-depth analysis. He did not however, take part in any experimental measurement or synthesis effort related to the content of this chapter.*

## I. Introduction

The elucidation of the ground state of **1** may now serve as a starting point to study the one- and two- electrons reductions of this complex. We thus aim to assign precisely the electronic structure of $[Fe(TPP)]^{-}$ ($\mathbf{1}^{-}$) and $[Fe(TPP)]^{2-}$ ($\mathbf{1}^{2-}$), which has been experimentally assigned by cyclic voltammetry[16] as the reactive species in the $CO_2$-to-CO reduction reaction.

$\mathbf{1}^{-}$ and $\mathbf{1}^{2-}$ have already been extensively studied. The former has been unambiguously characterized with EPR studies as an overall S=1/2 system,[179,206,207,208] while the second is diamagnetic (S=0 system).[179] However, contradictory assignments about whether the one- and two-electron reduction are ligand-centered or metal-center have been made.

For instance, $^{1}H$ and deuterium NMR proton studies[206,209,210] have shown that the chemical shift patterns of the porphyrin protons in $\mathbf{1}^{-}$ are incompatible with a ligand-centered radical. Those studies conclude that the reduction is iron-centered and the iron is a $d^7$ Fe(I). Furthermore, several EPR studies[179,206,207,208] revealed that the g-values show axial symmetry with $g_{\perp} = 2.15 - 2.3$ with a slight solvent dependency and $g_{\parallel} = 1.93$. The g-values are too anisotropic for a porphyrin radical EPR signal and thus suggest that the unpaired electron is on the metal rather than on the ring. The disappearance of the EPR signal at 300K further corroborates this assumption, as organic radical have much larger relaxation times and their EPR signals are more likely to subsist at high temperature than metal signals. Interestingly however, we note here that all the studies cited show that the presence of spin density on the

ring is unlikely, but do not exclude the possibility of a strong antiferromagnetic spin coupling between the ring and the metal. On the other hand, zero-field Mössbauer studies on [Fe(TPP)][Na(THF)$_3$] suggested an iron-centered reduction.[211] The reported isomer shift of $\delta = 0.65$ mm/s, significantly higher than the isomer shift of four-coordinated **1** (0.52-0.57).[160b] This may indicate an iron-centered reduction because the increase in d-population increases the screening of the 4s orbital,[145] therefore decreasing the density at the nucleus, although several other factors such as axial interactions with the [Na(THF)$_3$]$^+$ cation might also take part in the significant increase of the isomer shift.

By contrast, several studies point out to a ring-centered reduction. UV-vis spectroscopic studies have shown a consistent splitting of the Soret band upon reduction to **1**$^-$ and **1**$^{2-}$ [207,209,212,213] This behavior has been attributed by some authors as evidence for a ligand-centered reduction,[211] although this assumption is controversed.[213] More compelling, an X-ray diffraction study of [Fe(TPP)][Na(DB-18-crown-6)(THF)$_2$] and [Fe(TPP)][Na(THF)$_3$]$_2$ by Scheidt[179] has compared the ligand bond distances of the one- and two- electron reduced species with that of a 6-coordinated low-spin [Fe(II)(TPP)] with a similarly planar core. They found that the C-C and C-N bond lengths shifted significantly upon reduction, which suggests a ligand-centered reduction. Finally, A zero-field Mössbauer study of [Fe(TPP)][Na(THF)$_3$]$_2$ reported an isomer shift $\delta = 0.48$ mm/s,[211] very close to the isomer shift of the iron(II) complex **1**, and strongly suggests that [Fe(TPP)][Na(THF)$_3$]$_2$ is best described as a Fe(II) center coupled to a doubly-reduced ring. Furthermore, a $^1$H NMR study found that the addition of electron withdrawing substituents in meso or $\beta$ position on the porphyrin rings changed completely the pattern of paramagnetic shifts of the protons in derivates of **1**$^-$. The resulting pattern was found closer to that of a $\pi^*$ radical.[210] Although this result suggests that **1**$^-$ is not a ligand-centered radical, it provides evidences of very low-lying $\pi^*$orbitals in iron-porphyrins, which in turns gives credence to the hypothesis of a spin coupling between the metal and the ring.

As far as the electronic structure of the iron in the reduced species is concerned, the NMR data of several studies,[206,210,214] based on previous paramagnetic NMR studies on iron(II)-porphyrins[168] showed that the negative Fermi contact shift of the pyrrole ring was typical of a $\sigma$-spin transfer to the ring and indicated that either the $d_{x2-y2}$ or the $d_{z2}$ orbital is singly-populated ($x$,$y$ and $z$ axes are chosen collinear to those chosen in Chapter 1). Because of the square-planar environment of the iron, the population of the $d_{z2}$ is much more likely. The electronic structure of the doubly-reduced species has to the best of our knowledge, never been elucidated unambiguously.

All the cited studies are contradictory regarding the electronic structure of $\mathbf{1}^{-}$ and $\mathbf{1}^{2-}$. Furthermore, in some of those studies, [179] the influence of the counterion is unclear, as the Fe-Na distances are rather short (3 Angstrom in $[Fe(TPP)][Na(THF)_3]_2$).[179] In the present chapter, the electronic structure of $\mathbf{1}^{-}$ and $\mathbf{1}^{2-}$ is unambiguously determined by probing directly the local oxidation state of the iron via XANES and Mössbauer spectroscopies. To get rid of the possible counterion effect, the sodium was captured using a 18-crown-ether cage whenever possible. More importantly, we provide a quantitative and qualitative understanding of these experimental results by successfully simulating them with a unique quantum chemistry-based DFT model. Finally, we compare the present model to available rRaman data published in literature to insure the consistency of our assignment.

## II. Experimental and computational details

### A. Synthesis protocols

Synthesis of reduced four-coordinated iron-porphyrin complexes have been already described elsewhere,[179] and the present protocol is elaborated in details below. All reduction reactions were performed in THF using [Fe(TPP)Cl] as starting material and sodium anthracenide as a reductant. $[Fe(TPP)][Na(THF)_3]$ and $[Fe(TPP)][Na(THF)_3]_2$ were then crystallized and washed using heptane (*vide infra*). The powder crystals thus obtained were re-dissolved in Me-THF, a slightly weaker Lewis base than THF,[215] together with 18-crown-ether to capture sodium ions and remove any possible axial interaction between the anions $\mathbf{1}^{-/2-}$ and their counterions.

**$[Fe(TPP)(THF)_2]$ and 1** were prepared according to the method described in the last chapter.
**Sodium anthracenide**: Anthracene (1.26 g, 7.07 mmol, 1.1 equivalents) is dissolved in THF or MeTHF, respectively (32 mL). Metallic sodium (148 mg, 6.44 mmol, 1 equivalent) is added to the solution. The reaction mixture is stirred for 24 hours. No further workup is needed; the dark blue solution can be directly used as reducing agent.
**$[Fe(TPP)][Na(THF)_3]$**: FeClTPP (100 mg, 0.142 mmol, 1 equivalent) is dissolved in THF or MeTHF (12 mL). Sodium anthracenide (0.2 M solution, 1.78 mL, 2.5 equivalents) is added slowly via a syringe to prevent local excess of reducing agent. The solution is stirred at room temperature for 20 minutes. When THF is used as solvent, the solution is filtered over a PTFE

syringe filter, layered with heptane (48 mL) and set aside for crystallization at -40 °C for 2-3 days. The mother liquor is removed and the remaining solid is washed with little heptane (3 x 1 mL). When MeTHF is used as solvent, crystallization does not occur. Therefore, MeTHF is only used for preparation of samples where spectroscopy was carried out in solution.

**[Fe(TPP)][Na(THF)$_3$]$_2$**: FeClTPP (150 mg, 0.213 mmol, 1 equivalent) is dissolved in THF or MeTHF (10 mL). Then, sodium anthracenide (0.2 M solution, 5.1 mL, 4.8 equivalents) is added via a syringe. The solution is stirred at room temperature for 2 hours. When THF is used as solvent, the solution is filtered over a PTFE syringe filter, layered with heptane (40 mL) and set aside for crystallization at -40 °C for 2-3 days. The mother liquor is removed and the remaining solid is washed with little heptane (3 x 1 mL). When MeTHF is used as solvent, crystallization does not occur. Therefore, MeTHF is only used for preparation of samples where spectroscopy was carried out in solution.

## B. Mössbauer spectroscopy measurements

Mössbauer spectra were recorded on a conventional spectrometer with alternating constant acceleration of the γ-source. The minimum experimental line width was 0.24 mm/s (full width at half-height). The sample temperature was kept constant in an Oxford Instruments Variox or in an Oxford Instruments Mössbauer-Spectromag. The latter is a split-pair superconducting magnet system for applied fields up to 8 T where the temperature of the sample can be varied in the range of 1.5−250 K. The field at the sample is perpendicular to the γ-beam. The $^{57}$Co/Rh source (1.8 GBq) was positioned at room temperature inside the gap of the magnet system at a zero-field position, by using a re-entrant bore. Isomer shifts are quoted relative to iron metal at 300 K. Magnetic Mössbauer spectra of fully reduced compound 4b were simulated with the program MX (by E.B.) by using the usual nuclear Hamiltonian with an applied field only and zero internal field due to electronic spin S = 0. Zero-field spectra were measured at 80 K. For solid-state measurements, the obtained solid was filled into a self-sealing Delrin capsule in the glovebox. The capsule was additionally wrapped airtight in aluminum foil and placed in liquid nitrogen directly after being discharged from the glovebox. Handling and mounting of the samples were performed under liquid nitrogen. For solution measurements, the preparation of the reduced species was performed according to the previously described procedures. The starting compound was enriched with 20% [$^{57}$Fe(TPP)Cl]. The reaction solution was filtered and directly used for Mössbauer experiments. The solution capsule was placed in a Schlenk

flask, discharged from the glovebox, and placed in liquid nitrogen until the solution was frozen. Handling and mounting of the samples were performed under liquid nitrogen.

## C. XAS measurement details

For solid-state XAS experiments, the samples were diluted in boron nitride, sealed in an aluminum spacer (1 mm layer thickness) between 38 μm Kapton tape windows, and stored in liquid nitrogen. Handling and transportation of the samples were performed under a nitrogen atmosphere. XAS measurements were performed on ESRF beamline BM23, which is equipped with a liquid $N_2$-cooled Si(111) double-crystal mono- chromator, which was used for energy selection. Energy calibration was performed by setting the first inflection of an Fe foil to 7111.2 eV. A beam size of 500 μm × 3 mm was used. A continuous flow dual- chamber liquid He cryostat at 10 K was used. All samples were continuously monitored for signs of radiation damage throughout the course of data collection. Data were measured over an energy range of 7056−7970 eV. Data calibration and averaging were performed using Athena from the IFEFFIT package. Peak positions of the pre-edge and rising edge were determined by calculating the center of mass of the second-derivative minima of five-point smoothed spectra.

## D. Computational details

All calculations were performed using the ORCA 4.0 package.[183] All calculations use normal SCF convergence settings ($1x10^{-6}$ Eh), and Grid5. The geometry of the anions $\mathbf{1}^-$ and $\mathbf{1}^{2-}$ were optimized in gas-phase with normal geometry convergence settings using the basis sets Def2-TZVP for iron and Def2-SVP for all other atoms.[144] The GGA functional BP86[184] which often yields very reliable geometries[216] at an affordable computational cost, was used. Grimme dispersion correction was included to all energies.[217,218] All calculations described below are performed on the resulting geometries.

For calculation of the Mössbauer properties, single-point calculations were then performed at the B3LYP/Def2-TZVP level of theory, using the basis set CP(PPP) for iron, as detailed in the Theory chapter (subsection V.B). Grimme dispersion correction was also included to all single-point energies. To get a better description of the electronic density around the iron nucleus, a grid 7 was used for the iron only. The isomer shifts were deduced from the density at the nucleus thus calculated using calibration curves published by Ye et. Al.[149] (see Theory chapter, subsection V.B).

For calculation of the XAS spectra, single-point TD-DFT calculations[127] were performed using the CAM-B3LYP functional,[219] which has proven reliable to describe pre-edge structures (Figure 33). For each calculation, 150 roots consisting exclusively of excitations involving the 1s orbital were requested. Obviously, the electric quadrupole transition intensities were calculated in addition to the usual electric dipole. To speed up the calculation, the RIJCOSX approximation was used.[220] Relativistic effects were accounted for using the scalar relativistic Zero-Order Regular Approximation (ZORA).[221] For a more accurate description of the s-type density, the basis set CP(PPP) was used for iron in combination with a grid 7 setting, and the ZORA-TZVP basis set[222] was used for all other atoms. Due to the systematic errors of pre-edge energies calculated with DFT, all pre-edge energies were shifted by 22.37 eV. This value was obtained by building a calibration curve from the calculated and experimental pre-edge energies of 9 ferrous and ferric complexes (Figure 33). The systems and values are shown in the annex of this chapter (Table A1).

For the orbital analysis of $\mathbf{1}^{-}$ and $\mathbf{1}^{2-}$, the magnetic orbitals[223] were directly extracted from the unrestricted corresponding orbitals set (UCO).[146] For the rest of the set, the orbitals of the alpha set was assimilated to the doubly-occupied space, since no overlap integral is lower than 0.95. The orbitals of the alpha set were localized using a Pipek-Mezey algorithm,[187] and the orbitals with primarily 3d character (according to a Löwdin population analysis) were labelled as d-orbitals. For the analysis of the XAS spectra, the natural transition orbitals (NTO)[224] were constructed from the TD-DFT calculations.

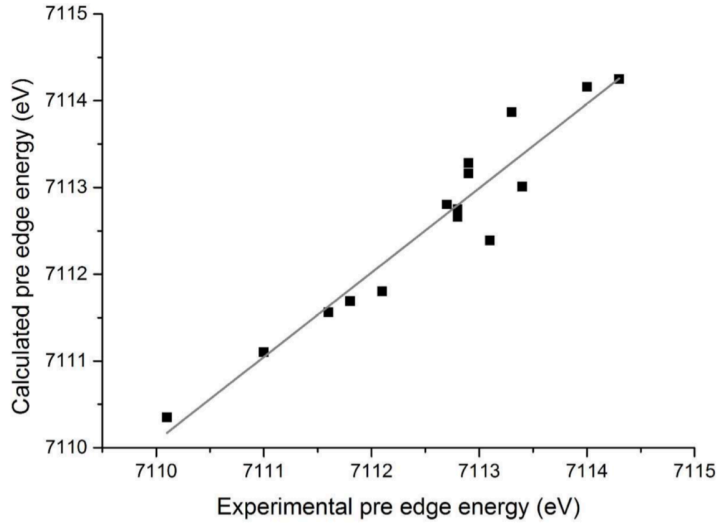


**Figure 33:** Experimental vs. calculated pre-edge structure energies for 9 ferrous and ferric complexes. The dots represent the calculated values shifted by 22.37 eV. The solid line represents the perfect calculation-experiment agreement.

## III. Experimental results

### A. Mössbauer spectroscopy

**Table 12**: Zero-field Mössbauer parameters, i.e. isomer shift ($\delta$) and quadrupole splitting ($\Delta E_Q$) for the species under investigation. The sign of $\Delta E_Q$ is reported when known. Experimentally, **1**$^{-}$ and **1**$^{2-}$correspond to the singly- and doubly-reduced species in frozen solution in presence of 18-crown-ether cages. The calculated parameters for each of these species are included (B3LYP/CP(PPP) level of theory, see subsection II.D for computational details), and discussed in section IV.

| Species | $\delta(Exp)$ (mm/s) | $\delta(calc)$ (mm/s) | $\Delta E_Q(Exp)$ (mm/s) | $\Delta E_Q(calc)$ (mm/s) |
|---|---|---|---|---|
| **1** | 0.52[a]-0.56[b] | 0.42 | +1.31[b]-1.51[a] | +0.60 |
| **1**$^{-}$ | 0.52[b]- | 0.41 | ±2.21[a] | +0.40 |
| [Fe(TPP)][Na(THF)$_3$] | 0.65[c] | | ±2.23[c] | |
| **1**$^{2-}$ | 0.45[b] | 0.43 | +1.50 | +0.34 |
| [Fe(TPP)][Na(THF)$_3$]$_2$ | 0.49[b] | | ±1.35[b] | |

a) Taken from ref. 160b

b) This work

c) Taken from ref. 179

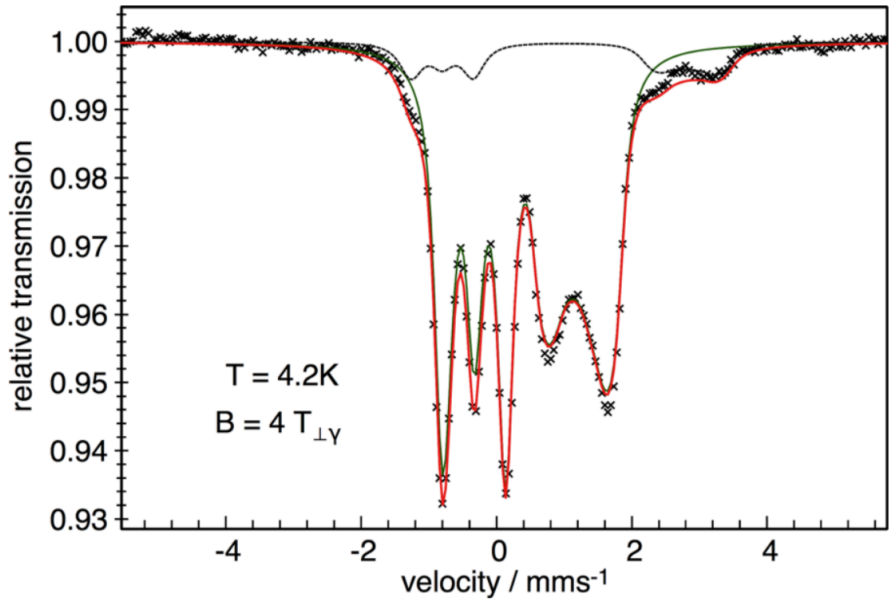


**Figure 34**: $^{57}$Fe Mössbauer spectrum of $\mathbf{1}^{2-}$ in frozen THF and in presence of 18-crown-ether at 4.2 K under 4 T (perpendicular mode). The dots correspond to the experimental measurements. The red line corresponds to the best spin Hamiltonian fit. The fit consists of the superposition of two subspectra. The principal subspectrum (90% of the total iron, green solid line) is assigned to $\mathbf{1}^{2-}$ with the parameters $\delta = 0.45$ mm/s, $\Delta E_Q = +1.50$ mm/s, $\eta = 0.1$; the minor subspectrum (10% of the total iron, dashed black line) corresponds to an unknown impurity, with $\delta = 1.02$ mm/s, $\Delta E_Q = +3.61$ mm/s, $\eta = 0.1$

The Mössbauer zero-field parameters for $\mathbf{1}^{-}$, $\mathbf{1}^{2-}$ (in frozen solution with 18-crown-ether cage) and that of [Fe(TPP)][Na(THF)$_3$] and [Fe(TPP)][Na(THF)$_3$]$_2$ (in solid state) are shown in Table 12. For comparison, the parameters of **1** are shown as well. The applied field Mössbauer of $\mathbf{1}^{2-}$ is shown in Figure 34. The absence of any hyperfine coupling confirms the diamagnetic ground state of this specie.[179] The low-lying triplet and high-lying doublet line pattern of the magnetic splitting is characteristic of a positive quadrupole splitting ($\Delta E_Q = +1.5$ mm/s) with a low asymmetry parameter ($\eta = 0.1$) (see Theory chapter, subsection II.B.2).

The isomer shift of **1**, $\mathbf{1}^{-}$ and $\mathbf{1}^{2-}$ are remarkably identical. By opposition, isomer shifts are usually expected to increase as the oxidation state of the iron decreases, principally because the additional d-electrons screen the 4s electrons away from the nucleus.[145] On the contrary, this result suggests that the two reductions are primarily ligand-centered since they do not affect the isomer shift of $^{57}$Fe.

Interestingly, the quadrupole splitting value of $\mathbf{1}^{-}$ is significantly upshifted compared to **1**, suggesting a different electronic configuration. However, because the isomer shift is so

similar to that of **1**, it is unlikely that this change is due to a metal-centered reduction. Instead, it is possible that the configuration of the iron is different in $\mathbf{1}^-$ and **1**. This hypothesis is reasonable given that we found in Chapter 1 that in **1**, the $^3A_{2g}$ and $^3E_g$(A) states are separated by less than 1000 $cm^{-1}$, implying that subtle change in the molecular structure of the complex might lead to a change in the electronic ground state. Our DFT calculations in the previous chapter suggested that the configuration $^3E_g$(A) creates a substantially larger quadrupole splitting than the configuration $^3A_{2g}$, due to the promotion of an electron from the $d_{z2}$ orbital (large negative contribution) to the $d_{xz/yz}$ orbital (small negative contribution). In fact, assuming a positive sign, the quadrupole splitting value of $\mathbf{1}^-$ is similar to that reported for the complex **1** in a saddle core conformation (+2.21 mm/s), for which the assigned ground state is $^3E_g$(A).[160b]

On the other hand, the quadrupole splitting of $\mathbf{1}^{2-}$ is remarkably identical to that of **1**. This result, together with their similar isomer shifts, tends to suggest that the local electronic configuration of the iron center is identical in both systems, i.e., primarily $^3A_{2g}$ $(d_{xy})^2(d_{xz,yz})^2(d_{z2})^2$ (see previous chapter), and further strengthens the hypothesis of a double ring reduction. Note that the low asymmetry parameter determined in the fit of the applied-field Mössbauer spectrum is consistent with this electronic configuration. By contrast, the electronic configuration $^3E_g$(A) should have a large asymmetry parameter because the population of three electrons in the orbital pair $(d_{xz},d_{yz})$ should induce a non-equivalent x- and y- component of the EFG tensor.

It is worth noting that [Fe(TPP)][$Na(THF)_3$] has a significantly higher isomer shift than $\mathbf{1}^-$ in frozen solution. According to this value, it is tempting to say that in the former case, the reduction is iron-centered. However, this hypothesis is unlikely since the quadrupole splitting of [Fe(TPP)][$Na(THF)_3$] is identical to that of $\mathbf{1}^-$, which suggests that the local electronic structure of the iron is identical in both case. Instead, it is possible that this slightly higher isomer shift is the result of the crystal packing effect, which may have large effect on the Fe-N bond lengths in iron-porphyrins,[160b] or the interaction with the sodium counterion.

Hence the zero-field Mössbauer data strongly points out to a ring-centered reduction. The quadrupole splitting and isomer shift of $\mathbf{1}^-$ are compatible with a $^3E_g$(A) iron(II) center antiferromagnetically-coupled to a radical ligand, in agreement with the experimentally-resolved S=1/2 spin state.[179] Similarly, the quadrupole splitting and applied-field Mössbauer spectrum of $\mathbf{1}^{2-}$ points out to a $^3A_{2g}$ iron(II) center antiferromagnetically coupled with a diradical anionic ligand. The Mössbauer data is more ambiguous for [Fe(TPP)][$Na(THF)_3$], for which a metal-centered reduction cannot be unambiguously discarded due to the significant increase in

isomer shift, although the quadrupole splitting value suggests that the local electronic structure of the iron is the same as that of **1**$^{-}$.

## B. X-ray absorption spectroscopy

The iron K-edge spectrum of **1**, [Fe(TPP)][Na(THF)$_3$] and [Fe(TPP)][Na(THF)$_3$] is shown in Figure 35. For useful comparison, the spectrum of [Fe(TPP)Cl] and [Fe(TPP)(THF)$_2$] is also shown. The very weak peaks between 7110 and 7114 eV correspond to the pre-edge structures of each of these species. Those peaks are reported in Table 13. For **1**, [Fe(TPP)][Na(THF)$_3$] and [Fe(TPP)][Na(THF)$_3$]$_2$, only one structure appears at a remarkably constant energy of 7110.1-7110.5 eV. For [Fe(TPP)Cl], one structure is also visible, although clearly upshifted compared to the formers (7112.9 eV). Finally, for [Fe(TPP)(THF)$_2$], two structure appear (7110.5, 7113.5). For **1**, [Fe(TPP)][Na(THF)$_3$] and [Fe(TPP)][Na(THF)$_3$]$_2$, an additional, much more intense peak appears around 1118 eV. This feature is absent from the spectrum of [Fe(TPP)Cl] and [Fe(TPP)(THF)$_2$]. Finally, the rising edges of **1**, [Fe(TPP)][Na(THF)$_3$] and [Fe(TPP)][Na(THF)$_3$]$_2$ are very similar. By contrast, the rising edge of [Fe(TPP)Cl] is clearly the most upshifted.

**Table 13**: Experimental pre-edge and low-lying rising edges peaks of all the investigated species. The energies of the structures calculated via TD-DFT at the CAM-B3LYP/CP(PPP) level of theory are included (after shifting the energies by 22.37 eV, see subsection II.D) and discussed in section IV. In the computational models, counterions are omitted.

| **Species** | Pre-edge peak (eV) (Exp.) | Pre-edge peak (eV) (Calc.) | Rising-edge peak (eV) (Exp.) | Rising edge peak (eV) (Calc.) |
|---|---|---|---|---|
| [Fe(TPP)Cl] | 7112.9 | 7113.2 | / | / |
| [Fe(TPP)(THF)$_2$] | 7110.5, 7113.5 | 7111.3, not found | / | / |
| **1** | 7110.5 | 7111.1 | 7115.9 | 7118.1 |
| [Fe(TPP)][Na(THF)$_3$] | 7110.5 | 7111.6 | 7116.3 | 7117.9 |
| [Fe(TPP)][Na(THF)$_3$]$_2$ | 7110.1 | 7111.6 | 7115.4 | 7117.6 |

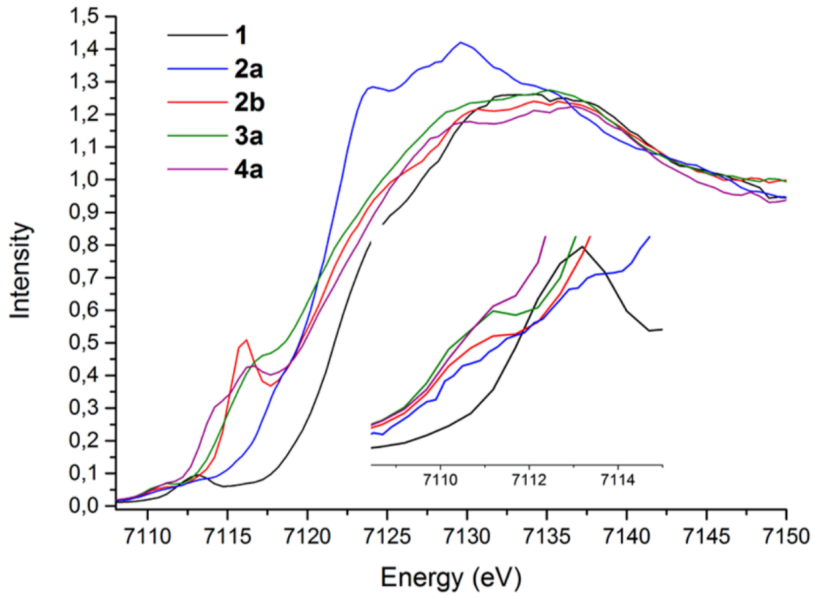


**Figure 35**: superimposed iron K-edge spectra of [Fe(TPP)Cl] (1), [Fe(TPP)(THF)$_2$] (2a), **1** (2b), [Fe(TPP)][Na(THF)$_3$] (3a), [Fe(TPP)][Na(THF)$_3$]$_2$ (4a). The inset corresponds to an enlargement of the pre-edge region between 7110 and 7114 eV.

The weak pre-edge structures of **1**, [Fe(TPP)][Na(THF)$_3$] and [Fe(TPP)][Na(THF)$_3$]$_2$ suggest that the local oxidation state of the iron remains constant over the one- and two-electron reduction. Pre-edge structures correspond to the 1s-3d transitions,[125] which are normally electric dipole-forbidden transition due to their $\Delta l = +2$ character and only appear weakly on the spectrum mainly due to electric quadrupole transitions. Because these transitions involve the 1s orbital, they are usually significantly downshifted upon metal-centered reduction. Hence, for instance, the pre-edge structure of **1** is significantly downshifted compared to that of [Fe(TPP)Cl]. This downshift can be attributed, at least partly, to the lower oxidation state of iron in the former (although other factors such as the different spin state and number of coordination may play a role). By contrast, the pre-edge structure of **1**, [Fe(TPP)][Na(THF)$_3$] and [Fe(TPP)][Na(THF)$_3$]$_2$ are almost identical, hence it is probable that the local oxidation state of iron remains constant in this series. As a side note, the two structures of [Fe(TPP)(THF)$_2$] are quite typical of S=2 Fe(II) complex in octahedral coordination and likely are due to the energy separation of the $t_{2g}$ and $e_g$ orbitals.[125]

Similarly, The rising edge of **1**, [Fe(TPP)][Na(THF)$_3$] and [Fe(TPP)][Na(THF)$_3$]$_2$ remain very similar, consistently with the previous hypothesis that the oxidation state of the iron is invariant in all three compounds. Rising edge transitions correspond to 1s-4p transition and, unlike the 1s-3d transitions, are very intense since their $\Delta l = +1$ makes them electric dipole allowed transitions. However, like pre-edge structures, they are sensitive to the local

oxidation state of iron and are significantly downshifted in case of metal-centered reduction. This explains, at least partly, why the rising edge of **1** is clearly downshifted compared to [Fe(TPP)Cl]. On the other hand, the constant rising edges of **1**, [Fe(TPP)][Na(THF)$_3$] and [Fe(TPP)][Na(THF)$_3$]$_2$ leads further credence to the hypothesis of a ligand-centered reduction. Of note, comparison of the pre-edge and rising edge of [Fe(TPP)(THF)$_2$] with that of **1**, [Fe(TPP)][Na(THF)$_3$] and [Fe(TPP)][Na(THF)$_3$]$_2$ is difficult because although the oxidation state of Fe is identical, the spin state and number of coordination are different.

Finally, note that **1**, [Fe(TPP)][Na(THF)$_3$] and [Fe(TPP)][Na(THF)$_3$]$_2$ all have an additional peak at around 1118 eV. This peak is rather intense compared to the pre-edge structures and probably corresponds to a low-lying 1s-4p$_z$ transition. This hypothesis is further strengthened by the observation that this peak disappears both in [Fe(TPP)(THF)$_2$] and [Fe(TPP)Cl], where axial ligands destabilize the Fe-4p$_z$ orbital.

This analysis thus further strengthens the hypothesis of a ring-centered reduction, consistently with the previous Mössbauer analysis. Furthermore, it removes the previous ambiguity concerning the local oxidation state of iron in [Fe(TPP)][Na(THF)$_3$] (see subsection III.A). While the present analysis of the experimental data provides a rationalization of the ring-centered reduction, a complete understanding of the electronic structure of **1**$^{-}$ and **1**$^{2-}$ requires the design of a theoretical model able to reproduce all data simultaneously. In section IV, we attach to develop such model with the help of computational chemistry methods.

## IV. Theoretical analysis

### A. Electronic and molecular structure of the DFT models

Our geometry optimized structure of **1**$^{-}$ and **1**$^{2-}$ in gas phase show a non-negligible saddle character, i.e. the pyrrole rings are bending alternatively below and above the mean plane of the 20 carbon and 4 nitrogen atoms of the porphyrin ring (Table 14). The highest distance to the mean plane (belonging to a $C_\beta$ atom of a pyrrole ring) is 0.7 A for both compounds. The iron-nitrogen, C-C and C-N distances and highest distance to the mean plane are shown in Table 14 and compared to the corresponding experimental distances published by Scheidt[179] for [Fe(TPP)][Na(DB-18-crown-6)(THF)$_2$] and [Fe(TPP)][Na(THF)$_3$]$_2$.

**Table 14**: Experimentally-resolved iron-nitrogen, nitrogen-carbon and carbon-carbon distances in [Fe(TPP)][Na(DB-18-crown-6)(THF)$_2$] (labelled as **1**$^-$) and [Fe(TPP)][Na(THF)$_3$]$_2$ taken from ref. 179 and corresponding calculated bond length by geometry optimization of the anions **1**$^-$ and **1**$^{2-}$ in gas phase.

| Distances | **1**$^-$ (Exp.) | **1**$^-$ (Calc.) | [Fe(TPP)][Na(THF)$_2$]$_2$ (Exp.) | **1**$^{2-}$ (Calc.) |
|---|---|---|---|---|
| Fe-N | 1.980(6) | 1.977 | 1.968(1) | 1.987 |
| N-$C_\alpha$ | 1.401(6) | 1.399 | 1.409(5) | 1.400 |
| $C_\alpha$-$C_\beta$ | 1.429(12) | 1.444 | 1.421(4) | 1.438 |
| $C_\alpha$-$C_m$ | 1.385(5) | 1.403 | 1.380(3) | 1.412 |
| $C_\beta$-$C_\beta$ | 1.338(1) | 1.375 | 1.352(5) | 1.383 |
| Highest out-of-plane distance | 0.05 | 0.7 | 0.08 | 0.7 |

The overall agreement between the experimental and calculated geometries is good compared to the usual performances of the BP86/Def2-TZVP and BP86/Def2-SVP levels of theory.[216] Although satisfying, the quality of the bond length description is slightly inferior for **1**$^{2-}$. More preoccupying, the calculations do not capture the experimental trend of Fe-N bond lengths shortening upon reduction. Furthermore, the molecular structure of **1**$^-$ and **1**$^{2-}$ have a significantly saddle core while experimental crystal structures show a very planar core conformation. However, metal-porphyrin are known to have a very flexible core and several almost iso-energetic configurations,[225] for which Fe-N distances may vary drastically.[160b] Subtle effects such as a change in crystal packing or in the interaction with counterions (neither of which are accounted for in these gas-phase calculations) may influence significantly those parameters.

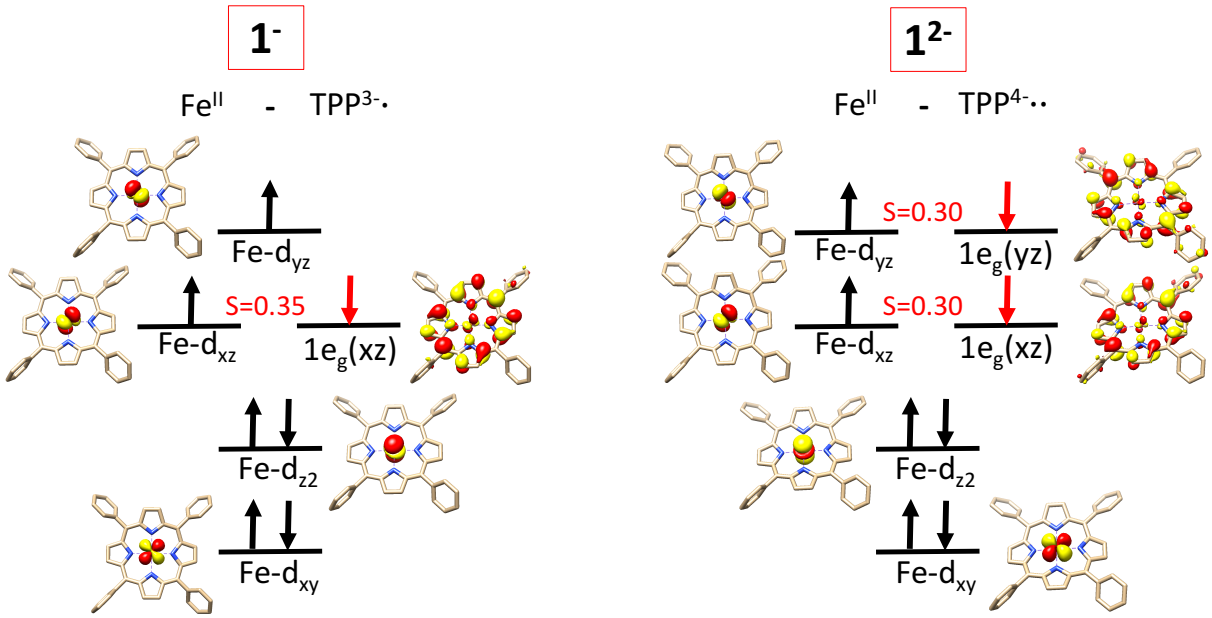


**Figure 36**: Calculated electronic configuration of iron in $\mathbf{1}^{-}$ (left) and $\mathbf{1}^{2-}$ (right). Hydrogens are omitted for clarity. Carbons are shown in beige, nitrogens in blue and iron in orange. Orbitals are represented in red (positive part) and yellow (negative part). The overlap between the magnetic orbitals is indicated in red. The electrons populating the ligand-centered orbitals $1e_g(xz)$ and $1e_g(yz)$ are represented by red arrows. The magnetic orbitals ($Fe\text{-}d_{xz}/1e_g(xz)$ in $\mathbf{1}^{-}$ ; $Fe\text{-}d_{xz}/1e_g(xz)$ and $Fe\text{-}d_{yz}/1e_g(yz)$ in $\mathbf{1}^{2-}$) are obtained from the unrestricted corresponding orbitals set. The $1e_g$ orbitals are labelled according to which quadratic function (xz or yz) they transform as in a $D_{4h}$ point group. The other orbitals correspond to the primarily Fe-d based occupied orbitals, obtained by localization of the rest of the occupied orbital set using a Pipek-Mezey algorithm.

The orbital analysis confirms the previous hypothesis according to which the iron center remains at the local oxidation state +II (Figure 36). For each successive reduction, the electron-accepting orbital ($1e_g(xz)$ for $\mathbf{1}/\mathbf{1}^{-}$ and $1e_g(yz)$ for $\mathbf{1}^{-}/\mathbf{1}^{2-}$) is primarily ring-centered. Furthermore, the DFT calculations of $\mathbf{1}^{-}$ and $\mathbf{1}^{2-}$ showed considerable spin contamination. The unrestricted corresponding orbital (UCO) analysis tracks down the origin of this contamination to one and two pairs of magnetic orbitals, respectively, with an overlap ranging from S=0.30 to S=0.35.

As suggested by the very large overlap between the magnetic orbitals, the spin coupling is strongly antiferromagnetic. In fact, although the systems are best described as Fe(II) centers and radical rings, the strong overlaps between the magnetic orbitals imply that in both case, the ground states have minor but non-negligible Fe(I) and Fe(0) characters, respectively. These significant configurational mixings are the expression of kinetic exchange phenomena, which explain the strong observed antiferromagnetic coupling. As developed in the next chapter, this

phenomenon is of critical importance in the reactivity of $\mathbf{1}^{2-}$ in $CO_2$-to-CO reduction. According to Yamaguchi's formula,[226] the calculated exchange coupling constant is $J = -1501$ cm$^{-1}$ and $J = -475$ cm$^{-1}$ for $\mathbf{1}^{-}$ and $\mathbf{1}^{2-}$, respectively. Strong antiferromagnetic spin coupling is permitted here because the magnetic orbitals (Fe-$d_{xz/yz}$ and $1e_g(xz/yz)$) share the same symmetry ($e_g$ in the $D_{4h}$ point group limit) which enables considerable mixing between them. This behavior is coherent with the experimental magnetism of these two systems. Indeed, both behave as an overall S=1/2 and S=0 system, respectively.[179,206,207,208]

The calculated electronic structure of $\mathbf{1}^{-}$ corresponds to a $^2E_g$ configuration $(d_{xy})^2(d_{z2})^2(d_{xz})^1(d_{yz})^1 1e_g(xz,yz)^1$. Thus it is best described as a local $^3A_{2g}$ Fe(II) center antiferromagnetically coupled to a ligand *radical*. The calculated electronic structure of $\mathbf{1}^{2-}$ corresponds to a $^1A_{1g}$ configuration $(d_{xy})^2(d_{z2})^2(d_{xz})^1(d_{yz})^1 1e_g(xz)^1 1e_g(yz)^1$. Hence it is best described as a local $^3A_{2g}$ Fe(II) antiferromagnetically coupled to a ligand *di-radical*. Of note, for $\mathbf{1}^{-}$, another solution corresponding to a local $^3E_g$(A) iron configuration antiferromagnetically coupled with a ligand radical could be found only 503 cm$^{-1}$ above the calculated ground state. This finding is consistent with the small energy gap of the $d_{z2}$ and $d_{xz,yz}$ orbitals encountered in the analysis of **1** (see Chapter 1). An energy gap of this order of magnitude is below the accuracy range of hybrid DFT, hence the nature of the ground state of $\mathbf{1}^{-}$ cannot be unambiguously assessed on the basis of DFT calculations alone. However, a similar low-lying excited state could not be found for $\mathbf{1}^{2-}$. This finding is consistent with the hypothesis that kinetic exchange favors the local $^3A_{2g}$ iron configuration over the local $^3E_g$(A) iron configuration in $\mathbf{1}^{2-}$ but not in $\mathbf{1}^{-}$. Indeed, in the former system, efficient kinetic exchange is insured by electron transfer from the $\beta$-$1e_g(xz)$ orbital to the $\beta$-$d_{xz}$ orbital and from the β-$1e_g(yz)$ orbital to the β-$d_{yz}$ orbital. This is only possible if both $\beta$-$d_{xz}$ and $\beta$-$d_{yz}$ are unoccupied in the dominant configuration, which is the case for $^3A_{2g}$ but not $^3E_g$(A). Hence kinetic exchange participates in stabilizing the $^3A_{2g}$ configuration over the $^3E_g$(A) configuration. By contrast, in $\mathbf{1}^{-}$, because only one radical electron is stored on the ring, only one $\beta$-$d_{xz/yz}$ orbital must be unoccupied to maximize the kinetic exchange, while the population of the other does not influence the spin coupling. Hence in this case, kinetic exchange does not participate in stabilizing the local $^3A_{2g}$ iron configuration over the $^3E_g$(A) iron configuration.

Hence, our DFT calculations predict that the systems $\mathbf{1}^{-}$ and $\mathbf{1}^{2-}$ are best described as an iron(II) iron center strongly antiferromagnetically coupled with a porphyrin radical and diradical, respectively. In $\mathbf{1}^{2-}$, the calculations point out to an overall $^1A_{1g}$ configuration best described as a local $^3A_{2g}$ Fe(II) antiferromagnetically coupled with a ligand di-radical. The

precise nature of the electronic ground state remains ambiguous for **1**$^{-}$. Although our results are consistent with a S=1 Fe(II) center antiferromagnetically coupled with a ligand radical, the local electronic configuration of the iron center, i.e. $^{3}E_{g}$ or $^{3}A_{2g}$ cannot be strongly assessed on the ground of DFT alone. Furthermore, although those results are in qualitative agreement with our previous hypothesis of a ligand-centered reduction, quantitative agreement between the experimental spectroscopic data and this in-silico model is required for its definitive validation.

## B. Description of the Mössbauer parameters

Calculated Mössbauer parameters for **1**, **1**$^{-}$ and **1**$^{2-}$ are reported in Table 12. As already developed in the previous chapter, both isomer shift and quadrupole splitting are significantly underestimated for **1**. Unsurprisingly, this tendency remains for the low-valent **1**$^{-}$ and **1**$^{2-}$ as well. However, the trends are more important than the absolute values because they are direct probe of the electronic structure change upon reduction.

Hence, the calculated isomer shifts are almost completely unaffected by the one- and two-electron reductions of the ring. This result is readily explained by the fact that the additional electrons are mostly localized on the ring, leaving the s-density on the metal mostly unaffected. This trend is consistent with the experimental observation. The calculated quadrupole splittings remain almost constant over the whole series, which is unsurprising given that the calculated local electronic structure of iron is identical ($^{3}A_{2g}$) for all three complexes. This trend reproduces the similarity between the experimental quadrupole splittings of **1** and **1**$^{2-}$. However, it does not reproduce the upshifted experimental quadrupole splitting of **1**$^{-}$ and [Fe(TPP)][Na(THF)$_3$] compared to **1** and **1**$^{2-}$. This discrepancy likely implies that the local electronic configuration of iron is $^{3}E_{g}$(A) rather than $^{3}A_{2g}$ in **1**$^{-}$ (see subsection III.A).[160b] The calculated quadrupole splitting of the low-lying local $^{3}E_{g}$(A) iron configuration solution found for **1**$^{-}$ is upshifted by +0.83 mm/s compared to the quadrupole splitting of **1**, which is very close to the experimental upshift of +0.70-0.90 mm/s. By contrast, the calculated quadrupole splitting of the predicted ground state of **1**$^{-}$ (local $^{3}A_{2g}$ configuration) is downshifted by 0.20 mm/s.

Although their absolute value is slightly underestimated by our DFT calculations, the trend of the calculated isomer shifts upon reduction reproduces the experimental trend and validates the hypothesis of a ligand-centered reduction. As far as the electronic structure of iron is concerned, comparison of our calculated quadrupole splitting values with the experimental values overall suggest that the local electronic configurations of iron in **1**$^{-}$ and **1**$^{2-}$ is $^{3}E_{g}$(A) and $^{3}A_{2g}$, respectively.

## C. TD-DFT description of the XAS spectra

Transitions between 7110 and 7120 eV were calculated by TD-DFT. Calculation of transitions closer to the continuum were not attempted since the description of barely bound states is poorly described by standard electronic structure methods. Calculated pre-edge structure and low-lying rising-edge peaks of the complexes [Fe(TPP)Cl], [Fe(TPP)(THF)$_2$], **1**, **1**$^{-}$ and **1**$^{2-}$ are reported in Table 13. The overall agreement between experiment and TD-DFT calculations is satisfying, especially for the description of pre-edge structures, for which TD-DFT is established as an accurate description method.[127] More importantly, the pre-edge structures of **1**, **1**$^{-}$ and **1**$^{2-}$ are almost identical, consistently with the experimental trend. Furthermore, the low-lying rising-edge found around 7118 eV follows the experimental trend upon reduction for the three four-coordinated compounds and is inexistent for the five and six-coordinated systems [Fe(TPP)Cl] and [Fe(TPP)(THF)$_2$], consistently with the experiment.

The remarkably constant energy of the pre-edge structure for **1**, **1**$^{-}$ and **1**$^{2-}$ is readily explained by the fact that the local oxidation state of iron remains identical upon one- and two-electron reductions. In details, the pre-edge structure is in fact constituted of four distinct transitions, each of which is dominated by the promotion of a 1s electron to one of the holes of the d-shell. In the local $^3A_{2g}$ electronic configuration of iron, those holes are in the $\overline{d_{xz}}$, $\overline{d_{yz}}$, $d_{x2-y2}$ and $\overline{d_{x2-y2}}$ unoccupied orbitals (Figure 37 and Figure 38). These excitations only marginally shift upon reduction of **1**, consistently with the fact that the additional electrons are mostly localized on the porphyrin ring, whereas the transitions are overwhelmingly iron-to-iron electronic transitions.

Notably, the predicted pre-edge structure of the $^3E_g$(A) solution of **1**$^{-}$ is very similar to the predicted spectrum of the $^3A_{2g}$ solution, even though the three constitutive excitations are different due to the change in electronic configuration of the ground state (Figure 38). This is consistent with the notion that Fe-$d_{xz}$, Fe-$d_{yz}$ and Fe-$d_{z2}$ orbitals are non-bonding and very closely lying. It also suggests that the electronic structure of the iron in **1**$^{-}$ cannot be elucidated by the analysis of XANES spectroscopy.

The low-lying rising-edge features of **1**, **1**$^{-}$ and **1**$^{2-}$ are characterized by two principal transitions, both of which are mainly constituted of $1s$ to $4p_z$ and $\overline{1s}$ to $\overline{4p_z}$ excitations, although they gain some non-negligible iron-to-ring charge transfer character as the charge of the complex increases. Similar to the pre-edge transitions and consistently with the experimental trend, the low-lying rising-edge transitions are marginally affected by the

reduction because the local oxidation of iron remains +II. Because of the absence of axial ligands, the $4p_z$ is essentially non-bonding, which explains why a rising edge feature may be observed at such a low transition energy. This explanation is consistent with the experimental observation that this transition disappears for the five and six coordinate systems, in which axial interactions significantly destabilize the $4p_z$.

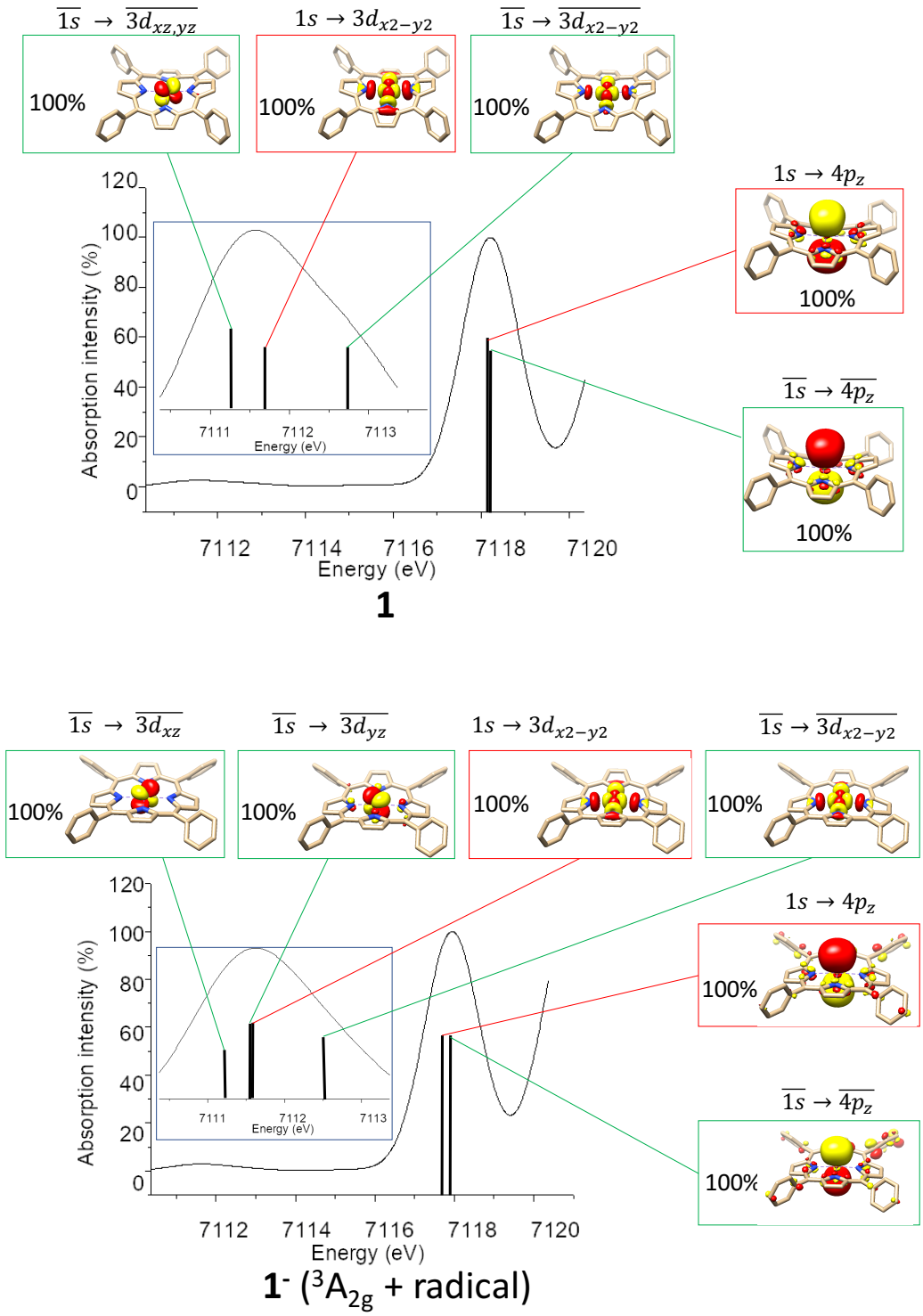


**Figure 37**: Decomposition of the calculated XAS spectra (from top to bottom, **1**, **1**$^-$ with Fe in a $^3A_{2g}$ configuration). The black bars below the envelope correspond to the individual transitions composing the pre-edge and low-lying rising-edge structures. Their hight is proportional to the squared transition intensity. The colour code refers to α→ α (red) or β→β (green) transitions. The black line corresponds to mixed α→ α and β→β transitions. The orbital

pictures in the rectangles correspond to the natural transition orbitals. Only the orbitals excitations having a weight superior to 5% are shown in the figure.

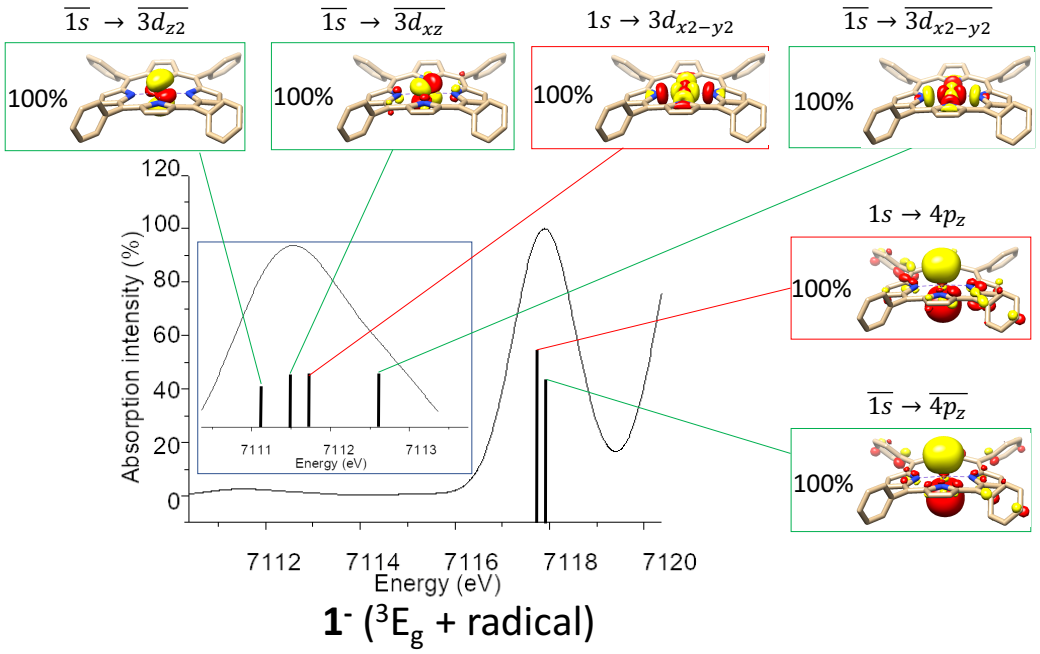


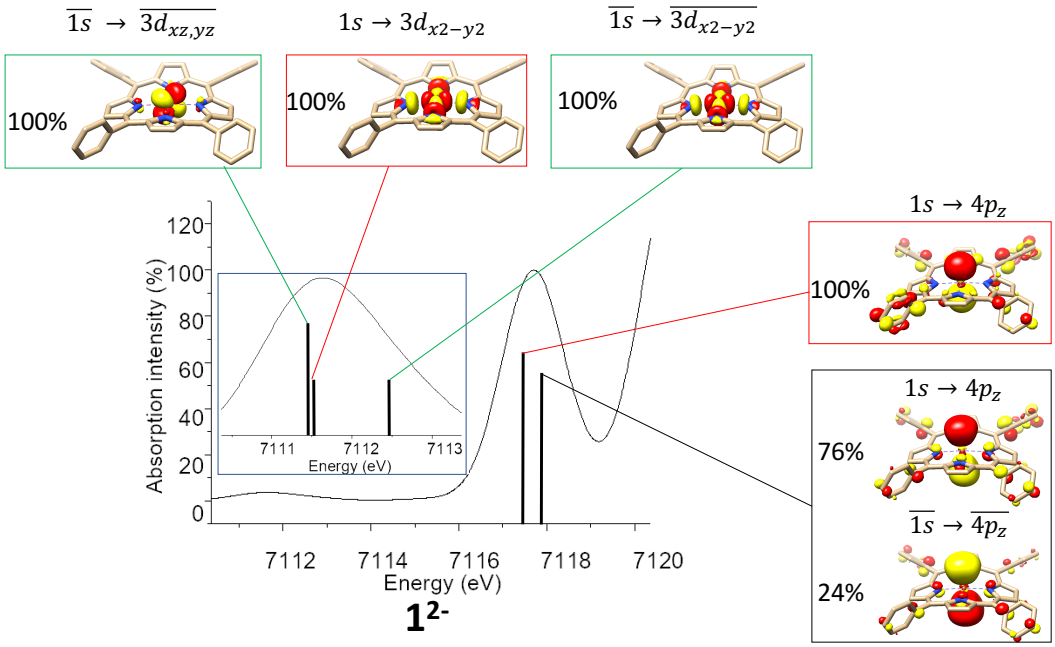


**Figure 38**: Continuation of Figure 37 (from top to bottom, **1**$^{-}$ with Fe in $^{3}E_{g}$(A) configuration and **1**$^{2-}$).

The TD-DFT calculations satisfyingly reproduce the experimental pre-edge structures and rising edge structure trends upon reduction. A deeper analysis of the underlying transitions confirmed that pre-edge structures are mostly composed of iron-centered 1s-to-3d transition and low-lying rising-edge structures are mostly composed of 1s to $4p_z$ transitions. Consequently, those structures are only marginally affected by the ring reduction. This computational analysis, together with the computational electronic structure and Mössbauer analyses, points out unambiguously to a ring-centered reduction, which means that $\mathbf{1}^{-}$ and $\mathbf{1}^{2-}$ are best described as a S=1 Fe(II) center antiferromagnetically coupled with a radical and diradical porphyrin ring, respectively. Note that the local electronic structure of $\mathbf{1}^{-}$ remains ambiguous and both candidate $^3E_g$(A) and $^3A_{2g}$ are consistent with the absorption pattern.

## D. A complementary rRaman study on $\mathbf{1}^{-/2-}$

So far, our approach to assign the electronic structure of $\mathbf{1}^{-}$ and $\mathbf{1}^{2-}$ has mostly consisted in probing the evolution of the local oxidation state of the iron center upon successive reduction of **1** to $\mathbf{1}^{-}$ and $\mathbf{1}^{-}$ to $\mathbf{1}^{2-}$. We have concluded that the iron center remains a local Fe(II), and therefore the reduction is ligand-centered Our hypothesis is strongly reinforced by a complementary study performed by our group.[18] Rather than focusing on the oxidation state of the iron center, this study probes the evolution of the electronic density on the porphyrin ligand by analyzing the evolution of the rRaman vibrational transitions of the ligand upon successive reduction.

Raman spectra of metalloporphyrins have been studied for decades.[212,213,227, 228,229] In particular, several bands corresponding to various vibration mode of the porphyrin ligand have been identified. Among them, two transition bands, usually named A and D, are of particular interest as they are sensitive to the reduction of the ring and/or reduction of the metal. In details, a benchmark study on 20 Fe(III) and Fe(II) porphyrin complexes has shown a consistent trend for these two bands.[227] Upon reduction of the metal and/or change in spin state, the band A is expected to be drastically downshifted. Conversely, the band D has been found rather insensitive to the change in oxidation state of the metal, but significantly affected by a change in spin state. On the other hand, upon ring reduction, band A is expected to remain essentially unaffected while the band D is expected to be strongly downshifted. This latter observation relies on the experimentally observed shift of the band A and D upon reduction of [Zn(TPP)] to $[Zn(TPP)]^{-}$, which has been clearly established as a ring-centered reduction.[230,231] Furthermore, DFT calculations have predicted a similar trend for band A and D upon reduction

of $H_2TPP$ to $H_2TPP^-$, and $H_2TPP^-$ to $H_2TPP^{2-}$ (Table 15). Hence the shift of the marker bands A and D upon successive reduction of **1** may be used as a spectroscopic signature either for the reduction of the ring or the reduction of the metal.

The rRaman spectra of the species [Fe(TPP)Cl], **1** , $\mathbf{1}^-$ and $\mathbf{1}^{2-}$ have been assigned by DFT and TD-DFT calculations[18] on the ground of two criteria: (1) the energy of the bands, since an agreement of ±25 $cm^{-1}$ with respect to the experimental Raman shifts is expected at this level of theory,[232,233] and (2) the agreement between calculated and experimental transition intensities at different excitation wavelength, since they are dependent on the nature of the resonant electronic states[234,235] and accounted for by the method used by the authors. Assignment of the bands A (1361 $cm^{-1}$) and D (1553 $cm^{-1}$) on the spectrum [Fe(TPP)Cl] was consistent with earlier assignments.[229] The associated vibration mode for band A is an asymmetric half-ring pyrrole vibration, and that of band D corresponds to a mixed mode composed of vibrations of the $C_\beta$-$C_\beta$ bonds, $C_\alpha$-$C_\alpha$ and $C_\beta$-H bonds (Figure 39).

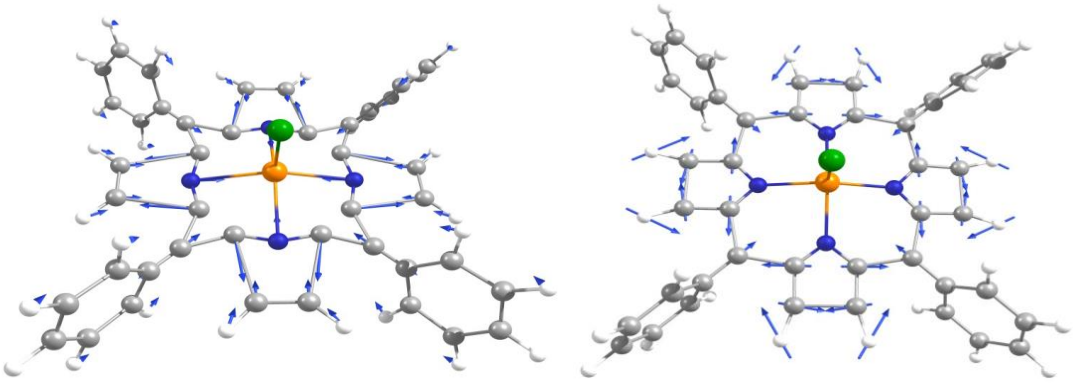

**Figure 39**: Schematic representation of band A (left) and D (right) in [Fe(TPP)Cl]. Hydrogens are shown in white, carbons in grey, nitrogens in blue, iron in orange and chlorine in green. The blue arrows represent the displacement vectors. Figure taken from ref. 18.

The assigned experimental bands A and D are reported in Table 15. The shift of band A upon the first and second reduction is -2 and -1 $cm^{-1}$, respectively. The shift of the band D is -28 and -7 $cm^{-1}$, respectively. Hence for both one-electron reductions, the band A remains rather constant and the band D is significantly downshifted. This is consistent with two ring-centered reduction, and is in perfect agreement with our findings so far. The predicted shifts of the computational models are in very good agreement with the experiment (Table 15) and the associated electronic structure is identical to our own DFT models. The local electronic structure of iron is Fe(II) in a $^3A_{2g}$ configuration, antiferromagnetically coupled with a radical or diradical ring. Note that the ambiguity on whether the local electronic structure of iron in $\mathbf{1}^-$

is $^3E_g$(A) or $^3A_{2g}$ is likely to not affect drastically the ring-based vibrations, since the $d_{xz,yz}$ and $d_{z2}$ are essentially non-bonding.

**Table 15**: experimental rRaman band shifts of the bands A and D (in $cm^{-1}$) upon one-electron reductions of selected porphyrin complexes. Non-available values are noted "N.A". Calculated values are noted in brackets.

| | $H_2TPP/H_2TPP^-$<br>$H_2TPP^-/H_2TPP^2$ | $[Zn(TPP)]/[Zn(TPP)]^-$ | **1**/**1**$^-$<br>**1**$^-$/**1**$^{2-}$ |
|---|---|---|---|
| | N. A. (+2)[18] | -1[231] | -2 (-2) [18] |
| $\Delta\nu\ (A)$ | N.A (-5) [18] | | -1 (+2) [18] |
| | N. A. (-17)[18] | -16[18] | -28 (-10) [18] |
| $\Delta\nu\ (D)$ | N. A. (-26)[18] | | -7 (-22) [18] |

Earlier studies on the rRaman spectrum of **1**$^-$ deserve a few words here.[213,228] Those studies found that band A and D remain unaffected upon one-electron reduction of **1**. The conclusion of these studies is that because the band D remains essentially unaffected by the reduction, the reduction must be metal-centered. However, the assignment of band D is inconsistent with the study from Neese et. Al. The use of quantum chemistry-based models to assign the bands gives higher credence to the latter study. Furthermore, these studies do not address the fact that the band A remains almost completely unaffected by the reduction although it has been clearly established as an oxidation state sensitive band.[227] Consequently, we cannot agree with the conclusion of the authors.

This study provides consistent results with our own. The shift of the marker bands A and D are consistent with two successive ring reductions and provides further credence to our hypothesis. The computational models are in good agreement with the experiment and their electronic structure is identical to our findings. Together with our computational, Mössbauer and XAS analysis, it assigns unambiguously the two successive one-electron reductions as ligand-centered, and establishes that **1** and **1**$^{2-}$ are best described as Fe(II) centers antiferromagnetically coupled with TPP radical and diradical, respectively.

## V. Conclusion

A joint use of spectroscopic methods and quantum-mechanics-based analysis enable us to unambiguously determine the electronic structure of $\mathbf{1}^{-}$ and $\mathbf{1}^{2-}$. The result of this study is that those two systems are best described as Fe(II) centers antiferromagnetically coupled with porphyrin radical and diradical, respectively. In details, this assignment is the result of a very satisfying agreement between our computed and experimental spectroscopic data. Our Mössbauer and X-ray absorption data consistently suggest that the local oxidation state of iron remains unchanged for both the reduction of **1** to $\mathbf{1}^{-}$ and $\mathbf{1}^{-}$ to $\mathbf{1}^{2-}$, and thus points out to a ligand-centered reduction. A rRaman study performed by Neese in addition to this work also pointed out a ligand-centered reduction. As far as the electronic structure of $\mathbf{1}^{-}$ and $\mathbf{1}^{2-}$ is concerned, Mössbauer data suggests that the electronic configuration of iron in **1** and $\mathbf{1}^{-}$ is different, but that of **1** and $\mathbf{1}^{2-}$ is similar.

Our DFT computational models confirm that the predicted electronic ground state of $\mathbf{1}^{-}$ and $\mathbf{1}^{2-}$ are best described as Fe(II) centers antiferromagnetically coupled with a radical and diradical porphyrin ring, respectively. The computed electronic local electronic configuration of iron for $\mathbf{1}^{2-}$ is a $^{3}A_{2g}$ configuration. In that configuration, both $\beta$-Fe-$d_{xz}$ and $\beta$-Fe-$d_{yz}$ orbitals are empty, which favors antiferromagnetic exchange pathways with the $1e_g$ porphyrin-based orbitals. The electronic configuration of $\mathbf{1}^{-}$ is more ambiguous. Our DFT computation predict two almost iso-energetic electronic states corresponding to a $^{3}A_{2g}$ and $^{3}E_{g}$(A) iron configuration antiferromagnetically coupled with a porphyrin radical, respectively.

Our DFT calculations reproduce very satisfyingly the trend of the Mössbauer isomer shift and pre-edge XANES structure upon reduction, which confirms that the experimental trend may be interpreted as a consequence of the ring-centered reduction. For $\mathbf{1}^{2-}$, the strong DFT assignment combined with the reproduction of the iron quadrupole splitting provide a strong electronic structure assignment. It suggests the electronic configuration of the iron in $\mathbf{1}^{2-}$ is $^{1}A_{1g}$, i.e. a $^{3}A_{2g}$ Fe(II) center antiferromagnetically coupled with a ligand diradical. For $\mathbf{1}^{-}$, the assignment is unfortunately less clear. Although experimental and computational data point out to a S=1 Fe(II) center antiferromagnetically coupled with a ligand radical, DFT calculations cannot assign the exact electronic configuration of iron. Comparison of the quadrupole splitting in $\mathbf{1}^{-}$ with that of **1** and $\mathbf{1}^{2-}$ suggests a $^{3}E_{g}$(A) Fe(II) antiferromagnetically coupled with a ligand diradical. Taken alone, one could argue that the quadrupole splitting argument is rather weak. It is sensitive to various effect beyond the electronic configuration of iron,[116] and the DFT description of the quadrupole splitting in four-coordinated iron-porphyrins

is severely underestimated. However, previous NMR studies[206,210,214] suggest that the spin density is localized in the Fe-$d_{z2}$ or Fe-$d_{x2-y2}$, which is consistent with a local $^3E_g$(A) Fe(II) iron configuration, but not with a $^3A_{2g}$ local iron configuration. Therefore, experimental and computational data seemingly point out to the $^3E_g$(A) Fe(II) iron configuration antiferromagnetically coupled with a ligand radical.

At the conclusion of this study, the electronic structures of **1**, $\mathbf{1}^-$ and $\mathbf{1}^{2-}$ have been assigned unambiguously. The simultaneous assignment of all three compounds allowed us to distinguish two main features of low-valent iron porphyrins. (1) the $d_{xz}$, $d_{yz}$ and $d_{z2}$ orbitals are almost degenerate which is the main reason for the very peculiar magnetism of **1**, and (2) the reduction of **1** to $\mathbf{1}^{2-}$ is ligand-centered, yielding a doubly-reduced species that is a local Fe(II) coupled with a tetra-anion porphyrin. There is little doubt that the ligand non-innocence of the porphyrin ring plays a central role in the reactivity of this system with respect to $CO_2$ activation. Since the accuracy of our computational model for low-valent iron-porphyrins has been validated, an in-silico study of the reactivity of this system with respect to $CO_2$ reduction appears as a method of choice to understand the origin of the performances of this catalyst and retrieve chemical insights for future catalyst design strategy. This is the subject of the next chapter.

# Chapter 3: Role of the non-innocent porphyrin ligand in $CO_2$ reduction

*All the work related to section has been entirely realized by the author of this dissertation thesis.*

## I. Introduction

As emphasized in the introduction of this thesis, **1** and its derivatives exhibit the highest catalytic performance, i.e. relatively low overpotentials, high turnover frequencies and a faradaic efficiency for CO generation close to 100% in the presence of sufficiently weak acid.[16,87,89,105,236,237] Experimental findings suggested that the active species responsible for $CO_2$ conversion is $\mathbf{1}^{2-}$, a formal $Fe^0$ complex, generated by two-electron reduction of **1**. It is generally accepted that the reaction is initiated by $CO_2$ binding to $\mathbf{1}^{2-}$ to yield a $\eta^1$-$CO_2$ adduct; however, the following transformation is rather controversial. An earlier experimental study[16] suggested that to activate the C-O bond being cleaved, two Brönsted acids interact with one oxygen of the bound $CO_2$ motif to form two hydrogen bonds. And subsequently the C-O bond scission is accompanied by a single proton transfer, thereby yielding a $Fe^{II}$-carbonyl adduct and releasing a hydroxylate anion. Although this mechanistic hypothesis likely accounted for the influence of the p$K_a$ value of the Brønsted acid on the reaction rate,[16] the postulated tri-molecular reaction usually suffers from a prohibitively large positive entropic term.[238] Theoretical calculations[95] instead point out that the $\eta^1$-COO adduct first gets protonated to afford a metallacarboxylic acid, which then undergoes C-O bond cleavage concerted with a second protonation, ultimately furnishing a $Fe^{II}$-carbonyl adduct and $H_2O$. Similar mechanisms have been proposed in the literature for the reaction mediated by related systems.[48,76,78,103,104,239,240]

To dissect reaction mechanisms, thoroughly elucidating the electronic structures of key intermediates is typically a prerequisite. Using a combined spectroscopic and computational approach, Chapters 1 and 2 of this thesis unequivocally reveal that $\mathbf{1}^{2-}$ in fact contains an intermediate spin ferrous center in a $^3A_{2g}$ electronic configuration that is antiferromagnetically

coupled to a porphyrin triplet diradical tetra-anion ($S_{TPP}$ = 1), thereby yielding an overall singlet ground state, viz. $[Fe^{II}(TPP^{\bullet\bullet 4-})]^{2-}$.[17,18] As such, the two electrons used to reduce $CO_2$ stored in the TPP ligand rather than the Fe center. However, the earlier mechanistic investigations did not provide any information about the role of the non-innocent TPP ligand played in the reaction. As a matter of fact, a significant portion of homogenous $CO_2$ catalysts reported thus far are supported by well-known redox active non-innocent ligands, such as porphyrins,[95,237] corroles,[77,241] pyridine-diimines,[48,80,242] polypyridines,[103,240,243,74,244,59] and N-heterocyclic carbenes[86,245] to name a few. Although ligand non-innocence has been intensely discussed in general catalysis, its implication with respect to $CO_2$ reduction has received relatively little attention. In a broad sense, this gives rise to an intriguing question about how the non-innocent ligand interacts with the metal center to trigger the two-electron reduction of $CO_2$ to CO, because not all coordination unsaturated transition metal complexes with non-innocent ligands can function as $CO_2$ reduction catalysts.

In the present chapter, we first investigate the possible mechanistic routes leading to CO generation and possible side-products, based on the mechanistic information gathered in the introduction of this thesis. We then present a detailed analysis of the electronic-structure evolution in the course of $CO_2$-to-CO conversion catalyzed by $\mathbf{1}^{2-}$, following the most probable route. We show that ligand non-innocence is at the core of the presently investigated reactivity. Then, we compare the reactivity of $\mathbf{1}^{2-}$ with that found for $CO_2$ reduction mediated by 12 other systems selectively catalyzing CO2-to-CO conversion reaction: 8 polypyridine systems, 3 pyridine-diimine derivatives, and 1 saturated macrocycle (Figure 40). The catalytic performances of these systems are summarized in Table 3 (Introduction, section II). All catalysts mentioned in Figure 40 contain non-innocent ligands except for $[Ni(cyclam)]^+$ (cyclam = 1,4,8,11-tetraazacyclotetradecane),[246] featuring an authenticated metal-centered reduction. Comparison of all systems under consideration enables us to easily identify the crucial role of non-innocent ligands in $CO_2$ activation. On the basis of that, we propose fundamental electronic-structure requirements for $CO_2$ reduction with transition metal complexes with non-innocent ligands, which can be used as a guideline for future design of similar catalytic systems.

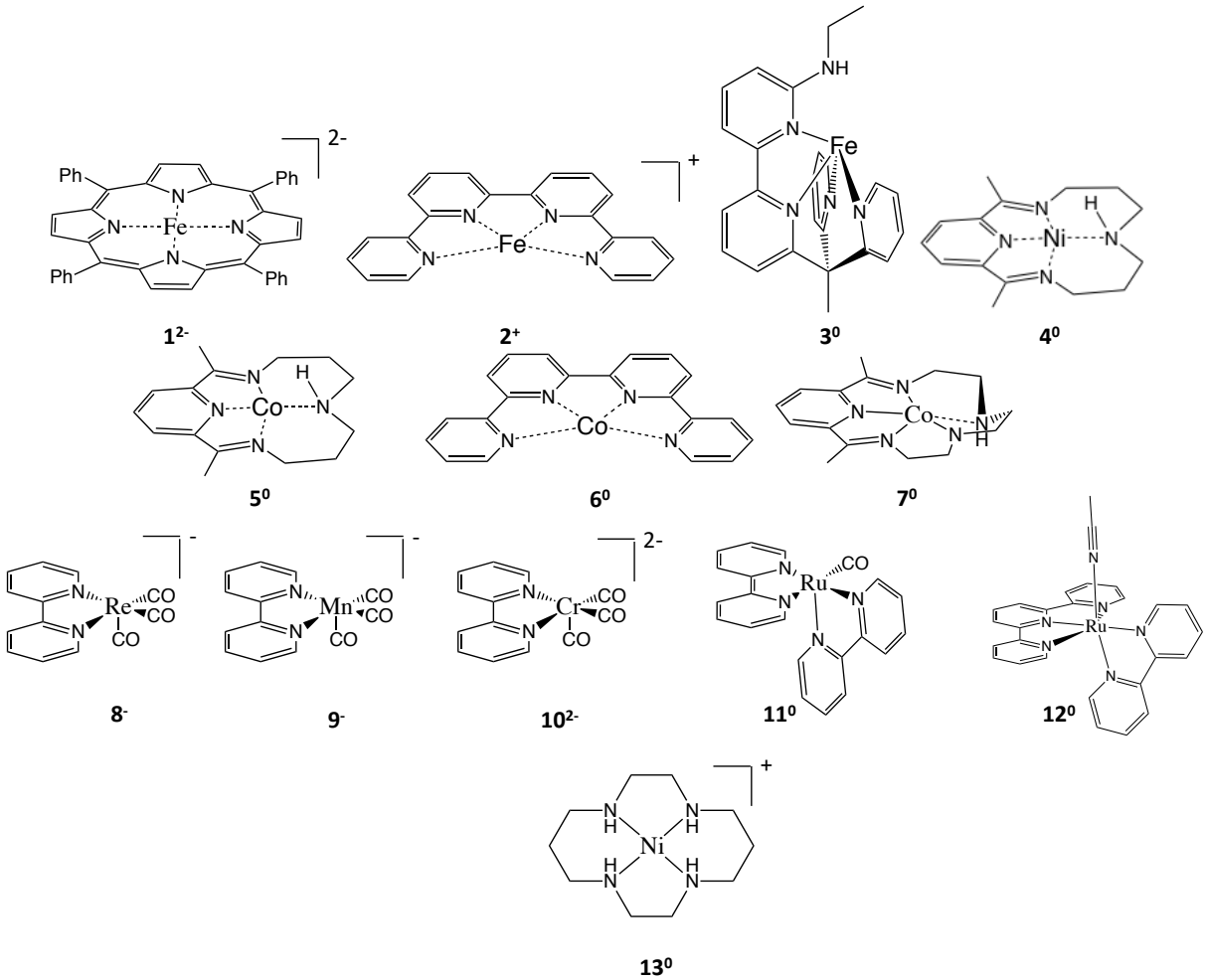


**Figure 40**: Representative examples of catalytic systems for $CO_2$-to-CO reduction with a non-innocent ligand platform, and nickel-cyclam, an example of "innocent" ligand platform. The represented systems correspond to [Fe(TPP)] (**1**$^{2-}$),[16,237,17,18] [M(qpy)] (M=Fe (**2**$^{+}$), Co (**6**$^{0}$); qpy = quaterpyridine),[76] [Fe(bpy$^{NHEt}$PY2Me)] (**3**$^{0}$, bpy$^{NHEt}$PY2Me=6'-(1,1-di(pyridin-2-yl)ethyl)-N-ethyl-[2,2'-bipyridin]-6-amine),[243] [M($N_4$H)] (M= Ni (**4**$^{0}$), Co (**5**$^{0}$); $N_4$H=2,12-dimethyl-3,7,11,17-tetraazabicyclo[11.3.1]-heptadeca-1(7),2,11,13,15-pentane),[80] [Co(L)] (**7**$^{0}$, L=2,13-dimethyl-3,6,9,12,18-pentaazabicyclo-[12.3.1]octadeca-1(18),2,12,14,16-pentaene),[48] [M(bpy)$(CO)_3$] (M= Re (**8**$^{-}$), Mn (**9**$^{-}$), Cr (**10**$^{2-}$); bpy=bipyridine), [64, 71,103,247] [Ru$(bpy)_2$(CO)] (**11**$^{0}$),[46] [Ru(tpy)(bpy)] (**12**$^{0}$, tpy=terpyridine),[59] and [Ni(cyclam)]$^{+}$ (**13**$^{+}$).[54,246]

## II. Computational details

All calculations were performed using the ORCA 4.0 program package.[183] All geometry optimizations used tight geometry convergence settings. All energy calculations used normal SCF settings ($1x10^6$ Eh). All calculations used a grid level 5. For geometry optimizations and frequency calculations, the hybrid functional B3LYP[184] was used in combination with the Def2-TZVP basis set for iron and the first coordination sphere, and Def2-SVP basis set for all remaining atoms, referred to as B3LYP/Def2-TZVP/Def2-SVP hereafter.[144] To account for solvation effects and non-covalent dispersion interactions, the solvation model CPCM[137] for DMF and D3BJ corrections due to Grimme were employed, respectively.[217,218] Electronic energies were calculated on the molecular structure obtained by geometry optimization. Final accurate electronic energies were computed at the B3LYP/Def2-TZVPP level of theory. All calculations were sped up by using the RIJCOSX approximations.[220]

Initial guesses of transition states geometries were obtained by running relaxed surface scans along the sensible normal modes or using the nudged elastic band method,[248] in particular for delicate transition states. The approximate transition-state geometries were then optimized by maximizing the energy along a given normal mode and minimizing the energy along all other normal modes. Subsequent frequency analysis on local minima revealed an occasional imaginary frequency of less than 16 $cm^{-1}$ and frequency analysis on transition states revealed an occasional imaginary frequency of less than 14 $cm^{-1}$ besides that associated with the transition state. Despite our efforts, these frequencies could not be removed neither by increasing the grid nor the geometry and SCF convergence settings. However, they can be safely attributed to numerical noises or a particularly flat energy surface owing to their magnitude.

Enthalpies were calculated following the section IV.A of the Theory chapter. In details, the zero-point energy ($E_{ZPE}$, eq. 39i), the thermal vibrational ($E_{th}$, eq. 39j), rotational ($E_{rot}$, eq. 39e) and translational ($E_{trans}$, eq. 39f) energy at 298 K calculated at the B3LYP/Def2-TZVP/Def2-SVP level of theory, were added to the electronic energy ($E_{el}$), calculated at the B3LYP/Def2-TZVPP level of theory. A $k_BT$ term was added to account for the PV term in an ideal gas approximation. To estimate the energy of the pure multiplets, an electronic energy correction ($\Delta E_{el}$) was added to the energy of the broken-symmetry wave function for intermediates featuring antiferromagnetic spin coupling between the ligand and the metal. This correction was calculated following the method by Malrieu and Trinquier.[147] Free energies at

298 K were calculated by adding the electronic ($S_{el}$, eq. 40c), rotational ($S_{rot}$, eq. 40d), translational ($S_{trans}$, eq. 40e) and vibrational ($S_{vib}$, eq. 40f) entropy contributions multiplied by the temperature to the enthalpy.[132] In the case of bimolecular reactions in gas phase, translational entropic contributions typically account for +10 to +15 kcal/mol to Gibbs free energy changes,[238] as suggested by an earlier work on $O_2$ and $CO_2$ association with transition metal centers.[54,249] As stated in the Theory chapter (subsection IV.C), the gas-phase approximation overestimates the condensed-phase free energy significantly for two reasons. First, translational freedoms are largely quenched in condensed phase, because of the volume occupied by the solvent.[134] Consequently, the translation entropy, which is directly dependent on the volume accessible to the solute, is affected by the passage from gas to condensed phase. The subsequent loss of entropy can be estimated by free-volume theory ($\Delta S_{FV}$, eq. 40e and 43). Second, gas-phase free energy does not account for the cavitation free energy ($\Delta G_{cav-disp}$, eq. 42). The latter corresponds to the free energy affording the formation of the solvent cage around the solutes. Typically, both the aforementioned effects induce negative Gibbs free energy variations for bimolecular reactions, which partially compensate the large gains of entropic origin calculated in gas phase. To account for these effects, we correct the free energy by adding two correction terms $\Delta S_{FV} T$ and $\Delta G_{cav-disp}$ according to eq. 62.

$$G = E_{el} + \Delta E_{el} + E_{ZPE} + E_{th} + E_{rot} + E_{trans} + k_B T + S_{el} T + S_{vib} + S_{trans} + S_{rot} + \Delta S_{FV} T + \Delta G_{cav-disp} \quad (62)$$

All redox potentials against the SCE electrode in DMF were calculated from the free energies of the species of the redox couple, according to eq. 37. For this purpose, $F$ the Faraday constant is taken as $F = 23.061$ kcal.V$^{-1}$.mol$^{-1}$,[250] and $E^{0}{}_{SCE}^{DMF}$, the absolute potential of the SCE electrode in DMF, is taken as 4.350 V.[251] The calculated redox potential associated with the couple **1**/**1**$^{-}$ and **1**$^{-}$/**1**$^{2-}$ are -1.17 and -1.76, respectively, which are in reasonable agreement with the experimental values of -1.07 and -1.64 V.[236,252,253] These results thus lend credence to the reliability of our present computational setup.

For orbital analysis, the doubly-occupied unrestricted corresponding orbitals (UCO)[146] (overlap between the alpha and beta orbital superior to 0.95) were localized using Pipek-Mezey algorithm.[187] The alpha and beta set in this subspace were approximated to be identical and orbitals thus obtained from the localized subspace were considered as doubly occupied. The singly-occupied UCO and the magnetic orbitals (overlap comprised between 0 and 0.95) were not localized. In the resulting set of orbitals, the d-orbitals were identified as the orbitals having predominant Fe-3d character according to the MO-wise Löwdin population analyses.

## III. Reactivity of $1^{2-}$ in $CO_2$ reduction

### A. Elucidation of the reaction pathway

#### 1) CO2-to-CO conversion: elucidation of the most probable pathway

The cyclic voltammetry data of **1** in the presence and absence of $CO_2$ suggests the activity of a type I or type III mechanism, as determined in the Introduction of this thesis (Figure 8).[16] The possibility of a type II pathway is investigated in subsection III.A.2. In details, $CO_2$ reduction to CO mediated by $\mathbf{1}^{2-}$ proceeds as follows. The reaction of $CO_2$ with catalytic active $\mathbf{1}^{2-}$ first leads to generation of the $\eta^1$-$CO_2$ adduct **A** (Figure 41), which then undergoes C-O bond cleavage to produce CO and $H_2O$ in acidic media. Clearly, the energy gained from formation of the OH bond in $H_2O$ compensates the energetic penalty required to break one C-O bond in $CO_2$. However, the mechanistic details of the C-O bond breaking have not been reached consensus yet.[16,95] To address this question, we first carefully examined two viable mechanistic scenarios (type I and III mechanisms). In mechanism III, one oxygen of the $CO_2$ moiety in **A** forms two hydrogen bonds with two phenols (PhOH), affording **C**. The subsequent C-O bond cleavage is assisted by transfer of two protons from PhOH to **A**, yielding [Fe(CO)(TPP)] (**F** in Figure 41) and $H_2O$ directly. Of note, in mechanism III as defined in the kinetic study by Costentin et. al.,[16] the cleavage of the bond releases **F** and $OH^-$, the latter being protonated in $H_2O$ in a subsequent step. However, our calculations could not reproduce that two-step mechanism, the two proton transfers occurring simultaneously upon elongation of the C-O bond. In mechanism I, a hydrogen bond is formed between a PhOH and the oxygen of the $CO_2$ moiety in **A** affording **B** (Figure 41). A proton transfer then affords the metallacarboxylic acid $[Fe(CO_2H)(TPP)]^-$ (**D** in Figure 41), and releases a phenolate ($PhO^-$). Subsequently, a second PhOH forms a hydrogen bond with the protonated oxygen of the COOH moiety in **D**, affording **E**. The subsequent bond breaking is coupled with a second proton transfer, thus leading to **F**, and releasing $H_2O$ plus a $PhO^-$. To further examine the importance of the second proton transfer in the C-O bond cleavage process in mechanism I, we also investigated a third channel (labelled mechanism IV in Figure 41). In this pathway, the C-O bond in **D** is cleaved in the absence of additional acid, yielding **F** and $HO^-$. All intermediates and pathways are summarized in Figure 41.

Although $\mathbf{1}^{2-}$ was irrefutably identified to possess a singlet ground state,[17,18] to explore possibility of spin crossover during the reaction, we investigated not only $S = 0$ but also $S = 1$ and S=2 potential energy surfaces. However, our theoretical results revealed that the aforementioned intermediates all lie at higher energy than the corresponding singlet ones and improbably participate into the actual reaction (for details, see subsection III.B.2 and Table A2). Therefore, in this subsection only discuss the singlet pathway is discussed. To avoid confusion, hereafter we add a superscript to each species to denote its spin multiplicity.

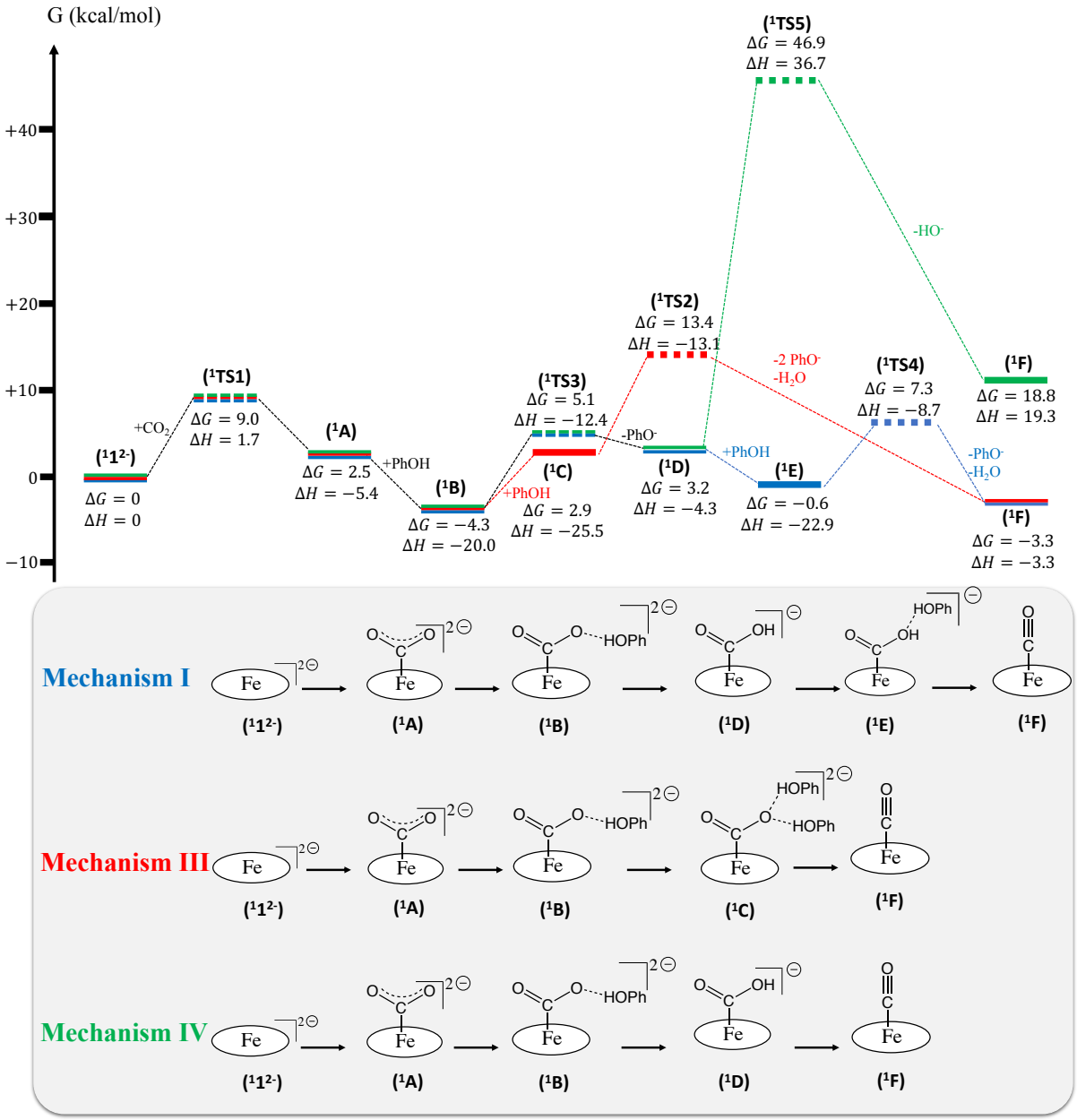


**Figure 41**: Free energy landscape of the intermediates involved in the $CO_2$-to-CO reductio1n according to type I, III and IV mechanisms. Intermediates are displayed in solid lines and transition states are displayed in dashed lines. The Gibbs free energy variation compared to the

reference, i.e. the intermediates $\mathbf{1}^{2-}$ and all reactants infinitely separated in DMF, is displayed below each intermediate. For a better understanding of the entropy contribution, the enthalpy variation (same reference) is shown below the Gibbs free energy. Intermediates belonging to mechanism I are represented in blue, those selectively belonging to mechanism III are represented in red, and those selectively belonging to mechanism IV are represented in green. (Bottom) Schematic representation of the reaction intermediates by order of generation for each pathway.

DFT calculations predicted that formation of **$^1$A** is slightly endergonic with $\Delta G$ = +2.5 kcal/mol and traverse a barrier of $\Delta G^{\neq}$ = +9.0 kca/mol of **$^1$TS1**. In fact, the positive $\Delta G$ values almost exclusively originates from the unfavorable entropic term ($-T\Delta S$), because this transformation was computed to be only slightly exothermic ($\Delta H$ = -5.4 kcal/mol), consistent with the fact that $CO_2$ is a typically weak ligand and the metal-$CO_2$ interaction is quite weak.[54,102,103] In line with this reasoning, the entropy contribution also accounts for more than 80% of the barrier.

In mechanism III, activation of the $CO_2$ motif in **$^1$A** is accomplished by forming two hydrogen bonds between the oxygen atom of the target C-O bond and two PhOH affording **$^1$C**. The formation of **$^1$C** was computed to be energetically neutral ($\Delta G$ = +0.4 kcal/mol) and no barrier could be found. In fact, the step was calculated to be highly exothermic ($\Delta H$=-20.1 kcal/mol), but this high exothermicity is compensated by an unfavorable entropic term due to the association of three fragments (**$^1$A** and 2 PhOH). The subsequent C-O bond cleavage in **$^1$C** is simultaneous with two proton transfers from the phenols to the oxygen, affording **$^1$F** and $H_2O$. The step was estimated to be significantly exergonic ($\Delta G$ = -6.2 kcal/mol), due to the tremendous entropic contribution arising from the dissociation of **$^1$C** into four fragments, i.e. the metal-carbonyl **$^1$F**, $H_2O$ and two $PhO^-$. Despite this, this step has to overcome a sizeable barrier of $\Delta G^{\neq}$ = +10.5 kcal/mol (**$^1$TS2**). This barrier can be attributed to lack of driving force associated with the C-O bond cleavage in **$^1$C** as suggested by the estimated enthalpy change ($\Delta H$ = +9.4 kcal/mol).

In mechanism I and IV, **$^1$A** interacts with one PhOH to afford **$^1$B** featuring a hydrogen bond between the O atom of the target C-O bond and the PhOH. No detectable kinetic barrier could be found for this step. The formation of complex **$^1$B** from **$^1$A** in mechanism I and IV ($\Delta G$ = –6.8 kcal/mol) is significantly favored over that of complex **$^1$C** in mechanism III ($\Delta G$ = +0.4 kcal/mol). Essentially, this difference originates from the entropy penalty associated with the formation of **$^1$C**. **$^1$B** then transforms into **$^1$D**, a significantly endergonic event ($\Delta G$ = +7.5

kcal/mol) traversing a sizeable barrier (**$^1$TS3**, $\Delta G^{\neq}$ = +9.4 kcal/mol). The free energy cost of this step originates from an unfavorable enthalpy contribution, despite **$^1$D** being stabilized by an intramolecular hydrogen bond between the COOH group and one nitrogen of the porphyrin ligand (as indicated by the short N-H interatomic distance of 2.02 Å). The barrier height mostly originates from the lack of driving force associated with the proton transfer ($\Delta H$ = +9.2 kcal/mol).

In mechanism I, the formation of complex **$^1$E** from **$^1$D** is slightly exergonic ($\Delta G$ = -3.8 kcal/mol). In more details, a strong enthalpic contribution is compensated by an unfavorable entropic term, owing to the association of two fragments (**$^1$D** and PhOH). No detectable kinetic barrier could be found for this step. The subsequent C-O bond scission in **$^1$E** ultimately affords **$^1$F**, $H_2O$ and $PhO^-$. Similar to the formation of **$^1$F** in mechanism III, this step is slightly exergonic by $\Delta G$ = -2.7 kcal/mol, owing to a tremendous entropy contribution following the dissociation of **$^1$E** into three fragments (**$^1$E**, $PhO^-$ and $H_2O$). The barrier was computed to pass through **$^1$TS4** with a barrier of +7.9 kcal/mol. This value is on par with that of **$^1$TS2** in mechanism III. In fact, the barrier largely stems from the driving force of the C-O bond cleavage, $\Delta H$ = +6.5 kcal/mol, which is is similar to that of the C-O bond breaking in mechanism III. However, although the barrier of **$^1$TS4** is commensurate with that found for **$^1$TS2** in mechanism III, **$^1$TS2** is destabilized by +6.1 kcal/mol relative to **$^1$TS4**. This difference largely arises from the prohibitive entropic term resulting from the association of **$^1$A** with two PhOH molecules, because the enthalpy of **$^1$TS2** is 4.4 kcal/mol lower than that of **$^1$TS4**.

In mechanism IV, the C-O bond in **$^1$D** cleaves without assistance of a second proton transfer, releasing **$^1$F** and a $OH^-$ ion. Unlike in mechanism I, this step is significantly uphill ($\Delta G$ = +15.6 kcal/mol) due to a prohibitive enthalpic difference ($\Delta H$ = +23.6 kcal/mol), and has to go through an impossibly high barrier of $\Delta G^{\neq}$ = +43.7 kcal/mol (**$^1$TS5**). In comparison with Pathway I and II, the high enthalpic cost in the present case stems from the absence of protons to produce $H_2O$, a thermodynamic sink, with the resulting $OH^-$. As a consequence of lack of sufficient driving force, the C-O bond breaking suffers from an exceedingly high kinetic barrier. This example confirms that the formation of a water molecule simultaneously with the C-O bond cleavage considerably lowers the associated barrier. On this basis, the pathway initially suggested by Costentin et. al.[237b] (where **$^1$C** dissociates into **$^1$F**, $PhO^-$ , PhOH and $OH^-$) is likely to go through a higher barrier than that of **$^1$TS2** in pathway I. Therefore, it can be ruled out from the most plausible pathways.

———Taken together, the present analyses suggested that mechanism I is the most favored of all explored mechanisms because the transition state associated with the C-O bond cleavage is

of the lowest energy of all the three pathways. This result is consistent with an earlier computational study.[95] However, this previous work only considered the reaction occurring on the triplet and quintet surfaces, the singlet pathways were completely ignored. Furthermore, on the basis of our theoretical results, we cannot unequivocally determine the nature of the rate-determining step to be either the formation of the $CO_2$ adduct ($\Delta G^{\neq}$=9.0 kcal/mol), the first proton transfer ($\Delta G^{\neq}$ = +9.4 kcal/mol) and the C-O bond cleavage in Pathway II ($\Delta G^{\neq}$ = +7.9 kcal/mol) since the estimated barrier differences between them fall within the typical uncertainty range of hybrid DFT functionals.[148] Despite this, the C-O bond breaking was found involve a significantly high barrier, as postulated in earlier experimental studies.[16,236] The high energy barrier associated with **$^1$TS4** ($\Delta G^{\neq}$ = 43.7 kcal/mol) show that the C-O bond cleavage must be concerted with a proton transfer, lest the step suffers from a substantial lack of driving force. This result is consistent with the experimental findings by Costentin.[16]

To verify whether our computational model satisfyingly reproduces the physics of the reaction, we computed the turnover frequency of the reaction, which requires the complete energy landscape including all intermediates and the transition states connecting them.[130,131] Indeed, the maximum turnover frequency was estimated for three different phenol concentrations ([PhOH] = 0.1, 0.75 and 3 M) using the method of Costentin et. al.[42] Our calculated values of $3.6\text{x}10^4$ $s^{-1}$, $2.6\text{x}10^5$ $s^{-1}$ and $1.10\text{x}10^6$ $s^{-1}$ are in very good agreement with the experimental values ($1.8\text{x}10^3$ $s^{-1}$, $1.5\text{x}10^4$ $s^{-1}$ and $1\text{x}10^5$ $s^{-1}$) (for details, see the annex of this chapter). This further lends credence to the reliability of our theoretical results, a necessary premise for the following analyses aiming at obtaining qualitive insights into the reaction mechanism. The turnover frequency was estimated at $2.5\text{x}10^5$ $s^{-1}$ using the method of Christiensen[129,130,131] (all reactants concentration of 1 M, for calculation details, see the annex of this chapter) also reasonably matches the experimental order of magnitude. This further lends credence to the reliability of our theoretical results, a necessary premise for the following analyses aiming at obtaining qualitive insights into the reaction mechanism.

2) Exploration of alternative type II mechanisms

The possibility that the reduction step follows the formation of the Fe-$CO_2$ adduct (type II.a mechanism) or the protonation of the adduct (type II.b mechanism) rather than preceding the formation of the adduct (type I mechanism) has been investigated (Figure 42). Unsurprisingly, the formation of the intermediate $^1$[Fe(TPP)($CO_2$)]$^-$ from **$^2$1**$^-$ requires a free energy cost of $\Delta G$ = +10.9 kcal, and has to go through a barrier of $\Delta G^{\neq}$ = +13.1 kcal/mol, mostly

due to the lack of driving force associated with the adduct formation. In mechanism II.a, the intermediate accepts an electron from the electrode, ($E^0$= -1.39 V) to form **$^1$A**, similar to mechanism I or III. In mechanism II.b, the oxidized adduct first undergoes protonation from a nearby phenol to afford the oxidized metallacarboxylic acid [Fe(TPP)($CO_2$H)]. However, this step is particularly uphill ($\Delta G$ = +18.0 kcal/mol). The intermediate subsequently accepts a second electron from the electrode to form **$^1$D** ($E^0$= -0.66 V), similar to pathway I.

In mechanisms II, the formation of the adduct is significantly more uphill than the corresponding step in mechanism I. This can be easily rationalized on the basis of the donating abilities of the metal being somewhat impaired by the higher charge of the overall complex. Because of the lack of driving force, the step admits a barrier that is about 3.7 kcal/mol higher than the highest computed barrier in mechanism I. Therefore, the kinetics of the reactions are expected to be drastically lower than that of pathway I, consistently with the experimental observation.[16]

Obviously, the redox potentials and formation energies of the intermediates are linked through a thermodynamic cycle (Figure 42). Consequently, mechanisms II can only afford milder potentials than mechanism I or III at the cost of a lower driving force for key-intermediates formation, which in turn can impair the reaction kinetics. In this case, the redox potentials of mechanism II.a ($E^0$= -1.39 V) and II.b ($E^0$= -0.66 V) are significantly milder than that of pathway I ($E^0$= -1.76 V), but intermediates and transition states in those mechanisms are significantly higher in energy than their counterparts in mechanism I. This negatively affects the kinetics and makes the mechanism I preferred over mechanism II, despite the slightly more negative required potentials. Generalizing from this case, it can be proposed that in $CO_2$ electrocatalytic reduction, the compromise between mild potential and fast kinetics determines the active mechanism: type II mechanism may prove too slow, while type I mechanisms may require the generation of active species at impossibly negative potentials, which may then undergo various facile decomposition or side reactions.

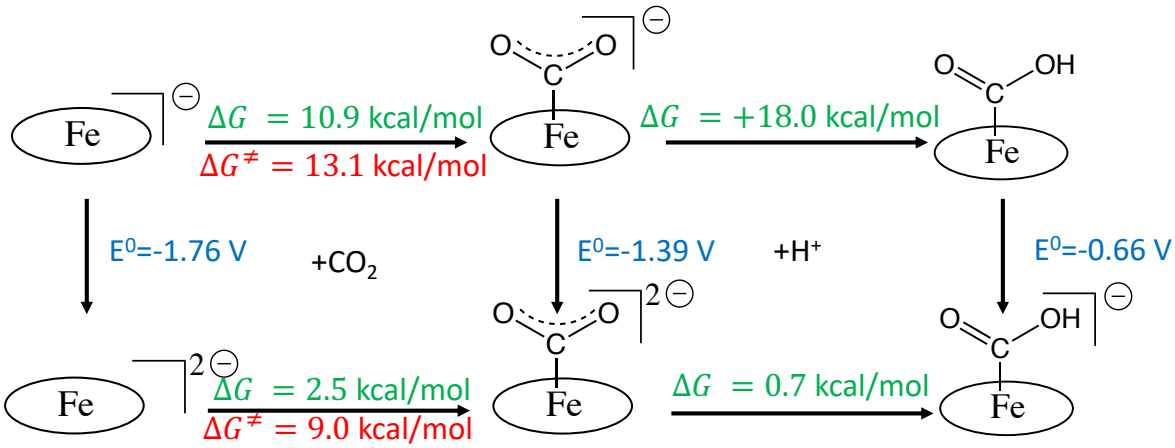


**Figure 42**: Schematic representation of the energetics of Type I versus type II.a mechanisms. Horizontal arrows represent chemical steps, while vertical arrows represent reductions at the electrode. Numbers in green represent the Gibbs free energy variation associated with each step; number in red represent the free energy barriers associated with the step; blue numbers represent the standard redox potentials (vs. SCE) of the couples.

3) Selectivity with respect to $H_2$ generation

We also computationally investigated the side reactions to furnish $H_2$ and formic acid (Figure 43). For each intermediate, three possible spin states have been calculated and only the lowest-lying is discussed here. Typically, these reactions start with formation of a metal-hydride $^1$**M** rather than the Fe-$CO_2$ adduct $^1$**A**.[52] In the case of $\mathbf{1}^{2-}$, this step is rather unfavorable ($\Delta G$= + 8.5 kcal/mol), and most importantly admits a rather large kinetic barrier ($\Delta G^{\neq}$= + 19.1 kcal/mol, $^1$**TS6**). Following this step, the reaction may proceed either towards HER or HCOOH formation. The formation of dihydrogen involves the attack of the subsequent metal-hydride on a second proton to form $^3$**1** and dihydrogen. This step is highly exergonic ($\Delta G$ = -18.4 kcal/mol), because of a favorable entropy and enthalpy variation. Alternatively, in the mechanism of formic acid generation, the next step consists in a insertion of a $CO_2$ molecule to form a Fe-OCHO adduct $^5$**N**. Our calculation show that this step is extremely exergonic ($\Delta G$= - 33.0 kcal/mol) despite an unfavorable entropy variation. An alternative pathway for HCOOH generation involves the direct interaction between the reduced metal and $CO_2$ to form an Fe-OCO adduct. However, we could not find a stable geometry for this adduct, which dissociates upon geometry optimization into $\mathbf{1}^{2-}$ and $CO_2$, showing this alternative pathway is not a viable source.

The experimental selectivity of the reaction for CO generation over HCOOH and $H_2$ generation thus originates from pure kinetic reasons. In fact, the driving force of the two latter

reactions are significantly higher than that of CO generation. However, we found that the formation of the metal-hydride admits an impossibly large barrier ($\Delta G^{\neq}$= + 19.1 kcal/mol), which prevents the formation of this key-intermediate. By comparison, the barrier controlling the formation of the Fe-$CO_2$ adduct is only $\Delta G$ = +9.0 kcal/mol. The relative accessibility of these two key intermediates is of the outmost importance, since it determines whether the reaction is driven towards CO or HCOOH/$H_2$ generation. Hence, our calculations predict the formation of HCOOH and $H_2$ is prohibited for kinetic reason, due to the impossibly high-lying transition state associated with the formation of the metal-hydride adduct. A similar result was found by Zhang and al. for a related iron-porphyrin system[105] and by Keith and al. for [Re(bpy)$(CO)_3$]K.[103]

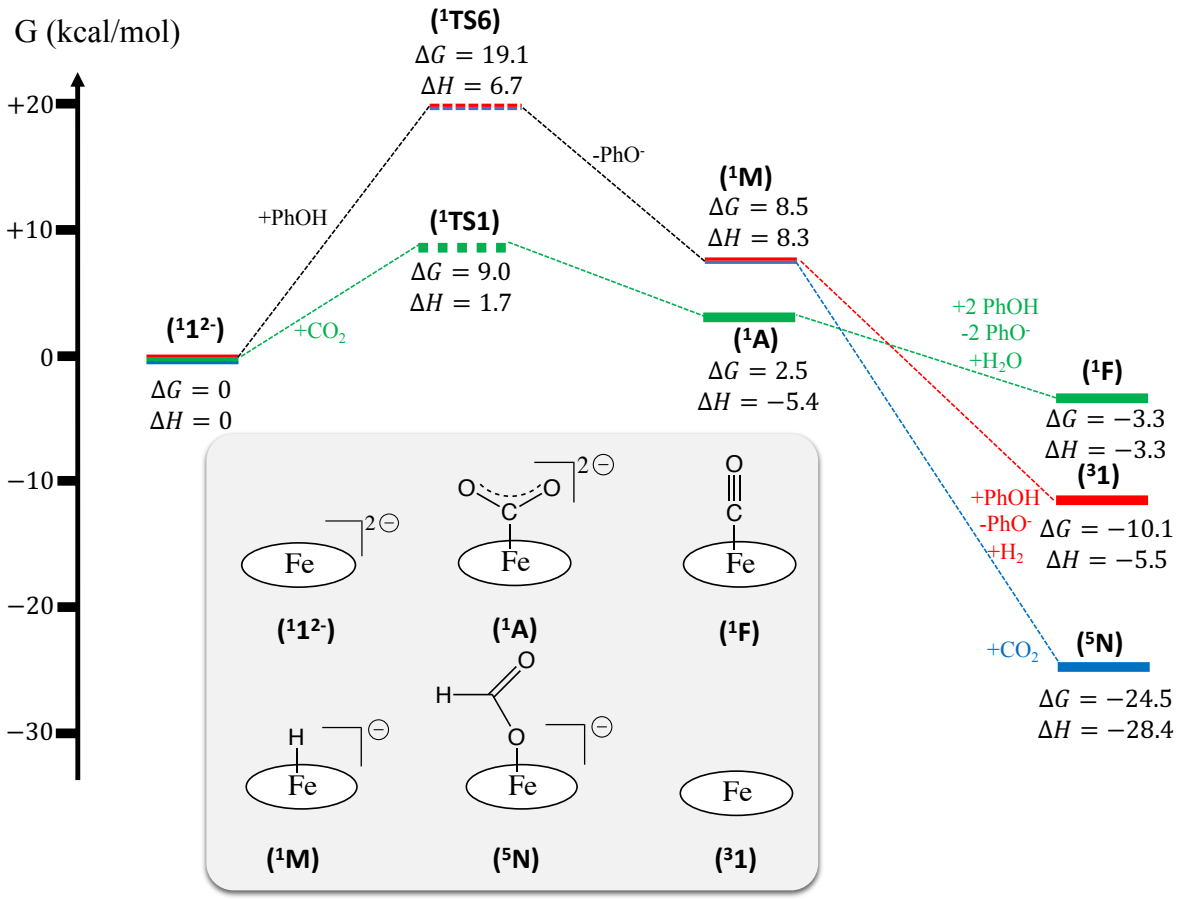


**Figure 43**: Free energy landscape of key-intermediates and transition states involved in the $CO_2$-to-CO conversion reaction (Pathway II, green lines), hydrogen evolution (red lines) and HCOOH generation (blue lines). Intermediates are displayed in solid lines and transition states are displayed in dashed lines. The Gibbs free energy variation and the enthalpy variation are displayed below each intermediate. The schematic representation of each intermediate is shown below the free energy surface.

## B. Electronic structure analysis of the reaction

### 1) Orbital analysis of the intermediates in mechanism I

In the following, the changes in the electronic structure of mechanism I, most probable of all investigated mechanisms, was scrutinized. On the basis of that, we attempted to correlate the electronic structure of $^{1}\mathbf{1}^{2-}$ with its exceedingly high activity of $CO_2$ functionalization, in particular, aiming to pinpoint the role played by the non-innocent TPP ligand.

As elaborated in Chapter 2, the bonding of $^{1}\mathbf{1}^{2-}$ is best described as an intermediate spin $Fe^{II}$ center ($S_{Fe}$ = 1) antiferromagnetically coupled to a triplet diradical TPP tetra-anion ($S_{TPP}$ = 1), thereby yielding an overall singlet ground state (Figure 44, A). Specifically, the Fe center features an electronic configuration of $(d_{xy})^2(d_{z2})^2(d_{xz})^1(d_{yz})^1$, and there are two electrons occupying the low lying TPP centered $\pi^*$ $e_g$ orbitals labelled as$1e_g(xz)$ and $1e_g(yz)$. The Fe-$d_{xz/yz}$ and $1e_g$ orbitals forms two spin-coupled pairs that represent two antiferromagnetic coupling pathways. It should be re-emphasized that the magnetic orbitals (Fe-$d_{xz/yz}$ and $1e_g$) belong to the same representation ($e_g$) of the effective $D_{4h}$ point group of $^{1}\mathbf{1}^{2-}$; therefore, their interactions are symmetry-allowed as indicated by the computed considerable overlap of the two spin coupled pairs (0.33). As such, in the resulting MOs, the Fe $d_{xz/yz}$ atomic orbitals (93.9 and 6.4% in the $\alpha$ and $\beta$ magnetic orbitals, respectively) mix heavily with the TPP-$1e_g$ (6.1 and 93.6%) fragment orbitals. If the fragment orbitals of the $TPP^{\bullet\bullet 4-}$ ligand and the Fe center transformed as different irreducible representation of the effective $D_{4h}$ point group, their exchange interaction would feature ferromagnetic coupling on the grounds of the Goodenough-Kanamori rule[254] rather than antiferromagnetic coupling as determined experimentally.[17,18,179] It is because of this symmetry-allowed exchange interaction that $^{1}\mathbf{1}^{2-}$ possesses a singlet ground state. The triplet and quintet states were computed to be destabilized by 5.6 and 12.1 kcal/mol, respectively, relative to the singlet state (Table A2).

As depicted in Figure 44, B, the driving force to generate $^{1}\mathbf{A}$ largely stems from the $\sigma$-donation from the doubly occupied Fe-$d_{z2}$ orbital to the vacant $CO_2$ in-plane $\pi^*$ orbital ($\pi_{ip}^*$). The latter constitutes one of the lowest unoccupied molecular orbitals (LUMOs) of $CO_2$ that has much larger lobe at the central C atom than those at the two terminal O atoms. The most notable geometric feature of $^{1}\mathbf{A}$ is bending of the $CO_2$ ligand with an O-C-O angle of $130^0$ compared to $180^0$ for uncoordinated $CO_2$ molecules. As elaborated earlier,[54] such a geometric distortion not only significantly decreases the energy of the LUMO, but also increases the C-p character in it. Thus, the energy difference between the $CO_2$-$\pi_{ip}^*$ and Fe-$d_{z2}$ orbitals drops and

their overlap becomes enlarged. Apparently, both factors enhance their interaction. Despite this, the resulting bonding MO (1σ) contains only 32% $CO_2$ π* parentage; hence, the bonding is quite weak, consistent with the estimated vanishing formation enthalpy of **$^1$A** (see subsection III.A). Nevertheless, this essentially dative interaction can be viewed as partial electron transfer from the Fe center to the $CO_2$ motif. Interestingly, the MO analyses revealed that the formation of **$^1$A** is accompanied with an intramolecular *β* electron transfer from the $1e_g(yz)$ MO to Fe-$d_{yz}$. This electron transfer occurs only for the spin-coupled pair consisting of the Fe-$d_{yz}$ and $1e_g(yz)$ MOs, instead of the other pair. Different from **$1^{2-}$**, the Fe-$d_{xz}$ and Fe-$d_{yz}$ orbitals in **$^1$A** are not energetically degenerate anymore, because the former is destabilized by the repulsion with the doubly occupied *σ* orbitals of the two C-O bonds; while the latter is stabilized by its back-donation to the $CO_2$ out-of-plane π* orbital ($\pi_{op}$*), the other LUMO of $CO_2$. Consequently, the electronic structure of **$^1$A** is best formulated as a low $Fe^I$ center ($S_{Fe}$ = ½) bound to an approximately charge-neutral $CO_2$, interacting with a TPP radical ligand ($S_{TPP}$ = 1/2) in an antiferromagnetic fashion, thus giving an overall singlet ground state. More importantly, the loss of the electron density of the Fe center resulting from the Fe-to-$CO_2$ σ- and backdonation is compensated by the TPP-to-Fe electron transfer, and during the $CO_2$ association process the electron density of the Fe center does not vary drastically.

In fact, the bending of the $CO_2$ motif in **$^1$A** is primed for the protonation to afford **$^1$D** (Figure 44, C), because, besides the electronic structure discussed above, such a geometric distortion also raises the energy of its highest occupied molecular orbital (HOMO), an antisymmetric combination of the two O lone pairs and in-plane C-p orbital, and simultaneously increases the weight of the O-p orbital in it.[54] Our theoretical results revealed that upon protonation, the $CO_2$-$\pi_{ip}$* character in the doubly occupied 1σ bonding MO increases from 32% to 56%, thereby indicating substantial covalent character for the Fe-$CO_2$ σ-bonding. In analogy to the preceding step, the protonation is companied by a *β* electron transfer from the porphyrin-based $1e_g(xz)$ MO to the Fe-$d_{xz}$ orbital, which again prevents drastic change in the electron density of the Fe center. The physical oxidation state of the Fe center cannot be unambiguously assigned because of the high covalency of the C-O bond. Instead, the bonding of **$^1$D** has to be described as a resonance hybrid of a low spin $Fe^{II}$ ion ($S_{Fe}$ = 0) bound to $(CO_2H)^-$ ligand and a low spin $Fe^0$ center ($S_{Fe}$ = 0) coordinated by a $(CO_2H)^+$ ligand. This complex electronic-structure description indeed suggest that one-electron reduction of the $CO_2$ ligand is complete, in line with the calculated Fe-$CO_2$ bond distance shortening from 2.02 Å in **$^1$A** to 1.89 Å in **$^1$D**. As such, conversion of **$^1$A** to **$^1$D** is best described as a concerted proton-electron transfer and C-O bond cleavage (CPETBC) as postulated by earlier experimental studies.[16,97,98,99]

As bored out from the MO diagram of **$^1$TS4** (Figure A2), in the following proton-assisted heterolytic C-O bond breaking, the two electrons originally occupying the $\sigma$-bonding C-O orbital enter into the lone pair of the oxygen in the nascent $H_2O$ molecule. Meanwhile, due to the exceedingly high electron-accepting capability of the resulting formal carbocation center, in **$^1$F** the bonding MO 1$\sigma$ acquire more CO character (61%) and the weight of the Fe-$d_{z2}$ atomic orbital decreases to 35%; thus, **$^1$F** contains a low spin ferrous center bound to a CO ligand and features strong back-donation from the doubly-occupied Fe-$d_{xz}$ and Fe-$d_{yz}$ orbitals to the C-O $\pi$* orbitals. At this stage, the two-electron transfer from the Fe $d_{z2}$ orbital to the $CO_2$-$\pi_{ip}$* orbital is largely completed. Taken together, this step can be interpreted as a concerted proton-electron transfer and C-O bond cleavage.

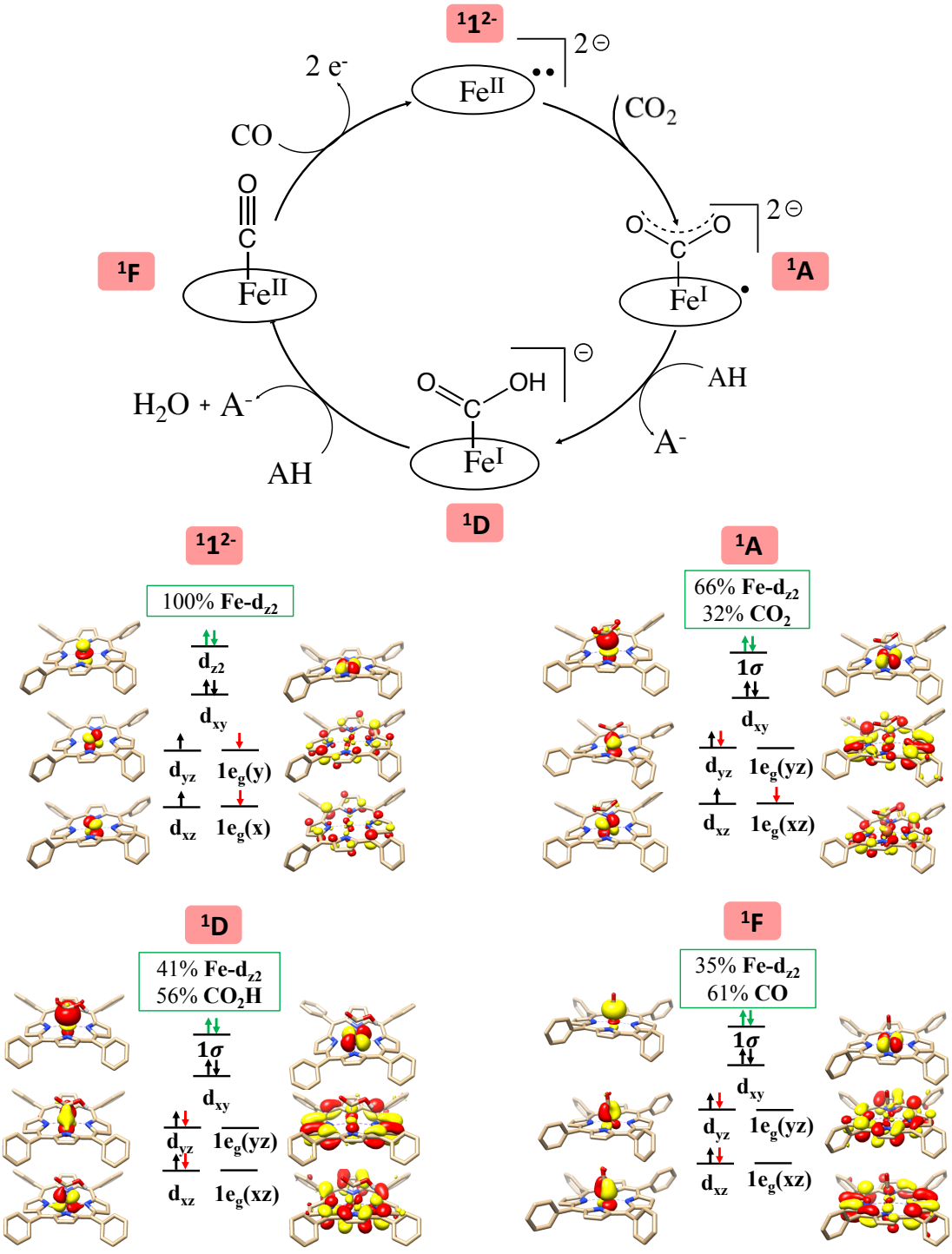


**Figure 44**: (Top) catalytic cycle of CO2-to-CO conversion catalyzed with $\mathbf{1}^{2-}$ (mechanism I). (Bottom) associated electronic structure of the intermediates $\mathbf{1}^{2-}$ (A), $^{1}\mathbf{A}$ (B), $^{1}\mathbf{D}$ (C) and $^{1}\mathbf{F}$ (D). The electrons occupying the d-orbitals of the iron, the 1σ orbital and the redox-active orbitals of the TPP ligand are represented by arrows. Electrons involved in the ligand-to-metal intramolecular transfer are shown as red arrows. Electrons involved in the metal-to-$CO_2$ charge transfer are shown as green arrows. The Fe and $CO_2$/$CO_2H$/CO Löwdin population of the 1σ bonding orbital formed by interaction of the iron center and the ligand is displayed circled in green. For clarity, all hydrogens are hidden except the hydrogen of the $CO_2H$ motif.

2) The role of the non-innocent porphyrin ligand in the reaction

Due to the non-innocence of the TPP ligand, the active species $^{1}\mathbf{1}^{2-}$ is formed from $^{3}\mathbf{1}$ by primarily ligand-centered two-electron reduction. This enables the generation of $^{1}\mathbf{1}^{2-}$ at a milder potential compared to what would be expected for a metal-centered reduction. In fact, because the electron acceptor is the highly delocalized $1e_g$ orbitals, the additional electronic density is delocalized over the 24 atoms of the porphyrin ligand and is expected to suffer moderate interelectronic repulsion. Furthermore, this electron transfer is expected to induce rather low degree of the geometric distortions and hence suffers from substantially attenuated reorganization energy. This contrast with metal centered redox processes with much more compact and localized d-orbitals functioning as the redox active orbitals. Typically, two-electron reduction of the metal center hardly occur, in particular for 3d transition metals. Even if such redox events could happen, the reduction potential should be exceedingly negative. The resulting highly reactive complexes are thus expected to undergo various more facile transformations and perhaps cannot participate in $CO_2$ reduction. By contrast, for $^{1}\mathbf{1}^{2-}$, the complete delocalization of the additional electrons onto the conjugated porphyrin π-system provides a certain degree of stabilization of such a highly charged species. This probably explains why $^{1}\mathbf{1}^{2-}$ can be generated at a rather mild potential and exhibits an almost quantitative Faraday efficiency for CO generation.

As discussed above, each elementary step of the reaction consists of two separate electron-transfer events. One is the two-electron transfer from Fe-$d_{z2}$ to $CO_2$ $\pi_{ip}$* orbitals that is required for conversion of $CO_2$ to CO, and the other is the two-electron transfer from $1e_g$ to Fe-$d_{xz/yz}$ orbitals. Indeed, in the present case, the $CO_2$ binding has to happen at the Fe center.[255] Due to the completely delocalized nature of the π-electrons, all atoms of TPP possess more or less identical electron density. On the contrary, the Fe center is more reactive, because its $d_{z2}$ orbital has appropriate shape and can preferentially interact with the $CO_2$ π* LUMOs.[54] Hence, the $CO_2$ reduction must happen at the Fe center, but the required reducing equivalents are stored at the ligand. In essence, the intrinsic electron donor is $TPP^{\bullet 4-}$, and the Fe center merely acts as a wire to effect the electron transfer from $TPP^{\bullet 4-}$ to $CO_2$.

Because the two aforementioned electron transfers are *synchronized*, the electron density of the Fe center does not vary significantly throughout the reaction; therefore, the iron center retains its donating abilities despite the metal-to-$CO_2$ electron transfer. Furthermore, the distortion energy resulting from the adjustments in the first coordination sphere of the Fe center during the electron transfer is considerably reduced. This analysis, at least in part, rationalizes

why $^{1}\mathbf{1}^{2-}$ featuring a non-innocent TPP ligand exhibits the exceedingly high catalytic activity towards $CO_2$ reduction. The fundamental importance of the electron transfer events synchronization is best illustrated by the investigation of the triplet and quintet energy surface (Figure 45, Table A2).

As detailed in Figure 45, the triplet state of $[Fe(TPP)]^{2-}$ ($^{3}\mathbf{1}^{2-}$) also contains an intermediate spin ferrous center but interacting with a singlet diradical TPP tetra-anion with one $\alpha$ electron and one $\beta$ electron occupying its $1e_g$ orbitals. Subsequently, the formation of the Fe-$CO_2$ adduct ($^{3}\mathbf{A}$) is characterized by a weak $\sigma$-donation from the Fe-$d_{z2}$ orbital to the $CO_2$ $\pi_{ip}$*, concomitant with a spin-allowed electron transfer of a $\beta$-electron from the $1e_g(yz)$ to the Fe-$d_{yz}$ orbital. Hence, $^{3}\mathbf{A}$, contains a local $Fe^{I}$ similar to $^{1}\mathbf{A}$, although the former is *ferromagnetically* coupled with a porphyrin tri-anion. Consequently, we find the formation cost of $^{3}\mathbf{A}$ ($\Delta G$ = - 0.1 kcal/mol) is similar to that of $^{1}\mathbf{A}$ ($\Delta$G = +2.5 kcal/mol) within the error range of DFT. On the other hand, the protonation of the adduct ($^{3}\mathbf{D}$) does not involve a second electron transfer like in its singlet counterpart because the transfer of the $\alpha$-electron from the $1e_g(xz)$ to the Fe-$d_{xz}$ metal is spin-forbidden. Hence, the metal center in $^{3}\mathbf{D}$ is best described as a resonance hybrid form of a $Fe^{III}$ ion bound to a $(CO_2H)^-$ ligand and a $Fe^{I}$ center bond to a $(CO_2H)^+$ ligand, ferromagnetically coupled to a porphyrin tri-anion. The iron in the $^{3}\mathbf{D}$ intermediate has a higher oxidation state than that of $^{1}\mathbf{D}$ (see subsection III.B.1). Consequently, the formation cost of $^{3}\mathbf{6}$ is highly unfavorable ($\Delta G$ = +10.4 kcal/mol) whereas the formation of $^{1}\mathbf{D}$, facilited by a second intramolecular electron transfer, is barely uphill ($\Delta$G = +0.7 kcal/mol). This example nicely illustrates how the coupling of the two electron transfer events (Fe-to-$CO_2$ and TPP-to-Fe) significantly reduces the energy of the intermediates, and thus has a positive effect on the kinetics of the reaction.

The quintet state of $[Fe(TPP)]^{2-}$ ($^{5}\mathbf{1}^{2-}$) contains a ferrous Fe(II) ($S_{Fe}$=1) ferromagnetically coupled with a porphyrin diradical ($S_{TPP}$=1), i.e. with two $\alpha$ electrons occupying its $e_g$ orbitals. Interestingly, the Fe-$CO_2$ adduct ($^{5}\mathbf{A}$) was found unstable and spontaneously dissociated into $^{5}\mathbf{1}^{2-}$ and $CO_2$ upon geometry optimization. This constitutes a major difference with the singlet and triplet pathways where the corresponding adduct is stable. Unlike in the singlet and triplet pathways where the adduct formation is companied with one TPP-to-Fe electron transfer, in this case any such transfer is spin-forbidden. Consequently, the donating ability of the metal center remains insufficient to bind $CO_2$. The protonated adduct ($^{5}\mathbf{D}$) is stable but significantly higher in energy than $^{1}\mathbf{D}$ ($\Delta G$ = +18.5 kcal/mol), at least in part due to the higher iron oxidation state in $^{5}\mathbf{D}$ compared to $^{1}\mathbf{D}$. Notably, $^{5}\mathbf{D}$ is even more high-lying than $^{3}\mathbf{D}$ ($\Delta G$ = +5.8 kcal/mol), although both intermediates contain an iron center in the same oxidation state. This difference

can be traced back to the electronic configuration of the iron. **$^5$D** differs from **$^3$D** by the promotion of one electron from the Fe-$d_{yz}$ orbital to the antibonding 1σ* (antibonding combination of the Fe-$d_{z2}$ and $CO_2$-$\pi_{ip}$*). The latter is much higher lying due to unfavorable repulsive interactions with the $CO_2H$ moiety, which explains why **$^5$D** is destabilized with respect to **$^3$D**.

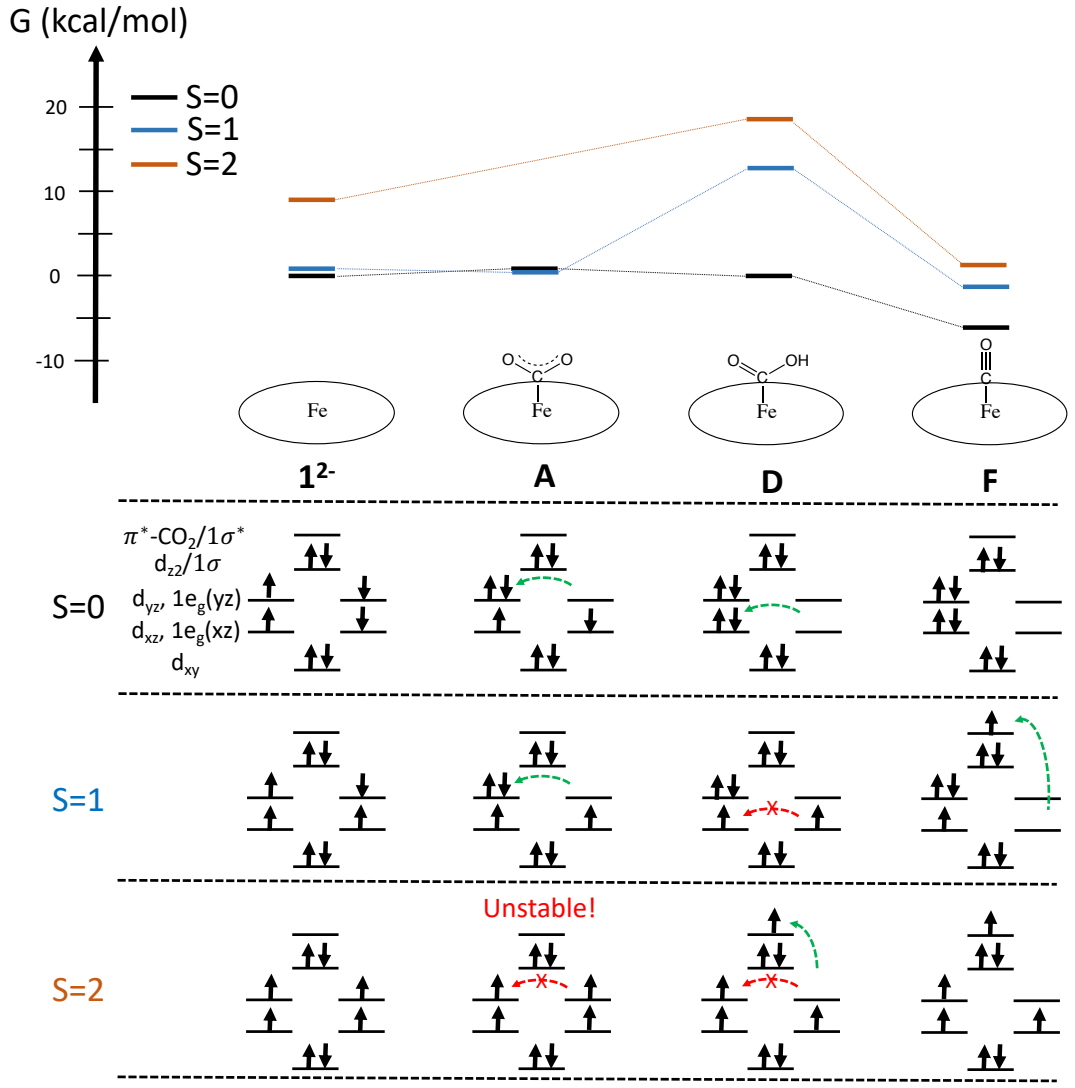


**Figure 45**: (Top) Representation of the singlet (black), triplet (blue) and quintet (brown) free energy landscape for the mechanism I, up until the formation of the metallacarboxylic acid. Each bar corresponds to the energy of the intermediate schematized below the diagram, i.e. **$1^{2-}$** , **A**, **D** and **F**. (Bottom) schematic representation of the electronic structure of the system , i.e. occupied d-shell of iron, redox-active orbitals of the TPP ligand ($1e_g$), bonding (1σ) and antibonding (1σ*) combination of the Fe-$d_{z2}$ and $CO_2$-π* orbitals in the intermediates **$1^{2-}$**, **2** and **6**, depending on the overall spin state of the intermediate, i.e. .S=0 (top), S=1 (middle) or S=2 (bottom). Of note, in **$1^{2-}$**, the Fe-$d_{z2}$ and $CO_2$-π* orbitals do not overlap, hence 1σ and 1σ* are

replaced by $d_{z2}$ and $CO_2$-$\pi^*$, respectively. Electrons in the orbitals are represented by black arrows. Green dashed arrows represent spin-allowed electron transfers, and red dashed arrows represent spin-forbidden electron transfers. For the electronic structure of the intermediate $^5$**2**, the mention "Unstable" accounts for the fact that the adduct dissociates spontaneously into $^5$[Fe(TPP)]$^{2-}$ and $CO_2$.

The above study on the triplet and quintet energy surfaces highlights the importance of the electron transfer synchronization. Hence, because ligand-to-metal electron transfers are prohibited, $^3$**D** and $^5$**D** both contains a metal center in a higher oxidation state than the iron of $^1$**D**. Consequently, both $^3$**D** and $^5$**D** admit a formation free energy cost that is higher than the highest barrier in the singlet mechanism. Likewise, the formation of $^5$**A** is entirely prohibited, because both electrons remain on the TPP platform and cannot participate in the metal-centered binding of $CO_2$. All these elements strengthen our assumption that the synchronization of two electron transfers is fundamentally crucial to the reaction kinetics.

How does the system synchronize the TPP-to-Fe electron transfer with the Fe-to-$CO_2$ electron transfer? First, the TPP-1$e_g$ and Fe-$d_{xz,yz}$ fragment orbitals have comparable energy, otherwise the electron transfer would not be thermodynamically feasible. Most importantly, both sets transform as the same irreducible representation of the effective $D_{4h}$ point group of $^1$**1**$^{2-}$. Consequently, they form two spin-coupled pairs with considerable overlap. The antiferromagnetic coupling between the ligand and the metal has two consequences. First, it lowers the energy of the singlet energy surface compared to that of higher spin multiplicities, and ensures the electron transfer does not incur an energetically unfavorable spin crossover.[256] Second, the system carries out the TPP to Fe transfer simultaneously with the Fe to $CO_2$ transfer as the latter increases the effective charge of Fe. In fact, the loss of Fe electronic density due to the Fe to $CO_2$ transfer is immediately compensated by an increasing TPP to Fe electron delocalization in the magnetic orbitals. Indeed, as seen in Figure 46, along the reaction coordinates of the formation of $^1$**A**, the Fe+$CO_2$ population of the $\beta$-1$e_g$(x) magnetic orbital slowly increases, stepping from about 6% in $^1$**1**$^{2-}$ to about 20% in $^1$**TS1**, to finally reach 98% in $^1$**A**. This mode of continuous transfer minimizes the variation of electronic density of the metal center along the reaction coordinates. In all likelihood, this participates in lowering the activation barrier by increasing the donating abilities of the metal center, even when a complete electron transfer is not thermodynamically feasible. Hence the antiferromagnetic coupling is pivotal in synchronizing the two electron-transfer events.

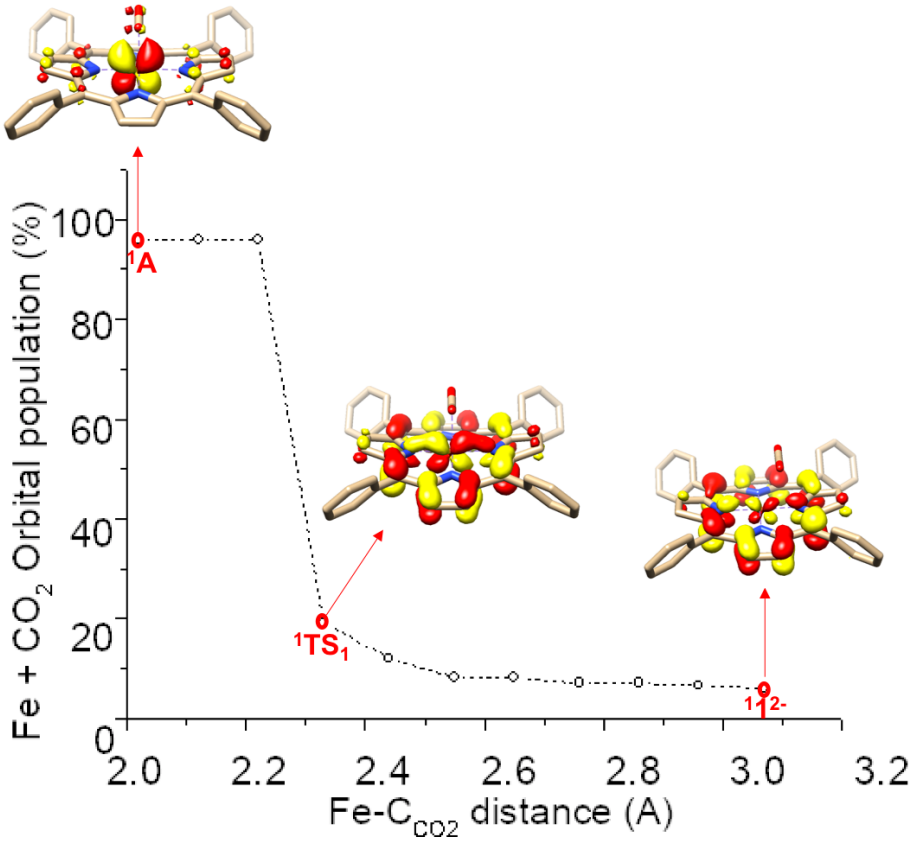


**Figure 46***:* Evolution of the $\beta$ (spin-down) magnetic orbital $1e_g(x)$ as a function of the Fe-$C_{CO2}$ distance during the formation of the intermediate **$^1$A**. The dots correspond to the structures calculated along the relaxed surface scan. The red dot corresponds to the transition state **$^1$TS1**.

## IV. General patterns of ligand non-innocence in $CO_2$ reduction

### A. Comparison with representative systems

Besides **$^1$1$^{2-}$**, we have analyzed the electronic structure evolution in the course of the $CO_2$-to-CO reactions mediated by at least eleven related catalysts (Scheme 1) that are also supported by non-innocent ligand platforms (for details see Supporting Information ). For all these systems, the metal center acts as the active site for $CO_2$ functionalization, but the non-innocent ligand acts as the electron reservoir. Like **$^1$1$^{2-}$**, this requires the metal-to-$CO_2$ electron transfer should be coupled to the ligand-to-metal electron transfer. Our results demonstrated that the main differences among them lies in the nature of the chemical steps involving a ligand-to-metal electron transfer. Based on this, these catalysts are divided into three categories.

Category I includes $^{1}\mathbf{1}^{2-}$, $^{2}\mathbf{2}^{+}$ (Figures A4) [76], $^{3}\mathbf{3}^{0}$ (Figure A5)[243] and $^{1}\mathbf{4}^{0}$ (Figure A6). The active species consists of a metal center in its usual oxidation state that is either antiferromagnetically coupled to a one- ($^{2}\mathbf{2}^{+}$) or two-electron reduced ligand diradical ($^{1}\mathbf{1}^{2-}$ and $^{3}\mathbf{3}^{0}$), or coupled with a closed-shell, doubly-reduced ligand ($^{1}\mathbf{4}^{0}$). The category is distinguished by the ligand-to-metal electron transfer being achieved by two separate one-electron transfers; one takes place during the $CO_2$ adduct formation step, and the other during the first protonation step.

1) Comparison with Category II

Category II is distinguished by the ligand-to-metal electron transfers taking place in two separate events: one takes place during the $CO_2$ adduct formation step; the other during the C-O bond cleavage step. Category II catalysts include, $^{2}\mathbf{5}^{0}$ , $^{2}\mathbf{6}^{0}$ and $^{2}\mathbf{7}^{0}$, [48,76,239] which either feature a metal center antiferromagnetically-coupled to a two-electron reduced ligand ($^{2}\mathbf{5}^{0}$, $^{2}\mathbf{6}^{0}$), or a metal center coupled to a closed-shell, doubly-reduced ligand ($^{2}\mathbf{7}^{0}$). Either way, the electron transfers describing the reaction mechanism are identical for these three catalysts. Here we take the reaction with $^{2}\mathbf{5}^{0}$ as an example to discuss the electronic structure evolution along the reaction coordinate, and summarize those for $^{1}\mathbf{6}^{0}$ and $^{2}\mathbf{7}^{0}$ in the Annex of this chapter (Figures A7, and A8).

The system $^{2}\mathbf{5}^{0}$ has been extensively studied and is known to catalyze selective $CO_2$ to CO conversion reaction in wet conditions. Computational and experimental studies suggest ligand non-innocence,[80,102] a notion in line with the notorious non-innocent character of the Pyridine-diimine (PDI) ligand platform resolved experimentally in several transition metal complexes. [242,257,258] In fact, our calculations suggest that $^{2}\mathbf{5}^{0}$ is best described as a low spin $Co^{II}$ ($S_{Co}$=1/2) antiferromagnetically coupled with a $N_4H^{\bullet 2-}$ di-anion radical ($S_{N4H}$=1). Specifically, our orbital analysis (Figure 47, A) suggests that two unpaired electrons populate the orbitals 1a' and 1a'', labelled according to their symmetry representation in the Cs point group. The former is mainly composed of the $N_4H$-centered $N_4H$-$\pi_{a'}$* fragment orbital. The latter is an admixture of Co-$d_{yz}$ fragment orbital (29%) and a ligand-based $N_4H$-$\pi_{a''}$* fragment orbital (71%). Consequently, both 1a'' and Co-$d_{yz}$ form a spin-coupled pair. Of note, the heavy mixing of the Co-$d_{yz}$ and $N_4H$- $\pi_{a''}$* fragment orbitals is only possible because both transform in a A'' representation in a Cs point group. Otherwise, the mixing would be energetically unfavorable.

The molecular structures of the intermediates involved in the $CO_2$-to-CO reduction have been extensively studied in the literature and are summarized in Figure 47.[94] Upon $CO_2$ binding (intermediate **$^2$G**, Figure 47, B), the doubly-occupied Co-$d_{z2}$ orbital slightly mixes with the empty $\pi_{ip}$* orbital of the $CO_2$. The resulting bond is essentially dative, as shown by the Löwdin population of the resulting 1σ bonding orbital (77% Co, 23% $CO_2$). This step is coupled with a first electron transfer from the $N_4H$-$\pi_{a''}$* orbital to the Co-$d_{yz}$, such that the resulting intermediate is best described as a low-spin $Co^I$ ($S_{Co}$=0) weakly bound to a neutral $CO_2$ ligand, plus a radical anion $N_4H^{\bullet-}$ ($S_{N4H}$=1/2). Hence, this step is companied with a one-electron transfer from the $N_4H$ ligand to the cobalt. The subsequent protonation of the adduct yielding the intermediate **$^2$H** (Figure 47, C) increases the covalence of the bond between the Co center and the $CO_2H$ motif, as illustrated by the Löwdin population of the bonding orbital 1σ (43% Co, 51% $CO_2H$). Of note, the step is characterized by a partial electron transfer from the ligand to the metal. Indeed, unlike in the previous intermediate the singly-occupied 1a' orbital corresponds to a mixture of the antibonding $1\sigma^*$ fragment orbital (antibonding counterpart of 1σ, Co-$d_{z2}$ 44% and $CO_2H$ 10%) and the $N_4H$-$\pi_{a''}$* fragment $\pi^*$ orbital (46%). This mixture is possible because (1) the $1\sigma^*$ and the ligand-based $N_4H$-$\pi_{a'}$* fragment orbitals are symmetry compatible (a' representation in a Cs point group), and (2) these orbitals overlap significantly owing to the axial interactions between the Co-$d_{z2}$ and the $CO_2H$ motif. Were these two conditions not fulfilled, the mixing of these fragment orbitals would not be energetically favorable, and the partial transfer would not happen. The oxidation state of the cobalt in this intermediate is ambiguous because of the covalence of the metal-$CO_2H$ bond and the delocalized nature of the radical electron. In fact, the cobalt can be described as a resonant structure between a $Co^{III}$ ($S_{Co}$=0) and $Co^0$ ($S_{Co}$=1/2) center, while the ligand is a resonant structure between a neutral $N_4H$ and an anion radical $N_4H^{\bullet-}$, and the $CO_2H$ motif is a resonant structure between a $(CO_2H)^-$ and $(CO_2H)^+$ ligand. In terms of electronic transfer events, this step can be interpreted as a one-electron transfer from the metal to the $CO_2$ concomitant with a partial electron transfer from the ligand to the metal. Finally, the subsequent cleavage of the C-O bond affords a metal-carbonyl adduct **$^2$I** and $H_2O$ (Figure 47, D). The formal carbocation has exceedingly high electron-accepting abilities compared to $CO_2$, thus increasing considerably the CO character of the bonding orbital 1σ (26% Co, 70% CO). This step is concerted with the completion of the electron transfer from the $N_4H$-$\pi_{a'}$* orbital to the antibonding $1\sigma^*$ orbital. Consequently, the cobalt is unambiguously described as a $Co^{II}$ center bound to a carbonyl ligand. Hence this step corresponds to the second metal-to-$CO_2$ electron transfer and the completion of the previously partial electron transfer from the ligand to the metal.

Like for $\mathbf{1}^{2-}$, the reaction process is associated with two intramolecular electron transfers events: a metal-to-$CO_2$ transfer happening through $\sigma$-donation of the doubly-occupied $d_{z2}$ to the unoccupied $CO_2$-$\pi_{ip}^*$ orbital, and a ligand-to-metal electron transfer compensating the loss of electronic density on the metal center. Much like $\mathbf{1}^{2-}$, these electron transfer events are synchronized efficiently via the mixing of the primarily ligand-based electron-donating orbitals ($N_4H$-$\pi_{a''}$*, $N_4H$-$\pi_{a'}$*) and the metal-based electron-accepting orbitals (Co-$d_{yz}$ and $1\sigma^*$). This mixing is allowed because the involved fragment orbitals (1) are symmetry compatible and (2) overlap significantly. The principal difference of this class of catalysts with that of $^{1}\mathbf{1}^{2-}$ originates from the nature of the electron-accepting orbitals in the ligand-to-metal electron transfer, i.e. the Co-$d_{yz}$ and $1\sigma^*$. This difference stems from the higher d-count of cobalt catalysts compared to iron. Indeed, unlike for $\mathbf{1}^{2-}$, the $d_{xz}$ orbital is doubly occupied. Therefore, the $\beta$-$d_{yz}$ and the antibonding $1\sigma^*$ orbital are the lowest-lying unoccupied d-orbitals. Of note, the latter is energetically very high compared to the electron-donating orbital. This explains why the second ligand-to-metal electron transfer is only partial in the metallacarboxylic acid intermediate $^{2}\mathbf{H}$, unlike for $^{1}\mathbf{1}^{2-}$ where the second electron transfer is complete in the intermediate $^{1}\mathbf{D}$.

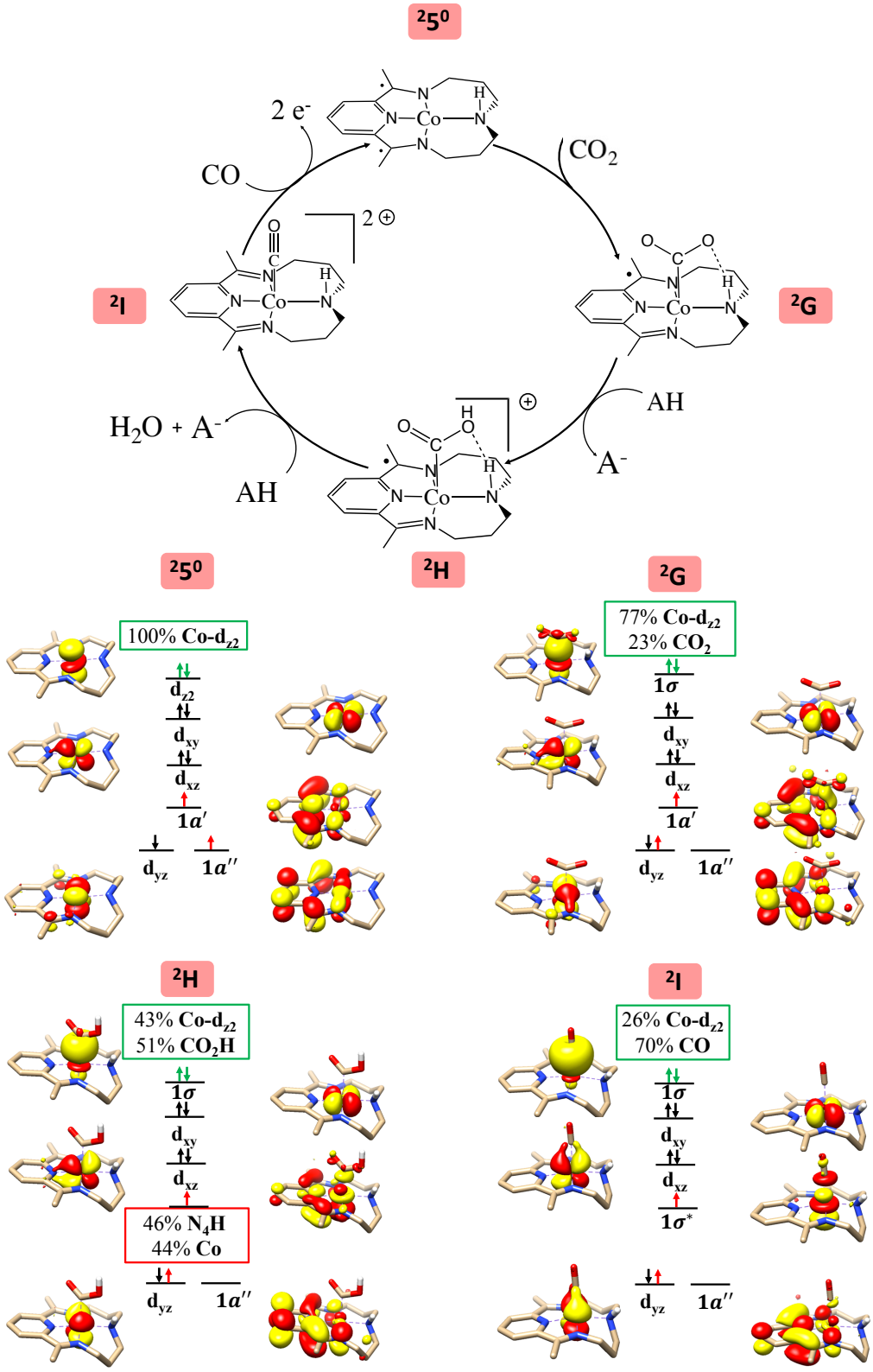


**Figure 47**: (Top) catalytic cycle of CO2-to-CO conversion catalyzed with [Co(N$_4$H)] (mechanism taken from ref. 94). Dashed straight lines between atoms represent hydrogen bonds. (Bottom) associated electronic structure of the intermediates [Co(N$_4$H)] ($^2$**5$^0$**, A), [Co(N$_4$H)(CO$_2$)] ($^2$**G**, B), [Co(N$_4$H)(CO$_2$H)]$^+$ ($^2$**H**, C) and [Co(N$_4$H)(CO)]$^{2+}$ ($^2$**I,** D) . The electrons occupying the d-orbitals of the cobalt, the 1σ, 1σ$^*$ orbitals and the redox-active orbitals

of the ligand are represented by arrows. Electrons involved in the ligand-to-metal intramolecular transfer are shown as red arrows. Electrons involved in the metal-to-$CO_2$ charge transfer are shown as green arrows. The Co and $CO_2$/$CO_2H$/CO Löwdin population of the bonding orbital formed by interaction of the cobalt center and the ligand is displayed circled in green. In $[Co(N_4H)(CO_2H)]^+$, the Co and $N_4H$ Löwdin population of the orbital harboring the radical electron is displayed circled in red. Positive parts of the orbitals are represented in red. Negative parts are represented in yellow. For clarity, all hydrogens are hidden except the hydrogen of the $CO_2H$ motif and the hydrogen participating in the intramolecular hydrogen bond.

2) Comparison of $\mathbf{1^{2-}}$ with Category III

Category III is distinguished by a ligand-to-metal transfer entirely completed during the formation of the metal-$CO_2$ adduct. This category includes $\mathbf{^18^-}$,[103] $\mathbf{^19^-}$,[71,247] $\mathbf{^110^{2-}}$,[64] $\mathbf{^111^0}$,[46] and $\mathbf{^112^0}$.[59] All catalysts contain a metal center coupled with a closed-shell, doubly-reduced ligand. Here we take the reaction with $\mathbf{^18^-}$ as an example to discuss the electronic structure evolution along the reaction coordinate. $\mathbf{^19^-}$, $\mathbf{^110^{2-}}$, $\mathbf{^111^0}$ and $\mathbf{^112^0}$ are discussed in the Annex of this chapter (Figure A9, A10, A11 and A12).

$\mathbf{^18^-}$ and its derivates can catalyze selective $CO_2$-to-CO reduction with one of the best turnover frequencies reported for homogeneous catalysis (Table 3). The non-innocence of the ligand in the active form of the catalyst was revealed by earlier experimental and computational studies.[103,240,259] Notably, Keith and al.[103] suggested that the presence of a counter-cation in the vicinity of the active species played an important role in the reactivity. In the following investigation, a $K^+$ ion was added to the reaction intermediates to ensure consistency with this previous work. Consistently with these earlier investigations, our computations reveal that the diamagetic ground state of $[Re(CO)_3(bpy)]K$ is best formulated as a low spin $Re^I$ center ($S_{Re}$ = 0) ligated by a singlet $bpy^{2-}$ ligand. Specially, the centered HOMO of $\mathbf{^18^-}$ ($1\pi^*$) with dominant bpy-$\pi^*$ parentage (74%) contains considerable Re-$d_{z2}$ character (16%) (Figure 48, A). The mixing of these two fragment orbitals is symmetry-allowed, because they both belong to the representation A' in the Cs point group. Furthermore, the bipyridine ligand bends out of the equatorial plane such as the overlap between the fragments is non-zero (Figure 48).

The mechanism of $CO_2$ reduction by $\mathbf{^18^-}$ has been extensively studied in the past.[103,240] As $CO_2$ approaches the Re center to form the intermediate $\mathbf{^1J}$ (Figure 48, B), two-electron transfer from the bpy-$\pi^*$ orbital to the formally empty Re-$d_{z2}$ orbital takes place, and the latter

orbital donates the electron density into the $CO_2$ in-plane $\pi^*$ orbital. Indeed, the doubly-occupied, bonding orbital between the Re center and the carbon of the $CO_2$ ($1\sigma$) has a large $CO_2$ population (59% $CO_2$, 28% Re). Because of the high covalency of the Fe-$C_{CO2}$ bond, the oxidation state of Re is difficult to assign and the intermediate is best described as a resonant structure between a $Re^{I}$ center ($S_{Re}$=0) bound to a $(CO_2)^{2-}$ ligand and a $Re^{-I}$ center bount to a charge neutral $CO_2$ ligand. Thus, during this elemental step, two electrons are transferred from the ligand to the metal, and approximately one electron was transferred from the metal to the $CO_2$. After the protonation of the adduct and formation of $^{1}$**K** (Figure 48, C), the electron transfer to $CO_2$ increases as indicated by the population of the $1\sigma$ orbital (26% Re-$d_{z2}$, 66% $CO_2H$). Here, the oxidation state of the Re center is less ambiguous and the complex can be described as a $Re^{I}$ ($S_{Re}$=0) coupled to a $(CO_2H)^-$ motif. Hence this step can be viewed as the second electron transfer from the metal to the $CO_2$ ligand. Subsequently, an electron transfer from the electrode populates the $1\pi^*$ orbital now unoccupied. Hence the complex can be described as a $Re^{I}$ ($S_{Re}$=0) bound to a $(CO_2H)^-$ motif and a radical $bpy^{\bullet-}$ ligand ($S_{bpy}$=1/2, Figure A3). Finally, the C-O bond is cleaved, yielding a metal-carbonyl intermediate $^{2}$**J** best described as a $Re^{I}$ center bound to a radical $bpy^{\bullet-}$ ligand and a carbonyl ligand, and releasing a water molecule.

A great similarity with the electronic transfer patterns of $\mathbf{1}^{2-}$ can be observed, i.e. the presence of two coupled electron transfer events (metal-to-$CO_2$ and ligand-to-metal). Eventually, these events transfer the electrons stored on the ligand directly to the $CO_2$ motif while leaving the oxidation state of the metal unchanged. Like in $\mathbf{1}^{2-}$, the coupling of the two electron transfer events is ensured by mixing of the ligand-based electron-donating (bpy-$\pi^*$) and metal-based electron-accepting (Re-$d_{z2}$) fragment orbitals. Here also, this mixing is favored thermodynamically favored because the fragment orbitals (1) are symmetry compatible and (2) overlap significantly due to the geometric distortion of the bpy ligand. Different from $\mathbf{1}^{2-}$, where the electrons stored on the ligands are transferred to the $d_{xz,yz}$ orbitals, in this case the electrons stored on the ligand are transferred to the metal-based Re-$d_{z2}$ fragment orbital which directly interacts with the $CO_2$ molecule. This difference with respect to $\mathbf{1}^{2-}$ largely stems from the ligand-field symmetry (square-pyramidal), which greatly stabilizes $d_{xy}$, $d_{xz}$ and $d_{yz}$ orbitals over the $d_{z2}$. Hence the latter is likely to harbor the lowest-lying d-holes. Because the electron-accepting orbital is greatly stabilized by interaction with the $CO_2$-$\pi_{ip}^*$, $CO_2$ association triggers the direct bpy-to-Re two-electron transfer. This contrasts with the two categories discussed above, whose ligand-to-metal electron transfers are separated into two events.

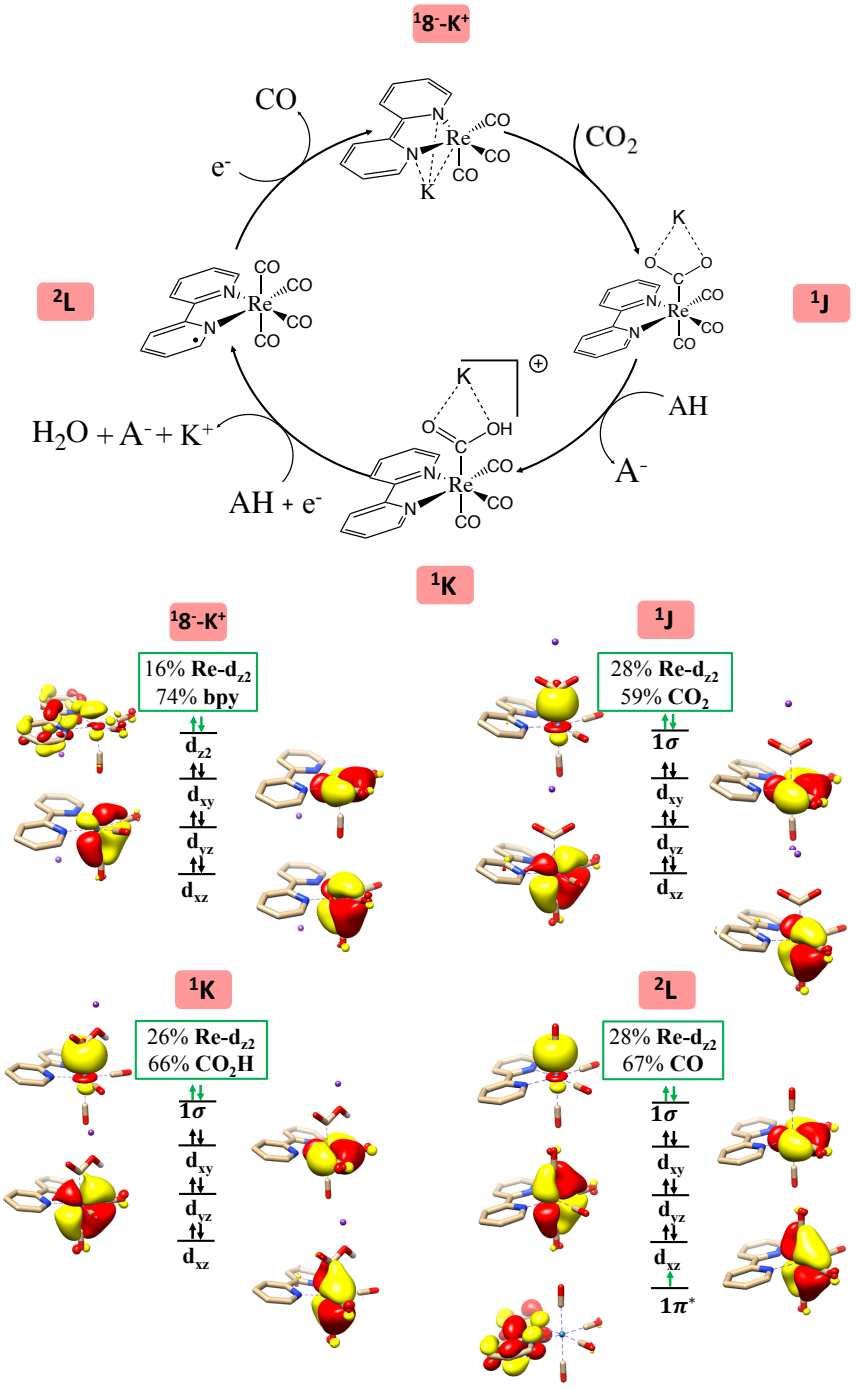


**Figure 48**: (Top) catalytic cycle of CO2-to-CO conversion catalyzed with $[Re(bpy)(CO)_3]K$ (mechanism taken from ref. 103). (Bottom) associated electronic structure of the intermediates $[Re(bpy)(CO)_3]K$ ($^1$**8**$^-$, A), $[Re(bpy)(CO_2)(CO)_3]K$ ($^1$**J** , B), $[Re(bpy)(CO_2H)(CO)_3]K^+$ ($^1$**K**, C) and $[Re(bpy)(CO)_4]$ ($^2$**L**, D) The electrons occupying the d-orbitals of the rhenium and the redox-active orbitals of the ligand are represented by arrows.. Electrons involved in the ligand-to-metal and metal-to-$CO_2$ intramolecular transfer are shown as green arrows. The Re, bpy and $CO_2$/$CO_2H$/CO Löwdin population of the bonding orbital formed by interaction of the metal center, the bpy and the $CO_2$ ligands is displayed circled in green. Positive parts of the orbitals

are represented in red. Negative parts are represented in yellow. For clarity, all hydrogens are hidden except the hydrogen of the $CO_2H$ motif.

3) Comparison with $[Ni(cyclam)]^+$ ("innocent" ligand)

Unlike $\mathbf{1}^{2-}$, the nickel-cyclam catalyst, another catalyst for $CO_2$-to-CO reduction with excellent performances, is an example case of "innocent" ligand.[54] A comparison with the catalytic cycle of $\mathbf{1}^{2-}$ indicates that in both cases the two metal-to-$CO_2$ electrons is mainly achieved by $\sigma$-donation from the metal-$d_{z2}$ to the $CO_2$ in-plane $\pi^*$ orbital. However, the role of the ligand is fundamentally different in both cases. In the case of nickel-cyclam, the ligand itself, a saturated macrocycle, has no low-lying $\pi^*$ orbital susceptible to serve as electron-accepting orbitals. Consequently, all the reductions are metal-centered. Unlike in the case of $\mathbf{1}^{2-}$, where the two electrons necessary for the eventual reduction of $CO_2$ are transferred to the molecular catalyst before the formation of the adduct, in the nickel-cyclam catalytic cycle the transfer of the second electron from the electrode to the catalyst would involve the population of a second electron in the antibonding Ni-$d_{x2-y2}$ orbital, a highly unfavorable event. Instead, the second electron transfer from the electrode to the catalyst is only favorable at a later stage, when concerted with a proton transfer to the adduct (type IIc mechanism). As developed in subsection III.A.2, this type of mechanism involves the generation of uphill intermediates and/or transition states that can hinder the reaction kinetics, compared to a case where both electrons necessary for the $CO_2$ reduction can be incorporated into the catalyst before the metal-$CO_2$ interaction. Of course, it is not to say that a catalyst with non-innocent ligand platform is always superior to a catalyst with an innocent ligand platform; this is not true. Many factors are always at play to explain the catalytic performance of a specific system. However, perhaps by storing electrons at a low energy cost *and* making them readily available to the metal center, non-innocent ligands platforms circumvent the necessity of generating high-lying intermediates or transition states. This in turn, may have a positive effect on the catalytic performances of a given system.

## B. General electronic and molecular structure requirements for catalysts with non-innocent ligands

1) General electronic and molecular structure requirements for catalysts with non-innocent ligands

All the $CO_2$-to-CO catalytic reactions studied above can be broken down into two synchronized electron transfer events: (1) a metal-to-$CO_2$ two-electrons transfer, and (2) a ligand-to-metal one- or two-electron transfer. The former is always effected mainly via $\sigma$-donation of two electrons from the doubly-occupied $d_{z2}$ orbital of the metal into the empty $CO_2$ $\pi_{ip}$* orbital. The latter transfer connects highly delocalized occupied $\pi$* orbitals of the ligand with formally unoccupied metal d-orbital. The ligand-metal cooperativity is at the core of the reactivity for all these complexes, hereby ensuring that the electrons stored on the ligand are transferred to the $CO_2$ via the metal.

What ensures the synchronization of the two electron transfer events? All the investigated catalysts feature a heavy coupling between the ligand-based electron-donating $\pi$* orbital and the metal-based electron-accepting d-orbital. This coupling may give rise to an antiferromagnetic spin coupling, or more generally a molecular orbital delocalized over the ligand platform and the metal. Hence, for instance, in $^{1}\mathbf{1}^{2-}$, the TPP-$1e_g$ orbitals couple with the Fe-$d_{xz,yz}$ atomic orbitals to yield a delocalized $1e_g$ molecular orbital; in $^{2}\mathbf{5}^{0}$, the $N_4H$ $\pi_{1a''}$* fragment orbital mixes with the Co $d_{yz}$ atomic orbital and, at later stage, the $N_4H$ $\pi_{1a'}$* fragment orbital mixes with the $\sigma^*_{Co\text{-}C}$ fragment orbital to yield the orbitals 1a'' and 1a', respectively; in $^{1}\mathbf{8}^{-}$, the bpy-$\pi$* fragment orbital mixes with the Re-$d_{z2}$ orbital to yield the $1\pi$* molecular orbital. Either way, the coupling of ligand-based and metal-based orbitals is central in ensuring that even small losses of electron density on the metal center is compensated by a continuous ligand-to-metal electron delocalization, as developed for the case of $^{1}\mathbf{1}^{2-}$. This phenomenon is permitted because the aforementioned orbitals have (1) compatible symmetries, and (2) similar energies, otherwise such coupling could not happen.

This work is perfectly in line with the earlier works on ligand non-innocence in general catalysis.[260,261,262,263] In terms of reactivity, although some cases of ligand-centered mechanisms have been reported,[264,265] in many cases the reactivity is completely metal-centered. In the latter case, the ligand plays two fundamental roles. (1) The ligand serves as an "electron reservoir", thus enabling the metal center to remain at stable oxidation state along the reaction pathway.[266,267] (2) The electrons stored on the ligand are transferred to the metal during the reaction.[260,268] Several studies have also noted significant mixing between the primarily ligand-based redox-active orbitals and formally unoccupied metal d-orbitals in complexes featuring non-innocent ligands.[269] All these findings are consistent with our present analysis.

So, how to design catalytic systems taking the best advantage of the aforementioned properties? First of all, systems with pending coordination sites are to be preferred, to facilitate

the $\sigma$-bonding with the $CO_2$. This step often lacks suitable driving force,[59,95,103] and kinetics may be further hindered if the metal-$CO_2$ interaction has to compete with a ligand coordination. In that regard, four-coordinated planar or five-coordinates square-pyramidal complexes are excellent candidates.

The synchronization of the ligand-to-metal electronic transfer is also dependent on the coupling between the ligand and the metal, which requires orbitals of similar energies and compatible symmetry. Typically, large $\pi$-systems have a wide range of available molecular orbital which energies are comparable to the metal d-orbitals. A large manifold of low-lying available orbitals with various symmetries also ensures that such coupling is symmetry compatible. For these two reasons, highly conjugated ligand platforms are clearly excellent candidates. Furthermore, to maximize the ligand-metal interaction, the atoms of the ligand interacting with the metal center should also have $p_z$-orbitals participating in the $\pi$-system, in order to maximize overlap between the lobes of the aforementioned fragment orbitals. For instance, conjugated sp2 nitrogen donors or carbenes are excellent candidates.

2) Further implications of ligand non-innocence

Generalizing the role of the ligand in the case of $\mathbf{1}^{2-}$, it can be speculated that non-innocent ligands endorse many roles in $CO_2$-to-CO electrocatalysis. First and foremost, ligand-centered reductions enhance the stability of the active species by providing low-lying redox-active orbitals. By contrast, metal-centered reduction would involve the formation of highly reactive species more likely to be deactivated by side reactions.[267] Likewise, stable active species also afford a high selectivity for $CO_2$-to-CO compared to other electrocatalytic reduction reactions such as HCOOH or $H_2$ generation. Indeed, our calculations suggest that in $\mathbf{1}^{2-}$ the two latter reactions are prohibited mainly for kinetic reasons, because the metal-hydride formation step admits an impossibly high barrier (see subsection III.A.3). A more reactive species would likely find a lower barrier and have a negative impact on selectivity. Several computational studies of catalysts for $CO_2$-to-CO conversion featuring non-innocent ligands also found that the selectivity originates from the height of the barrier in the metal-hydride formation step.[103,105] This pattern therefore suggests that the role of redox-active ligands in ensuring a high selectivity for $CO_2$-to-CO conversion can be generalized.

As developed in the case of $\mathbf{1}^{2-}$, the ligand-metal cooperativity is essential to the kinetics of the reaction. Owing to the synchronization of both electron transfer events, the metal oxidation state remains rather constant throughout the reaction. In the absence of such synchronization,

the reaction involve extremely unfavorable intermediates as was shown in the investigation of the triplet surface of $^{3}\mathbf{1}^{2-}$. It is likely that this kinetic effect is further enhanced by the coupling of the metal with the ligand. For instance, the continuous ligand-to-metal electron transfer during the formation of $^{1}\mathbf{A}$ likely helps reducing the kinetic barrier. The formation of the intermediate $^{2}\mathbf{H}$ is favored by the partial delocalization of the 1a' orbital, mitigating the loss of electron density on the metal center and probably stabilizing $^{2}\mathbf{H}$. It is likely that the metal-ligand cooperativity fulfills the same role in all the catalysts investigated in this study. However, the variable metal electronic configuration in the aforementioned catalysts warrants that different electron-accepting d-orbitals are involved in the ligand-to-metal electronic transfer. The nature and energy of these orbitals influence the synchronization of the two electron transfer events, which may induce differences in reactivity. For instance, in category I, two electrons are transferred from the ligand to the metal after the first protonation step. On the other hand, in category II, the second electron transfer is complete only after the cleavage of the C-O bond. Therefore, in the latter category the metallacarboxylic acid intermediates involve metal centers with higher oxidation states, with a possible negative repercussion on the reactivity.

## V. Conclusion

Our computational investigation of the $CO_2$-to-CO reduction reaction catalyzed by $^{1}\mathbf{1}^{2-}$ proposes the following mechanism. (1) formation of the adduct, (2) protonation of the adduct, (3) cleavage of the C-O bond, (4) reduction of the metal-carbonyl and release of a CO molecule. We found a satisfying agreement between the predicted pathway and the available thermodynamic and kinetic data at our disposal. In particular, we found that the highest barrier was indeed compatible with the large turnover frequency of this catalyst, and that the system exhibited a high selectivity for CO generation rather than HCOOH or $H_2$ generation.

Most importantly, our present investigation provides a profound understanding of the catalyst's structure-activity relationship. Indeed, the reaction can be broken down into two electron transfers events: (1) a metal-to-$CO_2$ transfer, and (2) a ligand-to-metal electron transfer. The two aforementioned transfers are synchronized in such a way that the oxidation state of the metal hardly varies along the reaction coordinates. It was shown through comparison with higher spin state surfaces that the synchronization of the two electron transfer events is fundamental to the reactivity, because it circumvents the formation of intermediates with unfavorable oxidation states. Optimal synchronization is facilitated by the antiferromagnetic spin coupling between the porphyrin ligand and the metal. The latter connects the electron

density on the metal with that of the ligand such that along the reaction coordinates, the continuous transfer of electronic density from the metal to the $CO_2$ is compensated by a continuous electronic transfer from the ligand to the metal.

Comparison of the reactivity of $\mathbf{1}^{2-}$ with that of 10 other catalysts with non-innocent ligand platform enables to generalize the feature of ligand non-innocence in $CO_2$ reduction observed in $\mathbf{1}^{2-}$. On the basis of these findings, we propose that ligand non-innocence in $CO_2$ reduction plays a central role in ensuring a high selectivity and stability, while maintaining fast kinetics through ligand-metal cooperativity. Finally, fundamental requirements to design catalysts with non-innocent ligands are provided. Importantly, the present contribution does not claim to provide guideline for the synthesis of catalysts with turnover frequencies and selectivity equal or superior to that of $^{1}\mathbf{1}^{2-}$ or its derivates. Ligand non-innocence is a key component of the reactivity in molecular systems with high activity towards $CO_2$-to-CO reduction; however, it is certainly not the only factor at play, as demonstrated by the variable catalytic performances of the investigated compounds.

# General Conclusion

The focus of this dissertation was to unambiguously determine the electronic structure of $[Fe(TPP)]^{n-}$ at different charge states, using an approach of combined spectroscopic and computational chemistry methods. The profound understanding of the electronic structure of [Fe(TPP)], $[Fe(TPP)]^{-}$ and $[Fe(TPP)]^{2-}$ enabled us to correlate its peculiar electronic structure with its remarkable reactivity towards $CO_2$ reduction. We propose that the non-innocence of the porphyrin ligand in $[Fe(TPP)]^{-}$ and $[Fe(TPP)]^{2-}$ is at the core of its reactivity, and suggest orienting future research efforts in the development and analysis of non-innocent ligands.

In the first chapter, we used a combination of Mössbauer spectroscopy, magnetometric measurements, ab-initio calculations and "pen-and-paper" theory to understand the electronic structure of [Fe(TPP)]. In details, we developed a simple effective Hamiltonian based on first-principle calculation reproducing the explicit spin-orbit couplings between the magnetic sublevels arising from the configuration $^3A_{2g}$ $(d_{xy})^2(d_{xz})^1(d_{yz})^1(d_{z2})^2$ and $^3E_g$ $(d_{xy})^2(d_{xz,yz})^3(d_{z2})^1$ (labelled according to the $D_{4h}$ point group). This effective Hamiltonian was able to simultaneously reproduce *all* magnetometric and Mössbauer data obtained in this project. The best fit reveals that at the Born-Oppenheimer level, the ground state is $^3A_{2g}$, but the degenerate $^3E_g$ states is lying only 950 $cm^{-1}$ higher than the ground state. In fact, the $^3A_{2g}$ and $^3E_g$ electronic states are so close that they are considerably mixed via spin-orbit coupling. After considering this effect, the lowest-lying magnetic sublevels correspond to a singlet separated from a doublet by 90 $cm^{-1}$. All three of these magnetic sublevels are highly multiconfigurational since they exhibit more than 12% $^3E_g$ character. In fact, it is the multiconfigurational nature of the ground state that gives to the system its unusual magnetic properties, i.e. a large field-induced orbital angular momentum along the porphyrin plane. The present Hamiltonian is more physically transparent and proved more adapted to the present situation than the usual spin Hamiltonian. The latter neglects a significant part of the system's physics, i.e. Zeeman coupling between the three lowest-lying magnetic sublebvels and the rest of the magnetic sublevels arising from spin-orbit coupling between $^3E_g$ and $^3A_{2g}$ states. However, in the interest of comparison with available spectroscopic data, the spin Hamiltonian parameters were extracted from the effective Hamiltonian and yield $D$=94 $cm^{-1}$, $E/D$=0, $g_\perp$=3.05, $g_{/\!/}$=1.85, $A_\perp/g_N\beta_N$=+47.5 T, $A_{/\!/}/g_N\beta_N$=4.6 T. Beyond the case of this system alone, it is proposed that two large and identical $g_{xx}$ and $g_{yy}$

values and a smaller $g_{zz}$ value are a spectroscopic signature for systems with a non-degenerate electronic ground state closely-lying to a symmetry-enforced degenerate state *and* a less than half-filled nearly-degenerated orbital subshell (here $d_{z2}$, $d_{xz}$ and $d_{yz}$).

In the second chapter, we determined the electronic structure of the reduced species $[Fe(TPP)]^{-}$ and $[Fe(TPP)]^{2-}$ using a combination of DFT, X-ray absorption and Mössbauer techniques, and using the electronic structure of [Fe(TPP)] as a starting point. In fact, the remarkable consistency of Mössbauer isomer shifts and X-ray near-edge structures of [Fe(TPP)], $[Fe(TPP)]^{-}$ and $[Fe(TPP)]^{2-}$ lead to the conclusion that the one- and two-electrons reduction of [Fe(TPP)] are both ligand-centered. Furthermore, pre-existing magnetic data confirms that the overall spin states of the one- and two-electron reduced species are S=1/2 and S=0, respectively. In other terms, $[Fe(TPP)]^{-}$ and $[Fe(TPP)]^{2-}$ are best described as triplet iron(II) centers antiferromagnetically coupled with a porphyrin ligand radical and diradical, respectively. Of note, a complementary rRaman study consistently identified the reductions of [Fe(TPP)] as ligand-centered, further strengthening our conclusion. Our DFT calculations reproduce the trend of pre-edge structures and isomer shifts upon reduction. In terms of electronic structure, DFT calculations assigned to $[Fe(TPP)]^{2-}$ an iron(II) with a $^3A_{2g}$ electronic configuration antiferromagnetically coupled to a ligand diradical. This conclusion was further strengthened by the experimental similarity between the quadrupole splitting of iron in [Fe(TPP)] and $[Fe(TPP)]^{2-}$. On the other hand, the electronic configuration of the iron center in $[Fe(TPP)]^{-}$ remains ambiguous. Although our calculations pointed out to an iron(II) with a $^3A_{2g}$ electronic configuration antiferromagnetically coupled with a ligand radical, several elements contradict this prediction. First, our calculations predict a low-lying excited state within the error range of hybrid DFT functionals. This state corresponds to an iron(II) with a $^3E_g$ configuration antiferromagnetically coupled with a ligand radical. This observation is consistent with the orbital near-degeneracy verified in Chapter 1 for [Fe(TPP)]. Furthermore, the comparison of the quadrupole splitting of iron in $[Fe(TPP)]^{-}$ with that of [Fe(TPP)] and $[Fe(TPP)]^{2-}$ rather point out to an iron(II) with a $^3E_g$ configuration antiferromagnetically coupled with a ligand radical. Consistently, a previous NMR studies suggesting that the unpaired electron resides in the $d_{z2}$ orbital also indicates a $^3E_g$ local electronic configuration.

In chapter 3, we explored the effect of ligand non-innocence on the reactivity of $[Fe(TPP)]^{-}$ and $[Fe(TPP)]^{2-}$ with respect to CO2-to-CO reduction. In a first step, we explored different possible pathways for $CO_2$ reduction and compared them with pre-existing kinetic data. We found that the most probable pathway corresponds to the following sequence: (1) reduction of $[Fe(TPP)]^{-}$ to $[Fe(TPP)]^{2-}$, (2) formation of a $[Fe(TPP)(CO2)]^{2-}$ adduct, (3) protonation of the

adduct forming the metallacarboxylic acid $[Fe(TPP)(CO_2H)]^-$, (4) cleavage of the CO bond and generation of the metal-carbonyl intermediate [Fe(TPP)(CO)], (5) reduction of the catalyst and departure of the carbonyl ligand, which regenerates the catalyst. The calculated energy landscape associated with this mechanism satisfyingly reproduced the tremendous experimental turnover frequency of [Fe(TPP)]. The orbital analysis of the intermediates involved in the reaction gave deeper insight on the role of the ligand during the reaction. In fact, two distinct types of electron transfer events happen during the reaction. The first type of event corresponds to electrons transfers from the metal center to the $CO_2$ molecule via σ-donation of the doubly-occupied Fe-$d_{z2}$ into the $CO_2$-$\pi^*$ orbital. These two electrons are necessary for the reduction of $CO_2$ into CO. The second type of transfer event corresponds to a transfer from the primarily-ligand-based radical electrons to the metal center. The coupling of these events enables a metal-centered reactivity while preventing the oxidation state of the metal to vary drastically over the course of the reaction. In particular, the oxidation state of the metal never goes below +I neither above +II. This considerably stabilizes the intermediates of the reaction which has the double effect of preventing the catalyst from undergoing side-reactions and avoiding prohibitive kinetic barriers. Furthermore, we found that the antiferromagnetic coupling between the metal and the ligand plays a central role in the reactivity. It has the triple effect of (1) coupling the ligand-to-metal and metal-to-$CO_2$ electron transfers, (2) enhancing the donating abilities of the metal, and (3) ensuring the ligand-to-metal electron transfers are spin-allowed. It was shown that ligand non-innocence is a rather common trait in homogeneous $CO_2$ reduction catalysts. In details, by studying 11 other catalysts with non-innocent ligands *in silico*, we found a general pattern. (1) The reduction of all these catalysts by the electrode is ligand-centered. (2) The primarily ligand-based orbitals harboring the electrons accepted from the electrode couples with metal-based d-orbitals. This coupling either takes the form of an antiferromagnetic spin coupling or formation of delocalized closed-shell molecular orbital. Either way, this metal-ligand coupling has a similar effect to the antiferromagnetic coupling in $[Fe(TPP)]^{2-}$. (3) In all these catalysts, a metal-to-$CO_2$ electron transfer is coupled to a ligand-to-metal electron transfer. The former occurs through σ-donation of the doubly-occupied $d_{z2}$ into the $CO_2$-$\pi^*$ orbital is coupled with a ligand-to-metal electron transfer, similar to [Fe(TPP)], while the latter connects the redox-active low-lying $\pi^*$ orbitals of the ligands to various available d-orbitals of the metal. The nature of these electron-accepting orbitals varies depending on the catalyst, specifically the nature of the metal center and symmetry of the ligand field. It is likely that the nature of the electron-accepting orbital affects the reactivity and selectivity of the catalyst with respect to $CO_2$ reduction.

Although some insights into the design of catalysts with non-innocent ligands have been given in the last chapter, it is important to stress here that many questions related to the effect of ligand non-innocence on the reactivity remain to be elucidated. For instance, investigating how precisely the nature of electron-accepting orbitals involved in ligand-to-metal transfers influences the reactivity and selectivity might be a valuable next step in harnessing ligand non-innocence properties for the design of $CO_2$-to-CO catalysts. In that regards, we stress that computational chemistry, coupled with experimental kinetic and spectroscopic techniques, may be a valuable tool.

The present state of the field of $CO_2$ reduction in homogeneous catalysis focuses mostly on design of new catalysts and improvement of already available catalysts. Hundreds of these catalysts presently exist, most of which likely will be forgotten once the next generation has been reported. This approach, while unavoidable to a certain degree, is perhaps not the most efficient in a long-term perspective. Instead, we believe it must be coupled to a rational approach, i.e focusing on understanding the electronic structure of successful catalysts, and the origin of their efficiency. This type of valuable information will provide a lasting insight for future catalysts design; instead, a plethora of reported homogeneous catalysts provide more background noise than useful information.

The properties of a given catalyst arise from its electronic structure. To access it, we believe the use of computational chemistry together with spectroscopy is an invaluable approach. The latter provides direct, experimental probes of the electronic structure, and the former provides a model for our understanding, to be validated by reproducing the spectroscopic data. This is the method we have been using successfully throughout this dissertation. In the end, it provides a strong confidence in the electronic structure of [Fe(TPP)], $[Fe(TPP)]^{-}$ and $[Fe(TPP)]^{2-}$ that the use of neither computational chemistry nor spectroscopy alone could have provided. In that regard, we stress here that the role of computational chemistry in research is not only to predict numbers, but rather to provide models for understanding. Like synthesizing cohorts of catalysts does not provide significant insights for future research efforts, neither does calculating hundreds of energy landscapes without interpretation. As computational power increases, it is tempting to orient research efforts exclusively towards the prediction of energies within chemical accuracy. While this is useful, one must not forget what computational chemistry, like theory in general, is as much about understanding as it is about predicting.

# Annex

## I. Annex: Chapter 1

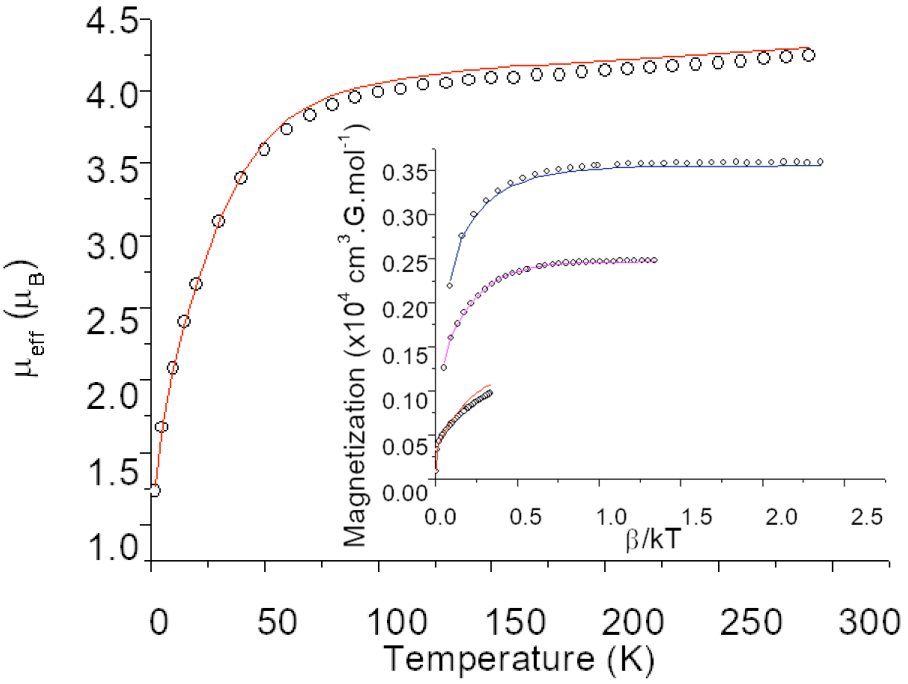


**Figure A1**: Effective magnetic moment of a powder sample of **1** recorded with a field of 1 T, and temperature dependence of the magnetization with applied fields of 1 (red), 4 (magenta) and 7 T (blue) (inset). The solid lines represent the best fits obtained by the simulation using the spin Hamiltonian (parameters $g_{xx}$=$g_{yy}$=3.05, $g_{\parallel}$=1.7, $D$=94 cm$^{-1}$, $\frac{E}{D}$ = 0, TIP=1000 x 10$^{-6}$ emu). The simulation considers 5.2% $S$ = 5/2 impurity.

**Extraction of spin Hamiltonian parameters**

The relativistic states $|\phi_+\rangle$, $|\phi_-\rangle$ and $|\phi_0\rangle$ constitute the space in which the electronic Zeeman, SOC and hyperfine coupling operators are expressed (if second-order Zeeman effects are neglected, see main text). In parallel, the fictitious pseudo-spin eigenstates $|\tilde{S} = 1, M_{\tilde{S}} = +1\rangle$, $|\tilde{S} = 1, M_{\tilde{S}} = -1\rangle$ and $|\tilde{S} = 1, M_{\tilde{S}} = 0\rangle$ constitute the space in which the spin Hamiltonian Zeeman, ZFS and hyperfine field operators are expressed. The extraction method consists in finding the spin Hamiltonian parameters such as the matrix elements of the electronic operators are one-by-one equivalent to their spin Hamiltonian counterpart.

## A. Calculation of the Magnetic moment and hyperfine field parameters

We will not derive a general method to extract spin Hamiltonian parameters. This has been published by Chibotaru and will not be repeated here. Instead, we attach to obtain simple expressions for the g- and A- values in this specific system. Because of the high $C_4$ symmetry axis of the system, the g- and A- matrices must be already diagonal in the chosen molecular framework, and the x- and y- components of both these matrices must be identical. This considerably simplify our task as the total number of independent spin Hamiltonian parameters must be equal to 4 ($g_\perp$, $A_\perp$ , $g_\parallel$, and $A_\parallel$). The magnetic moment parameters ($g_\perp$ and $g_\parallel$) will be extracted first. A similar demonstration may then be done to extract the hyperfine field parameters ($A_\perp$and $A_\parallel$).

First, using time-reversal symmetry arguments, we identify the independent matrix elements one must parametrize to describe the effective Hamiltonian magnetic moment matrices. Second, we identify the corresponding matrix elements to parametrize in order to describe the spin Hamiltonian magnetic moment matrices. Then, we establish all the independent relationships between spin Hamiltonian and effective Hamiltonian matrix elements that need to be fulfilled in order to have an equivalency between both matrices. Finally, we extract the spin Hamiltonian parameters by using the established relationship as a requirement.

In the basis of $|\phi_+\rangle$, $|\phi_-\rangle$ and $|\phi_0\rangle$, the magnetic moment vector is described by 3 Hermitian matrices $\mu_x$, $\mu_y$ and $\mu_z$. Each of these matrices have 6 *a priori* independent matrix elements. Three of these six matrix elements are off-diagonal and need to be described with two independent parameters potentially having a real and imaginary part. This adds up to a total of 18 matrix elements and 27 parameters to describe the three magnetic moment matrices. Because $|\phi_+\rangle$, $|\phi_-\rangle$ have opposite first-order angular momenta and $|\phi_0\rangle$ has no first-order angular momentum, we can make use of time-reversal symmetry to establish relationships between matrix elements and hence reduce the number of independent parameters necessary to describe the magnetic moment matrices. Indeed, let there be a state with a first-order angular momentum, for which:

$$\hat{\theta}|\phi_+^{TR}\rangle = \langle\phi_-^{TR}| \tag{A1a}$$

And let there be a state without first-order angular momentum,

$$\hat{\theta}|\phi_0^{TR}\rangle = \langle\phi_0^{TR}| \tag{A1b}$$

Since the states $|\phi_+\rangle$, $|\phi_-\rangle$ and $|\phi_0\rangle$ have undefined phase factors, they relate to the states $|\phi_\pm^{TR}\rangle$, $|\phi_0^{TR}\rangle$ by the following relationship

$$|\phi_0\rangle = e^{i\Theta_0}|\phi_0^{TR}\rangle \quad \text{(A2a)}$$

$$|\phi_\pm\rangle = e^{i\Theta_\pm}|\phi_\pm^{TR}\rangle \quad \text{(A2b)}$$

Where $\Theta_0$, $\Theta_\pm$ are the respective phase angles.

and because the magnetic moment operator is time-odd, we have the following equalities:

$$\langle\phi_+|\mu_\alpha|\phi_+\rangle = \langle\theta\phi_-|\mu_\alpha|\theta\phi_-\rangle = \langle\phi_-|\theta^\dagger\mu_\alpha\theta|\phi_-\rangle = -\langle\phi_-|\mu_\alpha|\phi_-\rangle \quad \text{(A3a)}$$

$$\langle\phi_0|\mu_\alpha|\phi_0\rangle = \langle\theta\phi_0|\mu_\alpha|\theta\phi_0\rangle = -\langle\phi_0|\mu_\alpha|\phi_0\rangle = 0 \quad \text{(A3b)}$$

$$\langle\phi_-|\mu_\alpha|\phi_+\rangle = e^{i(\Theta_+-\Theta_-)}\langle\phi_-^{TR}|\mu_\alpha|\phi_+^{TR}\rangle = e^{i(\Theta_+-\Theta_-)}\langle\theta\phi_-^{TR}|\mu_\alpha|\theta\phi_+^{TR}\rangle =$$

$$-e^{i(\Theta_+-\Theta_-)}\langle\phi_-^{TR}|\mu_\alpha|\phi_+^{TR}\rangle = -\langle\phi_-|\overrightarrow{\mu_\alpha}|\phi_+\rangle \quad \text{(A3c)}$$

Obviously, relationship (A3c) becomes:

$$\langle\phi_-|\overrightarrow{\mu_\alpha}|\phi_+\rangle = 0 \quad \text{(A3d)}$$

Finally,

$$\langle\phi_0|\overrightarrow{\mu_\alpha}|\phi_+\rangle = e^{i(\Theta_+-\Theta_0)}\langle\phi_0^{TR}|\overrightarrow{\mu_\alpha}|\phi_+^{TR}\rangle = e^{i(\Theta_+-\Theta_0)}\langle\phi_-^{TR}|\theta^\dagger\overrightarrow{\mu_\alpha}\theta|\phi_0^{TR}\rangle =$$

$$-e^{i(\Theta_+ + \Theta_- -2\Theta_0)}\langle\phi_-|\overrightarrow{\mu_\alpha}|\phi_0\rangle \quad \text{(A3e)}$$

Similarly, the phase factor $= e^{i(\Theta_+ + \Theta_- -2\Theta_0)}$ is undefined and may be taken so that:

$$\langle\phi_0|\overrightarrow{\mu_\alpha}|\phi_+\rangle = \langle\phi_-|\overrightarrow{\mu_\alpha}|\phi_0\rangle \quad \text{(A3f)}$$

We may verify that A3f is respected for the chosen overall phase factor chosen in the Main Text for $|\phi_0\rangle$, $|\phi_\pm\rangle$. Taking those relationships into accounts greatly decreases the number of independent matrix elements down to one diagonal and one off-diagonal for each matrix, i.e. a total of 6 matrix elements, i.e. $\langle\phi_+|\mu_x|\phi_+\rangle$, $\langle\phi_+|\mu_y|\phi_+\rangle$, $\langle\phi_+|\mu_z|\phi_+\rangle$ $\langle\phi_0|\mu_x|\phi_+\rangle$, $\langle\phi_0|\mu_y|\phi_+\rangle$, $\langle\phi_0|\mu_y|\phi_+\rangle$ (9 parameters).

It is trivial to show with ladder operator techniques that the spin Hamiltonian magnetic moment matrices in the basis $|\tilde{S}=1, M_{\tilde{S}}\rangle$ follow the exact same constraints. Specifically, the pseudospin eigenstates $|\tilde{S}, M_{\tilde{S}}\rangle$ have the same time-reversal properties as the $|\phi_+\rangle$, $|\phi_-\rangle$ and $|\phi_0\rangle$ states, i.e.

$$\langle\tilde{\mathrm{S}},+1|\mu_\alpha^{SH}|\tilde{\mathrm{S}},+1\rangle = -\langle\tilde{\mathrm{S}},-1|\mu_\alpha^{SH}|\tilde{\mathrm{S}},-1\rangle \quad \text{(A4a)}$$

$$\langle\tilde{\mathrm{S}},0|\mu_\alpha^{SH}|\tilde{\mathrm{S}},0\rangle = 0 \quad \text{(A4b)}$$

$$\langle\tilde{\mathrm{S}},+1|\mu_\alpha^{SH}|\tilde{\mathrm{S}},-1\rangle = 0 \quad \text{(A4c)}$$

$$\langle\tilde{\mathrm{S}},0|\mu_\alpha^{SH}|\tilde{\mathrm{S}},+1\rangle = \langle\tilde{\mathrm{S}},-1|\mu_\alpha^{SH}|\tilde{\mathrm{S}},0\rangle \quad \text{(A4d)}$$

Where $\mu_\alpha^{SH}$ is the $\alpha$- component of the magnetic moment operator described in the spin Hamiltonian formalism. Those relationships make the number of independent matrix elements decrease down to 6 (9 parameters), i.e.

$$\langle\tilde{\mathrm{S}},+1|\mu_x^{SH}|\tilde{\mathrm{S}},+1\rangle = g_{xz} \quad \text{(A5a)}$$

$$\langle\tilde{\mathrm{S}},+1|\mu_y^{SH}|\tilde{\mathrm{S}},+1\rangle = g_{yz} \quad \text{(A5b)}$$

$$\langle \tilde{S}, +1 | \mu_z^{SH} | \tilde{S}, +1 \rangle = g_{zz} \quad \text{(A5c)}$$

$$\langle \tilde{S}, 0 | \mu_x^{SH} | \tilde{S}, +1 \rangle = \frac{g_{xx} + i g_{xy}}{\sqrt{2}} \quad \text{(A5d)}$$

$$\langle \tilde{S}, 0 | \mu_y^{SH} | \tilde{S}, +1 \rangle = \frac{g_{yx} + i g_{yy}}{\sqrt{2}} \quad \text{(A5e)}$$

$$\langle \tilde{S}, 0 | \mu_z^{SH} | \tilde{S}, +1 \rangle = \frac{g_{zx} + i g_{zy}}{\sqrt{2}} \quad \text{(A5f)}$$

Hence, the spin Hamiltonian and effective Hamiltonian magnetic moment matrices are equivalent under the following conditions:

$$\langle \phi_+ | \mu_\alpha | \phi_+ \rangle = \langle \tilde{S}, +1 | \mu_\alpha^{SH} | \tilde{S}, +1 \rangle \quad \text{(A6a)}$$

$$\langle \phi_0 | \mu_\alpha | \phi_+ \rangle = \langle \tilde{S}, 0 | \mu_\alpha^{SH} | \tilde{S}, +1 \rangle \quad \text{(A6b)}$$

Those relationships enable the expression of the g-values in terms of the effective Hamiltonian magnetic moment matrix elements, which are known from our effective Hamiltonian analysis. We immediately find that the g-matrix is diagonal, i.e. $g_{xz} = g_{zx} = g_{xy} = g_{yx} = g_{yz} = g_{zy} = 0$, which confirms that the molecular framework is the proper axis of the g-matrix, consistently with the high symmetry of the molecule. The diagonal g-values may be expressed in terms of the effective Hamiltonian magnetic moment matrix elements, i.e.:

$$|g_{zz}| = |\langle \phi_+ | \overrightarrow{\mu_z} | \phi_+ \rangle| \quad \text{(A7a)}$$

$$|g_{xx}| = \sqrt{2} |\langle \phi_0 | \overrightarrow{\mu_x} | \phi_+ \rangle| \quad \text{(A7b)}$$

$$|g_{yy}| = \sqrt{2} |i \langle \phi_0 | \overrightarrow{\mu_y} | \phi_+ \rangle|. \quad \text{(A7c)}$$

It is verified that $|g_{xx}| = |g_{yy}| = |g_\perp|$ (the sign of the g-values was not investigated and arbitrarily set positive for simplicity).

Eq. A7a-c correspond to the extracted g-values shown in the main text. This demonstration is heavily inspired by Chibotaru's method, but is adapted for this specific case. Rather than building the Abragam-Bleaney tensor, it makes use of symmetry arguments to establish a simple relationship between g-values and matrix elements.

The procedure used to extract the A values is completely equivalent to the demonstration above. One simply replaces the magnetic moment matrices with the hyperfine field matrices. In total analogy, one finds that $A_{xz} = A_{zx} = A_{xy} = A_{yx} = A_{yz} = A_{zy} = 0$.

For the diagonal values,

$$\frac{A_\perp}{g_N \beta_N} = \sqrt{2} \left| \langle \phi_0 | \overrightarrow{B_{int,x}} | \phi_+ \rangle \right| \quad \text{(A8a)}$$

$$\frac{A_{zz}}{g_N \beta_N} = \left| \langle \phi_+ | \overrightarrow{B_{int,z}} | \phi_+ \rangle \right| \quad \text{(A8b)}$$

Eq. A8a and A8b correspond to the extracted A-values shown in the main text. In principle, the three A values appear from this treatment with a sign that is consistent with the sign of g. In

our case, since we arbitrarily set the sign of all g-values to be positive, we instead calculated the absolute value of A and then chose the sign to be consistent with the experimental direction of the internal field.

## B. Calculation of the ZFS operator

The SOC matrix is a 3x3 hermitian matrix with 6 *a priori* independent matrix elements, three of which are potentially complex numbers, i.e. having a real and imaginary part, which accounts for a total of 9 parameters to describe the matrix.

Unlike the hyperfine couplings, the SOC is a product of angular momenta operators, and is therefore even by time-reversal symmetry, or:

$$\theta^{\dagger} H_{SOC} \theta = H_{SOC} \tag{A9a}$$

One can infer that:

$$\langle \phi_+ | H_{SOC} | \phi_+ \rangle = \langle \phi_- | H_{SOC} | \phi_- \rangle \tag{A9b}$$

$$\langle \phi_0 | H_{SOC} | \phi_+ \rangle = e^{i(\Theta_+ + \Theta_- - 2\Theta_0)} \langle \phi_- | H_{SOC} | \phi_0 \rangle \tag{A9c}$$

Which, under the conditions leading to eq. A3f, leads to:

$$\langle \phi_0 | H_{SOC} | \phi_+ \rangle = - \langle \phi_- | H_{SOC} | \phi_0 \rangle \tag{A9d}$$

These two relationships allow to lower the number of independent $H_{SOC}$ matrix elements down to 4, i. e. 2 real diagonal values, and 2 off-diagonal values each of which counts one real and one imaginary part ($\langle \phi_+ | H_{SOC} | \phi_+ \rangle$, $\langle \phi_0 | H_{SOC} | \phi_0 \rangle$, $\langle \phi_- | H_{SOC} | \phi_+ \rangle$ and $\langle \phi_0 | H_{SOC} | \phi_+ \rangle$), which constitutes a total of 6 independent parameters.

Using Ladder-operator techniques, one may show that similar relationships between the spin Hamiltonian ZFS matrix elements may be obtained under the condition that the D matrix is symmetric (we neglect for now the condition that it is traceless), i.e.

$$\langle \tilde{S}, +1 | H_{ZFS} | \tilde{S}, +1 \rangle = \langle \tilde{S}, -1 | H_{ZFS} | \tilde{S}, -1 \rangle \tag{A10a}$$

$$\langle \tilde{S}, 0 | H_{ZFS} | \tilde{S}, +1 \rangle = - \langle \tilde{S}, -1 | H_{ZFS} | \tilde{S}, 0 \rangle \tag{A10b}$$

We thus reduce the number of matrix elements to 4 and the number of parameters to 6. We express here those matrices in terms of the components of D:

$$\langle \tilde{S}, +1 | H_{ZFS} | \tilde{S}, +1 \rangle = \frac{D_{xx} + D_{yy}}{2} + D_{zz} \tag{A11a}$$

$$\langle \tilde{S}, 0 | H_{ZFS} | \tilde{S}, 0 \rangle = D_{xx} + D_{yy} \tag{A11b}$$

$$\langle \tilde{S}, 0 | H_{ZFS} | \tilde{S}, +1 \rangle = \frac{D_{xz} + i D_{yz}}{\sqrt{2}} \tag{A11c}$$

$$\langle \tilde{S}, -1 | H_{ZFS} | \tilde{S}, +1 \rangle = \frac{D_{xx} - D_{yy}}{2} + i D_{xy} \tag{A11d}$$

Hence spin Hamiltonian ZFS and effective Hamiltonian SOC matrices are equivalent under the conditions:

$$\langle \tilde{S}, +1 | H_{ZFS} | \tilde{S}, +1 \rangle = \langle \phi_+ | H_{SOC} | \phi_+ \rangle \quad \text{(A12a)}$$

$$\langle \tilde{S}, 0 | H_{ZFS} | \tilde{S}, 0 \rangle = \langle \phi_0 | H_{SOC} | \phi_0 \rangle \quad \text{(A12b)}$$

$$\langle \tilde{S}, 0 | H_{ZFS} | \tilde{S}, +1 \rangle = \langle \phi_0 | H_{SOC} | \phi_+ \rangle \quad \text{(A12c)}$$

$$\langle \tilde{S}, -1 | H_{ZFS} | \tilde{S}, +1 \rangle = \langle \phi_- | H_{SOC} | \phi_+ \rangle \quad \text{(A12d)}$$

Those relationship enable us to express the components of D in terms of the effective Hamiltonian SOC matrix elements, which are known from our effective Hamiltonian analysis:

$$D_{zz} = \langle \phi_+ | H_{SOC} | \phi_+ \rangle - \frac{1}{2} \langle \phi_0 | H_{SOC} | \phi_0 \rangle \quad \text{(A13a)}$$

$$D_{xx} = Re\ (\langle \phi_- | H_{SOC} | \phi_+ \rangle) + \frac{1}{2}\ \langle \phi_0 | H_{SOC} | \phi_0 \rangle \quad \text{(A13b)}$$

$$D_{yy} = -\ Re\ (\langle \phi_- | H_{SOC} | \phi_+ \rangle) + \frac{1}{2}\ \langle \phi_0 | H_{SOC} | \phi_0 \rangle \quad \text{(A13c)}$$

$$D_{xy} = Im\ (\langle \phi_- | H_{SOC} | \phi_+ \rangle) \quad \text{(A13d)}$$

$$D_{xz} = \sqrt{2}\ Re(\langle \phi_0 | H_{SOC} | \phi_+ \rangle) \quad \text{(A13e)}$$

$$D_{yz} = \sqrt{2}\ Im\ (\langle \phi_0 | H_{SOC} | \phi_+ \rangle) \quad \text{(A13f)}$$

Since $H_{SOC}$ is diagonal in the basis of $|\phi_+\rangle$, $|\phi_-\rangle$ and $|\phi_0\rangle$, it immediately follows that $D_{xy} = D_{xz} = D_{yz} = 0$, which confirms that the molecular framework is indeed the proper axis of the D tensor, consistently with the high symmetry of the molecule.

Furthermore, one may realize that under those conditions, the trace of the matrix equals to:

$$D_{XX} + D_{YY} + D_{ZZ} = \langle \phi_+ | H_{SOC} | \phi_+ \rangle + \frac{1}{2}\ \langle \phi_0 | H_{SOC} | \phi_0 \rangle \quad \text{(A14a)}$$

Since $\langle \phi_+ | H_{SOC} | \phi_+ \rangle$ and $\langle \phi_- | H_{SOC} | \phi_- \rangle$ are degenerate,

$$D_{XX} + D_{YY} + D_{ZZ} = \frac{1}{2}\ (\langle \phi_+ | H_{SOC} | \phi_+ \rangle + \langle \phi_- | H_{SOC} | \phi_- \rangle + \langle \phi_0 | H_{SOC} | \phi_0 \rangle) \quad \text{(A14b)}$$

Choosing that origin for the energy,

$$D_{XX} = D_{YY} = -31.33 \quad \text{(A15a)}$$

$$D_{ZZ} = 62.67 \quad \text{(A15b)}$$

Therefore, one may calculate the parameters *D* and *E* as involved in the description of the ZFS (eq. 15b). They are calculated at 94 $cm^{-1}$ and 0 $cm^{-1}$, respectively.

## II. Annex: chapter 2

**Table A1**: Experimental and calculated (CAM-B3LYP/Def2-TZVP) pre-edge energies of a series of Fe compounds for the purpose of calibrating the predicted-experimental energy difference. All calculated energies are given after a systematic shift of 22.37 eV

| System | Experimental pre-edge energies $H_2TPP^-/H_2TPP^2$ | Calculated pre-edge energies |
|---|---|---|
| $[Fe(CN)_6]^{4-}$ | 7112.9 | 7113.3 |
| $[Fe(CN)_6]^{3-}$ | 7110.1; 7113.3 | 7110.4; 7113.9 |
| $[Fe(acac)_3]$ | 7112.8; 7114.3 | 7112.7; 7114.3 |
| [Fe(salen)Cl] | 7112.9 | 7113.2 |
| $[Fe(Cl)_6]^{4-}$ | 7111.8; 7113.4 | 7111.7; 7113.0 |
| $[Fe(Cl)_6]^{3-}$ | 7112.8; 7114.0 | 7112.8; 7114.2 |
| $[Fe(II)(prpep)_2]$ | 7112.1 | 7111.8 |
| $[Fe(prpep)_2]^+$ | 7111.0; 7112.7 | 7111.1; 7112.8 |
| $[Fe(Cl)_4]^{2-}$ | 7111.6; 7113.1 | 7111.6; 7112.4 |

## III. Annex: chapter 3

**Table A2**: Relative energy of the intermediates in the $CO_2$ to CO conversion reaction (mechanism I) in kcal/mol. The chosen reference corresponds to all the reactive infinitely separated in DMF ($[Fe(TPP)]^{2-}$ in singlet state).

| | S=0 | S=1 | S=2 |
|---|---|---|---|
| $[Fe(TPP)]^{2-}$ | 0 | +5.6 | +12.1 |
| $[Fe(TPP)(CO_2)]^{2-}$ | +2.5 | +5.5 | Unstable |
| $[Fe(TPP)(CO_2H)]^-$ | +3.2 | +15.9 | +21.7 |
| [Fe(TPP)(CO)] | -3.3 | +1.8 | +3.7 |

A. Calculation of the turnover frequency for mechanism I

We focus here on mechanism I. Assuming that one elementary step always connects two minima on the free energy surface via a transition state, the reaction can be modelled by the following sequence:

$$\mathbf{^2 1^-} + e^- \rightleftharpoons \mathbf{^1 1^{2-}} \qquad k_e, k_{-e} \qquad \text{(A16a)}$$

$$\mathbf{^1 1^{2-}} + CO_2 + PhOH \rightleftharpoons \mathbf{^1 B} \qquad k_1, k_{-1} \qquad \text{(A16b)}$$

$$\mathbf{^1 B} + PhOH \rightleftharpoons \mathbf{^1 E} + PhO^- \qquad k_2, k_{-2} \qquad \text{(A16c)}$$

$$\mathbf{^1 E} \rightarrow \mathbf{^1 F} + PhO^- + H_2O \qquad k_3 \qquad \text{(A16d)}$$

$$\mathbf{^1 F} + \mathbf{^1 1^{2-}} \rightarrow 2\,\mathbf{^2 1^-} + CO \qquad k_4 \qquad \text{(A16e)}$$

Following the method by Costentin and coworkers,[42]

$$TOF = \frac{k_{ap}}{1+e^{\frac{F}{k_B T}[E-E^0]}} \qquad \text{(A17)}$$

It is supposed that all elementary steps occurring in the homogeneous phase follow a steady-state regime. Thus, eq. 36b allow us to estimate $k_{ap}$ from the kinetic constants:

$$k_{ap} = \frac{r}{[\mathbf{^1 1^{2-}}]} = \frac{k_1 k_2 k_3 k_4 [CO_2][PhOH]^2[\mathbf{^1 1^{2-}}] - k_{-1}k_{-2}k_{-3}k_{-4}[CO][H_2O][PhO^-]^2}{k_2 k_3 k_4 [PhOH][\mathbf{^1 1^{2-}}] + k_{-1}k_3 k_4 [\mathbf{^1 1^{2-}}] + k_{-1}k_{-2}k_4 [PhO^-][\mathbf{^1 1^{2-}}] + k_{-1}k_{-2}k_{-3}[PhO^-][CO][\mathbf{^2 1^-}]} \qquad \text{(A18a)}$$

Supposing $[PhO^-] \sim 0$, the equation reduces to:

$$k_{ap} = \frac{k_1 k_2 [CO_2][PhOH]^2}{k_2[PhOH] + k_{-1}} \qquad \text{(A18b)}$$

From our DFT results, we may infer:

$$k_1 = \frac{h}{k_B T}\, e^{-\frac{9.0\ \text{kcal/mol}}{k_B T}} \qquad \text{(A19a)}$$

$$k_{-1} = \frac{h}{k_B T}\, e^{-\frac{13.3\ \text{kcal/mol}}{k_B T}} \qquad \text{(A19b)}$$

$$k_2 = \frac{h}{k_B T}\, e^{-\frac{9.4\ \text{kcal/mol}}{k_B T}} \qquad \text{(A19c)}$$

For three concentrations of phenol ([PhOH]=0.1 M, 0.75 M and 3 M), we obtain $k_{ap}$=1.6x10$^5$ s$^{-1}$.M, 1.2x10$^6$ s$^{-1}$.M and 4.8x10$^6$ s$^{-1}$.M. Maximum turnover frequencies may be obtain from Eq. A17 (E << E$^0$) for a $CO_2$ concentration of 0.23 mol/L, we obtain $TOF_{max}$= 3.6x10$^4$ s$^{-1}$, 2.76x10$^5$ s$^{-1}$ and 1.10x10$^6$ s$^{-1}$, a remarkable agreement with the experimentally-resolved values of 1.8x10$^3$ s$^{-1}$, 1.5x10$^4$ s$^{-1}$ and 1x10$^5$ s$^{-1}$.

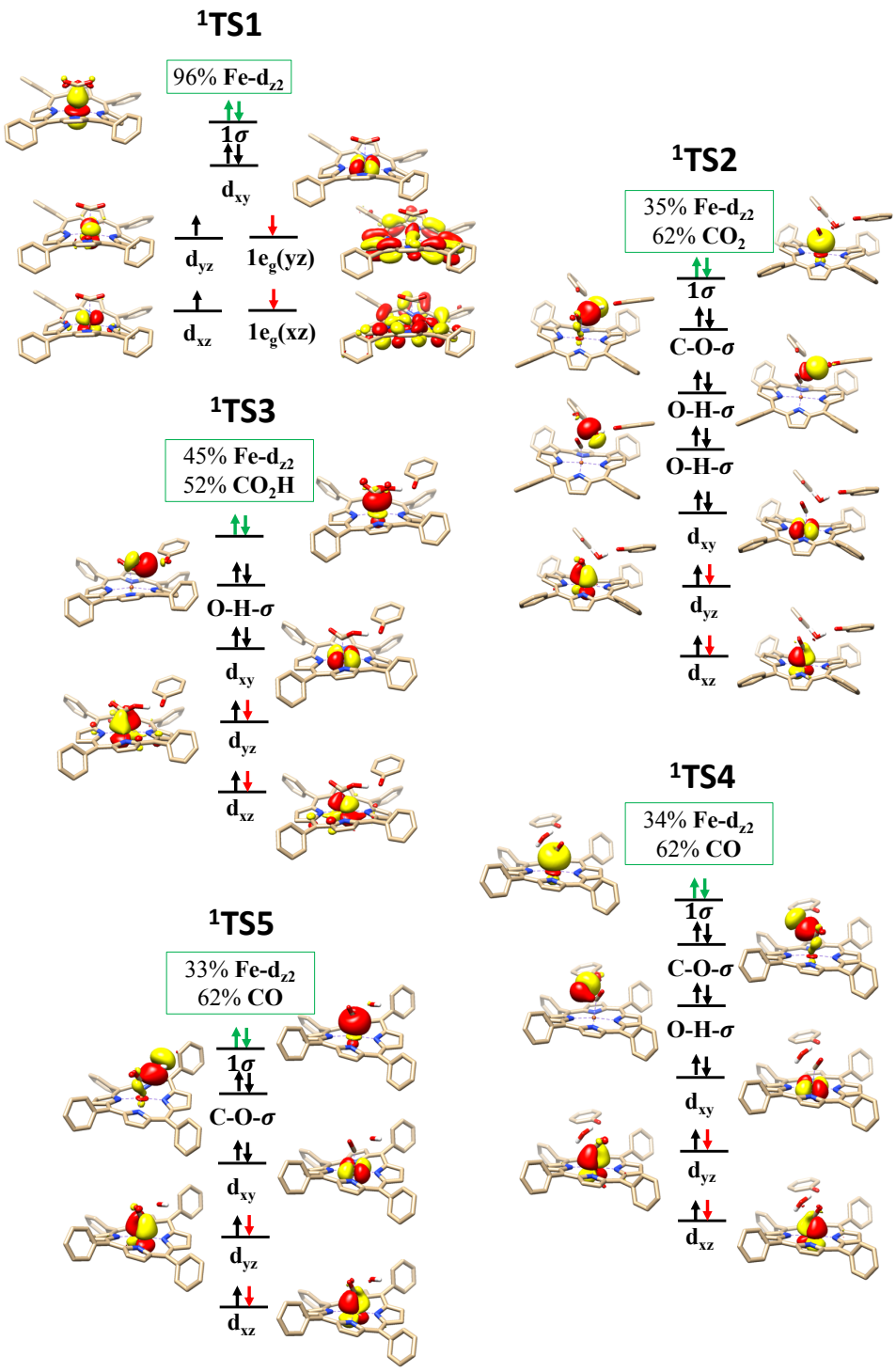


**Figure A2**: Electronic structure of the transition states TS1, TS2, TS3, TS4 and TS5 defined in the Main text (Figure 41). The electrons occupying the d-orbitals of iron, the redox-active orbitals of the TPP ligand, and the orbitals associated with the forming or cleaving bonds are represented by arrows. Electrons involved in the TPP-to-Fe electron transfers are represented as red arrows. Electrons involved in the metal-to-$CO_2$ are shown as green arrows. The Fe and $CO_2$/$CO_2H$/CO Löwdin population of the bonding orbital formed by interaction of the iron center and the ligand is displayed circled in green. Positive parts of the orbitals are represented

in red. Negative parts are represented in yellow. For clarity, all hydrogens are hidden except the hydrogen of the $CO_2H$ motif and the hydrogen of the PhOH in the process of being transferred to the reaction catalyst.

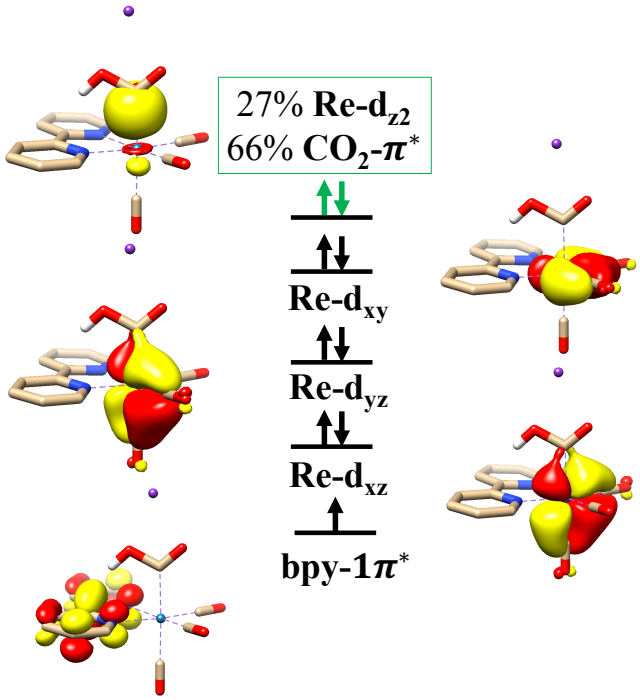


**Figure A3:** Electronic structure of the intermediate [Re(bpy)(CO)3(CO2H)]K. The electron occupying the orbitals of the rhenium center, and the ligand-centered redox-active orbitals are represented with arrows. Electrons involved in the ligand-to-metal and metal-to-$CO_2$ intramolecular transfer are shown as green arrows. The Re, bpy and $CO_2$/$CO_2H$/CO Löwdin population of the bonding orbital formed by interaction of the metal center, the bpy and the $CO_2$ ligands is displayed circled in green. Positive parts of the orbitals are represented in red. Negative parts are represented in yellow. For clarity, all hydrogens are hidden except the hydrogen of the $CO_2H$ motif.

## B. Electronic structure of the intermediates

### 1) Intermediates in the reduction of $CO_2$ catalyzed with $[Fe(qpy)]^+$

**Table A3**: Electronic energy difference (in kcal/mol) between the spin states of each intermediate involved in the mechanism of $CO_2$ reduction catalyzed with $[Fe(qpy)]^+$. For each line, the energy is given relative to the lowest-lying spin state of the intermediate. Notably, the mention "dissociates" signals that the intermediate $[Fe(qpy)(CO_2)]^+$ spontaneously dissociates into $[Fe(qpy)]^+$ and $CO_2$ upon geometry optimization.

| Intermediate | Low-spin | Intermediate spin | High spin |
|---|---|---|---|
| $[Fe(qpy)]^+$ | 0 (S=1/2) | 19.1(S=3/2) | 6.8 (S=5/2) |
| $[Fe(qpy)(CO_2)]^+$ | 0 (S=1/2) | Dissociates (S=3/2) | Dissociates (S=5/2) |
| $[Fe(qpy)(CO_2)]$ | 0 (S=0) | 3.1 (S=1) | 4.6 (S=2) |
| $[Fe(qpy)(CO_2H)]^+$ | 0 (S=0) | 6.2 (S=1) | 1.6 (S=2) |
| $[Fe(qpy)(CO)]^{2+}$ | 0 (S=0) | 4.0 (S=1) | <1 |

The active species, $[Fe(qpy)]^+$, features a distorted square-planar environment. It is best described as a $Fe^{II}$ center ($S_{Fe}$=1) antiferromagnetically coupled to a $qpy^{\bullet-}$ ligand ($S_{qpy}$=1/2). In details, the Fe center features a configuration $(d_{xy})^2(d_{xz})^1(d_{yz})^1(d_{z2})^2$, one $\beta$-electron populates the primarily ligand-based $1\pi^*$ orbital, which is an admixture of the ligand-centered $\pi_{qpy}^*$ and Fe $d_{yz}$ atomic orbital. Consequently the orbitals Fe-$d_{yz}$ and $1\pi^*$ form two spin-coupled pairs. In the next step, the doubly-occupied Fe-$d_{z2}$ donates electrons to the unoccupied in-plane $CO_2$ $\pi_{ip}^*$ orbital. The resulting bonding orbital ($1\sigma$) remains mainly centered around Fe (81% Fe, 16% $CO_2$). Hence the system is best described as a $Fe^I$ center ($S_{Fe}$=1/2) bound to a neutral $CO_2$ ligand. Interestingly, the intramolecular electron transfer connects the $\pi_{qpy}^*$ to the Fe-$d_{xz}$ orbital rather than the Fe-$d_{yz}$, even though in $[Fe(qpy)]^+$, the $\pi_{qpy}^*$ is mixed with the Fe-$d_{yz}$. In fact, concomitantly with the intramolecular electron transfer from $1\pi^*$ to Fe-$d_{yz}$, a promotion from the Fe-$d_{yz}$ to the Fe-$d_{xz}$ is triggered because of the interelectronic repulsion between the electrons in the Fe-$d_{yz}$ orbital and those of the C-O bond. Hence, in total, the electron is transferred from the $\pi_{qpy}^*$ to the Fe-$d_{xz}$, even though these orbitals do not mix. This is an exception to the general rule according to which electron transfers occur between the mixing fragment orbitals. In the subsequent step, an electron is transferred from the electrode to the now vacant $1\pi^*$ orbital. The reduction takes place on the ligand, hence the polarity of the Fe-$C_{CO2}$ bond is only marginally affected and the weight of Fe-$d_{z2}$ orbital in the $1\sigma$ orbital remains predominant (70%). Hence the system is best described as a $Fe^I$ center ($S_{Fe}$=1/2) antiferromagnetically-coupled with a radical quaterpyridine ligand and bound to an approximately neutral $CO_2$ ligand. The subsequent step is the protonation of the $CO_2$ moiety affording the metallacarboxylic acid intermediate, which triggers a significant change in the

electronic structure. The Fe-$C_{CO2}$ bond becomes more covalent, as indicated by the weight of Fe in the 1σ orbital (40% Fe, 56% $CO_2H$). Hence this step can be interpreted as a concerted proton electron transfer (CPET) to the $CO_2$. Meanwhile, a second electron transfer from the $1\pi^*$ orbital to the Fe-$d_{yz}$ compensates the loss of electronic density due to the metal-to-$CO_2$ transfer. The complex has to be described as a resonant form between a $Fe^0$ bound to a $(CO_2H)^+$ ligand and a $Fe^{II}$ bound to a $(CO_2H)^-$ ligand, bound to a charge neutral quaterpyridine ligand. In total, this step thus corresponds to the transfer of one electron from the metal to the $CO_2$ ligand, and one electron from the quaterpyridine ligand to the metal center. The next step corresponds to the C-O bond cleavage and yields a metal-carbonyl. The 1σ bonding orbital is mainly centered around the CO (35% Fe, 61% CO), hence the system is best described as a $Fe^{II}$ center ($S_{Fe}$=0) bound to a carbonyl ligand (and a neutral quaterpyridine). This sequence of steps correspond to two electrons transfers from the metal to the $CO_2$, as well as one electron transfer from the electrode to the metal.

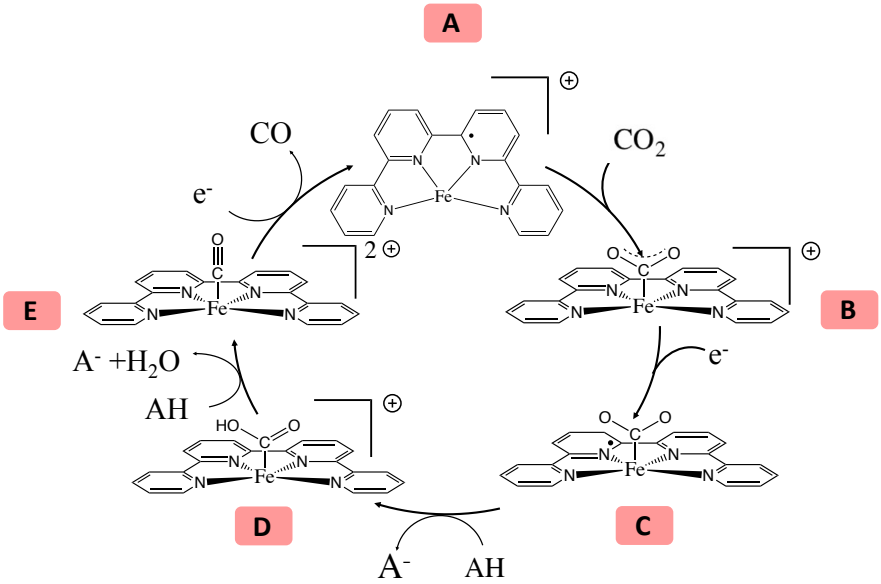
A
B
C
D
E
CO
e-
CO2
2
e-
A- +H2O
AH
A-
AH

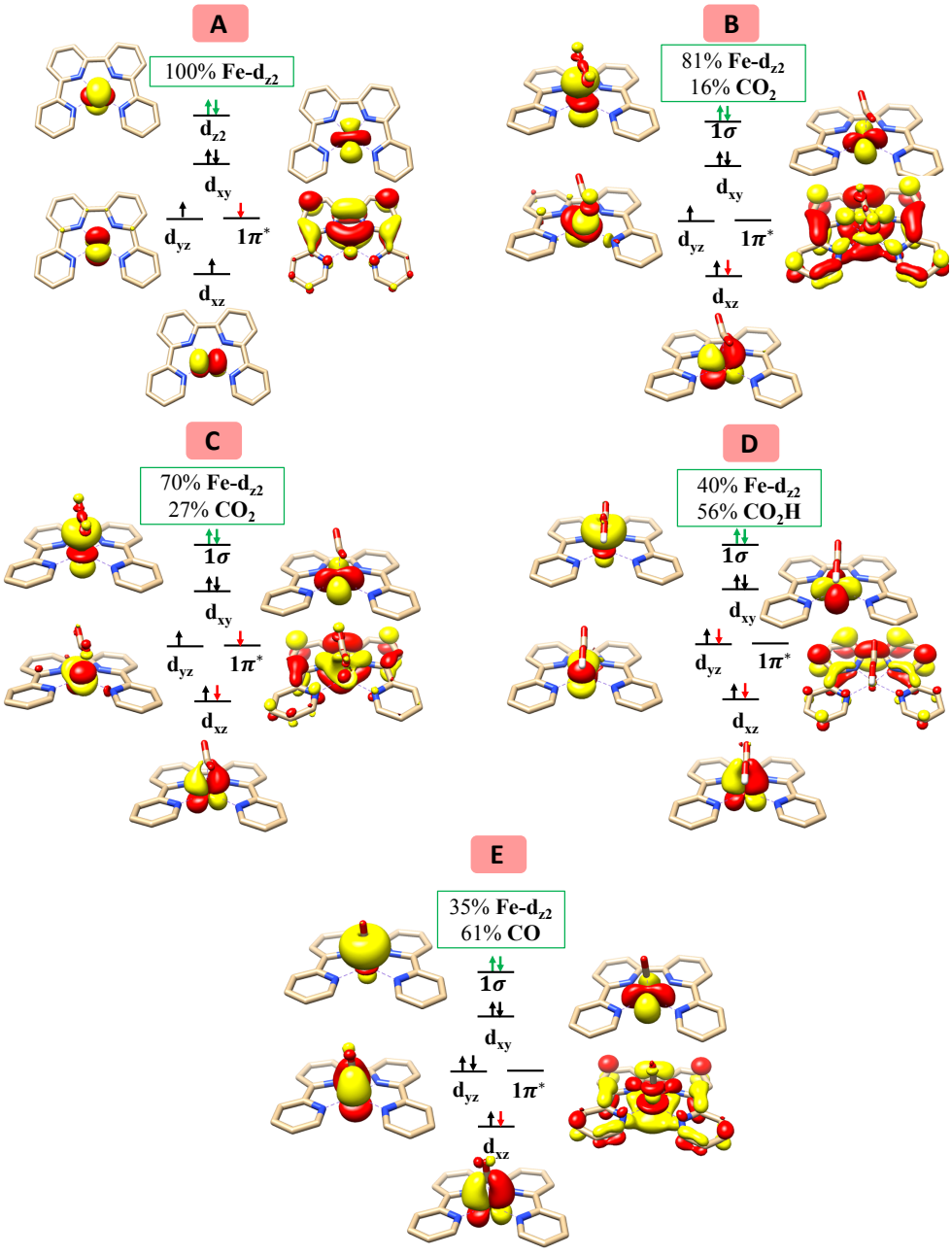
A
100% Fe-dz2
dz2
dxy
dyz
1π*
dxz
B
81% Fe-dz2
16% CO2
1σ
dxy
dyz
1π*
dxz
C
70% Fe-dz2
27% CO2
1σ
dxy
dyz
1π*
dxz
D
40% Fe-dz2
56% CO2H
1σ
dxy
dyz
1π*
dxz
E
35% Fe-dz2
61% CO
1σ
dxy
dyz
1π*
dxz

**Figure A4**: (Top) catalytic cycle of $CO_2$-to-CO conversion catalyzed with $[Fe(qpy)]^+$. The mechanism is taken from ref. 76. (Bottom) associated electronic structure of the intermediates $Fe(qpy)]^+$ (A), $[Fe(qpy)(CO_2)]^+$ (B), $[Fe(qpy)(CO_2)]$ (C), $[Fe(qpy)(CO_2H)]^+$ (D) and $[Fe(qpy)(CO)]^{2+}$ (E). The electrons occupying the d-orbitals of the metal and the redox-active orbitals of the ligand are represented by arrows. Electrons involved in the ligand-to-metal intramolecular transfer are shown as red arrows. Electrons involved in the metal-to-$CO_2$ intramolecular transfer are shown as green arrows. The Fe and $CO_2$/$CO_2H$/CO Löwdin population of the bonding orbital formed by interaction of the metal center and the $CO_2$ ligand is displayed circled in green. For clarity, all hydrogens are hidden.

2) Intermediates in the reduction of CO2 catalyzed with [Fe(bpy$^{NHEt}$PY2Me)]

**Table A4**: Electronic energy difference (in kcal/mol) between the spin states of each intermediate involved in the mechanism of $CO_2$ reduction catalysed with [Fe(bpy$^{NHEt}$PY2Me)]. For each line, the energy is given relative to the lowest-lying spin state of the intermediate.

| | S=0 | S=1 | S=2 |
|---|---|---|---|
| [Fe(bpy$^{NHEt}$PY2Me)] | +23.5 | 0 | +5.8 |
| [Fe(bpy$^{NHEt}$PY2Me)($CO_2$)] | +9.7 | 0 | +6.7 |
| [Fe(bpy$^{NHEt}$PY2Me)($CO_2H$)]$^+$ | +5.9 | 0 | +5.9 |
| [Fe(bpy$^{NHEt}$PY2Me)(CO)]$^{2+}$ | +5.1 | 0 | +21.4 |

The active species [Fe(bpy$^{NHEt}$PY2Me)] corresponds to a $Fe^{II}$ center ($S_{Fe}$=2) antiferromagnetically coupled to a diradical bpy$^{NHEt}$PY2Me$^{\bullet\bullet 2-}$ ligand ($S_{bpyNHEtPY2Me}$=1). In details, the Fe features the electronic configuration $(d_{xy})^1(d_{xz})^2(d_{yz})^1(d_{z2})^1(d_{x2-y2})^1$, and two β-electrons populate the $1\pi^*$ and $2\pi^*$. The former is an admixture of the PY2Me $\pi_{PY2Me}^*$ and Fe-$d_{xy}$ fragment orbitals, while the latter is an admixture of bpy-$\pi_{bpy}^*$ and Fe-$d_{yz}$ fragment orbitals. Consequently, $1\pi^*$, $2\pi^*$, $d_{xy}$ and $d_{yz}$ form two spin-coupled pairs. Of note, the Fe-$d_{z2}$ orbital is singly-occupied. However, the approach of the $CO_2$ moleule triggers a substantial electronic reorganization which can be summarized as follow: (1) the approach of $CO_2$ triggers the $\pi_{PY2Me}^*$-to-$d_{xy}$ electron transfer, (2) the energy of the 1σ is lowered due to the mixing of the Fe-$d_{z2}$ atomic orbital with the $CO_2$-$\pi_{ip}^*$ orbital, triggering a $d_{xy}$-to-1σ electron transfer. The 1σ orbital is therefore doubly-occupied with a strong Fe character (74% Fe, 22% $CO_2$). Hence, the system is best described as a $Fe^I$ center ($S_{Fe}$=3/2) antiferromagnetically-coupled with a bpy$^{NHEt}$PY2Me$^{\bullet -}$ ligand ($S_{bpyNHEtPY2Me}$=1/2). In terms of electronic transfers, the step

corresponds to an electron transfer from the ligand to the metal. The subsequent protonation of the adduct changes drastically the polarity of the bonding orbital $\sigma_{Fe\text{-}CO2H}$ orbital (35% Fe, 65% $CO_2H$). Furthermore, an electron is transferred from the ligand bpy-$\pi_{bpy}^*$ to the Fe-$d_{yz}$ orbital Hence, this species is best described as a $Fe^{II}$ ($S_{Fe}$=1) metal center bound to a $(CO_2H)^-$ ligand. This step corresponds to a two-electron transfer from the metal to the $CO_2$, coupled with a one-electron transfer from the ligand to the metal. Finally, the proton-assisted cleavage of the C-O bond yields a metal-carbonyl adduct in which the bonding 1σ is clearly CO-centered (29% Fe, 67% CO). This species is unambiguously described as a $Fe^{II}$ ($S_{Fe}$=1) metal center bound to a carbonyl ligand.

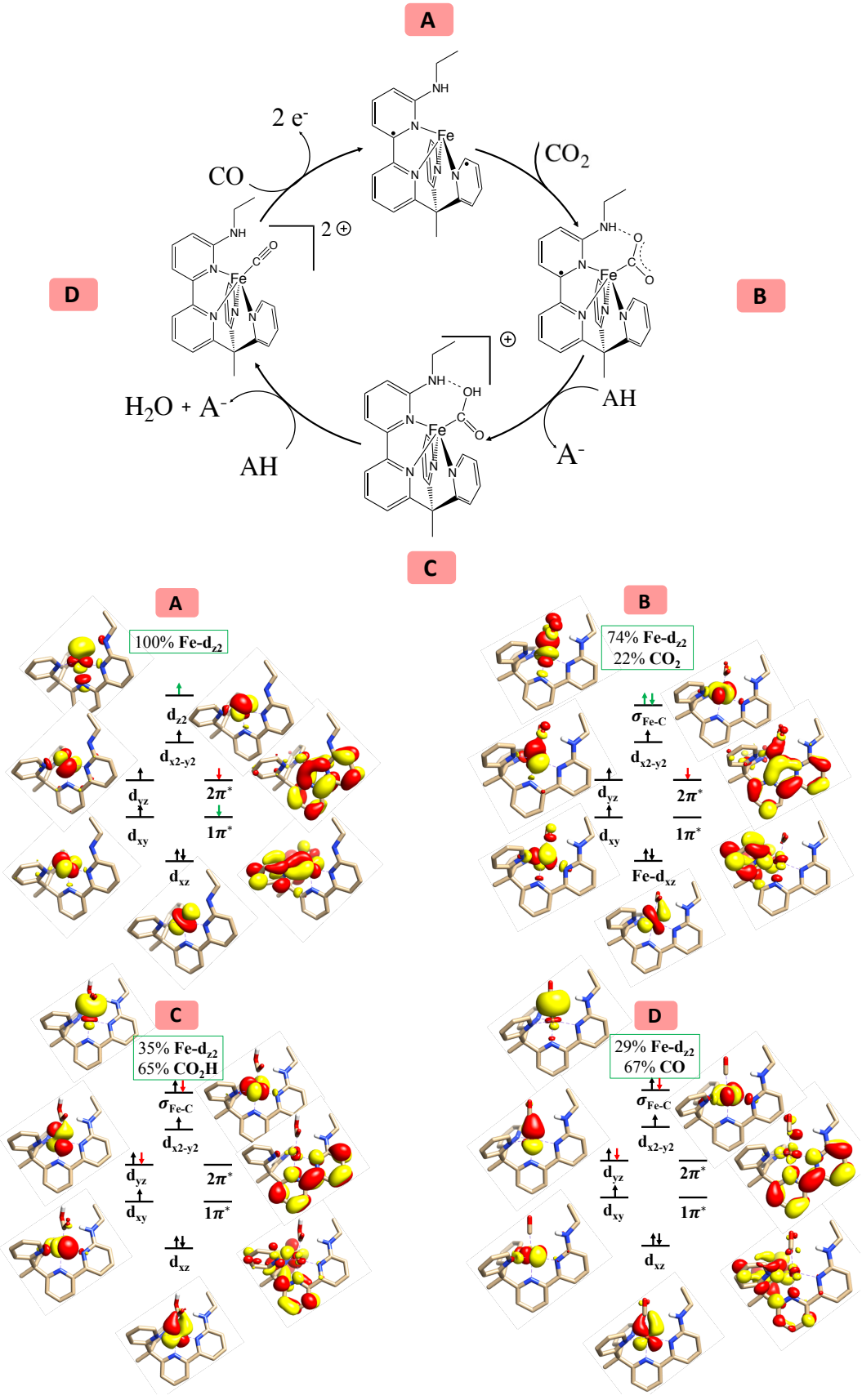


**Figure A5**: (Top) catalytic cycle of $CO_2$-to-CO conversion catalyzed with [Fe(bpy$^{NHEt}$PY2Me)]. The mechanism is taken from ref. 244. However, different from the

results of the authors, we found that the catalytic system remains in a triplet state for all investigated intermediates (Table A9). (Bottom) associated electronic structure of the intermediates [Fe(bpy$^{NHEt}$PY2Me)] (A), [Fe(bpy$^{NHEt}$PY2Me)($CO_2$)] (B), [Fe(bpy$^{NHEt}$PY2Me)($CO_2$H)]$^+$ (C), and [Fe(bpy$^{NHEt}$PY2Me)(CO)]$^{2+}$ (D). The electrons occupying the d-orbitals of the metal and the redox-active orbitals of the ligand are represented by arrows. Electrons involved in the ligand-to-metal intramolecular transfer are shown as red arrows. Electrons involved in the metal-to-$CO_2$ intramolecular transfer are shown as green arrows. The Fe and $CO_2$/$CO_2$H/CO Löwdin population of the bonding orbital $\sigma_{Fe\text{-}C}$ formed by interaction of the metal center and the $CO_2$ ligand is displayed circled in green. For clarity, all hydrogens are hidden except the hydrogen of the $CO_2$H motif and the hydrogens participating to the intramolecular hydrogen bond.

3) Intermediates in the reduction of CO2 catalyzed with [Ni($N_4$H)]

**Table A5**: Electronic energy difference (in kcal/mol) between the spin states of each intermediate involved in the mechanism of $CO_2$ reduction catalysed with [Ni($N_4$H)]. For each line, the energy is given relative to the lowest-lying spin state of the intermediate. Notably, the mention "dissociates" signals that the intermediate [Ni($N_4$H)($CO_2$)] spontaneously dissociates into [Ni($N_4$H)] and $CO_2$ or [Ni($N_4$H)] and CO upon geometry optimization.

| Intermediate | S=0 | S=1 | High spin |
|---|---|---|---|
| [Ni($N_4$H)] | 0 | 5.6 | 28.7 |
| [Ni($N_4$H)($CO_2$)] | Dissociates | 0 | 28.8 |
| [Ni($N_4$H)($CO_2$H)]$^+$ | 5.4 | 0 | 54.4 |
| [Ni($N_4$H)(CO)]$^{2+}$ | Dissociates | 0 | 58.9 |

The active species [Ni($N_4$H)] was calculated as a Ni$^{II}$ center ($S_{Ni}$=0) bound to a closed-shell $N_4H^{2-}$ ligand ($S_{N4H}$=0). In details, two electrons populate the ligand-centered $1\pi^*$ orbital. The approach of $CO_2$ triggers a significant electronic reorganization. First, the Ni-$d_{z2}$ orbital donates electrons to the unoccupied in-plane $\pi_{ip}$* orbital of the $CO_2$ ligand. The subsequently formed bonding $1\sigma$ orbital has a predominant Ni character (73% Ni, 23% $CO_2$). Second, an electron is transferred from the $1\pi^*$ orbital to the Ni-$d_{x2-y2}$. Furthermore, the $1\pi^*$ orbital, which still harbors one electron, is an admixture of the $N_4$H-$\pi_{N4H}$* fragment orbital and the antibonding $1\sigma^*$ orbital, although of predominant $N_4$H-$\pi_{N4H}$* parentage (60% $N_4$H, 28% Ni). Hence the system is best described as a Ni$^{I}$ center ($S_{Ni}$=1/2) ferromagnetically coupled with a

$N_4H^{\bullet-}$ ligand ($S_{N4H}$=1/2). In terms of electron transfers, the step corresponds to a simple one-electron transfer from the ligand to the metal. [Ni($N_4H$)] is the only example where the $d_{x2-y2}$ orbital serves as electron-accepting orbital. Most likely, this is due to the electronegativity of the nickel metal, due to which the Ni-$d_{x2-y2}$ orbital is low-lying enough with respect to the ligand-based orbital to accept an electron from the ligand, despite its highly antibonding nature. This contrasts with all other studied catalysts, in which the metal center is always less electronegative than the nickel. In the subsequent protonation of the adduct to yield a metallacarboxylic acid, the Ni-$C_{CO2}$ bond becomes strongly covalent, as indicated by the population of the 1σ bonding orbital (37% Ni, 59% $CO_2H$). Hence, this step corresponds to a one-electron transfer to the $CO_2$ moiety. Concomitantly, the electron previously populating the $N_4H$-$\pi_{N4H}$* orbital is fully transferred to the antibonding 1$\sigma^*$. Hence the system can be described as a resonance hybrid between a $Ni^{II}$ center ($S_{Ni}$=1) bound to a $(CO_2H)^-$ motif and a $Ni^0$ center bound to a $(CO_2H)^+$ motif. In total, the step corresponds to a one-electron transfer from the metal to the $CO_2H$ motif companied by a second electron transfer from the ligand to the metal. Finally, the cleavage of the C-O bond affords a metal-carbonyl adduct, in which the bonding orbital is mostly CO-centered (27% Ni, 70% CO), corresponding to the second metal-to-$CO_2$ transfer. Hence this species is best described as a $Ni^{II}$ center ($S_{Ni}$=1) bound to a carbonyl ligand.

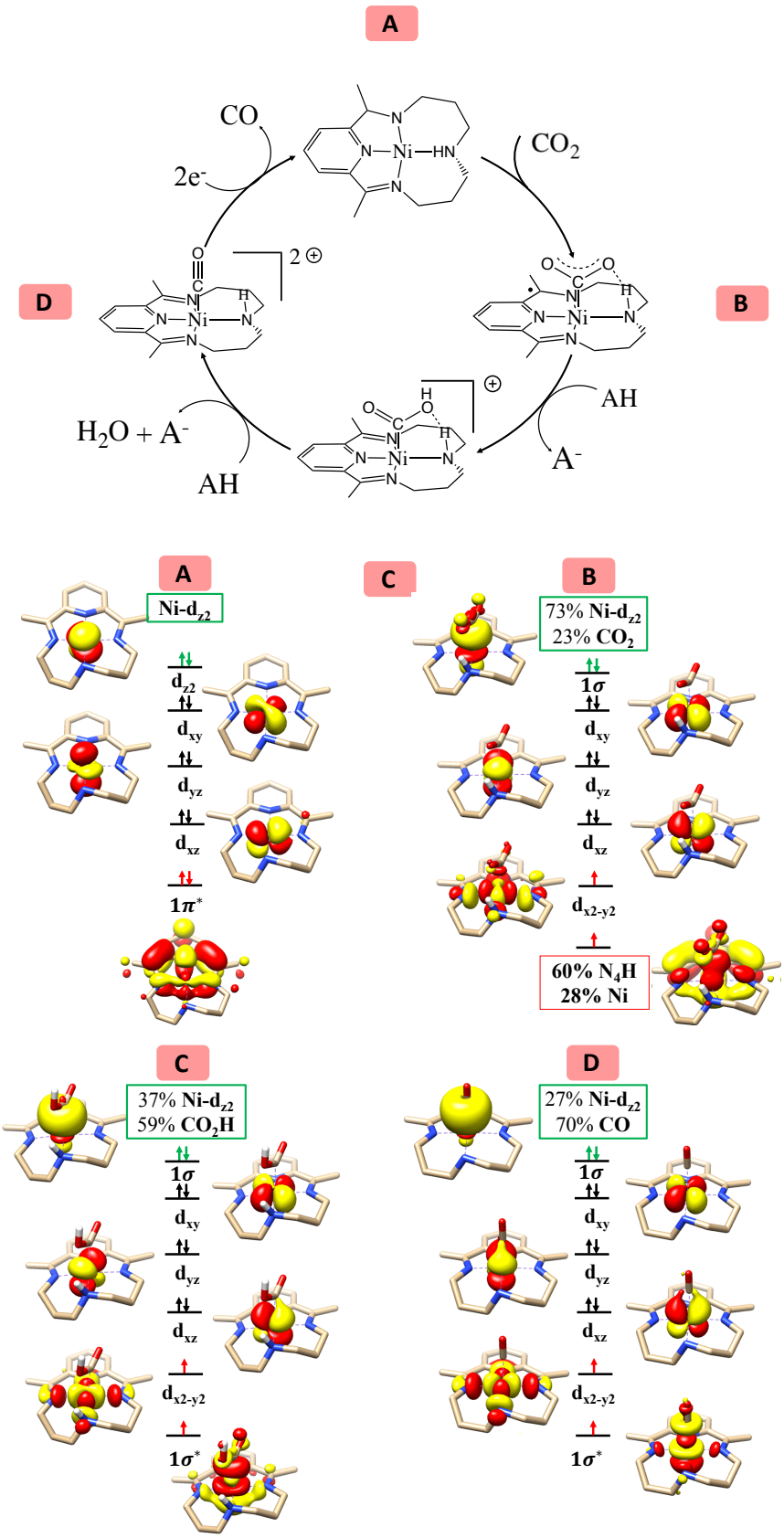


**Figure A6***:* (Top) catalytic cycle of $CO_2$-to-CO conversion catalysed with [Ni($N_4$H)]. The mechanism is assumed to be similar to that of [Co($N_4$H)]. Given the potential of the electrolysis in ref. 81 (-1.3 vs SCE) and the redox potential of the couple $[Ni(N_4H)]^+/[Ni(N_4H)]$ (-1.7 vs $Cp^+/Cp^0$ in MeCN, i.e. -1.3 vs SCE),[242a] the active species is assumed to be [Ni($N_4$H)]. (Bottom)

associated electronic structure of the intermediates [Ni($N_4$H)] (A), [Ni($N_4$H)($CO_2$)] (B), [Ni($N_4$H)($CO_2$H)]$^+$ (C), and [Ni($N_4$H)(CO)]$^{2+}$ (D). The electrons occupying the d-orbitals of the metal and the redox-active orbitals of the ligand are represented by arrows. Electrons involved in the ligand-to-metal intramolecular transfer are shown as red arrows. Electrons involved in the metal-to-$CO_2$ intramolecular transfer are shown as green arrows. The Ni and $CO_2$/$CO_2$H/CO Löwdin population of the bonding orbital 1σ formed by interaction of the metal center and the $CO_2$ ligand is displayed circled in green. In the intermediates [Ni($N_4$H)($CO_2$)] and [Ni($N_4$H)($CO_2$H)]$^+$, the Ni and $N_4$H Löwdin population of the MO harboring the radical electron delocalized over the metal and the ligand is displayed circled in red. For clarity, all hydrogens are hidden except the hydrogen of the $CO_2$H motif and the hydrogens participating to the intramolecular hydrogen bond.

4) Intermediates in the reduction of $CO_2$ catalyzed with [Co(qpy)]

**Table A6**: Electronic energy difference (in kcal/mol) between the spin states of each intermediate involved in the mechanism of $CO_2$ reduction catalysed with [Co(qpy)]. For each line, the energy is given relative to the lowest-lying spin state of the intermediate. Notably, the mention "dissociates" signals that the intermediate [Co(qpy)($CO_2$)] spontaneously dissociates into [Co(qpy)] and $CO_2$ upon geometry optimization

| | S=1/2 | S=3/2 | S=5/2 |
|---|---|---|---|
| [Co(qpy)] | 0 | +8.4 | +20.9 |
| [Co(qpy)($CO_2$)] | Dissociates | 0 | Dissociates |
| [Co(qpy)($CO_2$H)]$^+$ | 0 | +6.7 | +45.7 |
| [Co(qpy)(CO)]$^{2+}$ | 0 | +6.5 | +70.5 |

This mechanism is highly similar to that of [Co($N_4$H)]. In the active species [Co(qpy)], the cobalt has a distorted square-planar environment. It is best described as a Co(II) ($S_{Co}$=1/2) center antiferromagnetically coupled with a qpy$^{\bullet 2-}$ diradical dianion ($S_{qpy}$=1). In details, the Co center features a $(d_{xy})^2(d_{xz})^1(d_{yz})^2(d_{z2})^2$ and two electrons populate the primarily ligand-based $1\pi^*$ and $2\pi^*$ orbitals. Of note, the former is purely ligand-centered, while the latter is an admixture of the fragment orbital $\pi_{qpy\text{-}1}{}^*$ and the Co-$d_{xz}$ atomic orbital. Consequently, $2\pi^*$ and $d_{xz}$ form a spin-coupled pair leading to an antiferromagnetic spin coupling between the quaterpyridine ligand and the metal center. In the first step, the Co center binds the $CO_2$

molecule. However, our calculations showed that the adduct was unstable in a singlet state and spontaneously dissociates into [Co(qpy)] and $CO_2$. Arguably, this can be attributed to the weak bond between the cobalt center and $CO_2$ motif, and the unfavorable interelectronic repulsion between the doubly-occupied Co-$d_{yz}$ orbital and the electrons of the C-O bond. Indeed, the quartet state, in which one electron of the Co-$d_{yz}$ orbital is promoted to the Co-$d_{x2-y2}$ orbital, is stable, likely due to the lower interelectronic repulsion between the Co-$d_{yz}$ and the electrons of the C-O bond. The Co-$d_{z2}$ donates electrons to the in-plane $CO_2$-$\pi_{ip}$*. The resulting bonding orbital 1σ is strongly Co-centered (82% Co, 18% $CO_2$). Furthermore, one electron is transferred from the $\pi_{qpy-1}^*$ to the $d_{xz}$ orbital. Consequently, the Cobalt is best described as a $Co^I$ center ($S_{Co}$=1) bound to a $CO_2$ and *ferromagnetically* coupled with a $qpy^{\bullet-}$ ligand ($S_{qpy}$=1/2). In terms of electron transfer the step only corresponds to one electron transfer from the ligand to the metal. The subsequent protonation of the adduct yielding the metallacarboxylic acid intermediate triggers a significant electronic reorganization. Indeed, the 1σ bonding orbital is strongly covalent (58% Co, 42% $CO_2H$). Furthermore, the doublet state is significantly more stable than the quartet, hence the electron populating the $d_{x2-y2}$ is promoted back to the $d_{yz}$ orbital. Additionnally, in this intermediate the singly populated $1\pi^*$ orbital is a mixture of qpy $\pi_{qpy-2}^*$ fragment orbital and the $1\sigma^*$ orbital (53% Co, 39% qpy). In terms of electron transfer, this step corresponds to a one-electron transfer from the cobalt to the $CO_2H$ motif, and a partial electron transfer from the ligand to the cobalt. Finally, the proton-assisted C-O bond cleavage yields a metal-carbonyl adduct. The bonding 1σ orbital is mainly CO-centered (26% Co, 71% CO). Futhermore, the electron previously populating the $1\pi^*$ has relocated completely to the antibonding $1\sigma^*$. Hence this species is unambiguously assigned as a $Co^{II}$ center bound to a carbonyl ligand. In terms of electronic transfer, the step corresponds to a one-electron transfer from the cobalt to the CO motif, and the completion of the previously partial electron transfer from the ligand to the cobalt.

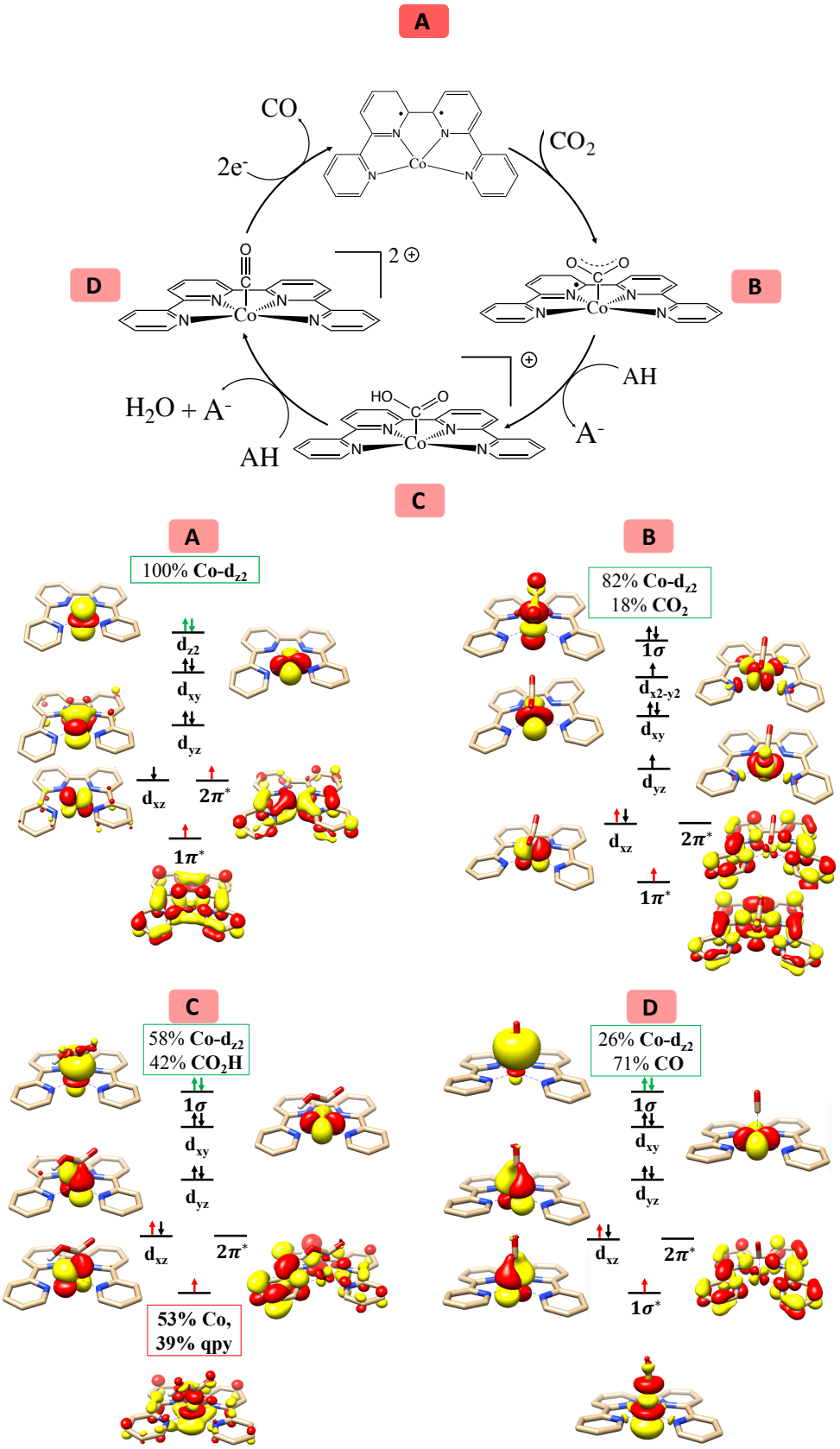


**Figure A7***:* (Top) catalytic cycle of $CO_2$-to-CO conversion catalysed with [Co(qpy)]. The mechanism is taken from the reference 76. (Bottom) associated electronic structure of the intermediates [Co(qpy)] (A), [Co(qpy)($CO_2$)] (B), [Co(qpy)($CO_2H$)]$^+$ (C), and [Co(qpy)(CO)]$^{2+}$ (D). The electrons occupying the d-orbitals of the metal and the redox-active orbitals of the

ligand are represented by arrows. Electrons involved in the ligand-to-metal intramolecular transfer are shown as red arrows. Electrons involved in metal-to-$CO_2$ intramolecular transfer are shown as green arrows. The Co, and $CO_2$/$CO_2H$/CO Löwdin population of the bonding orbital formed by interaction of the metal center and the $CO_2$ ligands is displayed circled in green. In the intermediate $[Co(qpy)(CO_2H)]^+$, the Co and qpy Löwdin population of the MO harboring the radical electron delocalized over the metal and the ligand is displayed circled in red. Positive parts of the orbitals are represented in red. Negative parts are represented in yellow. For clarity, all hydrogens are hidden except the hydrogen of the $CO_2H$ motif.

5) Intermediates in the reduction of $CO_2$ catalyzed with [Co(L)]

**Table A7**: Electronic energy difference (in kcal/mol) between the spin states of each intermediate involved in the mechanism of $CO_2$ reduction catalysed with [Co(L)]. For each line, the energy is given relative to the lowest-lying spin state of the intermediate.

| | S=1/2 | S=3/2 | S=5/2 |
|---|---|---|---|
| [Co(L)] | 0 | +5.8 | +13.3 |
| $[Co(L)(CO_2)]$ | 0 | +16.9 | +27.3 |
| $[Co(L)(CO_2H)]^+$ | 0 | +1.7 | +43.0 |
| $[Co(L)(CO)]^{2+}$ | +3.4 | 0 | +57.3 |

The mechanism of $CO_2$ reduction catalyzed by [Co(L)] is similar to that of $[Co(N_4H)]$. Like for $[Co(N_4H)]$, the ligand environment of [Co(L)] is best described as a square-planar ligand field, despite the presence of a fifth nitrogen donor weakly interacting with the cobalt. However, instead of being described as a $Co^{II}$ antiferromagnetically coupled to a diradical ligand like $[Co(N_4H)]$, it is best described as a low-spin $Co^{II}$ ($S_{Co}$=1/2) bound to a closed shell $L^{2-}$ ligand ($S_L$=0). In details, Co features the configuration $(d_{xy})^2(d_{xz})^2(d_{yz})^1(d_{z2})^2$ and two electrons populate the 1a'' orbital (nomenclature according to the Cs point group). This doubly-populated orbital is an admixture of the ligand-centered fragment orbital $\pi_{L\text{-}a''}^*$ and the singly-occupied Co $d_{yz}$ orbital. During the formation of the $[Co(L)(CO_2)]$ intermediate, the Co-$d_{z2}$ donates electrons to the $CO_2$-$\pi_{ip}^*$, forming a bonding orbital 1σ mainly centered on Co (61% Co, 35% $CO_2$). During this step, an electron is transferred from the $\pi_{L\text{-}a''}^*$ to the $d_{yz}$ orbital. Concomitantly, the other electron electron centered on the $\pi_{L\text{-}a''}^*$ orbital is promoted to another unoccupied orbital of the ring 1a'. The 1a' orbital has a different symmetry than that of 1a'', and in fact predominantly corresponds to the ligand-centered $\pi_{L\text{-}a'}^*$ fragment orbital, slightly

mixed with the antibonding $1\sigma^*$ orbital. Here, the system is best described as a $Co^I$ center ($S_{Co}=0$) bound to a $L^{\bullet-}$ ligand ($S_L=1/2$) and a $CO_2$ motif, and the step can be summarized as an electron transfer from the ligand to the metal. The subsequent protonation of the adduct affording a metallacarboxylic acid intermediate is characterized by a significant increase in covalence of the $1\sigma$ bonding orbital (41% Co, 59% $CO_2H$). Concomitantly, the mixing of the $\pi_{L\text{-}a'}{}^*$ with the $\sigma^*_{Co\text{-}C}$ orbital increases, such as the 1a' orbital is an equal mixture of both fragment (40% Co, 56% L). Hence, this step likely corresponds to the transfer of the first electron to the $CO_2$ moiety, accompanied by a partial electronic transfer from the ligand to the metal. Subsequently, the C-O bond scission occurs coupled with a second proton transfer. After this step is complete the $1\sigma$ is mainly centered around CO (24% Co, 73% CO). The electron previously populating the $\pi_{L\text{-}a'}{}^*$ orbital is entirely transferred to the antibonding $\sigma^*_{Co\text{-}CO}$ orbital. Hence, the oxidation state of this intermediate is clearly identified as a $Co^{II}$ bound to a carbonyl ligand. The step thus corresponds to a second metal-to-$CO_2$ electron transfer, and the completion of the previously partial electron transfer from the ligand to the metal.

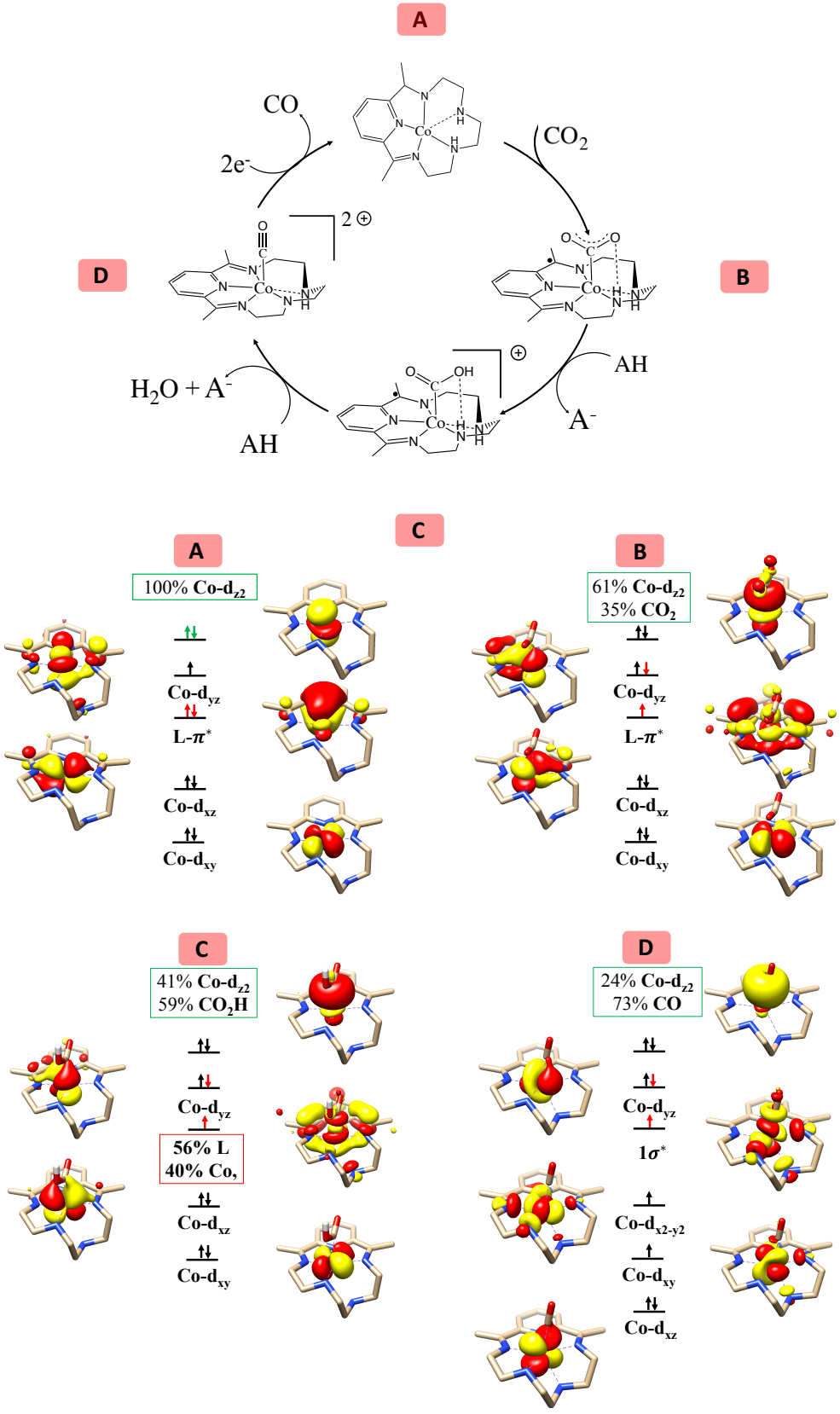


**Figure A8**: (Top) catalytic cycle of $CO_2$-to-CO conversion catalyzed with [Co(L)]. The mechanism is taken from the reference 48. On the basis of the system's structural and electronic similarity with [Co($N_4$H)], the mechanism is assumed to be identical. Dashed bonds between the oxygen of the CO2 or CO2H motif and the hydrogen of one amine ligand correspond to

hydrogen bonds. Dashed bond between the nitrogen of the amine ligand and the cobalt center correspond to weak axial interactions. (Bottom) associated electronic structure of the intermediates [Co(L)] (A), [Co(L)($CO_2$)] (B), [Co(L)($CO_2H$)]$^+$ (C), and [Co(L)(CO)]$^{2+}$ (D). The electrons occupying the d-orbitals of the metal and the redox-active orbitals of the ligand are represented by arrows. Electrons involved in the ligand-to-metal intramolecular transfer are shown as red arrows. Electrons involved in metal-to-$CO_2$ intramolecular transfer are shown as green arrows. The Co, and $CO_2$/$CO_2H$/CO Löwdin population of the bonding orbital formed by interaction of the metal center and the $CO_2$ ligands is displayed circled in green. In the intermediate [Co(L)($CO_2H$)]$^+$, the Co and L Löwdin population of the MO harboring the radical electron delocalized over the metal and the ligand is displayed circled in red. Positive parts of the orbitals are represented in red. Negative parts are represented in yellow. For clarity, all hydrogens are hidden except the hydrogen of the $CO_2H$ motif and the hydrogens participating to the intramolecular hydrogen bonds.

6) Intermediates in the reduction of $CO_2$ catalyzed with [Mn (bpy)$(CO)_3$]K

The mechanism resembles closely that of [Re(bpy)$(CO)_3$]K. In the first intermediate [Mn (bpy)$(CO)_3$]K, the ligand field is square-pyramidal. The Mn features a configuration $(d_{xy})^2(d_{xz})^2(d_{yz})^2$ and the HOMO $1\pi^*$ is an admixture of Mn and bpy $\pi^*$ fragment orbitals (24% Mn and 62% bpy). Thus, it is best described as a $Mn^I$ center ($S_{Mn}$=0) bound to a doubly-reduced $bpy^{2-}$ ligand ($S_{bpy}$=0). During the formation of the adduct [Mn(bpy)$(CO)_3(CO_2)$]K, a two-electron transfer from the $1\pi$* orbital to the formally empty $d_{z2}$ orbital takes place, and the latter orbital donates the electron density into the $CO_2$ $\pi_{ip}$* orbital. The subsequently-formed bonding $1\sigma$ orbital has a strong covalent character (28% Mn and 55% $CO_2$), and the system is best described as a resonance form between a $Mn^I$ center ($S_{Mn}$=0) bound to a $(CO_2)^{2-}$ ligand and a $Mn^{-I}$ center bound to a neutral $CO_2$ ligand. The subsequent protonation of the adduct yielding a [Mn(bpy)$(CO_2H)(CO)_3$]$K^+$ further polarizes the Mn-$C_{CO2}$ bond since the bonding molecular orbital is about 28% Mn and 63% $CO_2H$. Hence, this intermediate is best described a $Mn^I$ center ($S_{Mn}$=0) bound to a $(CO_2H)^-$ motif. In two distinct subsequent steps, an electron is transferred to the catalyst from the electrodeand the C-O bond is cleaved concomitantly with a second proton transfer. As elaborated elsewhere,[91] the electron transfer may be before (reduction-first) or after (protonation-first) the proton-assisted cleavage of the bond. We did not investigate that level of details. However, this two-steps sequence yields a metal-carbonyl adduct In this

species, the 1σ orbital is mainly CO centered, and the Löwdin populations remain almost identical to those of the metallacarboxylic acid (30% Mn, 64% CO). The additional electron transferred from the electrode resides in the $1\pi^*$, here primarily composed of the bpy $\pi^*$ fragment orbital. Hence, the species is identified as a $Mn^I$ species ($S_{Mn}=0$) bound to a radical $bpy^{\bullet-}$ ($S_{bpy}=1/2$) and a CO ligand.

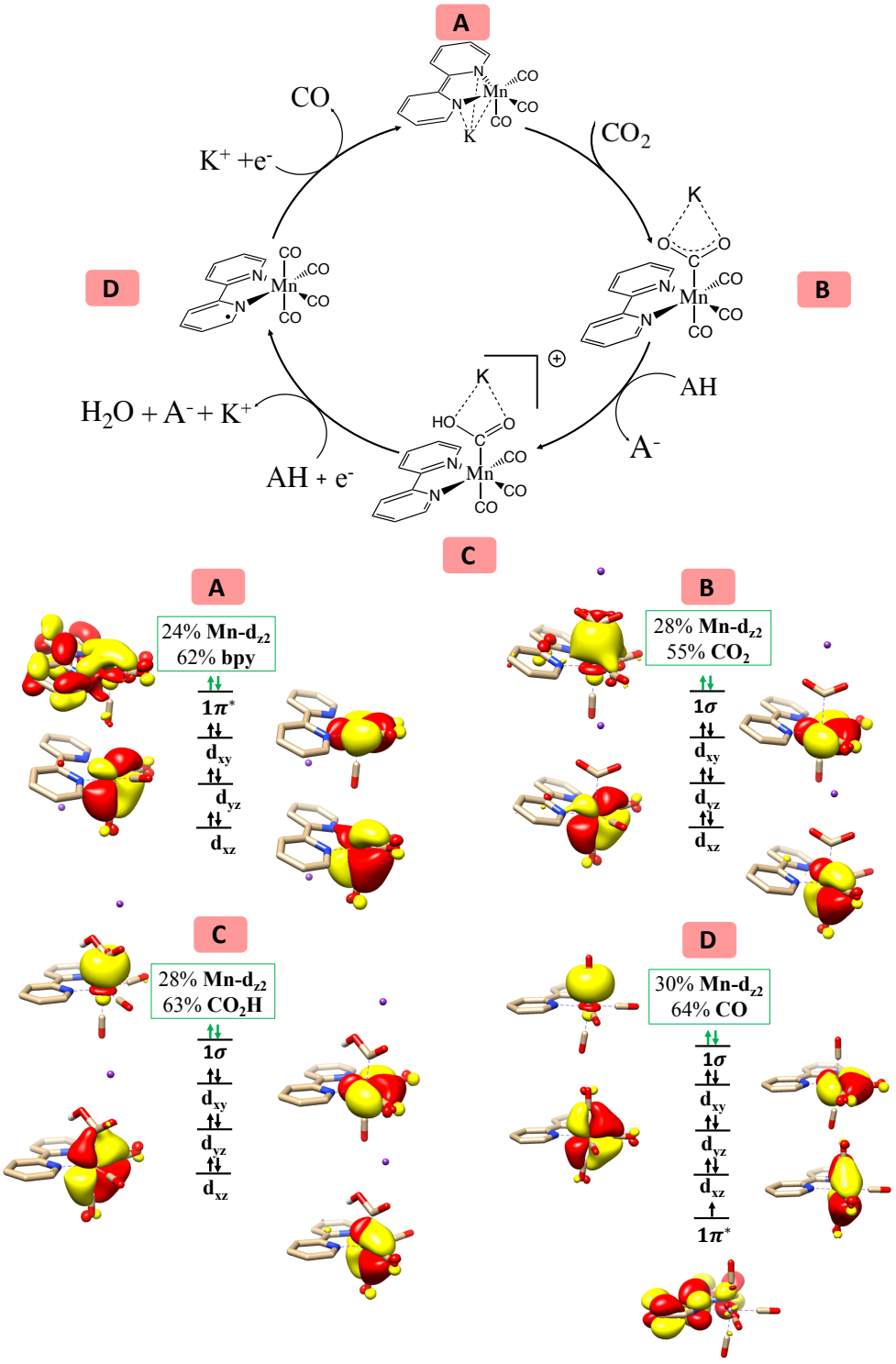


**Figure A9**: (Top) catalytic cycle of $CO_2$-to-CO conversion catalysed with $[Mn(bpy)(CO)_3]K$. The mechanism is taken from the reference 91. A $K^+$ counterion was added to the reaction complex, by analogy to the mechanistic studies on the very similar $[Re(bpy)(CO)_3]K$ complex described in reference 103. Dashed bond correspond to weak bonds formed with the $K^+$ ion. (Bottom) associated electronic structure of the intermediates $[Mn(bpy)(CO)_3]K$ (A), $[Mn(bpy)(CO_2)(CO)_3]K$ (B), $[Mn(bpy)(CO_2H)(CO)_3]K^+$ (C), and $[Mn(bpy)(CO)_4]$. The electrons occupying the d-orbitals of the metal and the redox-active orbitals of the ligand are

represented by arrows. Electrons involved in the ligand-to-metal and metal-to-$CO_2$ intramolecular transfer are shown as green arrows. The Mn, bpy and $CO_2$/$CO_2H$/CO Löwdin population of the bonding orbital 1σ formed by interaction of the metal center, the bpy and the $CO_2$ ligands is displayed circled in green. Positive parts of the orbitals are represented in red. Negative parts are represented in yellow. For clarity, all hydrogens are hidden except the hydrogen of the $CO_2H$ motif.

7) Intermediates in the reduction of $CO_2$ catalyzed with $[Cr(bpy)(CO)_3]^{2-}$

**Table A8**: Electronic energy difference (in kcal/mol) between the spin states of each intermediate involved in the mechanism of $CO_2$ reduction catalysed with $[Cr(bpy)(CO)_3]^{2-}$. For each line, the energy is given relative to the lowest-lying spin state of the intermediate.

| | S=0 | S=1 | S=2 |
|---|---|---|---|
| $[Cr(bpy)(CO)_3]^{2-}$ | 0 | 18.3 | 52.5 |
| $[Cr(bpy)(CO_2)(CO)_3]^{2-}$ | 0 | 11.8 | 50.7 |
| $[Cr(bpy)(CO_2H)(CO)_3]^{-}$ | 0 | 25.8 | 62.9 |
| $[Cr(bpy)\ (CO)_4]$ | 0 | 45.6 | 74.5 |

This mechanism is similar to that of $[Re(bpy)(CO)_3]^{-}$. The active species, $[Cr(bpy)(CO)_3]^{2-}$ possesses a square-pyramidal ligand field. It is identified as a $Cr^0$ center ($S_{Cr}$=0) bound to a doubly-reduced $bpy^{2-}$ ligand ($S_{bpy}$=0). In details, the Cr center has a $(d_{xy})^2(d_{xz})^2(d_{yz})^2$ configuration, and the HOMO of $[Cr(bpy)(CO)_3]^{2-}$ ($1\pi^*$) is an admixture of Cr $d_{z2}$ and bpy $\pi^*$ fragment orbitals (17% Cr, 75% bpy). During the formation of the adduct $[Cr(bpy)(CO)_3(CO_2)]^{2-}$, a two-electron transfer from the 1π* orbital to the formally empty $d_{z2}$ orbital takes place, and the latter orbital donates the electron density into the $CO_2$ in-plane $\pi_{ip}$* orbital. The subsequently formed bonding orbital 1σ demonstrates a significant covalent Cr-$C_{CO2}$ bond (31% Cr, 51% $CO_2$), although the orbital remains partially delocalized to the bipyridine and the carbonyl ligands. This intermediate is best described as a resonant structure between a $Cr^0$ center ($S_{Cr}$=0) bound to a $(CO_2)^{2-}$ ligand and a $Cr^{-II}$ center bound to a $CO_2$ ligand. The proton transfer step affording the metallarboxylic acid intermediate increases the weight of the $CO_2H$ motif in the bonding orbital (28% Cr, 64% $CO_2H$). Here, the system is best described as a $Cr^0$ ($S_{Cr}$=0) bound to a $(CO_2H)^{-}$ ligand. The two subsequent steps are the proton-assisted C-O bond cleavage and electron transfer from the electrode, in an unknown order. Determining whether this species follows a "protonation-first" or "reduction-first" pathway is beyond the

scope of this study. However, this two-step sequence yields a metal-carbonyl adduct. The $\sigma_{Cr\text{-}CO}$ bonding orbital remains mainly centered around CO (29% Cr, 65% CO) but does not further polarize. The electron is transferred from the electrode to the $1\pi^*$ orbital, entirely centered around the ligand. Hence the system is best described as a $Cr^0$ ($S_{Cr}$=0) bound to a carbonyl and a $bpy^{\bullet-}$ ligand ($S_{bpy}$=1/2).

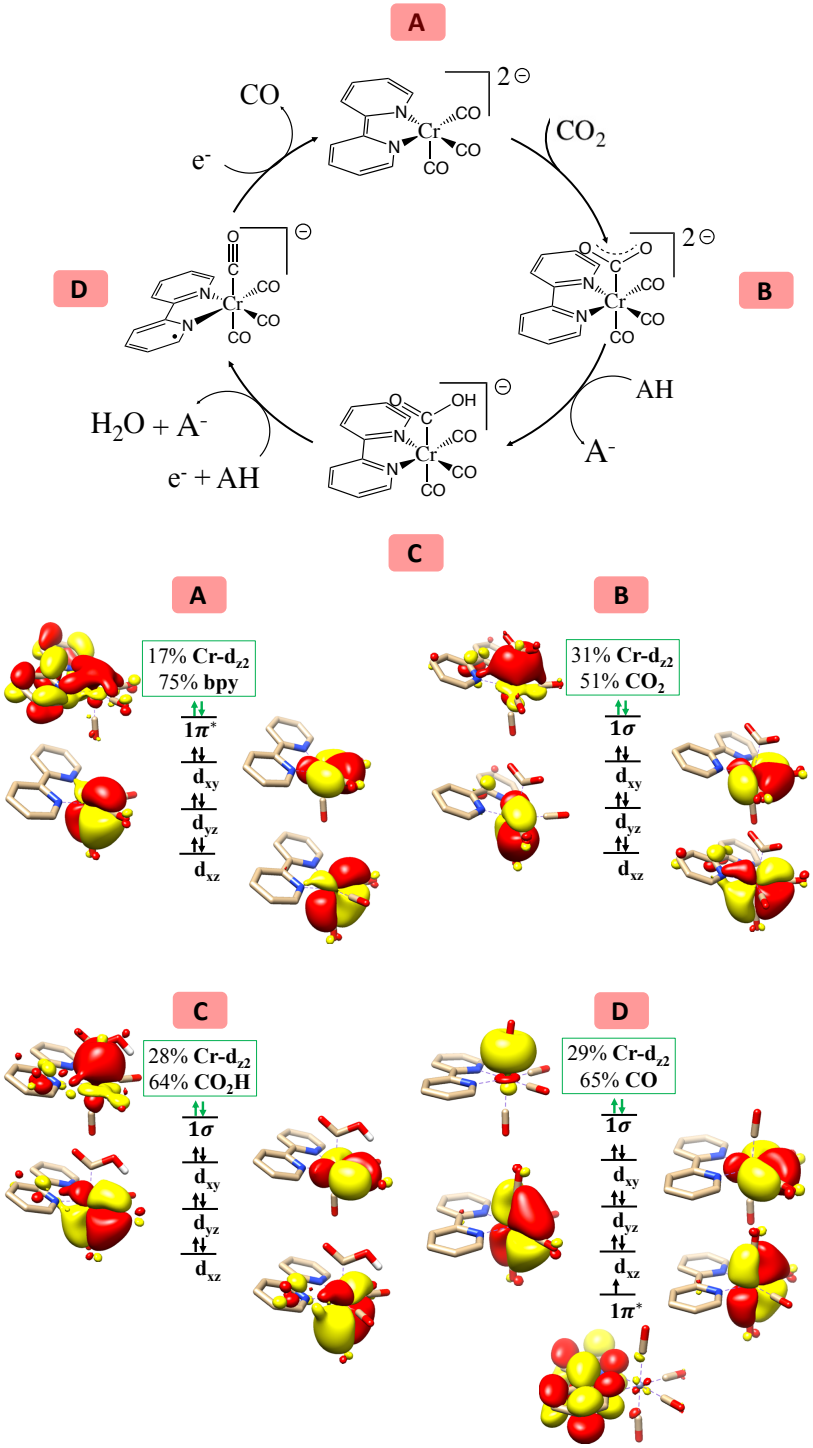


**Figure A10**: (Top) catalytic cycle of $CO_2$-to-CO conversion catalysed with $[Cr(bpy)(CO)_3]^{2-}$. The type of mechanism is postulated to be similar to that of $[Re(bpy)(CO)_3]K$ and

$[Mn(bpy)(CO)_3]K$. Cyclic voltammetry data suggests the active species is $[Cr(bpy)(CO)_3]^{2-}$.[64] (Bottom) associated electronic structure of the intermediates $[Cr(bpy)(CO)_3]^{2-}$ (A), $[Cr(bpy)(CO)_3(CO_2)]^{2-}$ (B), $[Cr(bpy)(CO)_3(CO_2H)]^{-}$ (C), and $[Cr(bpy)(CO)_4]$ (D). The electrons occupying the d-orbitals of the metal and the redox-active orbitals of the ligand are represented by arrows. Electrons involved in the ligand-to-metal and metal-to-$CO_2$ intramolecular transfer are shown as green arrows. The Cr, bpy and $CO_2$/$CO_2H$/CO Löwdin population of the bonding orbital formed by interaction of the metal center, the bpy and the $CO_2$ ligands is displayed circled in green. For clarity, all hydrogens are hidden except the hydrogen of the $CO_2H$ motif.

8) Intermediates in the reduction of $CO_2$ catalyzed with $[Ru(bpy)_2(CO)]$

**Table A9**:Electronic energy difference (in kcal/mol) between the spin states of each intermediate involved in the mechanism of $CO_2$ reduction catalysed with $[Ru(bpy)_2(CO)]$. For each line, the energy is given relative to the lowest-lying spin state of the intermediate.

| **Intermediate** | S=0 | S=1 | S=2 |
|---|---|---|---|
| $[Ru(bpy)_2(CO)]$ | 0 | +8.6 | +40.7 |
| $[Ru(bpy)_2(CO)(CO_2)]$ | 0 | +30.3 | +63.8 |
| $[Ru(bpy)_2(CO)(CO_2H)]^+$ | 0 | +53.0 | +118.5 |
| $[Ru(bpy)_2(CO)_2]^{2+}$ | 0 | +64.8 | +128.7 |

The active species, $[Ru(bpy)_2(CO)]$, has a square-pyramidal ligand-field symmetry similar to $[Re(bpy)(CO)_3]^-$. The ruthenium has a $(d_{xy})^2(d_{xz})^2(d_{yz})^2$ electronic configuration. The HOMO of $[Ru(bpy)_2(CO)]$ ($1\pi^*$) is strongly delocalized and mainly corresponds to an admixture of Ru $d_{z2}$ (44%) and bpy $\pi^*$ (33%) from one bipyridine ligand. Hence the system is best described as a hybrid form between a $Ru^{II}$ ($S_{Ru}$=0) system bound to a $(bpy)^{2-}$ ($S_{bpy}$=0), and a $Ru^0$ bound to a neutral bpy ligand. During the formation of the adduct $[Ru(bpy)_2(CO)(CO_2)]$, two electron transfers from the $1\pi^*$ orbital to the $d_{z2}$ orbital takes place, and the latter orbital donates two electrons into the $CO_2$ in-plane $\pi^*$ orbital. The subsequently-formed bonding orbital $1\sigma$ is strongly covalent (46% Ru and 49% $CO_2$), such that the species is best described as a resonant hybride between a $Ru^{II}$ center ($S_{Ru}$=0) bound to a $(CO_2)^{2-}$ ligand and a $Ru^0$ center ($S_{Ru}$=0) bound to a $CO_2$ ligand. The bpy ligand is neutral. Hence, this step corresponds to an overall electron transfer from the bpy ligand to the $CO_2$. The subsequent protonation further polarizes the bonding orbital (37% Ru and 59% $CO_2H$). However, the bond is still strongly

covalent and the oxidation state of the ruthenium remains ambiguous. Finally, the proton-assisted cleavage of the C-O bond yields a metal-carbonyl adduct. 1σ is largely CO-centered at this stage, (32% Ru, 64% CO) and the system unambiguously described as a $Ru^{II}$ center ($S_{Ru}$=0) bound to a carbonyl ligand.

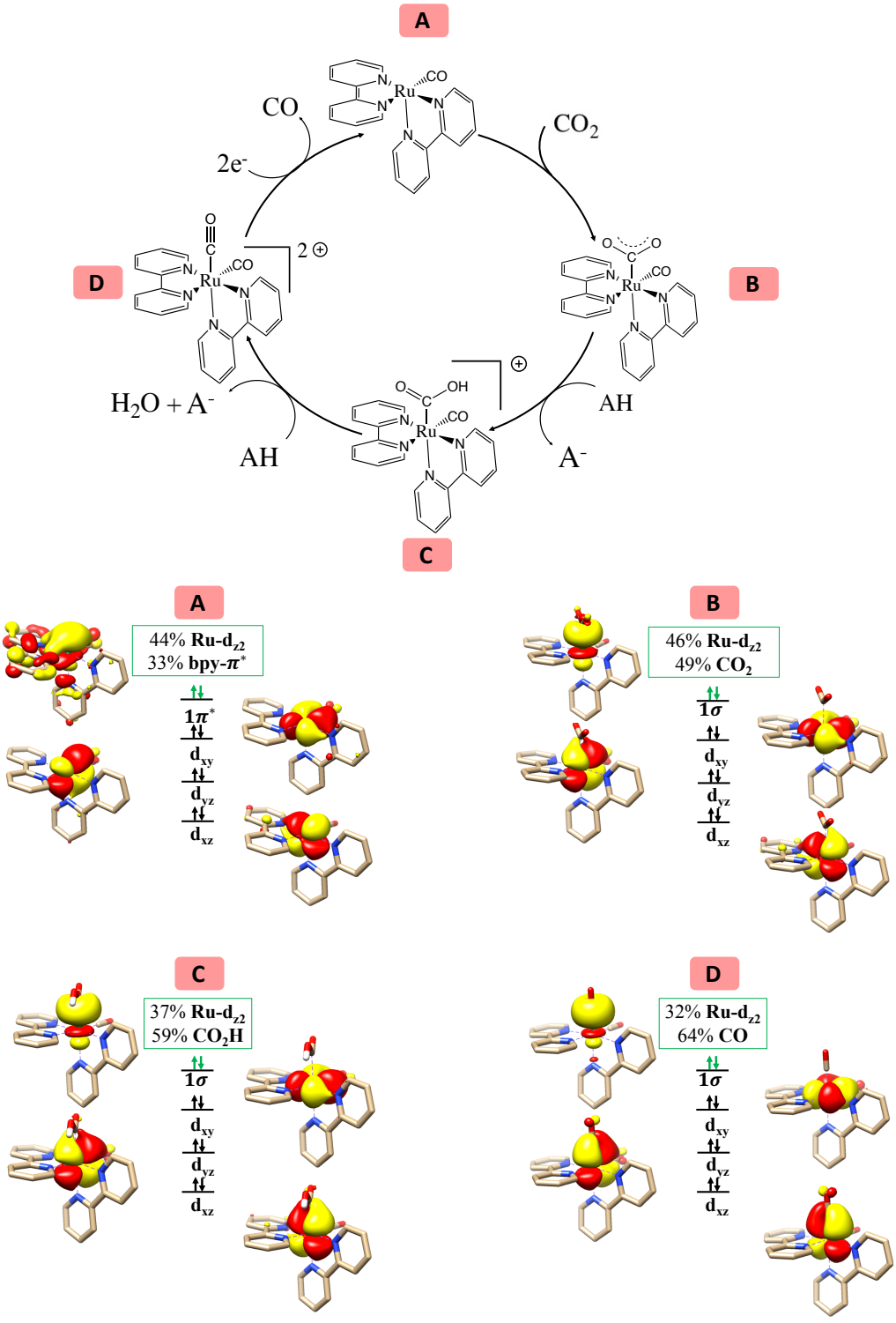


**Figure A11**: (Top) catalytic cycle of $CO_2$-to-CO conversion catalysed with $[Ru(bpy)_2(CO)]$. The mechanism is taken from reference 46. (Bottom) associated electronic structure of the

intermediates $[Ru(bpy)_2(CO)]$ (A), $[Ru(bpy)_2(CO)(CO_2)]$ (B), $[Ru(bpy)_2(CO)(CO_2H)]^+$ (C), and $[Ru(bpy)_2(CO)_2]^{2+}$ (D). The electrons occupying the d-orbitals of the metal and the redox-active orbitals of the ligand are represented by arrows. Electrons involved in the ligand-to-metal and metal-to-$CO_2$ intramolecular transfer are shown as green arrows. The Ru, bpy and $CO_2$/$CO_2H$/CO Löwdin population of the bonding orbital 1σ formed by interaction of the metal center, the tpy and the $CO_2$ ligands is displayed circled in green. Positive parts of the orbitals are represented in red. Negative parts are represented in yellow. For clarity, all hydrogens are hidden except the hydrogen of the $CO_2H$ motif.

9) Intermediates in the reduction of $CO_2$ catalyzed with [Ru(bpy)(tpy)]

**Table A10**: Electronic energy difference (in kcal/mol) between the spin states of each intermediate involved in the mechanism of $CO_2$ reduction catalysed with [Ru(bpy)(tpy)]. For each line, the energy is given relative to the lowest-lying spin state of the intermediate.

| **Intermediate** | S=0 | S=1 | S=2 |
|---|---|---|---|
| [Ru(bpy)(tpy)] | 0 | 7.7 | 34.1 |
| [Ru(bpy)(tpy)($CO_2$)] | 0 | 58.7 | 63.7 |
| [Ru(bpy)(tpy)(CO)] | <0.1 | 0 | 50.7 |

Unlike most investigated catalysts, this catalyst yields CO under aprotic conditions, following the stochiometric equation:

$$2CO_2 + 2\,e^- \rightarrow CO + CO_3^{2-} \qquad (13)$$

Very similar to $[Re(bpy)(CO)_3]K$, the active form of the catalyst exhibits a ligand field best described as a deformed square-pyramidal. The HOMO is a mixture of 27% Ru-$d_{z2}$ and 69% tpy-$\pi^*$ orbital. Hence, the species can be described as a $Ru^{II}$ ($S_{Ru}$=0) bound to a $tpy^{2-}$ ligand. During the formation of the adduct [Ru(bpy)(tpy)($CO_2$)], a two-electron transfer from the tpy-π* orbital to the formally empty Ru-$d_{z2}$ orbital takes place, and the latter orbital donates the electron density into the $CO_2$ $\pi_{ip}$* orbital. The subsequently-formed bonding orbital 1σ is strongly covalent (44% Ru and 49% $CO_2$), such that the species is best described as a resonant hybride between a $Ru^{II}$ center ($S_{Ru}$=0) bound to a $(CO_2)^{2-}$ ligand and a $Ru^0$ center ($S_{Ru}$=0) bound to a $CO_2$ ligand. Thus it is safe to consider this step as a first electron transfer to the $CO_2$ motif. Subsequently, the catalyst accepts two electrons from the electrode. The electron-accepting

orbitals are entirely ligand-based, i.e. the bpy-$\pi^*$ and the tpy-$\pi^*$. The subsequent C-O bond cleavage yields a metal-carbonyl. In the latter species, the bonding orbital 1σ is largely CO-centered (33% Ru, 63% CO) due to the superior electron-attracting properties of $CO^{2+}$ compared to $CO_2$. This step can be interpreted as the second electron transfer to CO. Meanwhile, the two electrons previously transferred from the electrode remained centered on the ligand. Hence, this species can be interpreted as a $Ru^{II}$ center ($S_{Ru}$=0) bound to a carbonyl, a $bpy^{\bullet-}$ and a $tpy^{\bullet-}$ ligands. Notably, the energy the present triplet state and the singlet state is below the error range of DFT for this intermediate. The latter is a closed-shell system in which a $Ru^{II}$ ($S_{Ru}$=0) is bound to a closed shell $tpy^{2-}$ ligand instead of a $Ru^{II}$ bound to two radical ligands $bpy^{\bullet-}$ and a $tpy^{\bullet-}$.

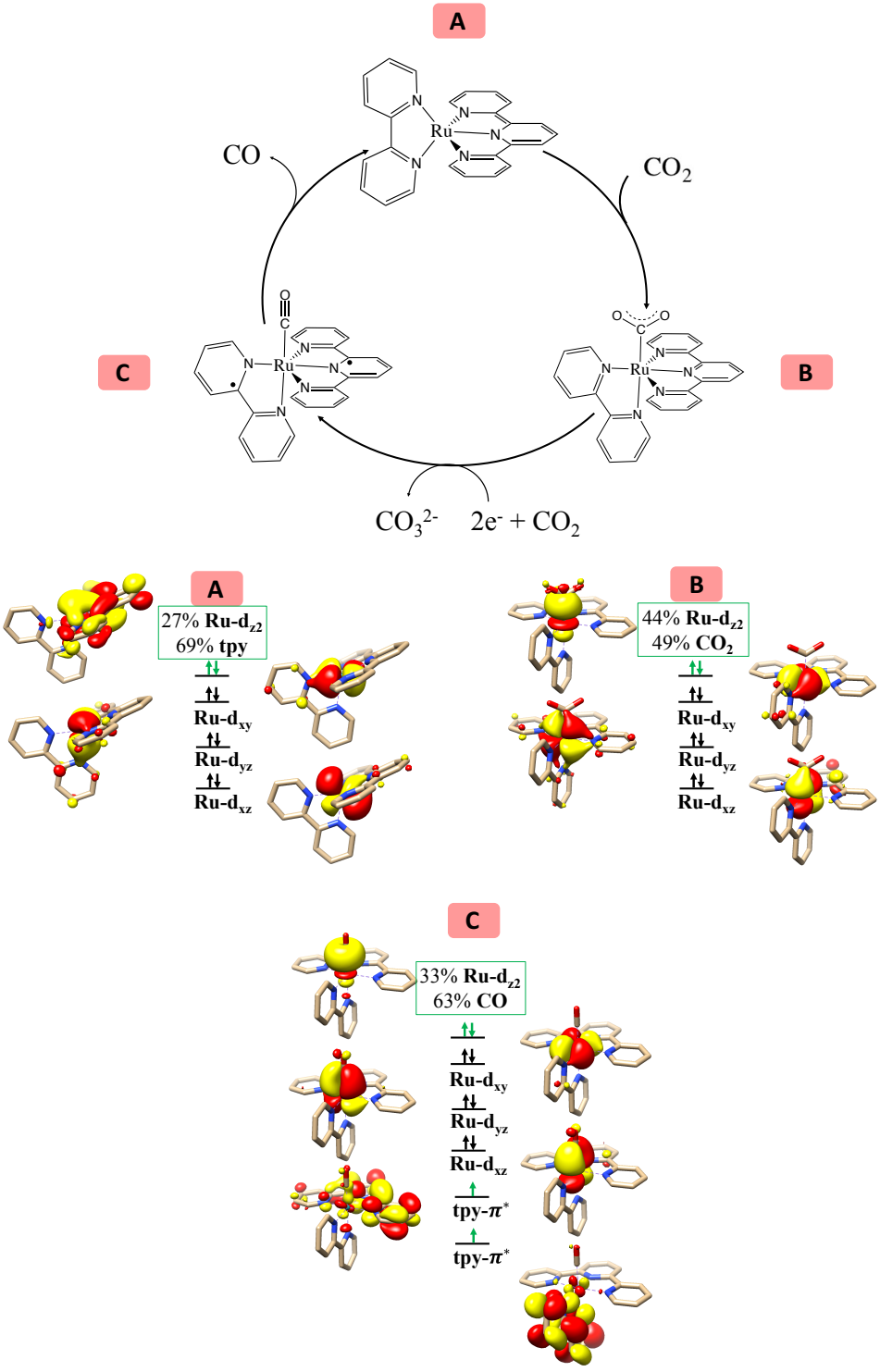


**Figure A12**: (Top) catalytic cycle of $CO_2$-to-CO conversion catalysed with [Ru(bpy)(tpy)]. The mechanism is taken from reference 59. (Bottom) associated electronic structure of the intermediates [Ru(bpy)(tpy)] (A), [Ru(bpy)(tpy)($CO_2$)] (B), and [Ru(bpy)(tpy)(CO)] (C). The electrons occupying the d-orbitals of the metal and the redox-active orbitals of the ligand are represented by arrows. Electrons involved in the ligand-to-metal and metal-to-$CO_2$ intramolecular transfer are shown as green arrows. The Ru, tpy and $CO_2$/CO Löwdin population of the bonding orbital 1σ formed by interaction of the metal center, the tpy and the $CO_2$ ligands

is displayed circled in green. Positive parts of the orbitals are represented in red. Negative parts are represented in yellow. For clarity, all hydrogens are hidden.

# References


([1]) Manabe, S. ; Wetherald, R. T., The effects of doubling the CO2 consentration on the climate of a general circulation model, *J. Atmos. Sci.*, **1975**, 32, 3-15

([2]) Mercer, J. H., West antartic ice sheet and $CO_2$ greenhouse effect: a threat of disaster, *Nature,***1978**, 271, 321-325.

([3]) Sultan, B. ; Parkes, B. ; Gaetani, M., Direct and indirect effects of $CO_2$ increase on crop yield in west Africa, *Int. J. Climatol.*, **2019**, 39, 2400-2411

([4]) Tans, P.; Keeling, R. NOAA/ESRL (www.esrl.noaa.gov/gmd/ccgg/trends/) and Scripps Institution of Oceanography (scrippsco2. ucsd.edu/) (accessed March 18, 2019)

([5]) Schlögl, R., Put the sun in the tank: future developments in sustainable energy systems, *Angew. Chem. Int.*, **2019**, 58, 343-348.

([6]) Smit, B., Carbon capture and storage: introductory lecture, Faraday Discuss., 2016, 192, 9-25. (b) Rochelle, G. T., Amine scrubbing for $CO_2$ capture, *science*, **2009**, 325, 1652-1654

([7]) Song, C., Global challenges and strategies for control, conversion and utilization of $CO_2$ for sustainable development involving energy, catalysis, adsorption and chemical processing, *Catal. Today*, **2006**, 115, 2-32

([8]) Parida, B. ; Iniyan, S. ; Goic, R., A review of solar photovoltaic technologies, *Renew. Sust. Energ. Rev.,* **2011**, 15, 1625-1635.

([9]) Malik, K. ; Singh, S. ; Basu, S. ; Verma, Electrochemical reduction of $CO_2$ for synthesis of green fuel, *WIREs Energy Environ*, **2017**, 6, 1-17.

([10]) Wu, J. ; Huang, Y. ; Ye, W. ; Li, Y., $CO_2$ reduction: from the electrochemical to photochemical approach, *Adv. Sc.*, **2017**, 4, 1700194.

([11]) Zhang, W. ; Hu, Y. ; Ma, L. ; Zhu, G. ; Wang, Y. ; Xue, X. ; Chen, R, ; Yang, S. ; Jin, Z., Progress and perspective of electrocatalytic $CO_2$ reduction for renewable carbonaceous fuels and chemicals, *Adv. Sci.*, **2018**, 5, 1700275.

([12]) M. M. Halmann and M. Steinberg, Greenhouse gas carbon dioxide mitigation science and technology, *Lewis publishers*, **1999**.

([13]) Sutin, N.; Creutz, C.; Fujita, E. Photo-Induced Generation of Dihydrogen and Reduction of Carbon Dioxide Using Transition Metal Complexes. *Comments Inorg. Chem.,* **1997**, *19* (2), 67–92.

([14]) Dry, M. E., The Fischer-Tropsch process: 1950-2000, *Catal. Today*, **2002**, 71, 227-241.

([15]) Benson, E. E. ; Kubiak, C. P. ; Sathrum, A. J. ; Smieja, J. M., Electrocatalytic and homogeneous approaches to conversion of $CO_2$ to liquid fuels, *Chem. Soc. Rev.*, **2009**, 38, 89-99

([16]) Costentin, C. ; Drouet, S.; Passard, G. ; Robert, M. ; Saveant, J.M., Proton-coupled electron transfer cleavage of heavy atom bonds in electrocatalytic process. Cleavage of a C-O bond in the catalysed electrochemical reduction of CO2, *J. Am. Chem. Soc.*, **2013**, 135, 9023-9031.

([17]) Römelt, C. ; Song, J. ; Tarrago, M. ; Rees, J. A. ; Van Gastel, M. ; Weyhermüller, T. ; Debeer, S. ; Bill, E. ; Neese, F. ; Ye, S., Electronic Structure of a Formal Iron(0) Porphyrin Complex Relevant to CO2 Reduction. *Inorg. Chem*., **2017**, 56, 4745-4750.

([18]) Römelt, C.; Ye, S.; Bill, E.; Weyhermüller, T.; van Gastel, M.; Neese, F. Electronic Structure and Spin Multiplicity of Iron Tetraphenylporphyrins in Their Reduced States as Determined by a Combination of Resonance Raman Spectroscopy and Quantum Chemistry *Inorg. Chem.* **2018**, *57*, 2141–2148.

([19]) Goerigk, L. ; Grimme, S., A thourough benchmark of density functional methods for general main group thermochemistry, kinetics and noncovalent interactions, *Phys. Chem. Chem. Phys.*, **2011**, 13, 6670-6688.

([20]) Riplinger, C. ; Pinski, P. ; Becker, U. ; Valeev, E. F. ; Neese, F., Sparse maps – a systematic infrastructure for reduced-scaling electronic structure methods. II. Linear scaling domain based pair natural orbital, *J*. *Chem. Phys.*, **2016**, 144, 024109.

([21]) Federsel, C. ; Jackstell, R. ; Beller, M., State-of-the-art catalysts for hydrogenation of carbon dioxide, *Angew. Chem. Int. Ed.,* **2010**, 49, 6254-6257.

([22]) Junge, H. ; Boddien, A ; Capitta, F. ; Loges, B. ; Noyes, J. R. ; Gladiali, S. ; Beller, M., Improved hydrogen generation from formic acid, *Tetrahedron let.*, **2009**, 50, 1603-1606.

([23]) Ge, H. ; Jing, Y. ; Yang, X., Computational design of cobalt catalysts for hydrogenation of carbon dioxide and dehydrogenation of formic acid, *Inorg. Chem.*, **2016**, 55, 12179-12184

([24]) Jessop, P. G.; Joó, F.; Tai, C.-C. Recent Advances in the Homogeneous Hydrogenation of Carbon Dioxide. *Coord. Chem. Rev.,* **2004**, *248* (21–24), 2425–2442.

([25]) Tanaka, R. ; Yamashita, M. ; Nozaki, K., Catalytic hydrogenation of carbon dioxide using Ir(III)- pincer complexes, *J. Am. Chem. Soc.,* **2009**, 131, 14168-14169

([26]) Schmeier, T. J., Dobereiner, G. E. ; Crabtree, R. H., Hazari, N., Secondary coordination sphere interactions facilitate the insertion step in an iridium(III)$CO_2$ reduction catalyst, *J. Am. Chem. Soc.,* **2011**, 133, 9274-9277

([27]) Angermund, K.; Baumann, W.; Dinjus, E.; Fornika, R.; Görls, H.; Kessler, M.; Krüger, C.; Leitner, W.; Lutz, F. Complexes [($P_2$) Rh (Hfacac)] as Model Compounds for the Fragment [($P_2$) Rh] and as Highly Active Catalysts for $CO_2$ Hydrogenation: The Accessible Molecular Surface (AMS) Model as an Approach to Quantifying the Intrinsic Steric Properties of Chelating Ligands in Homogeneous Catalysis. *Chem-Eur. J,* **1997**, *3* (5), 755–764.

([28]) Munshi, P.; Main, A. D.; Linehan, J. C.; Tai, C.-C.; Jessop, P. G. Hydrogenation of Carbon Dioxide Catalyzed by Ruthenium Trimethylphosphine Complexes: The Accelerating Effect of Certain Alcohols and Amines. *J. Am. Chem. Soc.,* **2002**, *124* (27), 7963–7971.

([29]) Leitner, W., Carbon dioxide as a raw material: the synthesis of formic acid and its derivative from $CO_2$, *Angew. Chem. Int. Ed. Engl.* **1995**, 34, 2207-2221.

([30]) Federsel, C. ; Boddien, A. ; Jackstell, R. ; Jennerjahn, R. ; Dyson, P. J. ; Scopelliti, R. ; Laurenczy, G. ; Belle, M., A well-defined iron catalyst for the reduction of bicarbonates and carbon dioxide to formates, alkyl formates and formamides, *Angew. Chem. Int.*, **2010**, 49, 9777-9780

([31]) Zhang, Y.; MacIntosh, A. D.; Wong, J. L.; Bielinski, E. A.; Williard, P. G.; Mercado, B. Q.; Hazari, N.; Bernskoetter, W. H. Iron Catalyzed CO 2 Hydrogenation to Formate Enhanced by Lewis Acid Co-Catalysts. *Chem. Sci.,* **2015**, *6* (7), 4291–4299.

([32]) Chakraborty, S ; Bhattacharya, P. ; Dai, H. ; Guan, H., Nickel and iron pincer complexes as catalysts for the reduction of carbonyl compounds, *Acc. Chem. Res.,* **2015**, 48, 1995-2003

([33]) Burgess, S. A. ; Kendall, A. J. ; Tyler, D. R. ; Linehan, J. C. ; Appel, A. M., Hydrogenation of $CO_2$ in water using a bis(disphosphine) Ni-H complex, *ACS Catal.,* **2017**, 7, 3089-3096

([34]) Jeletic, M. S. ; Mock, M. T. ; Appel, A. M. ; Linehan, J. C., A cobalt-based catalyst for the hydrogenation of CO2 under ambient conditions, *J. Am. Chem. Soc.*, **2013**, 135, 31, 11533-11536

([35]) Yang, X. ; Hydrogenation of carbon dioxide catalysed by PNP pincer iridium, iron and cobalt complexes: a computational design of base metal catalysts, *ACS catal*., **2011**, 1, 849-854.

([36]) Burgemeister, T. ; Kastner, F. ; Leitner, W., [(PP)2RhH] and [(PP)2[O2CH] complexes as models for the catalytically active intermediates in the Rh-catalyzed hydrogenation of CO2 to HCOOH, *Angew. Chem. Int. Ed. Engl.*, **1993**, 32, 739-741

([37]) Tanka, R. ; Yamashita, M. ; Wa Chung, L. ; Morokuma, K. ; Nozaki, K., Mechanistic studies on the reversible hydrogenation of carbon dioxide catalysed by an Ir-PNP comples, *Organometallics*, **2011**, 30, 6742-6750.

([38]) Hutschka, F. ; Dedieu, A. ; Eichberger, M. ; Fornika, R. ; Leitner, W., Mechanistic aspects of the Rhodium-catalyzed hydrogenation of CO2 to formic acid – a theoretical and kinetic study, *J. Am. Chem. Soc.*, **1997**, 119, 4432-4443.

([39]) Yang, X., Bio-inspired computational design of iron catalysts for the hydrogenation of carbon dioxide, *Chem. Commun.*, **2015**, 51, 13098-13101

([40]) Mondal, B. ; Neese, F. ; Ye, S, Towards rational design of 3d transition metal catalysts for CO2 hydrogenation based on insights into hydricity-controlled rate-determining steps, *Inorg. Chem.,* **2016**, 55, 5438-5444

([41]) Wiedner, E. S. ; Chambers, M. B. ; Pitman, C. L. ; Bullock, R. M. ; Miller, A. J. M. ; Appel, A. M., Thermodynamic hydricity of transition metal hydrides, *Chem. Rev.,* **2016**, 8655-8692

([42]) Costentin, C. ; Drouet, S. ; Robert, M. ; Savéant, J. M., Turnover numbers, turnover frequencies, and overpotential in Molecular catalysis of electrochemical reactions. Cyclic voltammetry and preparative-scale electrolysis, *J. Am. Chem. Soc.*, **2012**, 134, 11235-11242.

([43]) Francke, R.; Schille, B.; Roemelt, M. Homogeneously Catalyzed Electroreduction of Carbon Dioxide—Methods, Mechanisms, and Catalysts. *Chem. Rev.,* **2018**, *118* (9), 4631–4701.

([44]) Kang, P.; Cheng, C.; Chen, Z.; Schauer, C. K.; Meyer, T. J.; Brookhart, M. Selective Electrocatalytic Reduction of CO2 to Formate by Water-Stable Iridium Dihydride Pincer Complexes. *J. Am. Chem. Soc.,* **2012**, *134* (12), 5500–5503.

([45]) Paul, P.; Tyagi, B.; Bilakhiya, A. K.; Bhadbhade, M. M.; Suresh, E.; Ramachandraiah, G. Synthesis and Characterization of Rhodium Complexes Containing 2, 4, 6-Tris (2-Pyridyl)-1, 3, 5-Triazine and Its Metal-Promoted Hydrolytic Products: Potential Uses of the New Complexes in Electrocatalytic Reduction of Carbon Dioxide. *Inorg. Chem.,* **1998**, *37* (22), 5733–5742.

([46]) Ishida, H.; Tanaka, K.; Tanaka, T. Electrochemical $CO_2$ Reduction Catalyzed by Ruthenium Complexes $[Ru\ (Bpy)_2(CO)_2]^{2+}$ and $[Ru\ (Bpy)_2(CO)Cl]^{+}$. Effect of PH on the Formation of CO and $HCOO^{-}$. *Organometallics* **1987**, *6* (1), 181–186.

([47]) Ghosh, D.; Kobayashi, K.; Kajiwara, T.; Kitagawa, S.; Tanaka, K. Catalytic Hydride Transfer to $CO_2$ Using Ru-NAD-Type Complexes under Electrochemical Conditions. *Inorg. Chem.,* **2017**, *56* (18), 11066–11073.

([48]) Chen, L. ; Guo, Z., Wie, X-G ; Gallenkamp, C. ; Bonin, J. ; Anxolabéhère-Mallart, E.t, M., Molecular catalysis of the electrochemical and photochemical reduction of $CO_2$ with earth-abundant metal complexes. Selective production of CO vs HCOOH by switching of the metal center, *J. Am. Chem. Soc.*, **2015**, 137, 10918-10921.

([49]) Roy, S.; Sharma, B.; Pécaut, J.; Simon, P.; Fontecave, M.; Tran, P. D.; Derat, E.; Artero, V. Molecular Cobalt Complexes with Pendant Amines for Selective Electrocatalytic Reduction of Carbon Dioxide to Formic Acid. *J. Am. Chem. Soc.,* **2017**, *139* (10), 3685–3696.

([50]) Cope, J. D.; Liyanage, N. P.; Kelley, P. J.; Denny, J. A.; Valente, E. J.; Webster, C. E.; Delcamp, J. H.; Hollis, T. K. Electrocatalytic Reduction of $CO_2$ with CCC-NHC Pincer Nickel Complexes. *Chem. Comm.,* **2017**, *53* (68), 9442–9445.

([51]) Göttle, A. j. ; Koper, M. T. M., Determinant role of electrogenerated reactive nucleophilic species on selectivity during reduction of $CO_2$ catalyzed by metalloporphyrins, *J. Am. Chem. Soc.*, **2018**, 140, 4826-4834.

([52]) Schneider, J. ; Jia, H. ; Muckerman, J. T. ; Fujita, E., Thermodynamics and kinetics of $CO_2$, CO and $H^+$ binding to the metal center of $CO_2$ reduction catalysts, *Chem. Soc. Rev.*, **2012**, 41, 2036-2051

([53]) Collin, J-P. ; Jouaiti, A ; Sauvage, J-P., Electrocatalytic properties of $Ni(cyclam)^{2+}$ and $Ni_2(biscyclam)^{4+}$ with respect to $CO_2$ and $H_2O$ reduction, *Inorg. Chem.*, **1988**, 27, 1986-1990.

([54]) Song, J. ; Klein, E. L. ; Neese, F. ; Ye, S., The mechanism of homogeneous $CO_2$ reduction by Ni(cyclam): product selectivity, concerted proton-electron transfer and C-O bond cleavage, *Inorg. Chem.*, **2014**, 53, 7500-7507

([55]) Clark, M. L.; Cheung, P. L.; Lessio, M.; Carter, E. A.; Kubiak, C. P. Kinetic and Mechanistic Effects of Bipyridine (Bpy) Substituent, Labile Ligand, and Brønsted Acid on Electrocatalytic $CO_2$ Reduction by Re(bpy) Complexes. *ACS Catal.,* **2018**, *8* (3), 2021–2029.

([56]) Johnson, F. P. A. ; George, M. W. ; Hartl, F. ; Turner, J. J., Electrocatalytic reduction of CO2 using the complexes $[Re(bpy)(CO)_3L]^n$ (n=+1, L=P(OEt)3, $CH_3CN$; n=0, L=$Cl^-$, $Otf^-$; bpy = 2,2'- Bipyridine; $Otf^-$=$CF_3SO_3$) as catalyst precursors: infrared spectroelectrochemical investigation, *Organometallics*, **1996**, 15, 3374-3387

([57]) Hawecker, J. ; Lehn, J. M. ; Ziessel, R., Electrocatalytic reduction of carbon dioxide mediated by $Re(bipy)(CO)_3Cl$ (bipy = 2,2'-bipyridine), *J. Chem. Soc., Chem. Commun.*, **1984**, 328-330

([58]) Tanaka, H ; Nagao, H. ; Peng, S. M. ; Tanaka, K., Crystal structure of cis-(carbonyl)(.eta.1-carbon dioxide)bis(2,2'-bipyridyl)ruthenium, an active species in catalytic carbon dioxide reduction affording carbon monoxide and $HCOO^-$, *Organometallics*, **1992**, 11, 1450-1451.

([59]) Chen, Z. ; Weinberg, D. R. ; Kang, P. ; Concepcion, J. J. ; Harrison, D. P. ; Brookhart, M.S. ; Meyer, T. J., Electrocatalytic reduction of $CO_2$ to CO by polypyridyl ruthenium complexes, *Chem. Commun.*, **2011**, 47, 12607-12609

([60]) Machan, C. W.; Sampson, M. D.; Kubiak, C. P. A Molecular Ruthenium Electrocatalyst for the Reduction of Carbon Dioxide to CO and Formate. *J. Am. Chem. Soc.,* **2015**, *137* (26), 8564–8571.

([61]) Koizumi, T.; Tomon, T.; Tanaka, K. Synthesis, Structures and Electrochemical Properties of Ruthenium (II) Complexes Bearing Bidentate 1, 8-Naphthyridine and Terpyridine Analogous (N, N, C)-Tridentate Ligands. *J. Organomet. Chem.,* **2005**, *690* (19), 4272–4279.

([62]) Min, S.; Rasul, S.; Li, H.; Grills, D. C.; Takanabe, K.; Li, L.; Huang, K. Electrocatalytic Reduction of Carbon Dioxide with a Well-Defined PN3− Ru Pincer Complex. *ChemPlusChem* **2016**, *81* (2), 166–171.

([63]) Grice, K. A.; Saucedo, C. Electrocatalytic Reduction of $CO_2$ by Group 6 M (CO) 6 Species without “Non-Innocent” Ligands. *Inorg. Chem.,* **2016**, *55* (12), 6240–6246.

([64]) Tory, J.; Setterfield-Price, B.; Dryfe, R. A.; Hartl, F. [$M(CO)_4$(2, 2′-Bipyridine)](M= Cr, Mo, W) as Efficient Catalysts for Electrochemical Reduction of $CO_2$ to CO at a Gold Electrode. *ChemElectroChem* **2015**, *2* (2), 213–217.

([65]) Dubois, D. L., Development of transition metal phosphine complexes as electrocatalysts for $CO_2$ and CO reduction, Comm. *Inorg. Chem.*, **1997**, 19, 307-325

([66]) Hossain, A. M.; Nagaoka, T.; Ogura, K. Palladium and Cobalt Complexes of Substituted Quinoline, Bipyridine and Phenanthroline as Catalysts for Electrochemical Reduction of Carbon Dioxide. *Electrochim. Acta,* **1997**, *42* (16), 2577–2585.

([67]) Miedaner, A.; Noll, B. C.; DuBois, D. L. Synthesis and Characterization of Palladium and Nickel Complexes with Positively Charged Triphosphine Ligands and Their Use as Electrochemical $CO_2$-Reduction Catalysts. *Organometallics* **1997**, *16* (26), 5779–5791.

([68]) Therrien, J. A.; Wolf, M. O.; Patrick, B. O. Electrocatalytic Reduction of $CO_2$ with Palladium Bis-N-Heterocyclic Carbene Pincer Complexes. *Inorg. Chem.,* **2014**, *53* (24), 12962–12972.

([69]) Manbeck, G. F.; Garg, K.; Shimoda, T.; Szalda, D. J.; Ertem, M. Z.; Muckerman, J. T.; Fujita, E. Hydricity, Electrochemistry, and Excited-State Chemistry of Ir Complexes for $CO_2$ Reduction. *Faraday Discuss,* **2017**, *198*, 301–317.

([70]) Smieja, J. M.; Sampson, M. D.; Grice, K. A.; Benson, E. E.; Froehlich, J. D.; Kubiak, C. P. Manganese as a Substitute for Rhenium in $CO_2$ Reduction Catalysts: The Importance of Acids. *Inorg. Chem.,* **2013**, *52* (5), 2484–2491.

([71]) Sampson, M. D.; Nguyen, A. D.; Grice, K. A.; Moore, C. E.; Rheingold, A. L.; Kubiak, C. P. Manganese Catalysts with Bulky Bipyridine Ligands for the Electrocatalytic Reduction of Carbon Dioxide: Eliminating Dimerization and Altering Catalysis. *J. Am. Chem. Soc.,* **2014**, *136* (14), 5460–5471.

([72]) Rao, G. K.; Pell, W.; Korobkov, I.; Richeson, D. Electrocatalytic Reduction of $CO_2$ Using Mn Complexes with Unconventional Coordination Environments. *Chem. Comm.,* **2016**, *52* (51), 8010–8013.

([73]) Costentin, C.; Robert, M.; Savéant, J.-M. Catalysis of the Electrochemical Reduction of Carbon Dioxide. *Chem. Soc. Rev.,* **2013**, *42* (6), 2423–2436.

([74]) Zee, D. Z.; Nippe, M.; King, A. E.; Chang, C. J.; Long, J. R. Tuning Second Coordination Sphere Interactions in Polypyridyl–Iron Complexes to Achieve Selective Electrocatalytic Reduction of Carbon Dioxide to Carbon Monoxide. *Inorg. Chem.,* **2020**, *59* (7), 5206–5217.

([75]) Rosas-Hernández, A.; Junge, H.; Beller, M.; Roemelt, M.; Francke, R. Cyclopentadienone Iron Complexes as Efficient and Selective Catalysts for the Electroreduction of $CO_2$ to CO. *Catal. Sci. Technol.,* **2017**, *7* (2), 459–465.

([76]) Cometto, C.; Chen, L.; Lo, P.-K.; Guo, Z.; Lau, K.-C.; Anxolabéhère-Mallart, E.; Fave, C.; Lau, T.-C.; Robert, M. Highly Selective Molecular Catalysts for the $CO_2$-to-CO Electrochemical Conversion at Very Low Overpotential. Contrasting Fe vs Co Quaterpyridine Complexes upon Mechanistic Studies. *ACS Catal.,* **2018**, *8* (4), 3411–3417.

([77]) Grodkowski, J.; Neta, P.; Fujita, E.; Mahammed, A.; Simkhovich, L.; Gross, Z. Reduction of Cobalt and Iron Corroles and Catalyzed Reduction of $CO_2$. *The J. Phys. Chem. A* **2002**, *106* (18), 4772–4778.

([78]) Chapovetsky, A.; Do, T. H.; Haiges, R.; Takase, M. K.; Marinescu, S. C. Proton-Assisted Reduction of $CO_2$ by Cobalt Aminopyridine Macrocycles. *J. Am. Chem. Soc.,* **2016**, *138* (18), 5765–5768.

([79]) Elgrishi, N. ; Chambers, M. B. ; Artero, V. ; Fontecave, M., Terpyridine complexes of first row transition metals and electrochemical reduction of $CO_2$ to CO, *Phys. Chem. Chem. Phys.*, **2014**, 16, 13635-13644

([80]) Lacy, D. C. ; McCrory, C. C. L. ; Peters, J. C., Studies of cobalt-mediated electrocatalytic CO2 reduction using a redox-active ligand, *Inorg. Chem.*, **2014**, 53, 4980-4988.

([81]) Fisher, B. J.; Eisenberg, R. Electrocatalytic Reduction of Carbon Dioxide by Using Macrocycles of Nickel and Cobalt. *Journal of the American Chemical Society* **1980**, *102* (24), 7361–7363.

([82]) Alenezi, K. Electrocatalytic Study of Carbon Dioxide Reduction By Co(TPP)Cl Complex. *J. Chem.,* **2016**, *2016*.

([83]) Froehlich, J. D. ; Kubiak, C. P., Homogeneous $CO_2$ reduction by Ni(cyclam) at glassy a carbon electrode, *Inorg. Chem.*, **2012**, 51, 3932-3934.

([84]) Beley, M. ; Collin, J. P. ; Ruppert, R ; Sauvage, J. P., Nickel(II)-cyclam: an extremely selective electrocatalyst for reduction of $CO_2$ in water, *J. Chem. Soc., Chem. Commun.*, **1984**, 1315- 1316.

([85]) Beley, M. ; Collin, J. P. ; Ruppert, R. ; Sauvage, J. P., Electrocatalytic reduction of $CO_2$ by Ni $cyclam^{2+}$ in water: study of the factors affecting the efficiency and selectivity of the process, *J. Am. Chem. Soc.*, **1986**, 108, 7461-7467

([86]) Sheng, M.; Jiang, N.; Gustafson, S.; You, B.; Ess, D. H.; Sun, Y. A Nickel Complex with a Biscarbene Pincer-Type Ligand Shows High Electrocatalytic Reduction of $CO_2$ over $H_2O$. *Dalton Trans.,* **2015**, *44* (37), 16247–16250.

([87]) Costentin, C. ; Drouet, S. ; Robert, M. ; Saveant, J.M., A local proton source enhances $CO_2$ electroreduction to CO by a molecular Fe catalyst, *Science*, **2012**, 338, 90-94.

([88]) Costentin, C. ; Robert, M. ; Savéant, J. M., Current issues in molecular catalysis illustrated by iron porphyrins as catalysts of the $CO_2$-to-CO electrochemical conversion, *Acc. Chem. Res.*, **2015**, 48, 2996-3006.

([89]) Costentin, C. ; Passard, G. ; Robert, M. ; Saveant, J.M., Pendant acid-base groups in molecular catalysts: H-bond promoters of proton relays? Mechanism of the conversion of $CO_2$ to CO by electrogenerated iron(0) porphyrins bearing prepositioned phenol functionalities, *J. Am. Chem. Soc.*, **2014**, 136, 11821-11829.

([90]) Azcarate, I. ; Costentin, C. ; Robert, M., Savéant ; J.M., Through-space interaction substituent effects in molecular catalysis leading to the design of the most efficient catalyst of $CO_2$-to-CO electrochemical conversion, *J. Am. Chem. Soc.*, **2016**, 138, 16639-16644.

([91]) Ngo, K. T.; McKinnon, M.; Mahanti, B.; Narayanan, R.; Grills, D. C.; Ertem, M. Z.; Rochford, J. Turning on the Protonation-First Pathway for Electrocatalytic $CO_2$ Reduction by Manganese Bipyridyl Tricarbonyl Complexes. *J. Am. Chem. Soc.,* **2017**, *139* (7), 2604–2618.

([92]) Machan, C. W.; Kubiak, C. P. Interrogating Heterobimetallic Co-Catalytic Responses for the Electrocatalytic Reduction of $CO_2$ Using Supramolecular Assembly. *Dalton Trans.,* **2016**, *45* (40), 15942–15950.

([93]) Machan, C. W.; Yin, J.; Chabolla, S. A.; Gilson, M. K.; Kubiak, C. P. Improving the Efficiency and Activity of Electrocatalysts for the Reduction of $CO_2$ through Supramolecular Assembly with Amino Acid-Modified Ligands. *J. Am. Chem. Soc.,* **2016**, *138* (26), 8184–8193.

([94]) Garza, A. J.; Pakhira, S.; Bell, A. T.; Mendoza-Cortes, J. L.; Head-Gordon, M. Reaction Mechanism of the Selective Reduction of $CO_2$ to CO by a Tetraaza $[Co(II)N_4H]^{2+}$ Complex in the Presence of Protons. *Phys. Chem. Chem. Phys.,* **2018**, *20* (37), 24058–24064.

([95]) Davethu, P. A.; de Visser, S. P. $CO_2$ Reduction on an Iron-Porphyrin Center: A Computational Study. *J. Phys. Chem. A,* **2019**, *123* (30), 6527–6535.

([96]) Oberem, E.; Roesel, A. F.; Rosas-Hernández, A.; Kull, T.; Fischer, S.; Spannenberg, A.; Junge, H.; Beller, M.; Ludwig, R.; Roemelt, M. Mechanistic Insights into the Electrochemical Reduction of $CO_2$ Catalyzed by Iron Cyclopentadienone Complexes. *Organometallics* **2018**, *38* (6), 1236–1247.

([97]) Hammes-Schiffer, S. Proton-Coupled Electron Transfer: Classification Scheme and Guide to Theoretical Methods. *Energy Environ. Sci.,* **2012**, *5* (7), 7696–7703.

([98]) Koper, M. T. M., Theory of the transition from sequencial to concerted electrochemical proton-electron transfer, *Phys. Chem. Chem. Phys.,* **2013**, 15, 1399-1407.

([99]) Costentin, C.; Robert, M.; Savéant, J.-M.; Tard, C. Breaking Bonds with Electrons and Protons. Models and Examples. *Acc. Chem. Res,* **2014**, *47* (1), 271–280.

([100]) Mascetti, J. ; Tranquille, M, Fourier transform infrared studies of atomic Ti, V, Cr, Fe, Co, Ni, and Cu reactions with carbon dioxide in low-temperature matrices*, J. Phys. Chem.*, **1988**, 92, 2177- 2184.

([101]) Fachinetti, G. ; Floriani, C. ; Zanazzi, P. F., Bifunctional activation of carbon dioxide. Synthesis and structure of a reversible carbon dioxide carrier, *J. Am. Chem. Soc.*, **1978**, 100, 7405-7407.

([102]) Zhang, M.; El-Roz, M.; Frei, H.; Mendoza-Cortes, J.; Head-Gordon, M.; Lacy, D. C.; Peters, J. C. Visible Light Sensitized $CO_2$ Activation by the Tetraaza [CoIIN4H(MeCN)]$^{2+}$ Complex Investigated by FT-IR Spectroscopy and DFT Calculations, *J. Phys. Chem. C,* **2015**, *119* (9), 4645–4654.

([103]) Keith, J. A.; Grice, K. A.; Kubiak, C. P.; Carter, E. A., Elucidation of the selectivity of proton- dependent electrocatalytic CO2 reduction by a fac-Re(bpy)$(CO)_3$Cl, *J. Am. Chem. Soc.*, **2013**, 135, 15823-15829

([104]) Haviv, E.; Azaiza-Dabbah, D.; Carmieli, R.; Avram, L.; Martin, J. M.; Neumann, R. A Thiourea Tether in the Second Coordination Sphere as a Binding Site for $CO_2$ and a Proton Donor Promotes the Electrochemical Reduction of $CO_2$ to CO Catalyzed by a Rhenium Bipyridine-Type Complex. *J. Am. Chem. Soc.,* **2018**, *140* (39), 12451–12456.

([105]) Zhang, Y.; Chen, J.; Siegbahn, P. E.; Liao, R.-Z. Harnessing Non-Innocent Porphyrin Ligand to Circumvent Fe-Hydride Formation in the Selective Fe-Catalyzed $CO_2$ Reduction in Aqueous Solution. *ACS Catal.,* **2020**, 10, 11, 6332-6345.

([106]) Franco, F.; Cometto, C.; Vallana, F. F.; Sordello, F.; Priola, E.; Minero, C.; Nervi, C.; Gobetto, R. A Local Proton Source in a [Mn (Bpy-R)$(CO)_3$Br]-Type Redox Catalyst Enables

CO 2 Reduction Even in the Absence of Brønsted Acids. *Chem. Comm.,* **2014**, *50* (93), 14670–14673.

([107]) Kahn, O., *Molecular Magnetism*, VCH publishers, **1993**

([108]) Odom, B. ; Hanneke, D. ; D'Urso, B. ; Gabriele, G., New measurement of the electron magnetic moment using a one-electron quantum cyclotron, *Phys. Rev. Lett.*, **2006**, 97, 030801.

([109]) Neese, F. in Magnetism: Molecules to Material IV, J. S. Miller and M. Drillon, **2002**

([110]) Kwon, S. K. ; Min, B. I., Unquenched large orbital magnetic moment in NiO, *Phys. Rev. B.*, **2000**, 62, 73-75.

([111]) Reed, C. A. ; Mashiko, T. ; Bentley, S. P. ; Kastner, M. E. ; Scheidt, W. R. ; Spartalian, K. ; Lang, G., The missing heme spin state and a model for cytochrome c'. The mixed 3/2,5/2 intermediate spin ferric porphyrin: perchlorate(meso-tetraphenylporphyrinato)iron(III), *J. Am. Chem. Soc.*, **1979**, 101, 11, 2948-2958.

([112]) Chibotaru, L.F. ; Ungur, L., Ab-initio calculation of anisotropic magnetic properties of complexes. I. Unique definition of pseudospin Hamiltonians and their derivation, *J. Chem. Phys*., **2012**, 137, 064112

([113]) M. H. L. Pryce, Sign of g in magnetic resonance, and the sign of the quadrupole moment of $Np^{237}$, *Phys. Rev. Lett.*, **1959**, 3, 375.

([114]) Kramers, H. A., Theorie Générale de la rotation paramagnetique dans les cristaux, *Proc. Amsterdam Acad.*, **1930**, 33, 959

([115]) Atanasov, M. ; Aravena, D. ; Suturina, E. ; Bill, E. ; Manganas, D. ; Neese, F., First principles approach to the electronic structure, magnetic anisotropy and spin relaxation in mononuclear 3d-transition metal single molecule magnets, *Coord. Chem. Rev.*, **2015**, 289, 177

([116]) Gütlich, P. ; Bill, E. ; Trautwein, A. X. in Mössbauer spectroscopy and transition metal chemistry, *Springer-Verlag*, Berlin Heidelberg, **2011**.

([117]) Atkins, P.; De Paula, J.: Physical chemistry. *Oxford university press*, Oxford, **2006**.

([118]) C. P. Slichter, in Principles of magnetic resonance, Springer series in solid-state sciences, vol 1. *Springer-Verlag*, Berlin, Heidelberg, **1978**.

([119]) Abragam, in The principles of nuclear magnetism, *Oxford University Press*, London, **1961**.

([120]) Reiff, W. M. ; Frommen, C. M. ; Yee, G. T. ; Sellers, S. P., Observation of a very large internal hyperfine field (62.4T) in the ferromagnetically-ordered state of the S=1 $\alpha$-iron(II) octaethyltetraazaporphyrin, *Inorg. Chem*., **2000**, 39, pp 2076-2079.

([121]) Greenwood, N. N. ; Gibb, T. C. in Mössbauer Spectroscopy, Chapman and Hall, **1971**.

([122]) Johnson, C. E. , hyperfine interactions in ferrous fluorsilicate, *Proc. Phys. Soc*., **1967**, 92, 748-757.

([123]) Oosterhuis, W. T. ; Lang, G., Mössbauer effect in $K_3Fe(CN)_6$, *Phys. Rev*., **1968**, 178, 439-456.

([124]) Weissbluth, M. in Atoms and molecules, *Elsevier*, **2012**.

([125]) Westre, T. E.; Kennepohl, P.; DeWitt, J. G.; Hedman, B.; Hodgson, K. O.; Solomon, E. I. A Multiplet Analysis of Fe K-Edge 1s→ 3d Pre-Edge Features of Iron Complexes. *J. Am. Chem. Soc.,* **1997**, *119* (27), 6297–6314.

([126]) Shulman, G.; Yafet, Y.; Eisenberger, P.; Blumberg, W. Observations and Interpretation of X-Ray Absorption Edges in Iron Compounds and Proteins. *PNAS,* **1976**, *73* (5), 1384–1388.

([127]) DeBeer George, S. ; Petrenko, T. ; Neese, F., Prediction of iron K-edge absorption spectra using time-dependent density functional theory, *J. Phys. Chem. A*, **2008**, 112, 12936-12943.

([128]) Eyring, H., The activated complex in chemical reactions, *J. Chem. Phys.*, **1935**, 3, 107-115.

([129]) Christiansen, J. A. The Elucidation of Reaction Mechanisms by the Method of Intermediates in Quasi-Stationary Concentrations. In *Adv. Catal.*, **1953**; Vol. 5, pp 311–353.

([130]) Kozuch, S.; Shaik, S. A Combined Kinetic− Quantum Mechanical Model for Assessment of Catalytic Cycles: Application to Cross-Coupling and Heck Reactions. *J. Am. Chem. Soc.,* **2006**, *128* (10), 3355–3365.

([131]) Kozuch, S.; Shaik, S. Kinetic-Quantum Chemical Model for Catalytic Cycles: The Haber− Bosch Process and the Effect of Reagent Concentration. *J. Phys. Chem. A,* **2008**, *112* (26), 6032–6041.

([132]) Ochterski, J. W., Thermochemistry in Gaussian, *Gaussian Inc.*, **2000**.

([133]) Zhou, H-X. ; Gilson, M. K., Theory of free energy and entropy in noncovalent binding, *Chem. Rev.*, **2009**, 109, 9, 4092-4107.

([134]) Garza, A., Solvation entropy made simple, *J. Chem. Theory Comput*., **2019**, 15, 5, 3204-3214.

([135]) Leung, B. O. ; Reid, D. L., Armstrong, D. A. ; Rauk, A., Entropies in solution from entropies in gas phase, *J. Phys. Chem. A*, **2004**, 108, 2720-2725

([136]) König, G. ; Pickard IV, F. C. ; Mei, Y. ; Brooks, B. R., Predicting hydration free energies with a hybrid QM/MM approach: an evaluation of implicit and explicit solvation models in SAMPL4*, J. Comput Aided Mol Des*, **2014**, 28, 245-257.

([137]) Cossi, M. ; Rega, N. ; Scalamani, G. ; Barone, V., Energies, structures, and electronic properties of molecules in solution with the C-PCM solvation model, *J. Comput. Chem.*, **2002**, 24, 669-681.

([138]) Truong, T. N.; Stefanovich, E. V., A new method for incorporating solvent effect into the classical, ab initio molecular orbital and density functional theory frameworks for arbitrary shape cavity, *Chem. Phys. Lett.*, **1995**, 240, 253.

**(**[139]**)** Sitkoff, D. ; Sharp, K. A. ; Konig, B., Accurate calculation of hydration free energies using macroscopic solvent models, *J. Chem. Phys.*, **1994**, 98, 1978-1988.

([140]) Mammen, M.; Shakhnovich, E. I.; Deutch, J. M.; Whitesides, G. M.EstimatingtheEntropicCostofSelf-AssemblyofMultiparticle Hydrogen-Bonded Aggregates Based on the Cyanuric Acid-Melamine Lattice. *J. Org. Chem.*, **1998**, 63, 3821−3830.

([141]) Ewing, G. E. Spectroscopic Studies of Molecular Motion in Liquids. *Acc. Chem. Res.*, **1969**, 2, 168−174

([142]) Parr, R. G.; Yang, W., *Density Functional Theory of Atoms and Molecules.* Oxford University Press*,* **1989**.

([143]) Seminario, J. M. *Modern Density Functional Theory: A Tool for Chemistry*; Elsevier, **1995**.

([144]) F. Weigend, R. Alhrichs, Balanced basis sets of split valence, triple zeta valence and quadrupole zeta valence quality for H to Rn: Design and assessment of accuracy, *Phys. Chem. Chem. Phys.*, **2005**, 7, 3297-3305

([145]) Neese, F., Prediction and interpretation of the 57Fe isomer shift in Mössbauer spectra by density functional theory, *Inorg. Chim. Acta*, **2002**, 337, 181-192.

([146]) Neese, F., Definition of corresponding orbitals and the diradical character in broken-symmetry DFT calculations on spin-coupled systems, *J. Phys. Chem. Solids*, **2004**, 65, 781-785.

([147]) Malrieu, J.-P.; Trinquier, G. A Recipe for Geometry Optimization of Diradicalar Singlet States from Broken-Symmetry Calculations. *The Journal of Physical Chemistry A* **2012**, *116* (31), 8226–8237.

([148]) Korth, M. ; Grimme, S., "Mindless" DFT benchmarking, *J. Chem. Theory Comput*, **2009**, 5, 993-1003.

([149]) Römelt, M. ; Ye, S. ; Neese, F., Calibration of modern density functional theory methods for the prediction of 57Fe Mössbauer isomer shifts: meta-GGA and double-hybrid functionals, *Inorg. Chem.*, **2009**, 48, 784-785.

([150]) Sinnecker, S. ; Slep, L. D. ; Bill, E. ; Neese, F., Performance of non-relativistic and quasi-relativistic hybrid DFT for the prediction of electric and magnetic hyperfine parameters in $^{57}$Fe Mössbauer spectra, *Inorg. Chem.*, **2005**, 44, 2245-2254.

([151]) Bjornsson, R. ; Neese, F. ; DeBeer, S., Revisiting the Mössbauer isomer shift of the FeMoco cluster of nitrogenase and the cofactor charge, *Inorg. Chem.*, **2017**, 56, 1470-1477.

([152]) McWilliams, S. F.; Brennan-Wydra, E.; MacLeod, K. C.; Holland, P. L. Density Functional Calculations for Prediction of $^{57}$Fe Mössbauer Isomer Shifts and Quadrupole Splittings in β-Diketiminate Complexes. *ACS omega* **2017**, *2* (6), 2594–2606.

([153]) Moore, J. T.; Chatterjee, S.; Tarrago, M.; Clouston, L. J.; Sproules, S.; Bill, E.; Bernales, V.; Gagliardi, L.; Ye, S.; Lancaster, K. M. Enhanced Fe-Centered Redox Flexibility in Fe–Ti Heterobimetallic Complexes. *Inorg. Chem.,* **2019**, *58* (9), 6199–6214.

([154]) Dreuw, A.; Head-Gordon, M. Single-Reference Ab Initio Methods for the Calculation of Excited States of Large Molecules. *Chem. Rev.,* **2005**, *105* (11), 4009–4037.

([155]) Dreuw, A.; Head-Gordon, M. Failure of Time-Dependent Density Functional Theory for Long-Range Charge-Transfer Excited States: The Zincbacteriochlorin− Bacteriochlorin and Bacteriochlorophyll− Spheroidene Complexes. *J. Am. Chem. Soc.,* **2004**, *126* (12), 4007–4016.

([156]) Malmqvist, P.-Å.; Roos, B. O. The CASSCF State Interaction Method. *Chem. Phys. Lett.,* **1989**, *155* (2), 189–194.

([157]) Radon, M.; Pierloot, K., Binding of CO, NO and $O_2$ to heme by density functional and multireference ab-initio calculations, *J. Phys. Chem. A*, **2008**, *112*, 11824-11832.

([158]) Schapiro, I. ; Sivalingam, K. ; Neese, F., Assessment of n-electron valence state perturbation theory for vertical excitation energies, *J. Chem. Theory Comput.,* **2013**, 9, 3567-3580.

([159]) (a) Angeli, C. ; Cimiraglia, R. ; Evangelisti, S. ; Leininger, T ; Malrieu, J. P., Introduction of n-electron valence states for multireference perturbation theory, *J. Chem. Phys.*, **2001**, 114, 10252-10264. (b) Angeli, C. ; Cimiraglia, R. ; Malrieu, J. P., n-electron valence state perturbation theory: A spinless formulation and an efficient implementation of the strongly contracted and of the partially contracted variant, *J. Chem. Phys.*, **2002**, 117, 9138-9153.

([160]) (a) Collman, J. P. ; Hoard, J. L. ; Kim, N. ; Lang, G. ; Reed, C. A., Synthesis, Stereochemistry and Structure-related Properties of $\alpha,\beta,\gamma,\delta$-Tetraphenylporphyrinatoiron(II), *J. Am. Chem. Soc*., **1975**, 97, 2676-2681. (b) Hu, C. ; Noll, B. C. ; Schulz, C. E. ; Scheidt, W. R., Four-coordinate iron(II) porphyrinates: electronic configuration change by intermolecular interaction *Inorg. Chem.*, **2006**, 46, 619-621. (c) Boyd, P. D. W. ; Buckingham, D. A. ; McMeeking, R. F. ; Mitra, S., Paramagnetic anisotropy, average magnetic susceptibility, and electronic structure of intermediate-spin S = 1 (5,10,15,10-tetraphenylporphyrin)iron(II), *Inorg. Chem.*, **1979**, 18, 3585-3591

([161]) Kobayashi, H. ; Yanagawa, Y., Electronic spectra and electronic structure of iron(II) tetraphenylporphyrins, *Bull. Chem. Soc. Jap.*, **1972**, 45, 450-456

([162]) (a) Behere, D. V. ; Birdy, R. ; Mitra, S., Effect of axial interaction in high-spin iron(III) porphyrins. Paramagnetic anisotropy and zero-field splitting in (tetraphenylporphyrin)iron(III) thiocyanate and and iodide, *Inorg. Chem.,* **1981**, 20, 2786-2789. (b) Hanato, K. ; Scheidt, W. R., Molecular Stereochemistry of Iodo(mesa-tetraphenylporphinato)iron(III), *Inorg. Chem*, **1979**, 18, 877-879

([163]) Scheidt, W. R., Kastner, M.E., Hatano, K., Stereochemistry of the toluene solvate of $\alpha,\beta,\gamma,\delta$-tetraphenylporphyrinatozinc(II), *Inorg. Chem.*, **1978**, 17, 706-710

([164]) Sontum, S. F. ; Case, D. A. ; Karplus, M., Xa multiple scattering calculations on iron(II) porphine, *J. Chem. Phys*, **1983**, 79, pp 2881-2892.

([165]) Kashiwagi, H. ; Obara, S. ; Ab-initio MO studies of electronic states and Mössbauer spectra of high-, intermediate-, and low-spin Fe(II)-porphyrin complexes, *J. Chem. Phys.,* **1982**, 77, 3155-

([166]) Kitagawa, T. ; Teraoka, J., The resonance Raman spectra of intermediate-spin ferrous porphyrin, *Chem. Phys. Lett.,* **1979**, 63, 443-445

([167]) Goff, H., LaMar, G. N. ; Reed, C. A., Electron density studies of porphyrins and phtalocyanine. IV. Electron density distribution in crystals of (meso-tetraphenylporphyrinato)iron(II), *J. Am. Chem. Soc.*, **1979**, 99, 3641-3646.

([168]) Goff, H. ; LaMar, Gerd, Reed, C. A., Nuclear magnetic resonance investigation of magnetic and electronic properties of "intermediate spin" ferrous porphyrin complexes, *J. Am. Chem. Soc.*, **1977**, 99, 3641-3646.

([169]) Lang, G. ; Spartalian, K. ; Reed, C. A. ; Collman, J. P., Mössbauer effect study of the magnetic properties of S=1 ferrous tetraphenylporphyrin, *J. Chem. Phys.*, **1978**, 69, 5424-5427

([170]) (a) Choe, Y-K. ; Hashimoto, T. ; Nakano, H. ; Hirao, K., Theoretical study of the electronic ground state of iron(II) porphine, *Chem. Phys. Lett.,* **1998**, 295, 380-388. (b) Choe, Y. K. ; Nakajima, T. ; Hirao, K. ; Lindh, R., Theoretical study of the ground state of the electronic ground state of iron(II) porphine. II, *J. Chem. Phys.*, **1999**, 111, 3837.

([171]) Singh, S. K. ; Eng, J. ; Atanasov, M. ; Neese, F. N. , Covalency and chemical bonding in transition metal complexes: an ab-initio based ligand field perspective, *Coord. Chem. Rev.*, **2017**, 344, 2-25.

([172]) Radon, M., Spin-state energetics of heme-related models from DFT and coupled-cluster calculations, *J. Chem. Theory Comput*., **2014**, 10, 2306−2321.

([173]) Manni, G. L. ; Alavi, A., Understanding the mechanism stabilizing intermediate spin states in Fe(II)-porphyrin *J. Phys. Chem. A,* **2018**, 122, 22, 4935-4947

([174]) (a) Hirao, K., Multireference Møller-Plesset method, *Chem. Phys. Lett.,* **1992**, 190, 374-380. (b) Hirao, K., Multireference Møller-Plesset perturbation theory for high-spin open-shell systems, *Chem. Phys. Lett.*, **1992**, 196, 397-403. (c) Hirao, K., State-specific multireference Møller-Plesset perturbation treatment for singlet and triplet excited states, ionized states and electron attached states of $H_2O$, *Chem. Phys. Lett.*, **1993**, 201, 56-59. (d) Hirao, K., Multireference Møller-Plesset perturbation treatment of potential energy curve of $N_2$, Int. J. Quant. Chem., **1992**, 44, 517-526.

([175]) Rawlings, D. C. ; Gouterman, M., Theoretical investigations of the electronic states of porhyrins. III. Low-lying electronic states of porphinatoiron(II), *Int. J. Quantum Chem.*, **1985**, 28, 773-796

([176]) Pierloot, K. ; Phung, QM. ; Domingo, A., Spin state energetics in First-Row Transition Metal Complexes: Contribution of (3s3p) correlation and its description by second-order perturbation theory, *J. Chem. Theory Comput.*, **2017**, 13, 537−553.

([177]) Altun, A. ; Saitow, Masaaki ; Neese, F. ; Bistoni, G., Local energy decomposition of open-shell molecular systems in the domain-based local pair natural orbital coupled cluster framework, *J. Chem. Theory Comput.*, **2019**, 15, 1616-1632.

([178]) Merrill, B. A., in Encyclopedia of Reagents for Organic synthesis, *John Wiley and Sons*, **2001**.

([179]) Mashiko, T. ; Reed, C. A. ; Haller, K. J. ; Scheidt, W. R., Nature of iron(I) and iron(0) tetraphenylporphyrin complexes. Synthesis and molecular structure of (dibenzo-18-crown-6)bis(tetrahydrofuran)sodium (meso-tetraphenylporphinato)ferrate and bis[tris(tetrahydrofuran)sodium](meso-tetraporphinato)ferrate, *Inorg. Chem.*, **1984**, 23, pp 3192-3196.

([180]) (a) Nehrkorn, J.; Holldack, K.; Bittl, R.; Schnegg, A. Recent Progress in Synchrotron-Based Frequency-Domain Fourier-Transform THz-EPR. *J. Magn. Reson.* **2017**, *280*, 10–19. (b) Nehrkorn, J.; Martins, B. M.; Holldack, K.; Stoll, S.; Dobbek, H.; Bittl, R.; Schnegg, A. Zero-Field Splittings in MetHb and MetMb with Aquo and Fluoro Ligands: A FD-FT THz-EPR Study. *Mol. Phys.* **2013**, *111* (18–19), 2696–2707. (c) Schnegg, A.; Behrends, J.; Lips, K.;

Bittl, R.; Holldack, K. Frequency Domain Fourier Transform THz-EPR on Single Molecule Magnets Using Coherent Synchrotron Radiation. *Phys. Chem. Chem. Phys.* **2009**, *11* (31), 6820-6825.

([181]) Stoll, S.; Schweiger, A. EasySpin, a Comprehensive Software Package for Spectral Simulation and Analysis in EPR. *J. Magn. Reson.* **2006**, *178* (1), 42–55.

([182]) (a) Nehrkorn, J.; Schnegg, A.; Holldack, K.; Stoll, S. General Magnetic Transition Dipole Moments for Electron Paramagnetic Resonance. *Phys. Rev. Lett.* **2015**, *114* (1), 010801. (b) Nehrkorn, J.; Telser, J.; Holldack, K.; Stoll, S.; Schnegg, A. Simulating Frequency-Domain Electron Paramagnetic Resonance: Bridging the Gap between Experiment and Magnetic Parameters for High-Spin Transition-Metal Ion Complexes. *J. Phys. Chem. B* **2015**, *119* (43), 13816–13824.

([183]) (a) F. Neese, ORCA - An ab initio, Density Functional and Semi-empirical Electronic Structure Package, 4.0, *Universität Bonn*, Bonn, Germany, **2017**. (b) Neese, F., Software update: the ORCA program system, version 4.0, *WIREs Comput Mol Sci*, **2018**, 8:e1327.

([184]) Becke, A. D., Density-functional exchange-energy approximation with correct asymptotic behavior, *Phys. Rev. A,* **1988**, 38, 3098

([185]) Ikezaki, A. ; Nakamura, M., Effects on the Solvents on the Electron Configuration of the Low-Spin Dicyano[meso-tetrakis(2,4,6-triethylphenyl)porphyrinato]iron(III) Complex: Importance of the C-H…N Weak Hydrogen Bonding, *Inorg. Chem.,* **2002**, 41, 2761-2768.

([186]) Neese, F. Importance of Direct Spin− Spin Coupling and Spin-Flip Excitations for the Zero-Field Splittings of Transition Metal Complexes: A Case Study. *J. Am. Chem. Soc.,* **2006**, *128* (31), 10213–10222.

([187]) Pipek, J. ; Mezey, P. G., A fast intrinsic localization procedure applicable for ab-initio and semiempirical linear combination of atomic orbital wave-functions, *J. Chem. Phys.*, **1989**, 90, 4916-4926.

([188])Boso, B. ; Lang, G. ; Reed, C. A., A Mössbauer spectroscopic study of the six-coordinate high-spin ferrous compound (meso-tetraphenyloprphinato)bis(tetrahydrofuran) iron(II), *J. Chem. Phys.*, **1983**, 78, 2561-2567.

([189]) Strauss, S. H. ; Pawlik, M. J., ring-induced rhombicity in chlorin and isobacteriochlorin complexes of square-planar iron, *Inorg. Chem.,* **1986**, 25, 1921-1923

([190]) Strauss, S. H. ; Silver, M. E. ; Long, K. M. ; Thompson, R. G. ; Hudgens, R. A. ; Spartalian, K. ; Ibers, J. A., Comparison of the molecular and electronic structure of (2,3,7,8,12,13,17,18-octaethylporphyrinato)iron(II) and (trans-7,8-Dihydro-2,3,7,8,12,13,17,18-octaethylporphyrinato)iron(II), *J. Am. Chem. Soc.*, **1985**, 107, 4207-4215

([191]) Dolphin, D. ; Sams, J. R. ; Tsin, T. B. ; Wong, K.L., synthesis and Mössbauer spectra of octaethylporphyrin ferrous complexes, *J. Am. Chem. Soc*., **1976**, 98, 6970-6975

([192]) Filoti, G. ; Kuz'Min, M.D. ; Bartolomé, Mössbauer study oft he hyperfine interactions and spin dynamics in $\alpha$-iron(II) phtalocyanine, *J. Phys. Rev. B*, **2006**, 74, 134420

([193]) Zhang, Y.; Mao, J.; Godbout, N.; Oldfield, E. Mössbauer Quadrupole Splittings and Electronic Structure in Heme Proteins and Model Systems: A Density Functional Theory Investigation. *J. Am. Chem. Soc.* **2002**, *124* (46), 13921–13930.

([194]) Bhattacharjee, A. ; Chavarot-Kerlidou, M. ; Dempsey, J. L. ; Gray, H. B. ; Fujita, E. ; Muckerman, J. T. ; Fontecave, M. ; Artero, V. ; Arantes, G. M. ; Field, M. J., Theoretical modeling of low-energy electronic absorption bands in reduced cobaloximes, *ChemPhysChem*, **2014**, 15, 2951-2958

([195]) Dunn, T. M., Spin-orbit coupling in the first and second transition series, *Trans. Faraday Soc.*, **1961**, 57, 1441-1444

([196]) (a) Andres, H. ; Bominar, E. L. ; Smith, J. M. ; Eckert, N. A. ; Holland, P. L. ; Münck, E., Planar three-coordinate high-spin $Fe^{II}$ complexes with large orbital angular momentum: Mössbauer, Electron Paramagnetic Resonance, and electronic structure studies, *J. Am. Chem. Soc.*, **2002**, 124, 3012-3025. (b) Stoian, S. A. ; Yu, Y. ; Smith, J. M. ; Holland, P. L. ; Bominaar,

E. L. ; Münck, E., Mössbauer, Electron Paramagnetic Resonance and crystallographic characterization of a high-spin Fe(I) Diketiminate complex with orbital degeneracy, *Inorg. Chem.*, **2005**, 44, 4915-4922. (c) Zadrosny, J. M. ; Atanasov, M. ; Bryan, A. ; Lin, C-Y. ; Rekken, B. D. ; Power, P. P. ; Neese, F. ; Long, J. R., Slow magnetization dynamics in a series of two-coordinate iron(II) complexes, *Chem. Sci.*, **2013**, 4, 125-138.

([197]) Griffith, J. S. in the theory of transition metal ions, *cambridge university press*, **1961**

([198]) (a) Lang, G., Marshall, W., Mössbauer effect in some haemoglobin compounds, *J. Mol. Biol*., **1966**, 385-404. (b) Johnson, C. E., Hyperfine field of $^{57}$Fe in hemin, *Phys. Lett.,* **1966**, 21, 491-492. (c) Lang, G., Mössbauer spectroscopy of haem proteins, *Quarterly Reviews of Biophysics* 3, **1970**, 1, 1-60.

([199]) (a) Myers, W. K.; Scholes, C. P.; Tierney, D. L. Anisotropic Fermi couplings due to large unquenched orbital angular momentum: Q-band (1)H, (14)N, and (11)B ENDOR of bis(trispyrazolylborate) cobalt(II), *J. Am. Chem. Soc.* **2009**, *131*, 10421–10429; (b) McGarvey, B. R.; Nagy, S. Evidence for an anisotropic contact shift. Proton NMR study of line shapes in uranocene and tricyclopentadienyl uranium chloride, (C5H5)3UCl, powders, *Inorg. Chem.* **2002**, *26*, 4198–4203.

([200]) (a) Lin, W. C., Further work on the calculation of d-orbital energies of cobalt porphyrins from electron spin resonance data, *Inorg. Chem.*, **1980**, 19, 1072-1073. (b) Iwaizumi, M. ; Ohba, Y., EPR and ENDOR studies of charge transfer interaction of cobalt(II) and copper(II) porphyrins with $\pi$-donors and acceptors, *Inorganica Chimica Acta*, **1984**, 82, 47-52. (c) Baumgarten, M. ; Winscom, C. J. ; Lubitz, W., Probing the surrounding o a cobalt(II) porphyrin and its superoxo complex by EPR technique, *Appl. Magn. Res.*, **2001**, 20, 35-70.

([201]) Taylor, C. P. S., The EPR of low-spin heme complexes relation of the $\tau_{2g}$ hole model to the directional properties of the g-tensor, and a new method for calculating the ligand-field parameters, *Biochimica et biophysica Acta*, **1977**, 491, 137-149.

([202]) Walker, A., Magnetic spectroscopic (EPR, ESEEM, Mössbauer, MCD and NMR) studies of low-spin ferriheme centers and their corresponding heme proteins, *Coord. Chem. Rev.*, **1999**, 185-186, 471-534.

([203]) (a) Merill, W. A.; Stich, T. A.; Brynda, M.; Yeagle, G. J.; Fettinger, J. C.; De Hont, R.; Reiff, W. M.; Schulz, C. E.; Britt, R. D.; Power, P. P., Direct spectroscopic observation of large quenching of first-order orbital angular momentum with bending in monomeric, two-coordinate Fe(II) primary amido complexes and the profound magnetic effects in the absence of Jahn-Teller and Renner-Teller distortions in rigorously linear coordination, *J. Am. Chem. Soc.*, **2009**, *131*, 12693-12702; (b) Cheng, J.; Liu, J.; Leng, X.; Lohmiller, T.; Schnegg, A.; Bill, E.; Ye, S.; Deng, L. A Two-Coordinate Iron(II) Imido Complex with NHC Ligation: Synthesis, Characterization, and Its Diversified Reactivity of Nitrene Transfer and C–H Bond Activation, *Inorg. Chem.* **2019**, *58*, 7634–7644; (c) Zadrozny, J. M.; Xiao, D. J.; Long, J. R.; Atanasov, M.; Neese, F.; Grandjean, F.; Long, G. J. Mössbauer Spectroscopy as a Probe of Magnetization Dynamics in the Linear Iron(I) and Iron(II) Complexes [Fe(C(SiMe3)3)2]1-/0 . *Inorg. Chem.* **2013**, *52*, 13123-13131; (d) Bryan, A. M.; Lin, C.-Y.; Sorai, M.; Miyazaki, Y.; Hoyt, H. M.; Hablutzel, A.; LaPointe, A.; Reiff, W. M.; Power, P. P.; Schulz, C. E. Measurement of Extreme Hyperfine Fields in Two-Coordinate High Spin Fe2+ Complexes by Mössbauer Spectroscopy: Essentially FreeIon Magnetism in the Solid State, *Inorg. Chem.* **2014**, *53*, 12100-12107; (e) Reiff, W. M.; Schulz, C. E.; Whangbo, M.-H.; Seo, J. I.; Lee, Y. S.; Potratz, G. R.; Spicer, C. W.; Girolami, G. S. Consequences of a Linear Two-Coordinate Geometry for the Orbital Magnetism and Jahn-Teller Distortion Behavior of the High Spin Iron(II) Complex Fe[N(t-Bu)2]2; *J. Am. Chem. Soc.* **2009**, *131*, 404−405; (f) Reiff, W. M.; LaPointe, A. M.; Witten, E. H. Virtual Free Ion Magnetism and the Absence of Jahn-Teller Distortion in a Linear Two-Coordinate Complex of High-Spin Iron(II), *J. Am. Chem. Soc.* **2004**, *126*, 10206−10207.

([204]) Chang, H.-C.; Mondal, B.; Fang, H.; Neese, F.; Bill, E.; Ye, S. Electron Paramagnetic Resonance Signature of Tetragonal Low Spin Iron(V)-Nitrido and -Oxo Complexes Derived from the Electronic Structure Analysis of Heme and Non-Heme Archetypes, *J. Am. Chem. Soc.* **2019**, *141*, 2421–2434.

([205]) Bijl, D. Paramagnetic Resonance Absorption in Titanium Caesium Alum at Low Temperatures, *Proc. Phys. Soc. A* **1950**, *63*, 405–406.

([206]) Hickman, D. L.; Shirazi, A. ; Goff, H. M., Deuterium NMR spectroscopic studies of low-valent iron porphyrin species, *Inorg. Chem.*, **1985**, 24, 563-566.

([207]) Lexa, D. ; Momenteau, M. ; Mispelter, J., Characterization of the reduction steps of Fe(III) porphyrins, *Biochim. Biophys. Acta*, **1974**, 338, 151-163.

[208] Cohen, I. A. ; Ostfeld, D. ; Lichtenstein, B., Characterization of a $d^7$ iron system. Tetraphenylporphyrineiron(I) anion, *J. Am. Chem. Soc.,* **1972**, 94, 4522-4525.

([209]) Sinyakov, G. N. ; Shulga, A. M. 1H NMR spectra and electronic structure of reduced iron porphyrins: Fe(II), Fe(I) and Fe(0) porphyrins. *J. Mol. Struct.* **1993**, 295, 1−14.

([210]) Yamaguchi, K. ; Morishima, I., Low-valent iron porphyrins. NMR evidence for $\pi$-anion-radical character in two-electron-reduced iron(III) Meso- or $\beta$-Pyrrole substituted porphyrins, *Inorg. Chem.*, **1992**, 31, 3216-3222.

([211]) Reed, C. A., Iron(I) and iron(IV) porphyrins, *Adv. Chem. Ser.*, **1982**, 201, 33-356.

([212]) Anxolabéhère, E. ; Chottard, G. ; Lexa, D., Highly-reduced iron porphyrins: UV-vis and resonance Raman spectroelectrochemical studies of FeTPP and $FeTF_5PP$, *New J. Chem.*, **1994**, 18, 889-899.

([213]) Donohoe, R. J. ; Atamian, M. ; Bocian, D. F., Characterization of singly-reduced iron(II) porphyrins, *J. Am. Chem. Soc.*, **1987**, 109, 5593-5599.

([214]) Walker, F. A., Pulsed EPR and NMR spectroscopy of paramagnetic iron porphyrinates and related iron macrocycles: how to understand patterns of spin delocalization and recognize macrocycle radicals, *Inorg. Chem.*, **2003**, 42, 15, 4526-4544.

([215]) Aycock, D. F., Solvent applications of 2-methyltetrahydrofuran in organometallic and biphasic reactions, *Org. Process Res. Dev.*, **2007**, 11, 156-159.

([216]) Bühl, M. ; Kabrede, H., Geometries of transition-metal complexes from density functional theory, J. Chem. Theory Comput., 2006, 2, 1282-1290.

([217]) Grimme, S.; Antony, J.; Ehrlich, S.; Krieg, H. A Consistent and Accurate Ab Initio Parametrization of Density Functional Dispersion Correction (DFT-D) for the 94 Elements H-Pu. *J. Chem. Phys.,* **2010**, *132* (15), 154104.

([218]) Grimme, S.; Ehrlich, S.; Goerigk, L. Effect of the Damping Function in Dispersion Corrected Density Functional Theory. *J. Comput. Chem.,* **2011**, *32* (7), 1456–1465.

([219]) Yanai, T. ; Tew, D. P., Handy, N. C., A new hybrid exchange-correlation functional using the Coulomb-attenuating method (CAM-B3LYP), Chem. Phys. Let., 2004, 393, 51-57.

([220]) F. Neese, F. Wennmohs, A. Hansen, U. Becker, Efficient, approximate and parallel Hartree-Fock and hybrid DFT calculations. A 'chain-of-sphere' algorithm for the Hartree-Fock exchange, *Chem. Phys.*, **2009**, 356, 98-109.

([221]) Van Lenthe, E. ; Baerends, E. J. ; Snijders, J. G., Relativistic regular two-component Hamiltonians, *J. Chem. Phys.*, **1993**, 99, 6, 4597-4610.

([222]) Pantazis, D. A. ; Chen, X. Y. ; Landis, C. R. ; Neese, F., All-Electron Scalar Relativistic Basis Sets for Third-Row Transition Metal Atoms, *J. Chem. Theory Comput.*, 2008, 4, 908-919.

([223]) Cabrero, J. ; Calzado, C. J. ; Maynau, D. ; Caballol, R. ; Malrieu, J. P., Metal-ligand delocalization in magnetic orbitals of binuclear complexes, *J. Phys. Chem. A*, 2002, 106, 8146-8155.

([224]) Martin, R. L., Natural Transition Orbitals., *J. Chem. Phys.,* **2003**, *118* (11), 4775–4777.

([225]) Conradie, J. ; Gosh, A., Energetics of saddling versus rufling in metalloporphyrins: unusual ruffled dodecasubstituted porphyrins, *ACS Omega*, **2017**, 2, 6708-6714.

([226]) K. Yamaguchi Y. Takahara T. Fueno in: V.H. Smith (Ed.) *Applied Quantum Chemistry. Reidel*, Dordrecht (1986), pp 155

([227]) Oshio, H.; Ama, T.; Watanabe, T.; Kincaid, J.; Nakamoto, K. Structure Sensitive Bands in the Vibrational Spectra of Metal Complexes of Tetraphenylporphine. *Spectrochimica Acta Part A: Molecular Spectroscopy* **1984**, *40* (9), 863–870.

([228]) De Silva, C. ; Czarnecki, K. ; Ryan, M. D., Visible and resonance Raman spectra of low-valent iron porphyrins, Inorg. Chim. Acta, 1999, 287, 21-26.

([229]) Paulat, F.; Praneeth, V.; Näther, C.; Lehnert, N. Quantum Chemistry-Based Analysis of the Vibrational Spectra of Five-Coordinate Metalloporphyrins [M (TPP) Cl]. *Inorg. Chem.,* **2006**, *45* (7), 2835–2856.

([230]) Felton, R. H.; Linschitz, H. Polarographic Reduction of Porphyrins and Electron Spin Resonance of Porphyrin Anions1. *J. Am. Chem. Soc.,* **1966**, *88* (6), 1113–1116.

([231]) Reed, R. A.; Purrello, R.; Prendergast, K.; Spiro, T. G. Resonance Raman Characterization of the Radical Anion and Triplet States of Zinc Tetraphenylporphine. *J. Phys. Chem.,* **1991**, *95* (24), 9720–9727.

([232]) Jonas, V.; Thiel, W. Theoretical Study of the Vibrational Spectra of the Transition Metal Carbonyls M $(CO)_6$ [M= Cr, Mo, W], M$(CO)_5$ [M= Fe, Ru, Os], and M $(CO)_4$ [M= Ni, Pd, Pt], *J. Chem. Phys.,* **1995**, *102* (21), 8474–8484.

([233]) Jonas, V.; Thiel, W. Density Functional Study of the Vibrational Spectra of Octahedral Transition-Metal Hexacarbonyls: Neutral Molecules (M= Cr, Mo, W) and Isoelectronic Ions (M= V, Nb, Ta; Mn, Re; Fe, Ru, Os; Co, Rh, Ir; Pt; Au), *Organometallics,* **1998**, *17* (3), 353–360.

([234]) Lee, S.-Y.; Heller, E. J. Time-Dependent Theory of Raman Scattering. *The J. Chem. Phys.,* **1979**, *71* (12), 4777

([235]) Petrenko, T.; Neese, F. Analysis and Prediction of Absorption Band Shapes, Fluorescence Band Shapes, Resonance Raman Intensities, and Excitation Profiles Using the Time-Dependent Theory of Electronic Spectroscopy, *J. Chem. Phys.,* **2007**, *127* (16), 164319

([236]) Manbeck, G. F.; Fujita, E. A Review of Iron and Cobalt Porphyrins, Phthalocyanines and Related Complexes for Electrochemical and Photochemical Reduction of Carbon Dioxide. *Journal of Porphyr. Phthalocyanines,* **2015**, *19*, 45–64.

([237]) (a) Costentin, C. ; Passard, G. ; Robert, M. ; Saveant, J.M., Ultraefficient homogeneous catalyst for the CO2-to-CO electrochemical conversion, *PNAS*, **2014**, 111, 14990-14994. (b) Azcarate, I. ; Costentin, C. ; Robert, M., Savéant ; J.M., Through-space charge interaction substituent effects in molecular catalysis leading to the design of the most efficient catalyst of CO2-to-CO electrochemical conversion, *J. Am. Chem. Soc.*, **2016**, 138, 16639-16644. (c) Khadhraoui, A.; Gotico, P.; Boitrel, B.; Leibl, W.; Halime, Z.; Aukauloo, A. Local Ionic Liquid Environment at a Modified Iron Porphyrin Catalyst Enhances the Electrocatalytic Performance of CO 2 to CO Reduction in Water. *Chem. Comm,.* **2018**, *54* (82), 11630–11633.

([238]) Harvey, J. N.; Himo, F.; Maseras, F.; Perrin, L. Scope and Challenge of Computational Methods for Studying Mechanism and Reactivity in Homogeneous Catalysis. *ACS Catal.,* **2019**, *9* (8), 6803–6813.

([239]) (a) Tinnemans, A.; Koster, T.; Thewissen, D.; Mackor, A. Tetraaza-macrocyclic Cobalt (II) and Nickel (II) Complexes as Electron-transfer Agents in the Photo (Electro) Chemical and Electrochemical Reduction of Carbon Dioxide. *Recl. Trav. Chim. Pays Bas.*, **1984**, *103* (10), 288–295. (b) Sheng, H.; Frei, H. Direct Observation by Rapid-Scan FT-IR Spectroscopy of Two-Electron-Reduced Intermediate of Tetraaza Catalyst [CoIIN4H (MeCN)]$^{2+}$ Converting $CO_2$ to CO. *J. Am. Chem. Soc.,* **2016**, *138* (31), 9959–9967.

([240]) (a) Scheiring, T.; Klein, A.; Kaim, W. EPR Study of Paramagnetic Rhenium (I) Complexes (Bpy>>·>>–>>) Re $(CO)_3X$ Relevant to the Mechanism of Electrocatalytic $CO_2$ Reduction. *J. Chem. Soc., Perkin Trans. 2,* **1997**, No. 12, 2569–2572. (b) Smieja, J. M. ; Kubiac, C. P., Re(bipy-tBu)$(CO)_3$Cl – improved catalytic activity for reduction of carbon dioxide: IR-spectroelectrochemical and mechanistic studies, *Inorg. Chem.*, **2010**, 49, 9293-9289. (c) Benson, E. E.; Sampson, M. D.; Grice, K. A.; Smieja, J. M.; Froehlich, J. D.; Friebel, D.; Keith, J. A.; Carter, E. A.; Nilsson, A.; Kubiak, C. P. The Electronic States of Rhenium Bipyridyl Electrocatalysts for $CO_2$ Reduction as Revealed by X-ray Absorption Spectroscopy and Computational Quantum Chemistry. *Angew. Chem. Int. Ed.,* **2013**, *52* (18), 4841–4844. (d) Riplinger, C.; Sampson, M. D.; Ritzmann, A. M.; Kubiak, C. P.; Carter, E. A. Mechanistic Contrasts between Manganese and Rhenium Bipyridine Electrocatalysts for the Reduction of Carbon Dioxide. *J. Am. Chem. Soc.,* **2014**, *136* (46), 16285–16298.

([241]) Gonglach, S.; Paul, S.; Haas, M.; Pillwein, F.; Sreejith, S. S.; Barman, S.; De, R.; Müllegger, S.; Gerschel, P.; Apfel, U.-P. Molecular Cobalt Corrole Complex for the Heterogeneous Electrocatalytic Reduction of Carbon Dioxide. *Nat. Commun.,* **2019**, *10* (1), 1–10.

([242]) (a) Lewis, J.; Schröder, M., Reduction of Schiff-Base Macrocyclic Complexes. Stabilisation of Nickel (I) Conjugated Macrocyclic Complexes via a Reversible Ligand-to-Metal Electron-Transfer Process. *J. Chem. Soc., Dalton Trans.,* **1982**, No. 6, 1085–1089. (b) Ghosh, M.; Weyhermüller, T.; Wieghardt, K. Electronic Structure of the Members of the Electron Transfer Series $[NiL]^z$ (Z= 3+, 2+, 1+, 0) and [NiL(X)]n (X= Cl, CO, P (OCH 3) 3) Species Containing a Tetradentate, Redox-Noninnocent, Schiff Base Macrocyclic Ligand L: An Experimental and Density Functional Theoretical Study. *Dalton Trans.,* **2010**, *39* (8), 1996–2007.

[243] Elgrishi, N.; Chambers, M. B.; Wang, X.; Fontecave, M. Molecular Polypyridine-Based Metal Complexes as Catalysts for the Reduction of $CO_2$. *Chem. Soc. Rev.,* **2017**, *46* (3), 761–796.

([244]) Loipersberger, M.; Zee, D. Z.; Panetier, J. A.; Chang, C. J.; Long, J. R.; Head-Gordon, M. Computational Study of an Iron (II) Polypyridine Electrocatalyst for $CO_2$ Reduction: Key Roles for Intramolecular Interactions in $CO_2$ Binding and Proton Transfer. *Inorg. Chem.,* **2020**.

([245]) (a) Agarwal, J.; Shaw, T. W.; Stanton III, C. J.; Majetich, G. F.; Bocarsly, A. B.; Schaefer III, H. F. NHC-Containing Manganese (I) Electrocatalysts for the Two-Electron Reduction of $CO_2$. *Angew. Chem.,* **2014**, *126* (20), 5252–5255. (b) Liyanage, N. P.; Dulaney, H. A.; Huckaba, A. J.; Jurss, J. W.; Delcamp, J. H. Electrocatalytic Reduction of $CO_2$ to CO with Re-Pyridyl-NHCs: Proton Source Influence on Rates and Product Selectivities. *Inorg. Chem.,* **2016**, *55* (12), 6085–6094. (c) Su, X.; McCardle, K. M.; Panetier, J. A.; Jurss, J. W. Electrocatalytic $CO_2$ Reduction with Nickel Complexes Supported by Tunable Bipyridyl-N-Heterocyclic Carbene Donors: Understanding Redox-Active Macrocycles. *Chem. Comm.,* **2018**, *54* (27), 3351–3354.

([246]) (a) M. Beley, J. P. Collin, R. Ruppert, J. P. Sauvage, Electrocatalytic Reduction of Carbone Dioxide by Nickel Cyclam2+ in Water: Study of the Factors Affecting the Efficiency and the Selectivity of the Process, *J. Am. Chem. Soc.,* **1986**, 108, 7461-7467. (b) J. D. Froehlich, C. P.

Kubiak, Homogeneous Reduction by Ni(cyclam) at a Glassy Carbon Electrode, *Inorg. Chem.*, **2012**, *51*, 3932-3934.

([247])Bourrez, M.; Molton, F.; Chardon-Noblat, S.; Deronzier, A. [Mn (Bipyridyl)$(CO)_3$Br]: An Abundant Metal Carbonyl Complex as Efficient Electrocatalyst for $CO_2$ Reduction. *Angew. Chem. Int.,* **2011**, *50* (42), 9903–9906.

([248]) (a) Mills, G. ; Jónsson, H. ; Schenter, G. K., Reversible work transition state theory: application to dissociative adsorption of hydrogen, *Surf. Sc.*, **1994**, 324, 305-337. (b) Henkelman, G. ; Jónsson, H., improved tangent estimate in the nudged elastic band method for finding minimum energy paths and saddle points, *J. Chem. Phys.*, **2000**, 113, 9978-9985. (c) Henkelman, G. ; Uberuaga, B. P. ; Jónsson, H., A climbing image nudged elastic band method for finding saddle points and minimum energy paths, *J. Chem. Phys.*, **2000**, 113, 9901-9904.
([249]) (a) Xue, G.; Geng, C.; Ye, S.; Fiedler, A. T.; Neese, F.; Que Jr, L. Hydrogen-Bonding Effects on the Reactivity of [X–FeIII–O–FeIV O](X= OH, F) Complexes toward C–H Bond Cleavage. *Inorg. Chem.,* **2013**, *52* (7), 3976–3984. (b) Wirstam, M.; Lippard, S. J.; Friesner, R. A. Reversible Dioxygen Binding to Hemerythrin. *J. Am. Chem. Soc.,* **2003**, *125* (13), 3980–3987. (c) Ye, S.; Riplinger, C.; Hansen, A.; Krebs, C.; Bollinger, J. M.; Neese, F. Electronic Structure Analysis of the Oxygen-Activation Mechanism by FeII-and A-Ketoglutarate (AKG)-Dependent Dioxygenases. *Chem–Eur. J.,* **2012**, *18* (21), 6555–6567.

([250]) Roth, H. G. ; Romero, N. A. ; Nicewitcz, D. A., Experimental and calculated electrochemical potentials of common organic molecules for applications to single-electron redox chemistry, *Synlett*, **2016**, 27(05), 714-723.

([251]) Isse, A. A. ; Gennaro, A., Absolute potential of the standard hydrogen electrode and the problem of interconversion of potentials in different solvents, *J. Phys. Chem. B*, **2010**, 114, 7894-7899.

([252]) (a) Donohoe, R. J.; Atamian, M.; Bocian, D. F. Characterization of Singly Reduced Iron (II) Porphyrins. *J. Am. Chem. Soc.* **1987**, *109* (19), 5593–5599. (b) Takeda, H.; Cometto, C.; Ishitani, O.; Robert, M. Electrons, Photons, Protons and Earth-Abundant Metal Complexes for Molecular Catalysis of $CO_2$ Reduction. *Acs Catal.,* **2017**, *7* (1), 70–88.

(253) Konezny, S. J. ; Doherty, M. D. ; Luca, O. R.; Crabtree, R. H. ; Soloveichik, G. L. ; Batista, V., Reducttion of systematic uncertainty in DFT redox potentials of transition-metal complexes, *J. Phys. Chem. C.,* **2012**, 116, 10, 6349-6356.

(254) Weihe, H.; Güdel, H. U. Quantitative Interpretation of the Goodenough− Kanamori Rules: A Critical Analysis. *Inorg. Chem.,* **1997**, *36* (17), 3632–3639.

(255) Costentin, C.; Savéant, J.-M.; Tard, C. Ligand "Noninnocence" in Coordination Complexes vs. Kinetic, Mechanistic, and Selectivity Issues in Electrochemical Catalysis. *PNAS,* **2018**, *115* (37), 9104–9109.

(256) Harvey, J. N. Spin-forbidden Reactions: Computational Insight into Mechanisms and Kinetics. *Wiley Interdiscip. Rev. Comput. Mol. Sci.,* **2014**, *4* (1), 1–14.

(257) Wile, B. M.; Trovitch, R. J.; Bart, S. C.; Tondreau, A. M.; Lobkovsky, E.; Milsmann, C.; Bill, E.; Wieghardt, K.; Chirik, P. J. Reduction Chemistry of Aryl-and Alkyl-Substituted Bis (Imino) Pyridine Iron Dihalide Compounds: Molecular and Electronic Structures of [(PDI) 2Fe] Derivatives. *Inorg. Chem.,* **2009**, *48* (9), 4190–4200.

(258) Bowman, A. C.; Milsmann, C.; Bill, E.; Lobkovsky, E.; Weyhermüller, T.; Wieghardt, K.; Chirik, P. J. Reduced N-Alkyl Substituted Bis (Imino) Pyridine Cobalt Complexes: Molecular and Electronic Structures for Compounds Varying by Three Oxidation States. *Inorg. Chem.,* **2010**, *49* (13), 6110–6123.

(259) (a) Smieja, J. M.; Benson, E. E.; Kumar, B.; Grice, K. A.; Seu, C. S.; Miller, A. J.; Mayer, J. M.; Kubiak, C. P. Kinetic and Structural Studies, Origins of Selectivity, and Interfacial Charge Transfer in the Artificial Photosynthesis of CO. *PNAS,* **2012**, *109* (39), 15646–15650. (b) Benson, E. E.; Kubiak, C. P. Structural Investigations into the Deactivation Pathway of the $CO_2$ Reduction Electrocatalyst Re (Bpy)$(CO)_3$Cl. *Chem. Comm.,* **2012**, *48* (59), 7374–7376. (c) Wang, M.; Weyhermüller, T.; Bill, E.; Ye, S.; Wieghardt, K. Structural and Spectroscopic Characterization of Rhenium Complexes Containing Neutral, Monoanionic, and Dianionic Ligands of 2, 2′-Bipyridines and 2, 2′: 6, 2 ″-Terpyridines: An Experimental and Density Functional Theory (DFT)-Computational Study. *Inorg. Chem.,* **2016**, *55* (10), 5019–5036.

(260) Praneeth, V. K.; Ringenberg, M. R.; Ward, T. R. Redox-Active Ligands in Catalysis. *Angew. Chem. Int. Ed.,* **2012**, *51* (41), 10228–10234.

([261]) Boyer, J. L.; Cundari, T. R.; DeYonker, N. J.; Rauchfuss, T. B.; Wilson, S. R. Redox Activation of Alkene Ligands in Platinum Complexes with Non-Innocent Ligands. *Inorg. Chem.,* **2009**, *48* (2), 638–645.

([262]) Kaim, W.; Schwederski, B. Non-Innocent Ligands in Bioinorganic Chemistry—An Overview. *Coord. Chem. Rev.,* **2010**, *254* (13–14), 1580–1588.

([263]) Broere, D. L.; De Bruin, B.; Reek, J. N.; Lutz, M.; Dechert, S.; Van Der Vlugt, J. I. Intramolecular Redox-Active Ligand-to-Substrate Single-Electron Transfer: Radical Reactivity with a Palladium (II) Complex. *J. Am. Chem. Soc.,* **2014**, *136* (33), 11574–11577.

([264]) Que, L.; Tolman, W. B. Biologically Inspired Oxidation Catalysis. *Nature* **2008**, *455* (7211), 333–340.

([265]) Chaudhuri, P.; Hess, M.; Flörke, U.; Wieghardt, K. From Structural Models of Galactose Oxidase to Homogeneous Catalysis: Efficient Aerobic Oxidation of Alcohols. *Angew. Chem. Int. Ed.,* **1998**, *37* (16), 2217–2220.

([266]) Kaim, W. Manifestations of Noninnocent Ligand Behavior. *Inorg. Chem.,* **2011**, *50* (20), 9752–9765.

([267]) Chirik, P. J.; Wieghardt, K. Radical Ligands Confer Nobility on Base-Metal Catalysts. *Science,* **2010**, *327* (5967), 794–795.

([268]) Dzik, W. I.; van der Vlugt, J. I.; Reek, J. N.; de Bruin, B. Ligands That Store and Release Electrons during Catalysis. *Angew. Chem. Int. Ed.,* **2011**, *50* (15), 3356–3358.

([269]) (a) Mao, F.; Tyler, D. R.; Bruce, M. R.; Bruce, A. E.; Rieger, A. L.; Rieger, P. H. Solvent Effects on Electron Delocalization in Paramagnetic Organometallic Complexes: Solvent Manipulation of the Amount of 19-Electron Character in $Co(CO)_3L2$ (L2= a Chelating Phosphine). *J. Am. Chem. Soc.,* **1992**, *114* (16), 6418–6424. (b) Schut, D. M.; Keana, K. J.; Tyler, D. R.; Rieger, P. H. Measurement and Manipulation of the Unpaired Electron Density in 18+ δ Complexes. Correlation of the Charge Density with Reactivity. *J. Am. Chem. Soc.,* **1995**,

*117* (35), 8939–8946. (c) Klein, A.; Vogler, C.; Kaim, W. The δ in 18+ δ Electron Complexes: Importance of the Metal/Ligand Interface for the Substitutional Reactivity of "Re (0)" Complexes (α-Diimine-) ReI $(CO)_3$(X). *Organometallics* **1996**, *15* (1), 236–244.